

Reaction Mechanisms of One- and Two-Electron Oxidations of Alkanesulfinates in Aqueous Media

by

Rajakaruna Mudiyansele Pradeepa Indunil Rajakaruna

A dissertation submitted to the Graduate Faculty of Auburn University
in partial fulfillment of the requirements for the degree of

Doctor of Philosophy

Auburn, Alabama

May 1, 2021

Keywords: Electron-transfer, Methanesulfonyl Iodide, Cysteinesulfinic acid, stopped-flow

Copyright © 2021 by Pradeepa Rajakaruna

Approved by

David M. Stanbury, Chair, Professor Emeritus of Chemistry and Biochemistry

Holly R. Ellis, William P. Molette Professor of Chemistry and Biochemistry

Christian Goldsmith, Professor of Chemistry and Biochemistry

Michael L. McKee, Professor Emeritus of Chemistry and Biochemistry

Angela Calderon, Associate Professor of Harrison School of Pharmacy

Abstract

The one-electron oxidation reactions of the alkanesulfinates L-cysteinesulfinic acid (CSA) and methanesulfinate (MSA) with bis(1,4,7-triazacyclononane)nickel (III) and tris(1,10-phenanthroline)osmium(III) were investigated in aqueous media. Reaction kinetics are observed at 25 °C, $\mu = 0.1$ M (NaCl), under anaerobic as well as aerobic conditions. The reactions are slower under aerobic conditions. Under pseudo-first-order reaction conditions both the oxidation reactions with Ni(III) as well as CSA oxidation by Os(III) show first-order dependence on oxidant and alkanesulfinate concentration with mild inhibition by the reduced form of the oxidant. In Os(III) reaction with MSA, strong inhibition by Os(II) is observed requiring the presence of a spin trap to obtain good first-order fits under pseudo-first-order reaction conditions. In all four reactions, the corresponding alkanesulfonyl radical is formed during the first electron transfer step, consequently yielding the corresponding sulfonate as the major sulfur containing product. The empirical rate-law for the reaction of $[\text{Ni}(\text{tacn})_2]^{3+}$ with CSA in aqueous media is first-order in the alkanesulfinate and Ni(III), and takes the form $-d[\text{Ni(III)}]/dt = k_{\text{OBS}}[\text{Ni(III)}]$, where

$$k_{\text{OBS}} = \frac{K_{a1}[\text{CSA}]_{\text{TOT}}}{\left(\frac{1}{(k_1 K_{a2} + k_2 [\text{H}^+])} + \frac{k'}{K_{a2}}\right) [[\text{Ni}(\text{tacn})_3]^{2+}][\text{H}^+]^2 + [\text{H}^+]K_{a1} + K_{a1}K_{a2}}$$

with $k_1 = (2.70 \pm 0.08) \times 10 \text{ M}^{-1} \text{ s}^{-1}$, $k_2 = (9.6 \pm 0.7) \text{ M}^{-1} \text{ s}^{-1}$ and $k' = (4.7 \pm 0.5) \times 10 \text{ s}$. For the reaction of $[\text{Ni}(\text{tacn})_2]^{3+}$ with MSA, the empirical rate-law is $-d[\text{Ni(III)}]/dt = k_{\text{OBS}}[\text{Ni(III)}]$, where

$$k_{\text{OBS}} = \frac{k_1 K_a [\text{MSA}]_{\text{TOT}}}{(1 + k' [[\text{Ni}(\text{tacn})_3]^{2+}]) (K_a + [\text{H}^+])}$$

with $k_1 = (1.90 \pm 0.05) \times 10^2 \text{ M}^{-1} \text{ s}^{-1}$, and $k' = (2.7 \pm 0.2) \times 10^3 \text{ M}^{-1}$.

Oxidation of CSA by tris(1,10-phenanthroline)osmium(III) yields the empirical rate law $-d[\text{Os(III)}]/dt = k_{\text{OBS}}[\text{Os(III)}]$ where $k_{\text{OBS}} = k[\text{CysSO}_2\text{H}]_{\text{TOT}}/[\text{Os(II)}]$ in the pH range

3.5-5.5 with $k = (7.53 \pm 0.07) \times 10^{-3} \text{ s}^{-1}$. The empirical rate law for MSA oxidation by tris(1,10-phenanthroline)osmium(III) is $-d[\text{Os(III)}]/dt = k_{\text{OBS}}[\text{Os(III)}]^2$ with $k_{\text{OBS}} = k[\text{CH}_3\text{SO}_2\text{H}]/[\text{Os(II)}]$, where $k = (2.4 \pm 0.4) \times 10^3 \text{ M}^{-1} \text{ s}^{-1}$.

Methanesulfonyl iodide is produced in aqueous solutions from the reaction of triiodide with methanesulfinate. Dichroic crystals of $(\text{CH}_3\text{SO}_2\text{I})_4 \cdot \text{KI}_3 \cdot 2\text{I}_2$ are formed from KI/I_2 solutions with high concentrations of CH_3SO_2^- , while dichroic crystals of $(\text{CH}_3\text{SO}_2\text{I})_2 \cdot \text{RbI}_3$ are formed from RbI/I_2 solutions. X-ray crystallography of these two compounds shows that the $\text{CH}_3\text{SO}_2\text{I}$ molecules coordinate through their oxygen atoms to the metal cations and that the S-I bond length is 2.44 Å. At low concentrations of CH_3SO_2^- the solutions remain homogeneous and the sulfonyl iodide is formed in a rapid equilibrium: $\text{CH}_3\text{SO}_2^- + \text{I}_3^- \rightleftharpoons \text{CH}_3\text{SO}_2\text{I} + 2\text{I}^-$, $K_{\text{MSI}} = 1.07 \pm 0.01 \text{ M}$ at 25 °C ($\mu = 0.1 \text{ M}$, NaClO_4). The sulfonyl iodide solutions display an absorbance maximum at 309 nm with a molar absorptivity of $667 \text{ M}^{-1} \text{ cm}^{-1}$. Stopped-flow studies reveal that the equilibrium is established within the dead time of the instrument ($\approx 2 \text{ ms}$). Solutions of $\text{CH}_3\text{SO}_2\text{I}$ decompose slowly to form the sulfonate: $\text{CH}_3\text{SO}_2\text{I} + \text{H}_2\text{O} \longrightarrow \text{CH}_3\text{SO}_3^- + \text{I}^- + 2\text{H}^+$, k_{hyd} . In dilute phosphate buffer this decomposition occurs with $k_{\text{hyd}} = 2.0 \times 10^{-4} \text{ s}^{-1}$; the decomposition rate shows an inverse-squared dependence on $[\text{I}^-]$ because of the K_{MSI} equilibrium.

Acknowledgements

I wish to express my sincere gratitude to Prof. David Stanbury, my thesis advisor for the invaluable guidance he provided throughout my time as his student. His encouragement, unwavering patience, and contagious enthusiasm in research were key motivations for me to complete this work.

I am indebted to late Dr. Michael Meadows and Dr. Alvaro Herrera for their help with NMR data collection, Dr. John Gorden for the valuable tips on successful crystal growth and collecting XRD data, Dr. Melissa Boersma for her help with acquiring and analyzing mass spectra, and Dr. Byron Farnum for allowing me to use his ATR-IR instrument. I appreciate the help from my thesis committee members Prof. Christian Goldsmith, Prof. Holly Ellis, Prof. Michael McKee, and Prof. Angela Calderon for their guidance throughout this process, insightful advice and suggestions on this research work, and their help in preparation of this manuscript.

I am grateful to the American Chemical Society Petroleum Research Fund for partially supporting my research at Auburn and Auburn College of Science and Mathematics for allowing me the opportunity to present research findings at conferences.

I would also like to thank Dr. Ying Hu for helping me get acquainted with the lab instruments when I first joined the lab, undergraduate researchers Mr. David Drinnon and Ms. Summer Moon for their help in my research, and Ms. Yixuan Yang for the valuable research discussions we had and for her friendship.

Finally, I would like to thank my parents and sisters for instilling in me the value of scholarly achievement, and for their continued encouragement, and Isuru for his love and unconditional support.

Table of Contents

1	Introduction	18
1.1	General introduction	18
1.1.1	Alkanesulfinates: importance and functions	20
1.1.2	Reaction kinetics	25
1.1.3	Effect of ionic strength on rate	27
1.1.4	Steady state and pre-equilibrium approximations	28
1.2	Electron-transfer mechanisms	29
1.2.1	Inner and outer-sphere processes	29
1.2.2	Marcus theory and Franck Condon principle	31
1.3	The scope of the dissertation	32
2	Kinetics and mechanism of the oxidation of L-cysteinesulfinic acid by tris(1,10-phenanthroline)osmium(III)	34
2.1	Introduction	34
2.2	Reagents and solutions	35
2.2.1	Reagents used	35
2.2.2	[Os(phen) ₃](CF ₃ SO ₃) ₂ characterization	36
2.2.3	Preparation of solutions	38
2.3	Analytical methods	39
2.4	Results	40
2.4.1	Kinetics of the reaction	40
2.4.2	Rate dependence on [Os(phen) ₃] ²⁺	41
2.4.3	pH dependence of the kinetics	42
2.4.4	Rate dependence on CSA concentration	45
2.4.5	Light dependence of the rate	46
2.4.6	Oxygen effect on the kinetics of the reaction	47
2.4.7	Kinetics with radical scavengers	48
2.4.8	Effect of buffer	53
2.4.9	Effect of Br ⁻ on the reaction rate	55

2.4.10	Reaction stoichiometry	56
2.4.11	Product determination	58
2.4.12	Cyclic voltammetry	62
2.4.13	Yield of osmium containing product	63
2.5	Quantum Calculations	65
2.6	Discussion	67
2.7	Conclusions	70
3	Kinetics and mechanism of the oxidation of L-cysteinesulfinic acid by bis(1,4,7-triazacyclononane)	
	nickel (III)	71
3.1	Introduction	71
3.2	Reagents and solutions	73
3.3	Preparation of bis(1,4,7-triazacyclononane)Ni(II) perchlorate	73
3.4	Preparation of bis(1,4,7-triazacyclononane)Ni(III) perchlorate	74
3.5	Experimental methods	74
3.6	Results	75
3.6.1	Properties of bis(1,4,7-triazacyclononane)Ni(III)	75
3.6.2	Photosensitivity of bis(1,4,7-triazacyclononane)Ni(III)	77
3.6.3	Kinetics of the reaction	78
3.6.4	Rate dependence on presence of $[\text{Ni(II)(tacn)}_2]^{2+}$	79
3.6.5	Rate dependence on the concentration of CSA	80
3.6.6	pH dependence	81
3.6.7	Product identification and stoichiometry	84
3.6.8	Reaction stoichiometry	87
3.7	Discussion	90
3.8	Conclusions	93
4	Kinetics and mechanism of methanesulfinic acid oxidation by bis(1,4,7-triazacyclononane)	
	nickel (III)	94
4.1	Introduction	94

4.2	Reagents and solutions	95
4.3	Experimental methods	96
4.4	Computational Methods	97
4.5	Results	97
4.5.1	Kinetics of the reaction	97
4.5.2	Rate dependence on presence of $[\text{Ni(II)(tacn)}_2]^{2+}$	98
4.5.3	Rate dependence on the concentration of MSA	100
4.5.4	pH dependence	101
4.5.5	Product identification and stoichiometry	103
4.5.6	Yield of Ni(II) from the reaction between MSA and Ni(III)	107
4.6	Structures of CH_3SO_2^- and $\text{CH}_3\text{SO}_2^\bullet$	108
4.7	Discussion	111
4.8	Conclusions	115

5 Kinetics and mechanism of methanesulfinate oxidation by tris(1,10-phenanthroline) osmium(III) 116

5.1	Introduction	116
5.2	Reagents, solutions, and methods	117
5.2.1	Reagents	117
5.2.2	Preparation of solutions	118
5.2.3	Analytical instrumentation and methods	118
5.2.4	Computational Studies	119
5.3	Results	119
5.3.1	Kinetics of the reaction	119
5.3.2	Second-order fits of kinetic experiments	121
5.3.3	Kinetic traces with PBN	128
5.3.4	Stoichiometry of the reaction in the presence of PBN	134
5.3.5	Stoichiometry of the reaction without PBN	135
5.3.6	Yield of osmium containing product	136
5.4	Discussion	137

5.5	Conclusions	139
6	Kinetics and mechanism of the two-electron oxidation of methanesulfinate by aqueous tri-iodide	141
6.1	Introduction	142
6.2	Reagents and solutions	142
6.3	Instrumentation and methods	143
6.3.1	Solution-phase studies	144
6.3.2	Computational studies	144
6.4	Synthesis of $(\text{CH}_3\text{SO}_2\text{I})_4 \cdot \text{KI}_3 \cdot 2\text{I}_2$	144
6.5	Synthesis of $(\text{CH}_3\text{SO}_2\text{I})_2 \cdot \text{RbI}_3$	145
6.6	Results	145
6.6.1	$(\text{CH}_3\text{SO}_2)_2 \cdot \text{RbI}_3$	148
6.6.2	$(\text{CH}_3\text{SO}_2\text{I})_4 \cdot \text{KI}_3 \cdot 2\text{I}_2$	150
6.6.3	Quantum Structure, Polarity, and Energetics of $\text{CH}_3\text{SO}_2\text{I}$	152
6.6.4	$\text{CH}_3\text{SO}_2\text{I}$ Formation in Solution.	156
6.7	$\text{CH}_3\text{SO}_2\text{I}$ Decomposition in Solution.	161
6.8	Conclusions	165
	References	166
	Appendix A Further experimental details related to Chapters 2-6	175
A.1	Kinetic data tables for Chapter 2	176
A.2	Kinetic data tables for Chapter 3	181
A.3	Kinetic data tables for Chapter 4	185
A.4	Kinetic data tables for Chapter 5	189
A.5	Kinetic tables for Chapter 6	194
	Appendix B Preliminary results on the two-electron oxidation reaction of hypotaaurine by tri-iodide	196
B.1	Equilibrium between I_3^- , Htau, HtauI, and I^-	197

B.2	DFT calculations	203
Appendix C Crystallographic figures and tables		205
C.1	Crystallographic data for $(\text{CH}_3\text{SO}_2\text{I})_2 \cdot \text{RbI}_3$	206
C.1.1	Sample and crystal data for $(\text{CH}_3\text{SO}_2\text{I})_2 \cdot \text{RbI}_3$	208
C.1.2	Atomic coordinates and equivalent isotropic atomic displacement parameters (\AA^2) for $(\text{CH}_3\text{SO}_2\text{I})_2 \cdot \text{RbI}_3$	209
C.1.3	Bond lengths (\AA) for $(\text{CH}_3\text{SO}_2\text{I})_2 \cdot \text{RbI}_3$	211
C.1.4	Bond angles ($^\circ$) for $(\text{CH}_3\text{SO}_2\text{I})_2 \cdot \text{RbI}_3$	212
C.1.5	Torsion angles ($^\circ$) for $(\text{CH}_3\text{SO}_2\text{I})_2 \cdot \text{RbI}_3$	216
C.1.6	Anisotropic atomic displacement parameters (\AA^2) for the crystals of $(\text{CH}_3\text{SO}_2\text{I})_2 \cdot \text{RbI}_3$	216
C.1.7	Hydrogen atomic coordinates and isotropic atomic displacement parameters (\AA^2) for $(\text{CH}_3\text{SO}_2\text{I})_2 \cdot \text{RbI}_3$	218
C.2	Crystallographic data for $(\text{CH}_3\text{SO}_2\text{I})_4 \cdot \text{KI}_3 \cdot 2\text{I}_2$	218
C.2.1	Sample and crystal data for $(\text{CH}_3\text{SO}_2\text{I})_4 \cdot \text{KI}_3 \cdot 2\text{I}_2$	221
C.2.2	Atomic coordinates and equivalent isotropic atomic displacement parameters (\AA^2) for $(\text{CH}_3\text{SO}_2\text{I})_4 \cdot \text{KI}_3 \cdot 2\text{I}_2$	223
C.2.3	Bond lengths (\AA) for $(\text{CH}_3\text{SO}_2\text{I})_4 \cdot \text{KI}_3 \cdot 2\text{I}_2$	225
C.2.4	Bond angles ($^\circ$) for $(\text{CH}_3\text{SO}_2\text{I})_4 \cdot \text{KI}_3 \cdot 2\text{I}_2$	226
C.2.5	Torsion angles ($^\circ$) for $(\text{CH}_3\text{SO}_2\text{I})_4 \cdot \text{KI}_3 \cdot 2\text{I}_2$	229
C.2.6	Anisotropic atomic displacement parameters (\AA^2) for crystals of $(\text{CH}_3\text{SO}_2\text{I})_4 \cdot \text{KI}_3 \cdot 2\text{I}_2$	230
C.2.7	Hydrogen bond distances (\AA) and angles ($^\circ$) for $(\text{CH}_3\text{SO}_2\text{I})_4 \cdot \text{KI}_3 \cdot 2\text{I}_2$	231
C.2.8	Hydrogen atomic coordinates and isotropic atomic displacement parameters (\AA^2) for $(\text{CH}_3\text{SO}_2\text{I})_4 \cdot \text{KI}_3 \cdot 2\text{I}_2$	232
C.3	$\text{Ca}_2(\text{CH}_3\text{SO}_2)_2(\text{CH}_3\text{SO}_3)\text{I}_3 \cdot (\text{H}_2\text{O})_3$	232
C.3.1	Crystal data and structure refinement for the crystals of $\text{Ca}_2(\text{CH}_3\text{SO}_2)_2(\text{CH}_3\text{SO}_3)\text{I}_3 \cdot (\text{H}_2\text{O})_3$	235

C.3.2	Atomic coordinates and equivalent isotropic atomic displacement parameters (\AA^2) for $\text{Ca}_2(\text{CH}_3\text{SO}_2)_2(\text{CH}_3\text{SO}_3)\text{I}_3\cdot(\text{H}_2\text{O})_3$	236
C.3.3	Bond lengths (\AA) for $\text{Ca}_2(\text{CH}_3\text{SO}_2)_2(\text{CH}_3\text{SO}_3)\text{I}_3\cdot(\text{H}_2\text{O})_3$	238
C.3.4	Bond angles ($^\circ$) for $\text{Ca}_2(\text{CH}_3\text{SO}_2)_2(\text{CH}_3\text{SO}_3)\text{I}_3\cdot(\text{H}_2\text{O})_3$	239
C.3.5	Torsion angles ($^\circ$) for $\text{Ca}_2(\text{CH}_3\text{SO}_2)_2(\text{CH}_3\text{SO}_3)\text{I}_3\cdot(\text{H}_2\text{O})_3$	242
C.3.6	Anisotropic atomic displacement parameters (\AA^2) for the crystals of $\text{Ca}_2(\text{CH}_3\text{SO}_2)_2(\text{CH}_3\text{SO}_3)\text{I}_3\cdot(\text{H}_2\text{O})_3$	243
C.3.7	Hydrogen atomic coordinates and isotropic atomic displacement parameters (\AA^2) for $\text{Ca}_2(\text{CH}_3\text{SO}_2)_2(\text{CH}_3\text{SO}_3)\text{I}_3\cdot(\text{H}_2\text{O})_3$	245
C.3.8	Hydrogen bond distances (\AA) and angles ($^\circ$) for the crystals of $\text{Ca}_2(\text{CH}_3\text{SO}_2)_2(\text{CH}_3\text{SO}_3)\text{I}_3\cdot(\text{H}_2\text{O})_3$	246

List of Figures

Figure 1.1:	Various oxidized species of alkanethiols	19
Figure 1.2:	Structure of an a) alkanesulfinate b) alkylcarboxylate.	20
Figure 1.3:	Optimized geometries of the selected sulfinates	21
Figure 1.4:	Charge distribution of the selected sulfinates	21
Figure 1.5:	Possible fates of alkanesulfonyl radical	22
Figure 1.6:	Structures of a) L-cysteinesulfinic acid, b) 3-sulfinyl pyruvate, c) hypotaurine.	23
Figure 1.7:	Potential energy diagram for an outer-sphere electron transfer reaction	31
Figure 2.1:	The UV-VIS spectrum of aqueous tris phenanthroline osmium(II) and tris phenanthroline osmium(III)	37
Figure 2.2:	The cyclic voltammogram of 0.1 mM Os(II) at pH 3	38
Figure 2.3:	The kinetic trace at 610 nm for the reaction between CSA and Os(III)	41
Figure 2.4:	The plot of $1/k_{OBS}$ vs Os(II) concentration	42
Figure 2.5:	The plot of $\log k_{OBS}$ vs pH for CSA reaction with Os(III)	45
Figure 2.6:	The plot of k_{OBS} vs CSA concentration for CSA reaction with Os(III)	46
Figure 2.7:	The plot of k_{OBS} vs slit width of UV-VIS spectrophotometer	47
Figure 2.8:	Kinetic trace of the reaction carried out with O ₂ saturated solutions.	48
Figure 2.9:	The plot of k_{OBS} vs PBN concentration at pH 4.5 (acetate buffer).	49
Figure 2.10:	Effect of PBN concentration at higher PBN concentrations	50
Figure 2.11:	¹ H-NMR spectra of PBN and PBN with CSA	51
Figure 2.12:	Effect of allyl alcohol concentration on the reaction rate	52
Figure 2.13:	Kinetic trace of the oxidation of CSA by Os(III) in phthalate buffer	53
Figure 2.14:	Kinetic trace of the oxidation of CSA by Os(III) in citrate buffer	54
Figure 2.15:	The plot of absorbance at 610 nm vs volume of Os(III) added	57
Figure 2.16:	¹ H-NMR spectrum of the product mixture in D ₂ O	59

Figure 2.17:	Expansion of the $^1\text{H-NMR}$ spectrum to show peaks arising from $[\text{Os}(\text{phen})_3]^{2+}$	59
Figure 2.18:	Expansion of peaks from CSA	60
Figure 2.19:	Cyclic voltammograms of Os(II) and Os(III) with and without CSA	63
Figure 2.20:	UV-VIS spectra for determination of Os(II) yield.	64
Figure 2.21:	Optimized structures of a) cysteinesulfonyl radical b) rearranged β hydrogen removed radical	66
Figure 2.22:	Optimized structures of a) cysteinesulfonyl radical, b) cysteine thiyl peroxy radical	69
Figure 3.1:	Chemical structure of bis(1,4,7-triazacyclononane)Ni(III)	72
Figure 3.2:	The UV-VIS spectra of bis(1,4,7-triazacyclononane)Ni(II) and bis(1,4,7-triazacyclononane)Ni(III)	76
Figure 3.3:	Cyclic voltammogram of bis(1,4,7-triazacyclononane)Ni(III)	77
Figure 3.4:	Decrease of Ni(III) absorbance at 312 nm at two different cycle times	78
Figure 3.5:	Decrease of Ni(III) absorbance at 312 nm	79
Figure 3.6:	The plot of $1/k_{\text{OBS}}$ vs Ni(II) concentration at pH 4.5 (acetate buffer)	80
Figure 3.7:	The plot of k_{OBS} vs CSA concentration at pH 4.4-4.6 (10 mM acetate buffer)	81
Figure 3.8:	The plot of $\log k_{\text{OBS}}$ vs pH for reaction between CSA and Ni(III)	82
Figure 3.9:	The effect of the presence of air and oxygen in the reaction medium	83
Figure 3.10:	The $^1\text{H-NMR}$ of the product mixture for the reaction between CSA and Ni(III)	84
Figure 3.11:	ESI-MS ((-ve mode) of the product mixture after HILIC separation	85
Figure 3.12:	Cyclic voltammograms of product mixtures	86
Figure 3.13:	UV spectra for determining yield of Ni(II) from the reaction	87
Figure 3.14:	Change in UV spectrum after each addition of Ni(III)	88

Figure 3.15:	Change in absorbance at 312 nm after each addition of Ni(III)	89
Figure 3.16:	Optimized geometry of cysteinedisulfone	92
Figure 4.1:	Decay of absorbance at 312 nm during the reaction between MSA and Ni(III)	98
Figure 4.2:	The plot of $1/k_{\text{OBS}}$ vs Ni(II) concentration at pH 4.5 (acetate buffer)	99
Figure 4.3:	The plot of k_{OBS} vs MSA concentration at pH 3 (dilute HCl)	100
Figure 4.4:	The plot of $\log k_{\text{OBS}}$ vs pH for reaction between MSA and Ni(III)	103
Figure 4.5:	$^1\text{H-NMR}$ of a) pure methanesulfonate and b) the product mixture	104
Figure 4.6:	ESI-MS spectrum of the product mixture of the reaction between MSA and $[\text{Ni(III)(tacn)}_2]^{3+}$	104
Figure 4.7:	Change in UV spectrum after each addition of Ni(III) into MSA solution	105
Figure 4.8:	Change in absorbance at 312 nm after each addition of Ni(III)	106
Figure 4.9:	UV spectra for determining yield of Ni(II) from the reaction	107
Figure 4.10:	Optimized structure of methanesulfinate anion	108
Figure 4.11:	Optimized structure of methanesulfonyl radical	109
Figure 4.12:	Optimized structures of a) methanesulfonyl radical, b) methane thiyl peroxy radical	112
Figure 5.1:	Kinetic trace of the oxidation of MSA by Os(III) with first-order fit	120
Figure 5.2:	First and second order fits on the kinetic trace between MSA and Os(III)	122
Figure 5.3:	The dependence of second-order rate constant on Os(II) concentration at pH 4.5 (acetate buffer)	124
Figure 5.4:	The dependence of second-order rate constant on MSA concentration at pH 4.5 (acetate buffer)	125
Figure 5.5:	The plot of $\log k_{\text{OBS}}$ vs pH in aqueous medium	127
Figure 5.6:	Kinetic traces in the presence and in the absence of PBN	129
Figure 5.7:	Rate dependence on PBN concentration	130

Figure 5.8:	pH dependence of $\log k_{\text{OBS}}$ with PBN present	132
Figure 5.9:	Dependence of k_{OBS} on MSA concentration with PBN present .	133
Figure 5.10:	UV-VIS spectra for determination of Os(II) yield.	136
Figure 6.1:	The crystal structure of $(\text{CH}_3\text{SO}_2)_2\cdot\text{RbI}_3$	147
Figure 6.2:	The crystal structure of $(\text{CH}_3\text{SO}_2)_4\cdot\text{KI}_3\cdot 2\text{I}_2$	148
Figure 6.3:	Packing diagram of $(\text{CH}_3\text{SO}_2\text{I})_4\cdot\text{KI}_3\cdot 2\text{I}_2$	151
Figure 6.4:	Calculated charge distribution in $\text{CH}_3\text{SO}_2\text{I}$	154
Figure 6.5:	UV-VIS spectra of the reactants	157
Figure 6.6:	UV-VIS spectra of the product mixtures at various methanesulfinate concentrations	158
Figure 6.7:	MSA dependence of equilibrium tri-iodide concentration	159
Figure 6.8:	Iodide dependence of equilibrium tri-iodide concentration . . .	160
Figure 6.9:	Kinetics of H^+ production during hydrolysis of $\text{CH}_3\text{SO}_2\text{I}$	163
Figure B.1:	Typical kinetic trace of the reaction between Htau and tri-iodide	197
Figure B.2:	Dependence of Htau concentration on equilibrium tri-iodide concentration	200
Figure B.3:	Dependence of iodide concentration on equilibrium tri-iodide concentration	200
Figure B.4:	Plot of inverse tri-iodide concentration vs inverse square of iodide concentration	202
Figure B.5:	Optimized geometry of hypotaurine iodide	203
Figure B.6:	Charge distribution of hypotaurine iodide	204
Figure C.1:	Molecular packing diagram of $(\text{CH}_3\text{SO}_2\text{I})_2\cdot\text{RbI}_3$ viewed along the <i>ab</i> plane	206
Figure C.2:	Molecular packing diagram of $(\text{CH}_3\text{SO}_2\text{I})_2\cdot\text{RbI}_3$ viewed along the <i>ac</i> plane showing two different coordination modes of I_3^- with Rb.	206

Figure C.3:	Molecular packing diagram of $(\text{CH}_3\text{SO}_2\text{I})_2 \cdot \text{RbI}_3$ viewed along the bc plane showing two different coordination modes of I_3^- with Rb.	207
Figure C.4:	Molecular packing of $(\text{CH}_3\text{SO}_2\text{I})_4 \cdot \text{KI}_3 \cdot 2\text{I}_2$ showing the infinite chain of $[(\text{CH}_3\text{SO}_2\text{I})_4 \cdot \text{K}]$ extending along the c -axis	218
Figure C.5:	Portion of the unit cell of $(\text{CH}_3\text{SO}_2\text{I})_4 \cdot \text{KI}_3 \cdot 2\text{I}_2$ showing some of the close I–I contacts between the $\text{CH}_3\text{SO}_2\text{I}$ and the polyiodide components	219
Figure C.6:	Molecular packing diagram of $(\text{CH}_3\text{SO}_2\text{I})_4 \cdot \text{KI}_3 \cdot 2\text{I}_2$ viewed along the ab plane showing all iodine-iodine contacts less than 4.0 Å. (CH_3SO_2) and K removed for clarity	220
Figure C.7:	Asymmetric unit $\text{Ca}_2(\text{CH}_3\text{SO}_2)_2(\text{CH}_3\text{SO}_3)\text{I}_3 \cdot (\text{H}_2\text{O})_3$	232
Figure C.8:	Portion of $\text{Ca}_2(\text{CH}_3\text{SO}_2)_2(\text{CH}_3\text{SO}_3)\text{I}_3 \cdot (\text{H}_2\text{O})_3$ showing hydrogen bonding	233
Figure C.9:	Asymmetric unit of $\text{Ca}_2(\text{CH}_3\text{SO}_2)_2(\text{CH}_3\text{SO}_3)\text{I}_3 \cdot (\text{H}_2\text{O})_3$ showing network connectivity and hydrogen bonding. The I_3^- is eliminated for clarity	233
Figure C.10:	Molecular packing of $\text{Ca}_2(\text{CH}_3\text{SO}_2)_2(\text{CH}_3\text{SO}_3)\text{I}_3 \cdot (\text{H}_2\text{O})_3$ showing the two-dimensional polyiodide sheeting	234

List of Tables

2.1	k_{OBS} dependence on $[\text{Br}^-]$	55
2.2	Assignment of peaks in $^1\text{H-NMR}$ spectrum of the product mixture	61
4.1	Bond lengths of methanesulfinate anion and methanesulfonyl radical	109
4.2	Bond angles of methanesulfinate anion and methanesulfonyl radical	110
4.3	Free Energies Calculated with Gaussian 16	113
4.4	Free energies of formation for selected species	114
6.1	Selected crystallographic data for the MSI containing crystals	146
6.2	Comparison of Vibrational Frequencies Obtained for $(\text{CH}_3\text{SO}_2\text{I})_2 \cdot \text{RbI}_3$ with published values for methanesulfonyl halides.	150
6.3	Comparison of the Bond Lengths Obtained from the Crystal Structures with the Values Calculated	153
6.4	Comparison of the Bond Angles Obtained from the Crystal Structures with the Values Calculated	153
6.5	Gibbs Energies Calculated with Gaussian 16	155
6.6	Kinetics of $\text{CH}_3\text{SO}_2\text{I}$ Hydrolysis	162
A.1	$[\text{Os}(\text{phen})_3]^{2+}$ concentration dependence of k_{OBS}	176
A.2	pH dependence of k_{OBS}	177
A.3	The table of $[\text{CSA}]_{\text{TOT}}$, and corresponding k_{OBS}	178
A.4	Effect of slit width of the spectrophotometer on k_{OBS}	178
A.5	k_{OBS} dependence on $[\text{PBN}]$	179
A.6	k_{OBS} dependence on $[\text{allyl alcohol}]$	180
A.7	Effect of Ni(II) concentration of reaction rate	181
A.8	The table of $[\text{CSA}]_{\text{TOT}}$, and corresponding k_{OBS}	182
A.9	pH dependence on rate of the reaction between CSA and Ni(III)	183
A.10	Effect of the presence of O_2 and air on rate constant at different pH	184
A.11	Effect of Ni(II) concentration of reaction rate	185
A.12	The table of $[\text{MSA}]_{\text{TOT}}$, and corresponding k_{OBS}	186

A.13	pH dependence on rate of the reaction between MSA and Ni(III)	187
A.14	Absorbance of the product mixture at 312 nm after each addition of Ni(III)	188
A.15	$[\text{Os}(\text{phen})_3]^{2+}$ concentration dependence of k_{OBS}	189
A.16	The table of $[\text{MSA}]_{\text{TOT}}$, and corresponding k_{OBS}	190
A.18	pH dependence of k_{OBS}	191
A.17	The table of $[\text{PBN}]_{\text{TOT}}$, and corresponding k_{OBS}	192
A.19	pH dependence of k_{OBS} with PBN present	193
A.20	The table of $[\text{MSA}]_{\text{TOT}}$, and corresponding k_{OBS} with PBN present . . .	194
A.21	Corrected Values for $[\text{I}_3^-]_{\text{eq}}$ for the equilibrium reaction	194
B.1	Concentrations of Htau, Γ , and I_2 used	198

Chapter 1

Introduction

1.1 General introduction

Sulfur is a second row chalcogen that is essential for life.¹⁻⁷ The $[\text{Ne}]3s^23p^4$ electronic configuration allows sulfur to form species with valencies 2, 4 and 6 and sulfur oxidation states ranging from -2 to +6.⁸ Some example species of various sulfur oxidation states are shown in figure 1.1. Sulfur atoms have the capability to form hypervalent (non-octet) species.⁹⁻¹² Sulfoxides and sulfuranes are some examples for hypervalent sulfur compounds.

1.1.1 Alkanesulfinates: importance and functions

Alkanesulfinates have a superficial similarity to alkylcarboxylates. Despite this superficial analogy, there are crucial differences of geometry and reactivity between alkanesulfinates and alkylcarboxylates. For instance, the lone pair on sulfur atom imparts a pyramidal geometry to sulfinate sulfur center, whereas the carboxyl carbon possesses a planar geometry.¹³ Also, alkanesulfinic acids have pK_a 's ≈ 2 and for carboxylic acids the pK_a 's are approximately 4.¹⁴ Sulfinate functional group has a tetrahedral geometry. Therefore, the oxygens of sulfinates are prochiral.¹³

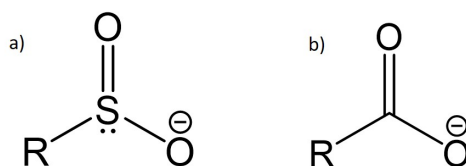


Figure 1.2: Structure of an a) alkanesulfinate b) alkylcarboxylate.

Sulfinates are soft nucleophiles,¹⁵ and undergo nucleophilic addition reactions with α , β -unsaturated alkenes,¹⁶ aldehydes¹⁷ as well as with epoxides¹⁸ to form sulfones. While the majority of the nucleophilic additions occur at the sulfur center, oxygen atoms of sulfinate are also capable of nucleophilic attack.¹⁹

Since sulfinic acids can easily undergo disproportionation reactions,^{20,21} they are commonly prepared by in-situ acidification of the sulfinate salts. To qualitatively and quantitatively analyze sulfinic acids, redox titrations with bromides, bromates, Ce^{4+} ,²² direct acid-base titrations,²³ ion-exchange chromatography,²⁴ as well as spectroscopic techniques²⁵ are used.

For the projects discussed here, L-cysteinesulfinic acid, methanesulfinate, and hypotaaurine were chosen to investigate their oxidation kinetics. Figures 1.3 and 1.4 show that the three sulfinates are electronically and structurally distinct, and therefore significant differences

in the oxidation mechanisms are expected.

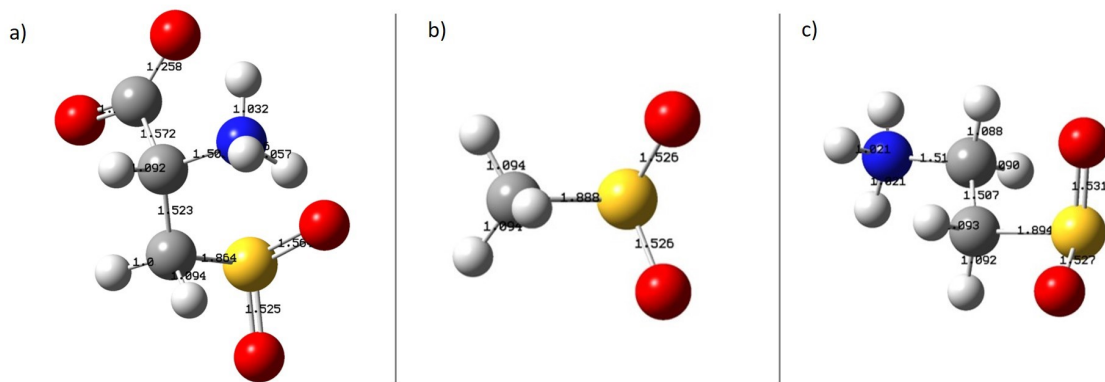


Figure 1.3: Optimized geometries of the selected sulfonates. a) L-cysteinesulfinate b) methanesulfinate c) hypotaurine. Structures are optimized using B3LYP method under 6-311G* basis set in implicit water.

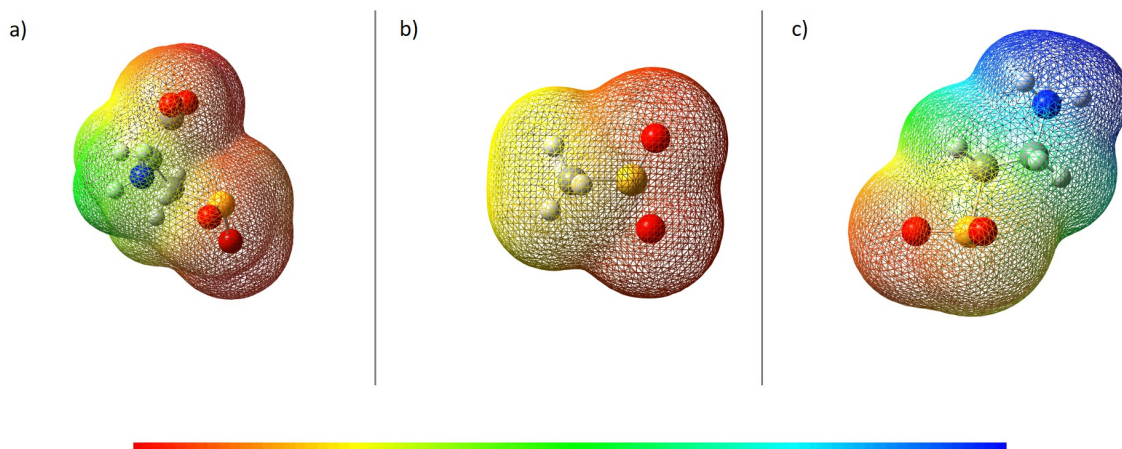


Figure 1.4: Charge distribution of the selected sulfonates. a) L-cysteinesulfinate b) methanesulfinate c) hypotaurine. Structures are optimized using B3LYP method under 6-311G* basis set in implicit water, red correlates to the highest negative charge and blue correlates to the highest positive charge.

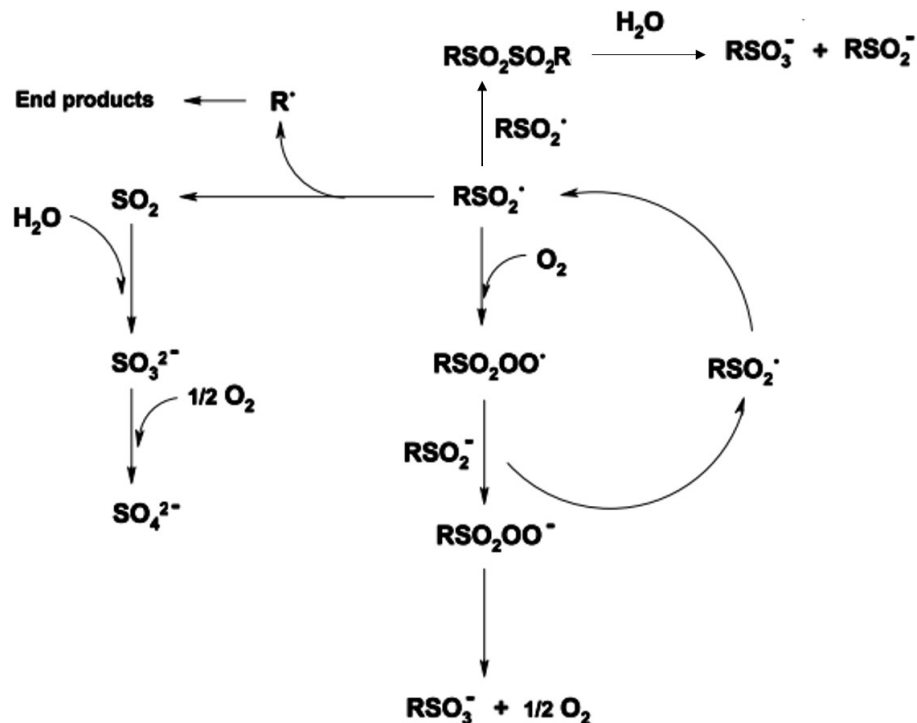


Figure 1.5: Possible fates of alkanesulfonyl radical^{26,27}

One electron oxidation of alkanesulfonates has been previously studied with oxidants OH^\bullet ,^{28,29} $\bullet\text{NO}_2$,³⁰ $\bullet\text{CO}_3^-$,³¹ ONOO^- ,³² and IrCl_6^{2-} .³³ ONOO^- reacts via rate-limiting hydrolysis at the N-O bond. The first step of alkanesulfinate oxidation by a one electron oxidant has been proposed as the formation of transient intermediate alkanesulfonyl radical ($\text{RSO}_2\bullet$). $\text{RSO}_2\bullet$ is a strong oxidizing species³⁴ and has been well characterized using optical absorption spectroscopy and electron paramagnetic resonance (EPR) spectroscopy.³⁵ Methanesulfonyl radical has been identified as the intermediate (absorbance maximum at 325 nm) during the reaction of $\bullet\text{OH}$ with methanesulfinate.²⁹ Conrado et al. report an absorbance maximum around 325 nm for the transient intermediate formed during the reactions of $\bullet\text{CO}_3^-$ with L-cysteinesulfinate and hypotaurine.³¹ In EPR investigations,

a g-factor of 2.0053 is expected for cysteinesulfonyl radical.³⁶ Chatgililoglu et al.³⁷ have discussed thermochemistry of sulfonyl radicals in detail. For self-reactions of methanesulfonyl radicals forming disulfones, a rate constant of $(1.0 \pm 0.2) \times 10^9 \text{ M}^{-1} \text{ s}^{-1}$ is reported.³⁸

If dissolved O_2 is present in the reaction medium, the sulfonyl radical may produce a sulfonyl peroxy radical $\text{RSO}_2\text{OO}\cdot$.²⁶ The peroxy radical then in turn will react with sulfinate anion generating peroxysulfinate anion and regenerate a sulfonyl radical. This process is depicted in figure 1.5

Several reports have described two-electron oxidation of alkanesulfinates. During hypotaurine oxidation by peroxynitrite, oxygen is directly transferred from the oxidant to hypotaurine, to form taurine at a rate of $77.4 \text{ M}^{-1} \text{ s}^{-1}$.²⁷ This process does not consume any oxygen from the media. The deciding factor between the one-electron oxidation process versus the two-electron process is the concentration of hypotaurine. At higher hypotaurine concentrations, a preference for two-electron oxidation has been seen. Two-electron oxidation of hypotaurine by NaIO forms taurine as the sulfur containing product.³⁹

Cysteinesulfinic acid

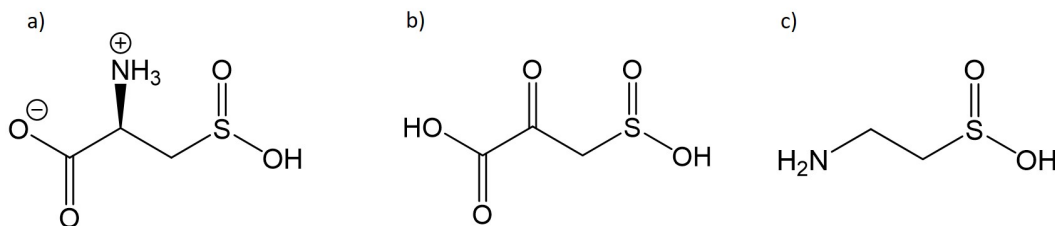


Figure 1.6: Structures of a) L-cysteinesulfinic acid, b) 3-sulfinyl pyruvate, c) hypotaurine.

L-cysteinesulfinic acid has significant biological importance due to its key physiological functions.⁴⁰⁻⁴⁴ In mammals, L-cysteinesulfinic acid is formed during catabolism of cysteine.⁴⁵

Also, oxidation to cysteinesulfinate may take place as a post-translational modification to cysteine residues.⁴⁶ Cysteine is acquired by the body from diet and also from trans-sulfuration pathway.⁴⁷ The enzyme cysteine dioxygenase (CDO) oxidizes cysteine to cysteinesulfinic acid (CSA, 3-sulfoalanine) in mammalian tissue.⁴⁵ This conversion is important since high concentrations of cysteine can be cytotoxic and neurotoxic.⁴⁵ In living organisms CSA may be decarboxylated to hypotaurine, which is then oxidized to taurine. An alternative fate of CSA is to form 3-sulfinyl pyruvate. 3-sulfinyl pyruvate is an unstable intermediate species which decomposes to form pyruvate and sulfite.⁴⁵ It has been found that the formation of CSA from cysteine moities balances antioxidant activity by inhibiting peroxyredoxins.¹³ Also, the conversion of cysteine 106 to CSA activates the chaperone activity of DJ-1 protein. DJ-1 protein offers protection against Parkinson's disease.⁴⁸ This conversion is also essential for nitrile hydratase catalytic activity.⁴⁹

Methanesulfinate

Metabolic processes of marine algae and phytoplankton release dimethyl sulfide (DMS) to the marine atmosphere.⁵⁰⁻⁵² The emitted DMS is then oxidized in the troposphere and dimethyl sulfoxide is formed.⁵³ Methanesulfinic acid is produced as the major product during dimethyl sulfoxide oxidation in the marine atmosphere.⁵⁴ Due to its part in atmospheric oxidation, aqueous phase kinetics of methanesulfinate oxidation has been investigated using several key atmospheric oxidants. OH•, N₃•, Cl atom, O₃, and dichloride radical (Cl₂⁻) are some such oxidants.^{29,34,38,54} In all these reactions the major product is methanesulfonate.

Hypotaurine

Hypotaurine (2-aminoethanesulfinic acid) is a non-peptidic amino acid present in millimolar concentrations in some mammalian cells.^{55,56} It is a major precursor in biosynthesis of taurine and a metabolite of cysteinesulfinic acid created via decarboxylation by sulfinioalanine

decarboxylase.⁵⁷ Hypotaurine is known to act as an antioxidant scavenging reactive oxygen species formed in cells. Also, hypotaurine acts as a protective agent and prevents ONOO⁻ mediated reactions.⁵⁸ Hypotaurine levels in body decrease with age. Though it was discovered in 1954 that under oxidizing conditions hypotaurine is oxidized to taurine,⁵⁹ a specific enzyme associated with the oxidation of the sulfinic group to the sulfonic group has not been reported. Reactions of hypotaurine in aqueous media with one-electron oxidants have been described considerably well in literature. Similar to the one-electron oxidation process of cysteinesulfinic acid, the corresponding transient sulfonyl radical is formed as a first step and, if oxygen is present in the reaction environment, a chain reaction with oxygen commences.³⁴ In the absence of oxygen, the sulfonyl radical may undergo dimerization to form a disulfone,⁶⁰ or dissociate into an alkyl radical and sulfur dioxide. The tendency to dissociate has been shown to be less in the sulfonyl radical derived from hypotaurine compared to cysteinesulfonyl radical.³⁰ UV light catalyzed oxidation of hypotaurine by Fenton's reagent has shown to form the corresponding disulfone as an intermediate.⁶¹ Reactions with biologically occurring oxidants such as singlet oxygen, OH radical, hypochlorite,⁶⁰ peroxyxynitrite, H₂O₂, and carbonate radical anion³⁰ as well as reaction with UV irradiation with hypotaurine have been investigated.

Chapters 2 through 5 of this thesis discuss oxidation reactions of alkanesulfinates by one-electron oxidants. Chapter 6 and appendix A present some results on two-electron oxidation of alkanesulfinates.

1.1.2 Reaction kinetics

The following sections describe some common kinetic terms and concepts used in the following chapters.

Chemical kinetics is the study of rates of chemical reactions. The change in concentration of a species involved in the reaction over unit time is the rate of a chemical reaction. Rate

of chemical reaction depends on physical state of reactants, concentration of reactants, temperature, and presence of catalysts.

$$\text{Rate of a reaction} = \frac{\Delta\text{Concentration}}{\Delta\text{Time}} \quad (1.1)$$

Rate of reaction has units of M s^{-1} . When a reaction progresses, the concentration of reactants decreases over time and the amount of product increases. Rate can be described using either the increase of products over time or the decrease of reactant concentration over time. Rate of a reaction changes over the course of a reaction if the concentration of any species involved in the reaction rate law is changed.

Rate equations (or rate laws) express the relationship between the reaction rate and the reactant concentrations. A simple rate law would take the form

$$\text{Rate} = k[\text{A}]^m[\text{B}]^n \quad (1.2)$$

Here the proportionality constant k is the rate constant. Units of k depends on the rate law. m and n are not necessarily the stoichiometric coefficients. To determine k as well as m and n experimental data is needed. In addition to reactant and product concentrations, the reaction rate expressions may contain catalyst concentrations. The sum of all exponents appearing in the overall rate law is the order of a reaction. The order of a reaction with respect to a particular reactant or product is the exponent on the concentration of that particular species in the rate law. The rate constant is dependent on temperature. In order to determine rate expression, method of initial rates may be used. Initial rate is the reaction rate at $t = 0$. Interference by reaction products, and side reactions are avoided when this method is used. The rate of a reaction is dependent on temperature. Collision theory shows that for a reaction to proceed molecules that react must collide, collisions must have sufficient energy to break bonds, and orientation of molecules during collision should be favorable. At higher temperature, a larger fraction of molecules will possess the

activation energy required for the reaction, and therefore increase of temperature would increase reaction rate. However, there are reactions that display negative temperature dependence on rate.⁶² The Arrhenius equation shows the dependence of rate constant on the temperature.

$$k = A \exp\left(\frac{-E_a}{RT}\right) \quad (1.3)$$

Here, A is the frequency factor, used to describe the number of collisions and the fraction with proper orientation. The exponential term contains the number of collisions with energy equal to or greater than the activation energy at temperature T. Presence of a catalyst causes the reaction to follow a different pathway with lower activation energy. Catalysts change the reaction mechanism.

The sequence of steps that converts reactants to products is a reaction mechanism. Each step in the sequence is an elementary step. A reaction mechanism cannot be proved. A single reaction may have several possible mechanisms. A plausible mechanism is useful in predicting the behavior of the reaction. The rate determining step (rate limiting step) is the slowest elementary step in the multistep sequence. Products of the reaction will not form faster than the rate of the slowest elementary step. This does not hold true for chain reactions. Overall stoichiometry cannot predict the rate equation. Rate equation for any elementary step however is defined by the stoichiometry of the elementary reaction.

1.1.3 Effect of ionic strength on rate

Ionic strength is the quantity of electrically charged species in a given solution. Ionic strength is given by

$$\mu = \frac{1}{2} \sum C_i Z_i^2 \quad (1.4)$$

where C_i is the concentration of the i th species in solution and Z_i is the charge of the i th species. Activity coefficients depend on ionic strength of the solution, as shown by the extended Debye-Huckel equation.⁶³

$$-\log\gamma = \frac{0.51Z^2\sqrt{\mu}}{1 + \left(\frac{\alpha\sqrt{\mu}}{305}\right)} \quad (1.5)$$

Where Z is the charge of the ion; α is the radius of the ion in pm; and μ is the ionic strength of the solution. In order to hold the change of activity coefficients with change of concentrations of reactants and products, an inert electrolyte at higher concentration than the reactants is used to maintain constant ionic strength.

1.1.4 Steady state and pre-equilibrium approximations

In order to simplify complex rate laws, steady-state approximation and pre-equilibrium approximation are used.⁶⁴ In a closed reaction system, the concentrations of highly reactive reaction intermediates remain constant. This is the steady-state approximation. This holds true only when a slow reaction precedes a faster reaction consuming the intermediate, because under that condition, intermediates are consumed as fast as they are produced. Pre-equilibrium approximation can be used instead of steady-state approximation when slow reactions follow a rapid reversible reaction. The pre-equilibrium approximation assumes that reactant and intermediate are in equilibrium throughout the reaction.



$$\frac{[B]}{[A]} = \frac{k_1}{k_2} \quad (1.7)$$

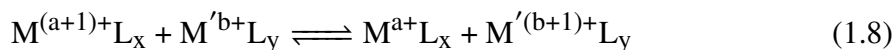
This is true when $k_3 \ll k_1, k_2$.

1.2 Electron-transfer mechanisms

Transfer of electrons between inorganic complexes in solution may occur via two mechanisms; outer-sphere electron transfer mechanism and inner-sphere electron transfer mechanism.⁶⁵ In outer-sphere electron transfer mechanism, no new bonds are formed or broken. The first coordination spheres of both the oxidant and the reductant remain intact. Inner-sphere electron transfer involves bond formation and breakage. At the time of electron transfer, the first coordination spheres of the two metal ions share a common ligand. Therefore, in order to have inner-sphere electron transfer, one reactant should possess at least one ligand capable of bridging and the other complex needs to be substitutionally labile.

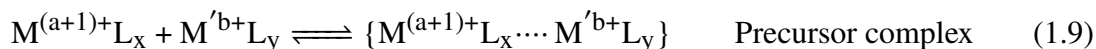
1.2.1 Inner and outer-sphere processes

Outer-sphere electron transfer

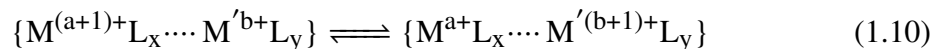


For a redox reaction as the one given above, outer-sphere electron transfer takes the following mechanism.

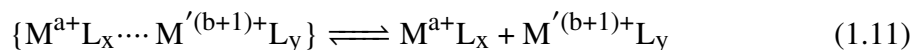
Step 1: Formation of the precursor complex. Generally, this is a fast step



Step 2: Chemical activation and reorganization of precursor complex, transfer of electrons, and relaxation of precursor complex to successor complex.



Step 3: Dissociation of the successor complex. This step is generally faster than the electron transfer step.



The total activation energy for outer-sphere electron transfer is a combination of the energy required to bring the reactants together, and overcome coulombic repulsions for like charged ions, energy needed for solvent reorganization, and the energy required for the rearrangement of first coordination sphere. Solvent reorganization energy can be minimized using large ligands. Since activation energy depends on the complex's ability to adjust bond lengths to make them the same in the transition state, a wide range of rates are observed for outer-sphere electron transfer reactions. If the ligands are incapable of electron transfer and the metal complex is substitutionally inert in both oxidized and reduced forms, outer-sphere electron-transfer mechanism must be in effect.

Inner-sphere electron transfer

Inner-sphere electron transfer occurs via the following steps. First, a ligand forms covalent bonds between the oxidant and the reductant to form precursor complex. Next, the precursor complex is activated, and an electron is transferred from one metal center to the other, forming the successor complex. Then, the successor complex is dissociated giving the products. Also, transfer of ligand between the complexes may happen. However, ligand transfer is not a requirement of inner-sphere electron transfer. The first demonstration of an inner-sphere electron transfer reaction was by Taube and coworkers.⁶⁶

1.2.2 Marcus theory and Franck Condon principle

Marcus theory

Marcus theory is typically applied to homogeneous outer-sphere electron transfer reactions in solution.⁶⁷ Marcus theory assumes reactants to be hard charged particles. The Franck Condon principle is used for the derivation of Marcus theory.

For electron transfer to occur the potential well of the reactant must distort from equilibrium state to transition state geometry.

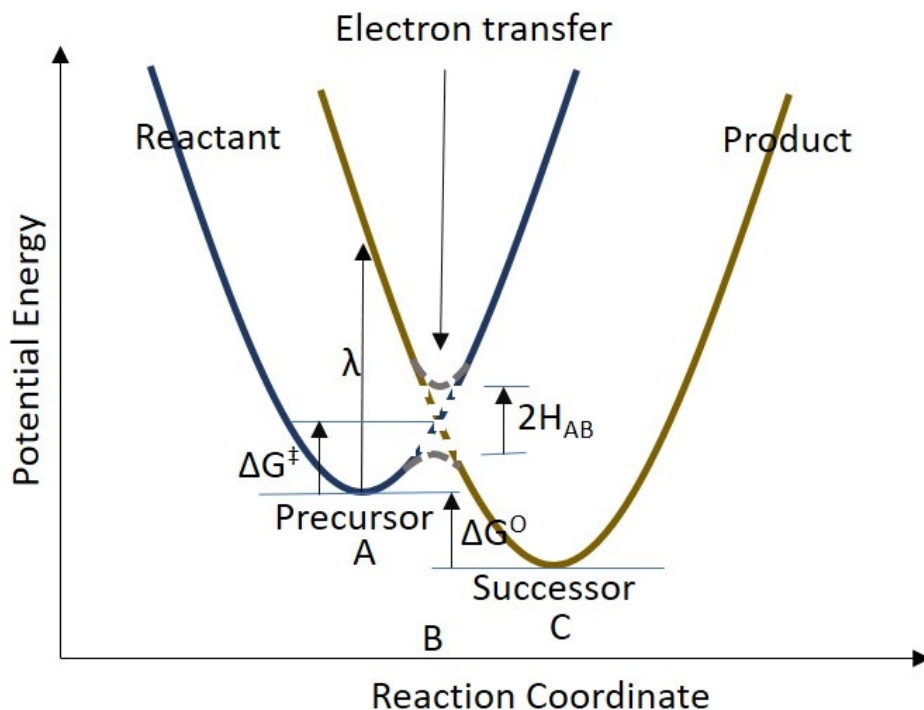


Figure 1.7: Potential energy diagram for an outer-sphere electron transfer reaction

$$\Delta G^\ddagger = \frac{(\lambda + \Delta G^0)^2}{4\lambda} \quad (1.12)$$

Where ΔG^\ddagger = activation energy for electron transfer, λ = reorganization energy.

To calculate the rate of electron transfer between two inorganic complexes, Marcus cross relationship can be used.⁶⁸

$$k_{12} = (k_{11}k_{22}K_{12}f_{12})^{1/2}W_{12} \quad (1.13)$$

Where k_{11} and k_{22} are self exchange rate constants, k_{12} is cross reaction rate constant, K_{12} is the equilibrium constant of the cross reaction.

$$\ln f_{12} = \frac{[\ln K_{12} + (w_{12} - w_{21})/RT]^2}{4[\ln(k_{11}k_{22}/Z^2) + (w_{11} + w_{22})/RT]} \quad (1.14)$$

$$W_{12} = \exp[(-w_{12} - w_{21} + w_{11} + w_{22})/2RT] \quad (1.15)$$

$$w_{ij} = \frac{17.7Z_iZ_j}{r_{ij}(1 + 0.328r_{ij}\sqrt{\mu})} \quad (1.16)$$

According to the Franck-Condon principle, electron transitions occur much faster than nuclear motion due to the size difference between electron and nuclei.⁶⁹ In order for electron transfer to satisfy the Franck-Condon principle, angular momentum cannot change during the electron transfer. Also, spin multiplicity must remain unchanged. Since internuclear distance remains unchanged during electron transfer, in transition state, the reactant bond lengths must approach product bond lengths.

1.3 The scope of the dissertation

The conversion of alkanesulfinates to alkanesulfonates in aqueous media plays a significant role in biochemistry and environmental chemistry. For example, methanesulfinate oxidation to methanesulfonate has an influence on atmospheric processes, due to its effect

on aerosol acidity. Also, oxidation modifications of cysteinesulfinic acid and hypotaurine are of interest due to their contribution to oxidative stress. In addition to its intrinsic importance, sulfinic acid oxidation to sulfonic acid is a part of thiol oxidation process. Thiol oxidation can yield both sulfinic and sulfonic acids as their final oxidation products. Investigation of sulfinic acid oxidation to sulfonic acid will help in understanding the final product distributions of thiol oxidation. Despite its importance, only a handful of studies have investigated the chemical mechanism of the alkanesulfinic acid oxidation reaction. To determine the role of sulfinic/sulfonic acid oxidation modifications, an explicit investigation on its reaction mechanisms is remarkably important. The goal of this work is to gain a thorough understanding of the factors that govern alkanesulfinic acid redox behaviors.

The Chapters 2-6 describe kinetic analyses, computational simulations, and intermediate identifications and characterizations carried out in order to achieve this goal. It is hoped that this work would be a valuable contribution to improving the current understanding of the mechanism of alkanesulfonic acid formation from alkanesulfinic acids in aqueous media, thus benefiting theoretical and application based research of the fields mentioned above.

Chapter 2

Kinetics and mechanism of the oxidation of L-cysteinesulfinic acid by tris(1,10-phenanthroline)osmium(III)

2.1 Introduction

The universal oxidation product of an alkanesulfinic acid (RSO_2H) is the sulfonate (RSO_3^-), and it is intriguing how an oxidant limited to one-electron pathways could result in a two-electron oxidation product.³⁰ With the ultimate goal of constructing a mechanism for the oxidation of sulfinic acids using one-electron oxidants, the oxidation of cysteinesulfinic acid ($\text{HO}_2\text{CH}(\text{NH}_2)\text{CH}_2\text{SO}_2\text{H}$) by the one-electron oxidant $[\text{Os}(\text{phen})_3]^{3+}$ was examined. Cysteinesulfinic acid (CSA) has important biological and medical applications. Though

for decades CSA was considered to be an over-oxidation product of cysteine, with the discovery of the sulfinic acid reductase, sulfiredoxin⁷⁰ in 1994, it was quickly evident that CSA plays an important role in biological systems.¹⁵ For example, the presence of sulfinic and sulfonic species is taken as an indication of diseases related to oxidative stress such as Parkinson's and Alzheimer's.^{47,71–73} To determine the specific role of sulfinate/sulfonate oxidation modifications, a thorough understanding about the factors that govern sulfinate redox behavior is remarkably important. However, a viable mechanism for cysteinesulfinate oxidation process is yet to be established. L-cysteinesulfinic acid oxidation by transition metal complexes have been studied using $[\text{Ir(IV)Cl}_6]^{2-33}$ and $[\text{Ni(III)(tacn)}_2]^{3+}$ (discussed in Chapter 3) as one-electron oxidants. It has been widely accepted that the first step in the oxidation of L-cysteinesulfinic acid (CSA) by one electron oxidants is the formation of cysteinesulfonyl radical $\text{CysSO}_2\cdot$.^{26,30}

In this study we examine one-electron oxidation of CSA using transition metal-based one-electron oxidant tris(1,10-phenanthroline)osmium(III). $[\text{Os(phen)}_3]^{3+}$ is a one-electron oxidant substitution-inert complex with $E_f^\circ [\text{Os(phen)}_3]^{3+/2+} = 0.839 \text{ V}$.⁷⁴ It has been successfully used to observe kinetics of oxidation of phenol,⁷⁵ and several sulfur-containing molecules such as thioglycolate⁷⁴ and thiosulfate.⁷⁶

2.2 Reagents and solutions

2.2.1 Reagents used

L-cysteinesulfinic acid monohydrate (99% Aldrich), L-cysteic acid monohydrate (Sigma), glacial acetic acid (Fischer Scientific), NaOH pellets (98% Sigma Aldrich), NaCl (Fischer Scientific), NaBr (J.T. Baker), 3-(trimethylsilyl)-1-propanesulfonic acid sodium salt (DSS) (Sigma-Aldrich), D₂O 99.8% isotopic (Alfa Aesar), NaCF₃SO₃ (Alfa Aesar), CH₃COONa anhydrous (Sigma), Br₂ (Alfa Aesar), CH₃CN (Fisher), 1,10-phenanthroline monohydrate

(Sigma-Aldrich), diethyl ether (J.T. Baker), ethyl acetate (Fischer Scientific), ethylene glycol (J.T. Baker), acetone (VWR), acetonitrile (Fischer Scientific), isopropyl alcohol (VWR) were used as supplied.

[Os(phen)₃](CF₃SO₃)₂ was synthesized starting from (NH₄)₂OsCl₆ using a modified procedure from literature.^{74–76} First, 0.177 g of (NH₄)₂OsCl₆ available from a prior study⁷⁴ and 0.232 g of 1,10-phenanthroline monohydrate were dissolved in 30 ml of ethylene glycol in a round bottom flask. The mixture was refluxed at 200 °C for 12 hrs. The resulting dark solution was extracted first using 4:1 diethyl ether:acetone mixture and then after dilution of the resulting solution with H₂O, the resulting solution was extracted with ethyl acetate to extract excess ethylene glycol. The H₂O was evaporated off using the rotary evaporator, and [Os(phen)₃](CF₃SO₃)₂ was precipitated by addition of saturated CF₃SO₃Na. The crude product was recrystallized by dissolving in a minimum of H₂O at 60 °C and precipitating by drop-wise addition of a saturated aqueous solution of CF₃SO₃Na.

2.2.2 [Os(phen)₃](CF₃SO₃)₂ characterization

The UV-VIS spectrum of [Os(phen)₃](CF₃SO₃)₂ was obtained by preparing a 0.03 mM solution of [Os(phen)₃](CF₃SO₃)₂ in H₂O. Two absorbance maxima are observed at 430 nm and 480 nm, and a shallow minimum is observed at 456 nm (Figure 2.1). $\epsilon = 2 \times 10^4$ M⁻¹ cm⁻¹ (430 nm). By comparing the UV-VIS spectra of salts [Os(phen)₃](CF₃SO₃)₂, [Os(phen)₃](Cl)₂, [Os(phen)₃](OAc)₂ it was found that the spectrum for [Os(phen)₃]²⁺ remains unchanged regardless of the anion of the salt.

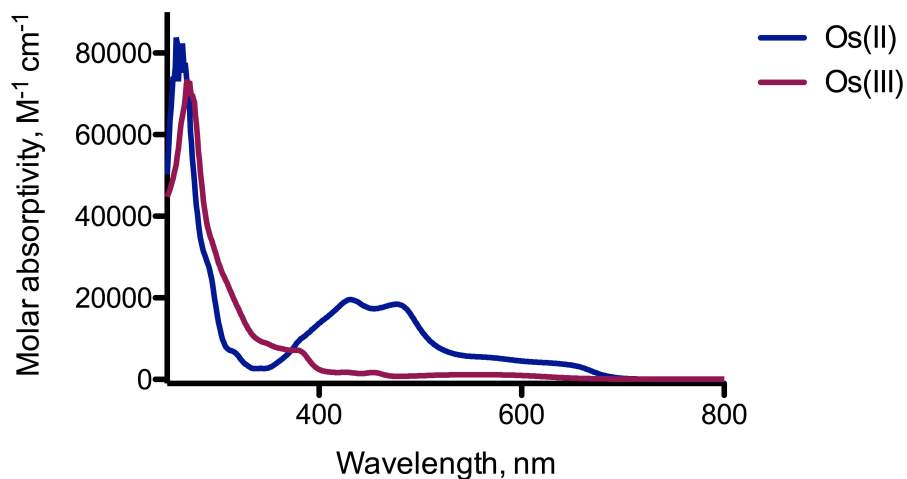


Figure 2.1: The UV-VIS spectrum of aqueous $[\text{Os}(\text{phen})_3](\text{CF}_3\text{SO}_3)_2$ at 25 °C, and spectrum of $[\text{Os}(\text{phen})_3]^{3+}$ formed after oxidation of $[\text{Os}(\text{phen})_3]^{2+}$ using $\text{Br}_2/\text{CH}_3\text{CN}$. ϵ ($[\text{Os}(\text{phen})_3]^{2+}$) at 610 nm = $4.32 \times 10^3 \text{ M}^{-1} \text{ cm}^{-1}$, ϵ ($[\text{Os}(\text{phen})_3]^{3+}$) at 610 nm = $8.62 \times 10^2 \text{ M}^{-1} \text{ cm}^{-1}$

A reversible cyclic voltammogram was obtained for 1 mM $[\text{Os}(\text{phen})_3]^{2+}$ with $E_{1/2} = 0.64 \text{ V}$ vs $\text{Ag}/\text{AgCl}(\text{s})$ ($E_{1/2} = 0.838 \text{ V}$ vs normal hydrogen electrode) which agrees with the value reported in literature (0.839 V).⁷⁴ (Figure 2.2)

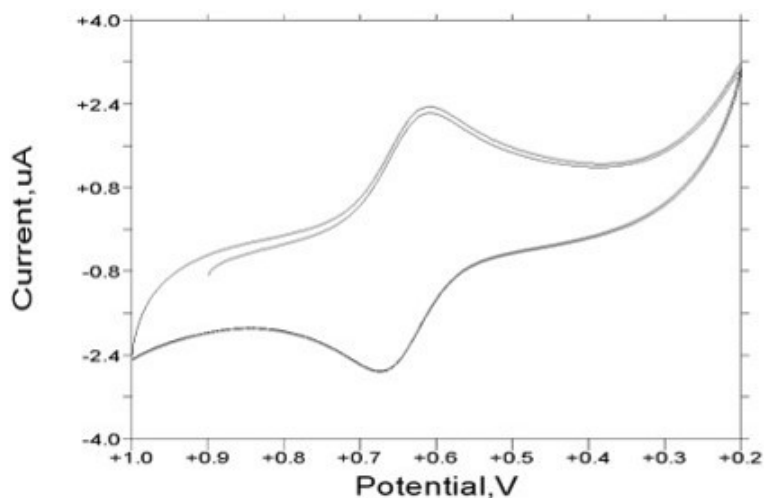


Figure 2.2: Cyclic voltammogram of 0.1 mM $[\text{Os}(\text{phen})_3](\text{CF}_3\text{SO}_3)_2$ in pH 3 (HCl) medium, $\mu = 0.1 \text{ M}$ (NaCl).

K_{sp} of $[\text{Os}(\text{phen})_3](\text{CF}_3\text{SO}_3)_2$ in H_2O was determined by preparing a saturated solution of $[\text{Os}(\text{phen})_3](\text{CF}_3\text{SO}_3)_2$ in water and obtaining its UV-VIS spectrum to determine the concentration of $[\text{Os}(\text{phen})_3]^{2+}$. Saturation $[\text{Os}(\text{phen})_3]^{2+}$ concentration is 3.2 mM. The K_{sp} of $[\text{Os}(\text{phen})_3](\text{CF}_3\text{SO}_3)_2$ at 25 °C is $1.31 \times 10^{-7} \text{ M}^3$.

2.2.3 Preparation of solutions

All the aqueous solutions were prepared using purified deionized water from a Barnstead Nanopure Infinity system. Stock solutions of L-cysteinesulfinic acid, glacial acetic acid and sodium acetate were prepared and stored in the refrigerator. All other solutions were freshly prepared for each experiment. All solutions were purged with Ar. $[\text{Os}(\text{phen})_3]^{3+}$ is unstable in aqueous solutions for prolonged periods of time. Therefore $[\text{Os}(\text{phen})_3]^{3+}$ solutions were generated just prior to experiments by adding a deficiency of $\text{Br}_2/\text{CH}_3\text{CN}$ drop-wise to solutions of $[\text{Os}(\text{phen})_3]^{2+}$. CSA stock solutions were standardized by titrating with KBrO_3 in the presence of bromide in acidic medium. The end point was determined

using methyl red indicator. Both the $[\text{Os}(\text{phen})_3]^{3+}$ and CSA solutions were purged with argon prior to experiments. In solutions with pH higher than 3, Os(III) reaction with water to give Os(II) is significant. Therefore, the pH of the Os(II)/Os(III) solutions were all kept at or below pH 3. All osmium containing solutions were protected from light.

2.3 Analytical methods

All UV-Vis data were obtained with an HP-8453 diode array spectrophotometer. ^1H -NMR spectra of the reactants and products were collected using D_2O as solvent and DSS as the reference on a Bruker AV 400 MHz spectrometer. The progress of kinetic experiments was monitored by observing the increase of absorbance at 610 nm using a Hi-Tech SF-51 stopped-flow spectrophotometer with OLIS 4300 data acquisition and analysis software along with a 590 nm optical cut-off filter. In each run, equal volumes of reactants were mixed. The progress of the reaction was monitored by observing decrease of absorbance at 312 nm. Data were stored using an OLIS 4300 data acquisition and analysis software and analyzed with GraphPad PRISM 8. To calculate the observed rate constants, the average rate constants of at least five reproducible runs were used. DataFit 9.1 software was used to fit the experimental data to overall rate-law. A Corning 450 pH/ion meter with a Mettler Toledo Inlab 421 pH electrode was used to obtain pH measurements. Electrochemical measurements were collected using a BAS 100B/W Electrochemical Analyzer, using a Ag/AgCl reference electrode, a glassy carbon working electrode, and a platinum wire auxiliary electrode; measurements were obtained at room temperature under N_2 . In kinetic experiments the CSA concentration was kept at least 20-fold higher than the concentration of $[\text{Os}(\text{phen})_3]^{3+}$ to achieve pseudo-first-order reaction conditions.

2.4 Results

2.4.1 Kinetics of the reaction



For the equation above, the rate law can be written as,

$$\frac{-d[[\text{Os}(\text{phen})_3]^{3+}]}{dt} = k[\text{CSA}][[\text{Os}(\text{phen})_3]^{3+}] \quad (2.2)$$

When $[\text{CSA}] \gg \gg [[\text{Os}(\text{phen})_3]^{3+}]$, $\Delta[\text{CSA}] \approx 0$

Therefore, the rate law could be re-written as

$$\frac{-d[[\text{Os}(\text{phen})_3]^{3+}]}{dt} = k_{\text{OBS}}[[\text{Os}(\text{phen})_3]^{3+}] \quad (2.3)$$

where $k_{\text{OBS}} = k[\text{CSA}]$

When 0.01 mM $[\text{Os}(\text{phen})_3]^{3+}$, 0.1 mM of $[\text{Os}(\text{phen})_3]^{2+}$, and 8.5 mM CSA are mixed to make a solution at pH 4.5 and $\mu = 0.1$ M (NaCl), pseudo-first-order kinetics can be observed from the kinetic trace at 610 nm. (Figure 2.3)

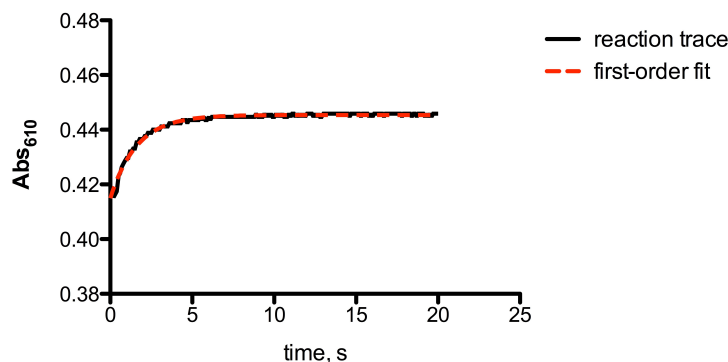


Figure 2.3: Kinetic trace of the oxidation of CSA by $[\text{Os}(\text{phen})_3]^{3+}$. $[[\text{Os}(\text{phen})_3]^{3+}]_0 = 0.01 \text{ mM}$, $[[\text{Os}(\text{phen})_3]^{2+}]_0 = 0.1 \text{ mM}$, $[\text{CSA}]_{\text{TOT}} = 8.5 \text{ mM}$, $\mu = 0.1 \text{ M}$ (NaCl), $T = 25 \text{ }^\circ\text{C}$, $\text{pH} = 4.5$ (acetate buffer), monitored at 610 nm, $k_{\text{OBS}} = 0.61 \text{ s}^{-1}$

The starting absorbances observed at 610 nm in stopped-flow kinetic data did not differ significantly from the expected absorbances for Os(II) at this wavelength.

2.4.2 Rate dependence on $[\text{Os}(\text{phen})_3]^{2+}$

Rate dependence on the reaction product $[\text{Os}(\text{phen})_3]^{2+}$ was monitored by adding varying amounts of $[\text{Os}(\text{phen})_3]^{2+}$ into the reaction mixture and determining the rate of the reaction using stopped-flow methods. The reaction mixture contained 0.01 mM $[\text{Os}(\text{phen})_3]^{3+}$ and 20 mM CSA at pH 5 and $\mu = 0.1 \text{ M}$ (NaCl) with 0.09 mM, 0.23 mM, 0.29 mM, 0.34 mM and 0.352 mM concentrations of $[\text{Os}(\text{phen})_3]^{2+}$ present. The rate of the reaction was found to decrease with increasing $[\text{Os}(\text{phen})_3]^{2+}$ concentration. (Table A.1, Figure 2.4)

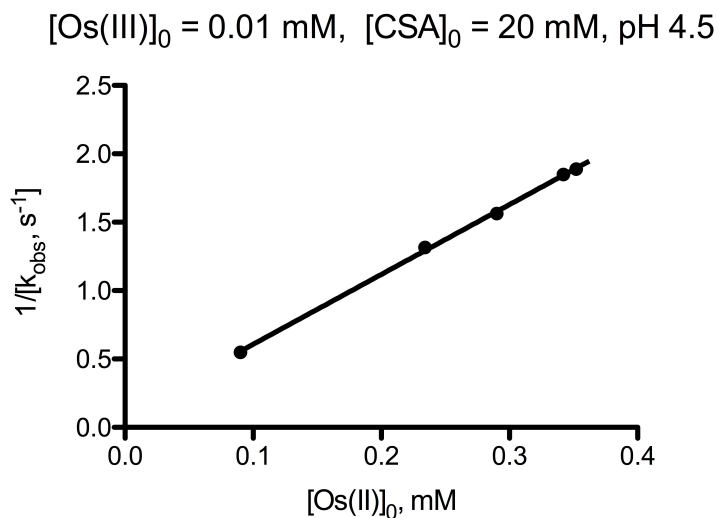


Figure 2.4: The plot of $1/k_{\text{OBS}}$ vs $[\text{Os}(\text{phen})_3]^{2+}$ at pH 5 (acetate buffer) $\mu = 0.1$ M (NaCl), $T = 25$ °C. Straight line fit with slope = $(6.31 \pm 0.08) \times 10^3 \text{ s M}^{-1}$, Y intercept = $(0.00 \pm 0.02) \text{ s}$.

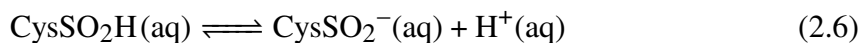
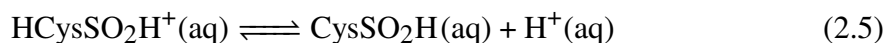
$$\frac{1}{k_{\text{OBS}}} = k'[\text{Os}(\text{II})] \quad \text{where } k' \text{ is a constant} \quad (2.4)$$

When data points in figure 2.4 are fit into equation 2.4, $k' = (6.31 \pm 0.08) \times 10^3 \text{ s M}^{-1}$.

2.4.3 pH dependence of the kinetics

pH dependence of the kinetics of the reaction between CSA and $[\text{Os}(\text{phen})_3]^{3+}$ was examined under anaerobic conditions by carrying out the reaction at different pH media ranging from pH 1 to pH 6 with $[\text{CSA}]_{\text{TOT}} = 3.75$ mM, $[\text{Os}(\text{phen})_3]^{3+}_0 = 0.01$ mM, $[\text{Os}(\text{phen})_3]^{2+}_0 = 0.1$ mM, 0.1 M ionic strength (NaCl) and monitoring the increase of absorbance at 610 nm using a stopped-flow instrument equipped with a spectrophotometer. A stock solution of CSA was prepared in pH 4.5 acetate buffer and diluted with different

buffers as required to attain the necessary pH. To prepare reaction media at pH 1-3, dilute HCl was used. For experiments done above pH 3, 10 mM acetate buffers were used to maintain the pH of the reaction mixture. Figure 2.5 shows the dependence of k_{OBS} on the pH of the medium. CSA has two pK_a 's (1.5 and 2.3) in the pH range the experiments are carried out, and thus CSA exists in 3 different forms.⁷⁷



$$K_{a1} = \frac{[\text{CysSO}_2\text{H}]_{(\text{aq})}[\text{H}^+]_{(\text{aq})}}{[\text{HCysSO}_2\text{H}^+]_{(\text{aq})}} \quad (2.7)$$

$$K_{a2} = \frac{[\text{CysSO}_2^-]_{(\text{aq})}[\text{H}^+]_{(\text{aq})}}{[\text{CysSO}_2\text{H}]_{(\text{aq})}} \quad (2.8)$$

Therefore, the rate constant for the reaction between CSA and $[\text{Ni}(\text{tacn})_2]^{3+}$ is expected to change with pH.

From equation 2.3,

$$\frac{-d[[\text{Os}(\text{phen})_3]^{3+}]}{dt} = k_{OBS}[[\text{Os}(\text{phen})_3]^{3+}] \quad (2.9)$$

Since $\text{HCysSO}_2\text{H}^+$, CysSO_2H , and CysSO_2^- are all present in the media, assuming that the effect of $\text{HCysSO}_2\text{H}^+$ on reaction rate is negligible in the given pH range, we can hypothesize that

$$k_{OBS} = k_1[\text{CysSO}_2^-]_{(\text{aq})} + k_2[\text{CysSO}_2\text{H}]_{(\text{aq})} \quad (2.10)$$

$$[\text{CSA}]_{\text{TOT}} = [\text{HCysSO}_2\text{H}^+]_{(\text{aq})} + [\text{CysSO}_2\text{H}]_{(\text{aq})} + [\text{CysSO}_2^-]_{(\text{aq})} \quad (2.11)$$

Substituting for $[\text{HCysSO}_2\text{H}^+]_{(\text{aq})}$, and $[\text{CysSO}_2\text{H}]_{(\text{aq})}$ from equations 2.7 and 2.8 into equation 2.11,

$$[\text{CysSO}_2^-]_{(\text{aq})} = [\text{CSA}]_{\text{TOT}} - \frac{[\text{CysSO}_2^-]_{(\text{aq})}[\text{H}^+]_{(\text{aq})}^2}{K_{a1}K_{a2}} - \frac{[\text{CysSO}_2^-]_{(\text{aq})}[\text{H}^+]_{(\text{aq})}}{K_{a2}} \quad (2.12)$$

Substituting 2.12 in equation 2.8

$$[\text{CysSO}_2\text{H}]_{(\text{aq})} = \frac{[\text{CSA}]_{\text{TOT}}K_{a1}[\text{H}^+]_{(\text{aq})}}{([\text{H}^+]_{(\text{aq})}^2 + [\text{H}^+]_{(\text{aq})}K_{a1} + K_{a1}K_{a2})} \quad (2.13)$$

Substituting for $[\text{CysSO}_2^-]_{(\text{aq})}$ and $[\text{CysSO}_2\text{H}]_{(\text{aq})}$ from equations 2.12 and 2.13 into equation 2.10,

$$k_{\text{OBS}} = k_1 \frac{[\text{CSA}]_{\text{TOT}}K_{a1}K_{a2}}{([\text{H}^+]_{(\text{aq})}^2 + [\text{H}^+]_{(\text{aq})}K_{a1} + K_{a1}K_{a2})} + k_2 \frac{[\text{CSA}]_{\text{TOT}}K_{a1}[\text{H}^+]_{(\text{aq})}}{([\text{H}^+]_{(\text{aq})}^2 + [\text{H}^+]_{(\text{aq})}K_{a1} + K_{a1}K_{a2})} \quad (2.14)$$

$[\text{Os(III)}]_0 = 0.01 \text{ mM}$, $[\text{CSA}] = 3.75 \text{ mM}$, $[\text{Os(II)}]_0 = 0.1 \text{ mM}$

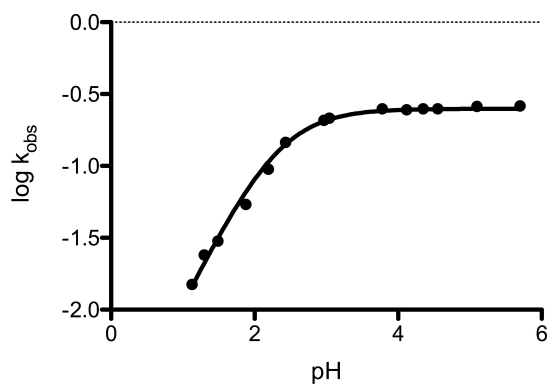


Figure 2.5: The plot of $\log k_{\text{OBS}}$ vs pH with $[\text{CSA}]_{\text{TOT}} = 3.75 \text{ mM}$, $[\text{Os(III)(phen)}_3]^{3+}]_0 = 0.01 \text{ mM}$, $[\text{Os(II)(phen)}_3]^{2+}]_0 = 0.1 \text{ mM}$, $\mu = 0.1 \text{ M (NaCl)}$, $T = 25 \text{ }^\circ\text{C}$, data is fit in to equation 2.14. $k_1 = (66.7 \pm 1.8) \text{ M}^{-1} \text{ s}^{-1}$, $k_2 = (9.5 \pm 0.7) \text{ M}^{-1} \text{ s}^{-1}$

2.4.4 Rate dependence on CSA concentration

Rate dependence on CSA concentration was determined by reacting $0.01 \text{ mM } [\text{Os(phen)}_3]^{3+}$ and $0.1 \text{ mM } [\text{Os(phen)}_3]^{2+}$ at pH 4.4-4.6 with solutions of varying CSA concentrations. (Table A.3, Figure 2.6)

$[\text{Os(III)}]_0 = 0.01 \text{ mM}$, $[\text{Os(II)}]_0 = 0.1 \text{ mM}$, pH 4.4-4.6 (0.1 M acetate buffer)

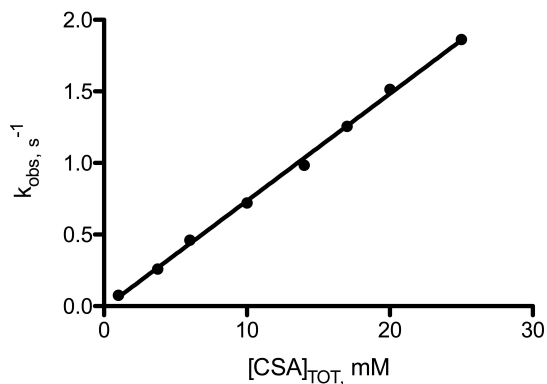


Figure 2.6: The plot of k_{OBS} vs $[\text{CSA}]_{\text{TOT}}$ at pH 4.4-4.6 (acetate buffer) with $[[\text{Os(phen)}_3]^{3+}]_0 = 0.01 \text{ mM}$ and $[[\text{Os(phen)}_3]^{2+}]_0 = 0.1 \text{ mM}$, $\mu = 0.1 \text{ M}$, $T = 25 \text{ }^\circ\text{C}$. Straight line fit with slope = $(7.5 \pm 0.1) \times 10^1 \text{ M}^{-1} \text{ s}^{-1}$ and Y intercept = $(-0.01 \pm 0.02) \text{ s}^{-1}$

From the results above, rate dependence on CSA concentration is determined to be of first-order.

2.4.5 Light dependence of the rate

The effect of light on the kinetics of the reaction between $[\text{Os(phen)}_3]^{3+}$ and CSA was determined by adjusting the slit width of the spectrophotometer attached to the stopped flow instrument and determining the rate of the reaction at different slit widths. 4 mM CSA solution and 0.01 mM $[\text{Os(phen)}_3]^{3+}$ were reacted at pH 5, in the presence of 0.1 mM $[\text{Os(phen)}_3]^{2+}$, at slit widths 1 mm, 1.5 mm, 2.0 mm, and 3.0 mm. A negligible change in rate constant was observed when the slit width was changed from 1 mm to 3 mm. (Table A.4, Figure 2.7)

pH 5, [CSA]₀ = 6 mM, [Os(III)]₀ = 0.01 mM, [Os(II)]₀ = 0.1 mM

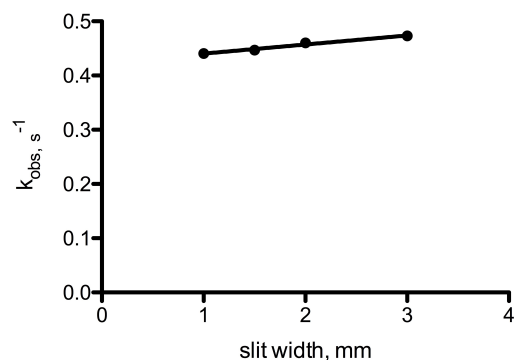


Figure 2.7: The plot of k_{OBS} vs slit width of UV-VIS spectrophotometer at pH 5 (acetate buffer). [CSA]_{TOT} = 6 mM, [[Os(III)(phen)₃]³⁺]₀ = 0.01 mM, [[Os(II)(phen)₃]²⁺]₀ = 0.1 mM, μ = 0.1 M, T = 25 °C. Straight line fit with slope = $(0.017 \pm 0.002) \text{ mm}^{-1} \text{ s}^{-1}$

2.4.6 Oxygen effect on the kinetics of the reaction

The effect the presence of O₂ has on the reaction rate was determined by preparing a 4 mM CSA solution, and a solution containing 0.1 mM [Os(phen)₃]²⁺, and 0.01 mM [Os(phen)₃]³⁺; both solutions at pH 4.5, and bubbling in oxygen through the solutions for 30 minutes prior to reacting them in stopped-flow instrument. The resulting kinetic trace showed a good first-order fit. (Figure 2.8) In the presence of O₂, the reaction rate is several times faster than the rate in the absence of O₂ in solution (see figure 2.6).

[Os(III)]₀ = 0.01 mM, [Os(II)]₀ = 0.1 mM, [CSA]₀ = 4 mM, pH 4.5

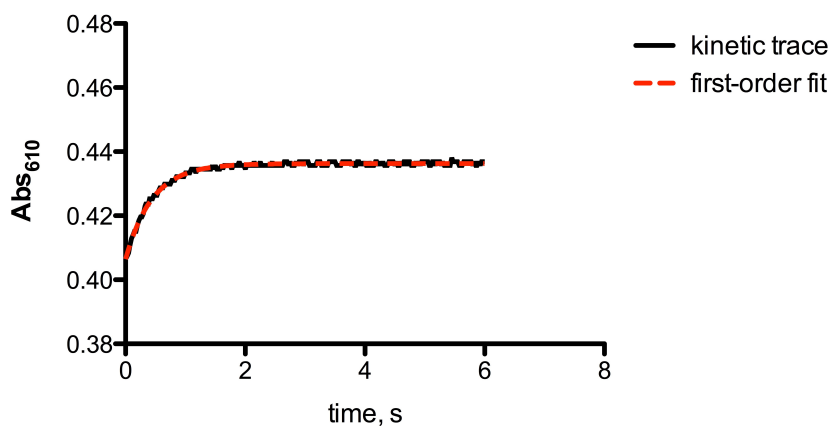


Figure 2.8: Kinetic trace of the reaction carried out with O₂ saturated solutions. $k_{\text{OBS}} = (2.32 \pm 0.05) \text{ s}^{-1}$

2.4.7 Kinetics with radical scavengers

The effect of radical trap PBN was determined by addition of varying concentrations of PBN into the reaction mixture by mixing it with CSA solutions. Reactions are done by completely converting Os(II) to Os(III). At low PBN concentrations, as the PBN concentration rises, a slight increase in the rate was observed. At $[\text{PBN}] \geq 1 \text{ mM}$, a linear relationship between $[\text{PBN}]$ and rate constant was observed. However, the slope of the graph differs from the slope of the graph below. The two slopes obtained indicate that two different species could be present, one when $[\text{PBN}] \ll [\text{CSA}]$ another when $\text{PBN} \geq [\text{CSA}]$. (Table A.5, figures 2.9 and 2.10)

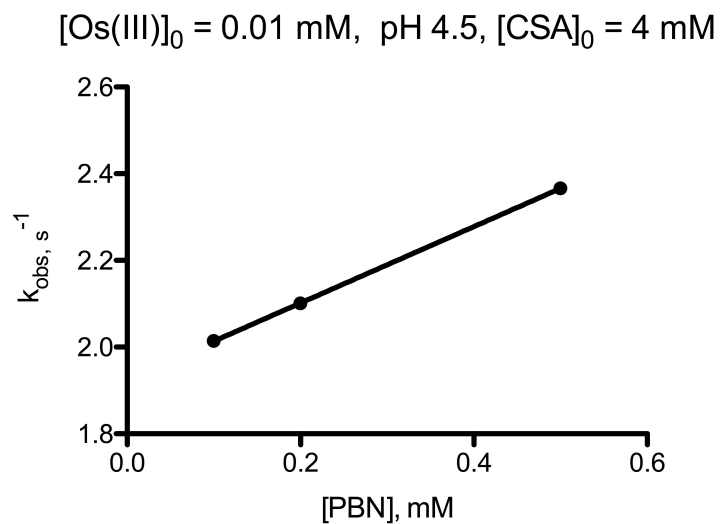


Figure 2.9: The plot of k_{OBS} vs PBN concentration at pH 4.5 (acetate buffer). $[\text{CSA}]_{\text{TOT}} = 4 \text{ mM}$, $[[\text{Os(III)(phen)}_3]^{3+}]_0 = 0.01 \text{ mM}$, $[[\text{Os(II)(phen)}_3]^{2+}]_0 \approx 0 \text{ mM}$, $\mu = 0.1 \text{ M}$, $T = 25 \text{ }^\circ\text{C}$. Straight line fit with slope = $(8.810 \pm 0.003) \times 10^2 \text{ s}^{-1} \text{ M}^{-1}$ and intercept = $(1.925 \pm 0.001) \text{ s}^{-1}$

Effect of PBN was also observed at higher PBN concentrations.

[Os(III)]₀ = 0.01 mM, pH 4.5, [CSA]₀ = 4 mM

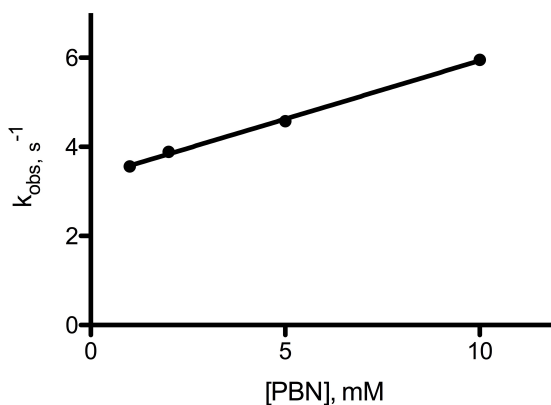


Figure 2.10: The plot of k_{OBS} vs PBN concentration with higher [PBN] at pH 4.5 (10 mM acetate buffer). [CSA]₀ = 4 mM, [[Os(III)(phen)₃]³⁺]₀ = 0.01 mM, [[Os(II)(phen)₃]²⁺]₀ ≈ 0 mM, μ = 0.1 M, T = 25 °C. Straight line fit with slope = $(2.620 \pm 0.007) \times 10^2 \text{ s}^{-1} \text{ M}^{-1}$ and intercept = $(3.32 \pm 0.04) \text{ s}^{-1}$

It can be hypothesized that the slope in Figure 2.10 corresponds to the reaction of Os(III) with the PBN-CSA adduct. Similarly, the intercept correlates to $k_{\text{et}}[\text{CysSO}_2^-]$. Therefore, $k_{\text{et}} = 8.2 \times 10^2 \text{ M}^{-1} \text{ s}^{-1}$.

The hypothesis that there is a new species forming at higher PBN concentrations was confirmed using ¹H NMR. (Figure 2.11) In the presence of CSA, the NMR spectrum of PBN shows the formation of a new peak. Using stopped-flow experiments, it was confirmed that Os(III) does not react with PBN. Nucleophilic addition reactions of nitrones have been previously reported.^{78–83} PBN is known to undergo nucleophilic addition reactions with carboxylates.⁸⁴ The carboxylate group of CSA may be attacking PBN to give rise to the species displaying the ¹H NMR peaks described above.

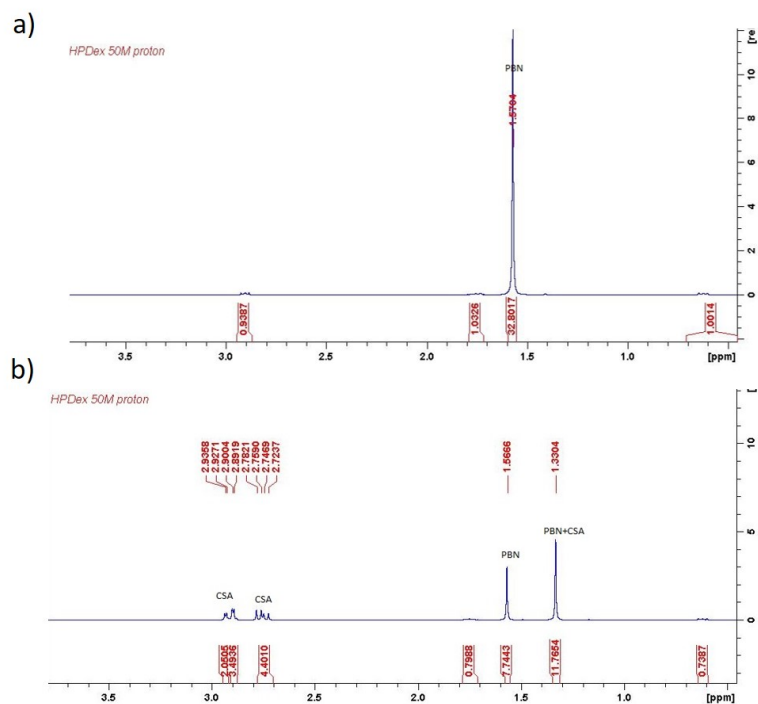


Figure 2.11: a) ¹H NMR spectrum of PBN in D₂O, [PBN] ≈ 0.1 M b) ¹H NMR spectrum of PBN and CSA in D₂O, [CSA]_{TOT} = 0.05 M, [PBN] = 0.1 M. From integrals of spectrum b, [CSA]_{unreacted} ≈ 0.01 M.

An attempt to use the spin trap 5,5-Dimethyl-1-pyrroline N-oxide (DMPO) was also made. However, it was found that DMPO consumes [Os(phen)₃]³⁺.

Olefins are often employed as free radical scavengers in aqueous media. For example, in aqueous media, allyl alcohol is known to scavenge •OH, •CH₃, and CH₃CO• radicals.^{85,86} When allyl alcohol is added to the reaction mixture, a slight increase in reaction rate was observed. (Figure 2.12)

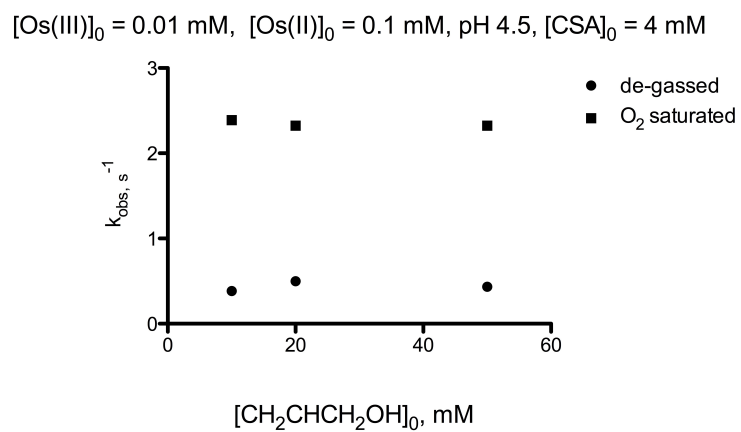
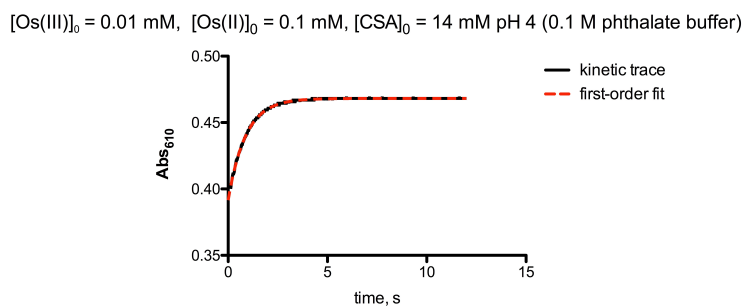


Figure 2.12: Effect of allyl alcohol concentration on the reaction rate in de-gassed and O_2 saturated solutions.

2.4.8 Effect of buffer

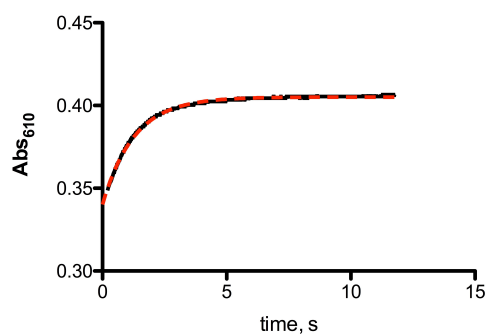
The effect of different types of buffer on the rate was determined by carrying out the reaction in phthalate and citrate buffers and comparing the rate constants with the rate constants of the reactions done with acetate buffer under respective reactant concentrations. (Figures 2.13 and 2.14)



$$k_{\text{OBS}} = (0.97 \pm 0.01) \text{ s}^{-1}$$

Figure 2.13: Kinetic trace of the oxidation of CSA by [Os(phen)₃]³⁺ in phthalate buffer. [[Os(phen)₃]³⁺]₀ = 0.01 mM, [[Os(phen)₃]²⁺]₀ = 0.1 mM [CSA]₀ = 14 mM, μ = 0.1 M (NaCl), T = 25 °C, pH = 4 (0.1 M phthalate buffer), monitored at 610 nm, $k_{\text{OBS}} = (0.97 \pm 0.01) \text{ s}^{-1}$. In acetate buffer, $k_{\text{OBS}} = 0.985 \text{ s}^{-1}$

$[\text{Os(III)}]_0 = 0.01 \text{ mM}$, $[\text{Os(II)}]_0 = 0.1 \text{ mM}$, pH 4.3 (0.1 M citrate buffer)



$$k_{\text{OBS}} = (0.713 \pm 0.007) \text{ s}^{-1}$$

Figure 2.14: Kinetic trace of the oxidation of CSA by $[\text{Os(phen)}_3]^{3+}$. $[[\text{Os(phen)}_3]^{3+}]_0 = 0.01 \text{ mM}$, $[[\text{Os(phen)}_3]^{2+}]_0 = 0.1 \text{ mM}$, $[\text{CSA}]_{\text{TOT}} = 10 \text{ mM}$, $\mu = 0.1 \text{ M}$ (NaCl), $T = 25 \text{ }^\circ\text{C}$, pH = 4.3 (0.1 M citrate buffer), monitored at 610 nm, $k_{\text{OBS}} = (0.713 \pm 0.007) \text{ s}^{-1}$. In acetate buffer, under the same reactant concentration, $k_{\text{OBS}} = 0.72 \text{ s}^{-1}$

2.4.9 Effect of Br⁻ on the reaction rate

To determine the effect of Br⁻ formed by the oxidation of Br₂ during oxidation of Os(II), a series of experiments were carried out by adding varying amounts of NaBr to Os(II)/Os(III) solution prior to the reaction. Table 2.1 shows the rate constants observed when different amounts of Br⁻ were present. All previous experiments conducted without addition of Br⁻, have 0.005 mM Br⁻ formed in the product mixture.

Table 2.1: k_{OBS} dependence on [Br⁻]

Exp.No.	[Br ⁻],mM	rate constant, s ⁻¹
1	0.005	0.23
2	0.01	0.24
3	0.025	0.23
4	0.03	0.23
5	0.05	0.24

[Os(III)]₀ = 0.01 mM, [CSA]_{TOT} = 4 mM, T = (25.0 ± 0.1) °C
μ = 0.1 M (NaCl), pH = 2.5 (dilute HCl).

From the results in table 2.1, it can be concluded that presence of up to 0.05 mM of Br⁻ in the reactant mixture, has negligible effect on the rate constant of the reaction.

2.4.10 Reaction stoichiometry

Stoichiometry of the reaction between CSA and $[\text{Os}(\text{phen})_3]^{3+}$ was determined using a spectrophotometric titration. For this experiment, first 1.8 ml of 2.0×10^{-5} M CSA solution in pH 4.5 acetate buffer was added into a quartz cuvette and the UV spectrum was recorded. Next, 0.05 ml of 6.6×10^{-4} M $[\text{Os}(\text{phen})_3]^{3+}$ (prepared by over-oxidizing a solution of $[\text{Os}(\text{phen})_3]^{2+}$ by $\text{Br}_2/\text{CH}_3\text{CN}$ and bubbling the solution with Ar to remove excess Br_2) in a pH 3 dilute HCl solution (to slow down the reaction of $[\text{Os}(\text{phen})_3]^{3+}$ with water) was added into the cuvette and allowed to react for 10 min. While the reaction was taking place, the solution in cuvette was bubbled with Ar to remove any O_2 present. When 10 minutes had passed, the UV spectrum of the reaction mixture was recorded. After that, the procedure was repeated adding 0.05 ml aliquots of $[\text{Os}(\text{phen})_3]^{3+}$ using a gastight syringe at 10 min intervals till the total amount of 6.6×10^{-4} M $[\text{Os}(\text{phen})_3]^{3+}$ added was 0.8 ml. Absorbance at 610 nm corrected for the increase of volume after addition of each aliquot of $[\text{Os}(\text{phen})_3]^{3+}$ was considered when determining the end point of the titration. (Figure 2.15)

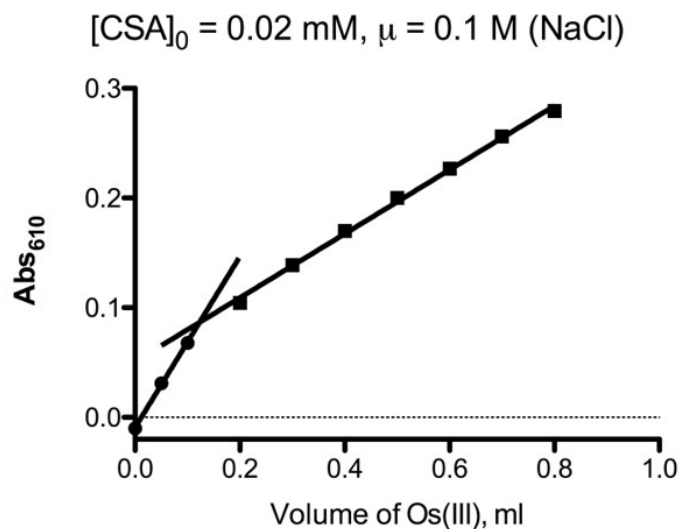


Figure 2.15: The plot of Absorbance (corrected for volume increase) at 610 nm vs volume of 6.6×10^{-4} M $[\text{Os}(\text{phen})_3]^{3+}$ added

The consumption ratio $\Delta[[\text{Os}(\text{phen})_3]^{3+}]/\Delta[\text{CSA}] = 2.2:1$ After attaining the end point, the absorbance continues to rise, albeit with a lower slope, as more Os(III) is added, since both Os(II), and Os(III) absorb in the wavelength range of approximately 320-700 nm. The titration was complete in 90 minutes.

2.4.11 Product determination

Both the osmium containing product and cysteine containing products were identified using $^1\text{H-NMR}$. The reaction was carried out using 0.9 mM $[\text{Os}(\text{phen})_3]^{3+}$, 0.6 mM $[\text{Os}(\text{phen})_3]^{2+}$, and 1.7 mM CSA in H_2O . The mixture was allowed to react under bubbled in argon for 40 min and then taken to dryness by rotary evaporation. The resulting mixture was dissolved in 0.7 ml D_2O and 1 mM DSS was added as the internal reference. From the spectrum (Figure 2.16) it can be observed that cysteic acid is the major cysteine containing product of this reaction. Peaks at δ 4.3 (d), δ 3.5 (d) and δ 3.3 (dd) arise from cysteic acid. Signals at δ 7.5 (t), δ 8.0 (d) and δ 8.2 (s), and δ 8.3 (d) originate from $[\text{Os}(\text{phen})_3]^{2+74}$ (figure 2.17). To confirm the identity of the cysteine-containing oxidation products, authentic cysteic acid was added to the product mixture and the $^1\text{H-NMR}$ spectrum was recorded again. When authentic CSA was added to the mixture, intensity of all the signals that were not assigned to DSS, cysteic acid or $[\text{Os}(\text{phen})_3]^{2+}$ increased. (figure 2.18) Therefore, by adding known samples of CSA and cysteic acid, we were able to account for all the major peaks present in the $^1\text{H-NMR}$ spectrum of the product mixture for the reaction between CSA and $[\text{Os}(\text{phen})_3]^{3+}$. The table 2.2 summarizes the identities of species that give rise to the signals in the product $^1\text{H-NMR}$ spectrum.

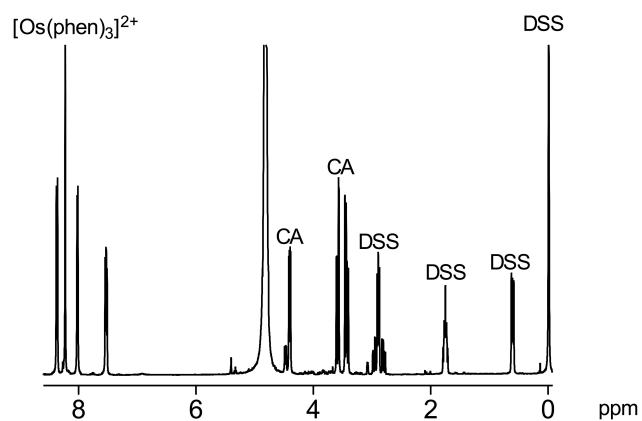


Figure 2.16: ^1H -NMR spectrum of the product mixture in D_2O , with DSS reference, 25 $^\circ\text{C}$

Expansions of the NMR spectra are given below.

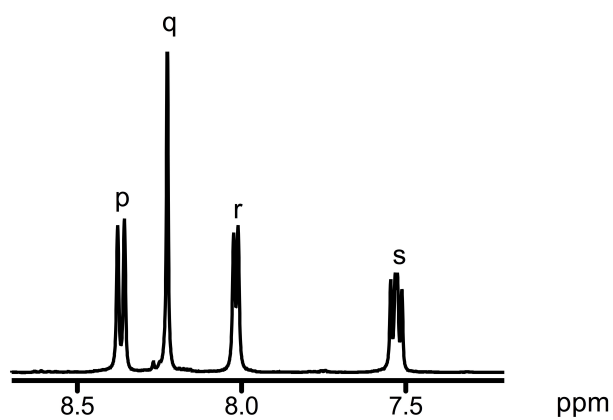


Figure 2.17: Expansion of the ^1H -NMR spectrum to show peaks arising from $[\text{Os}(\text{phen})_3]^{2+}$

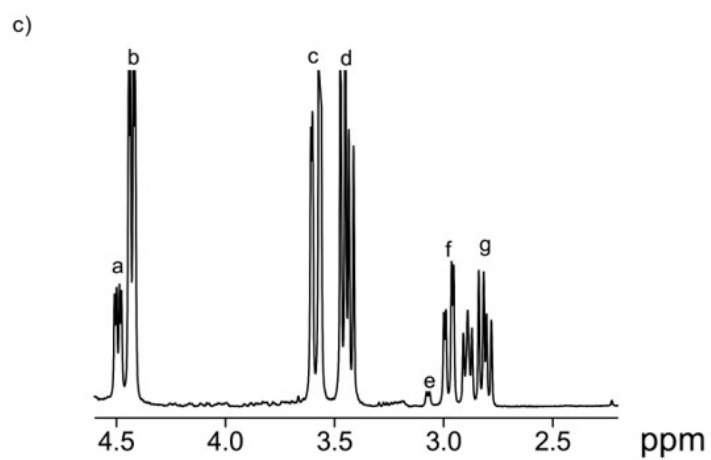
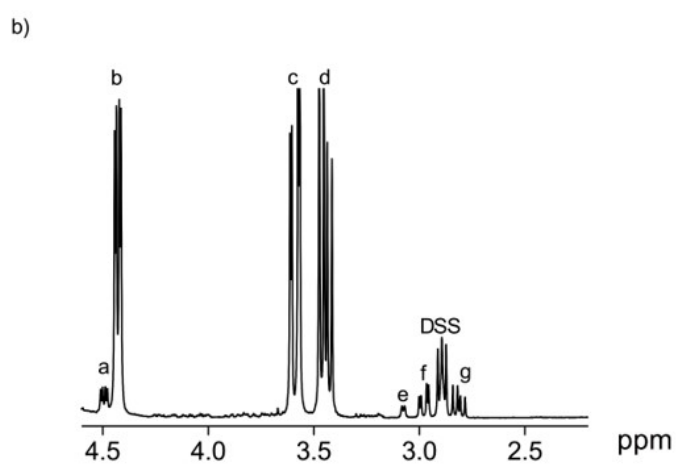
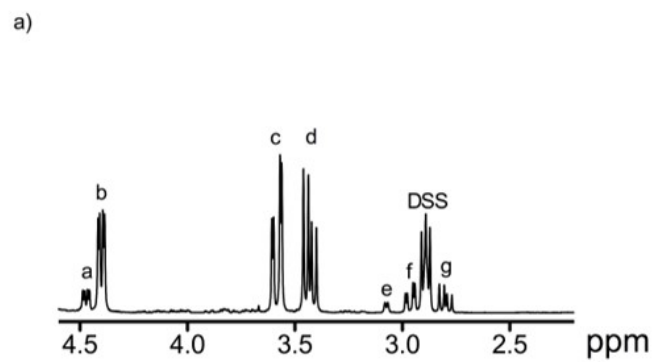


Figure 2.18: Expansion of the ^1H -NMR spectra a) product mixture b) after addition of cysteic acid c) after addition of CSA 60

Table 2.2: Assignment of peaks in ^1H -NMR spectrum of the product mixture

Chemical species	Corresponding signals
$[\text{Os}(\text{phen})_3]^{2+}$	p, q, r, s
Cysteic acid	b, c, d
CSA	a, f, g

2.4.12 Cyclic voltammetry

The cyclic voltammogram of a solution with 0.1 mM $[\text{Os}(\text{phen})_3]^{2+}$ and 2 mM CSA in $\mu = 0.1 \text{ M}$ (NaCl) was recorded. $E_{1/2} = 641 \text{ mV}$ vs Ag/AgCl(s) ($E_{1/2} = 0.838$ vs normal hydrogen electrode) Next, the cyclic voltammogram of a solution with 0.1 mM $[\text{Os}(\text{phen})_3]^{3+}$ (prepared by addition of an excess of $\text{Br}_2/\text{CH}_3\text{CN}$ and bubbling the solution with argon for 30 min to remove excess Br_2) 2 mM CSA in $\mu = 0.1 \text{ M}$ (NaCl) was recorded. $E_{1/2} = 636 \text{ mV}$ vs Ag/AgCl(s) ($E_{1/2} = 0.833$ vs normal hydrogen electrode) (Figure 2.19)

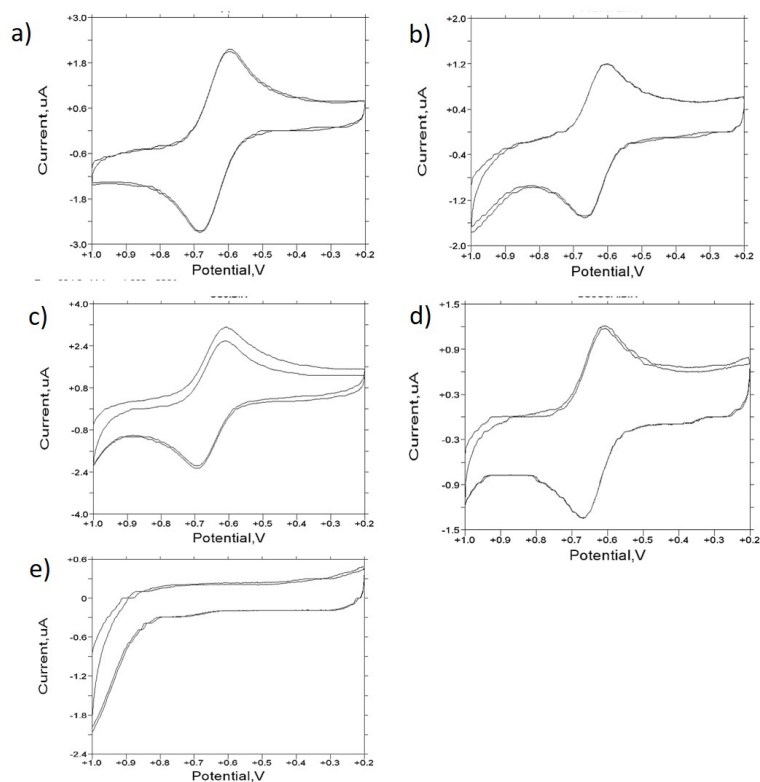


Figure 2.19: a) Cyclic voltammogram of 0.2 mM $[\text{Os}(\text{phen})_3]^{2+}$ at $\mu = 0.1$ M (NaCl) b) Cyclic voltammogram of 0.1 mM $[\text{Os}(\text{phen})_3]^{2+}$ and 0.2 mM CSA at $\mu = 0.1$ M (NaCl). c) Cyclic voltammogram of 0.2 mM $[\text{Os}(\text{phen})_3]^{3+}$ at $\mu = 0.1$ M (NaCl) d) Cyclic voltammogram of 0.1 mM $[\text{Os}(\text{phen})_3]^{3+}$ and 0.2 mM CSA at $\mu = 0.1$ M (NaCl) e) Cyclic voltammogram of 0.2 mM CSA at $\mu = 0.1$ M (NaCl)

2.4.13 Yield of osmium containing product

Yield of osmium containing product was determined using a diode array UV-VIS spectrophotometer. First a solution of 4×10^{-5} M $[\text{Os}(\text{phen})_3]^{2+}$ at pH 2 and 0.1 M ionic strength was prepared, and its UV-VIS spectrum was recorded. Next, all $[\text{Os}(\text{phen})_3]^{2+}$ was oxidized to $[\text{Os}(\text{phen})_3]^{3+}$ using an excess of $\text{Br}_2/\text{CH}_3\text{Cl}$ and bubbled with argon and the

UV-VIS spectrum of $[\text{Os}(\text{phen})_3]^{3+}$ was recorded. After that, 0.008 g of L-cysteinesulfinic acid monohydrate was added to the $[\text{Os}(\text{phen})_3]^{3+}$ solution, and the reactants were allowed to react under argon for 30 minutes. Finally, the UV-VIS spectrum of the product mixture was recorded. According to figure 2.20, all of the $[\text{Os}(\text{phen})_3]^{3+}$ is reduced to $[\text{Os}(\text{phen})_3]^{2+}$ by the excess of CSA added. This confirms that the electron transfer takes place at the metal center during the oxidation of CSA, and not at the ligands of the oxidant.

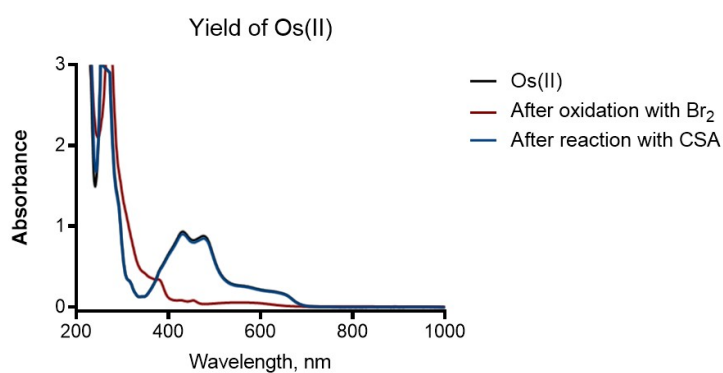


Figure 2.20: UV-VIS spectra for determination of Os(II) yield.

2.5 Quantum Calculations

Hydrogen transfer reactions from sulfur-based radicals to form carbon-based radicals have been reported for thiyl radicals.⁸⁷ For cysteine thiyl radicals, 1,2- and 1,3-hydrogen transfer reactions have been observed. Also, for cysteine analogous molecules such as cystamine and penicillamine exhibit hydrogen transfer reactions from sulfur-based radicals to form carbon based radicals.

To determine whether cysteinesulfonyl radical is capable of undergoing a similar reaction to transfer α or β hydrogens to form carbon radicals, quantum calculations were carried out. MP2(FC) method was used with the basis set 6-311G* for all the calculations. In gas phase calculations, transfer of β hydrogen to form a carbon radical was energetically more favorable than the transfer of an α hydrogen. The rearrangement of cysteinesulfonyl radical to the carbon based β hydrogen removed radical only requires +19.97 kJ/mol of Gibbs energy at 298 K, and this energy barrier is easily surpassable at room temperature. This preference for the removal of β hydrogen over removal of α hydrogen removal may be arising from the extended conjugation due to the near planarity of the amine and carboxylate groups attached to the carbon radical. The energy gap in aqueous medium between cysteinesulfonyl radical and β hydrogen removed cysteinesulfinate radical is even smaller. (+7.08 kJ/mol)

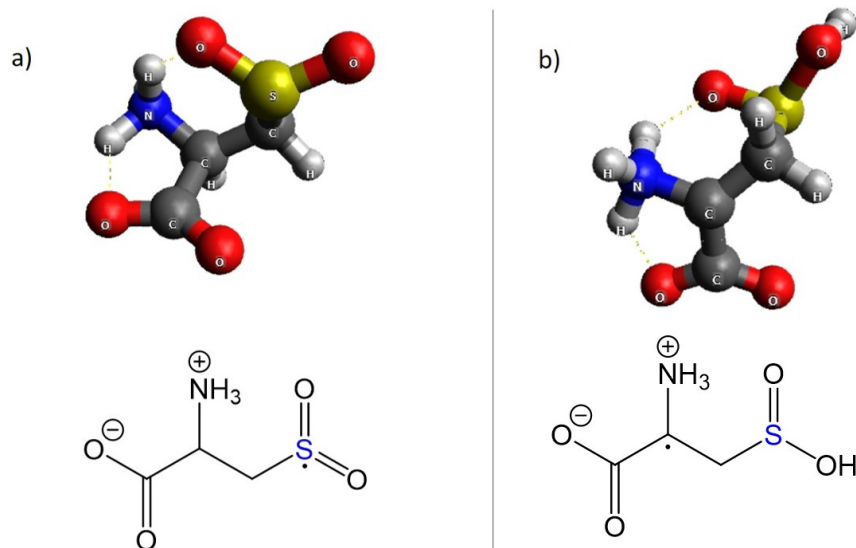


Figure 2.21: Optimized structures of a) cysteinesulfonyl radical b) rearranged β hydrogen removed radical. Structures are optimized using MP2(FC) method under 6-311G* basis set

2.6 Discussion

From the results presented above, the empirical rate law for CSA oxidation by $[\text{Os}(\text{phen})_3]^{3+}$ is

$$\frac{-d[[\text{Os}(\text{phen})_3]^{3+}]}{dt} = \frac{[\text{CSA}][[\text{Os}(\text{phen})_3]^{3+}]}{[[\text{Os}(\text{phen})_3]^{2+}]} \frac{K_{a1}(k'_1 K_{a2} + k'_2 [\text{H}^+]_{\text{(aq)}})}{([\text{H}^+]_{\text{(aq)}}^2 + [\text{H}^+]_{\text{(aq)}} K_{a1} + K_{a1} K_{a2}} \quad (2.15)$$

Using the data presented in the kinetics section of this chapter, values for k'_1 and k'_2 were determined. $k'_1 = (7.0 \pm 0.2) \times 10^{-3} \text{ s}^{-1}$, and $k'_2 = (7.1 \pm 0.9) \times 10^{-4} \text{ s}^{-1}$. Here $K_{a1} = 3.16 \times 10^{-2} \text{ M}$ and $K_{a2} = 4.17 \times 10^{-3} \text{ M}$.

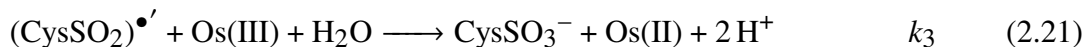
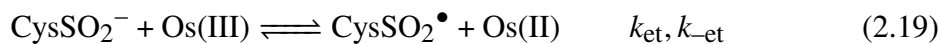
In the pH range 4-6, the rate is independent of pH. In this pH range the rate law reduces to

$$\frac{-d[[\text{Os}(\text{phen})_3]^{3+}]}{dt} = k'_1 \frac{[\text{CSA}][[\text{Os}(\text{phen})_3]^{3+}]}{[[\text{Os}(\text{phen})_3]^{2+}]} \quad (2.16)$$

In this rate-law, $k'_1 = (7.53 \pm 0.07) \times 10^{-3} \text{ s}^{-1}$.

The following mechanism is proposed for the reaction between CSA and $[\text{Os}(\text{phen})_3]^{3+}$. Here ${}^-\text{OOCCH}(\text{NH}_3^+)\text{CH}_2\text{SO}_2^-$ is the expanded form of CysSO_2^- .





Reversibility of the electron transfer step shown in equation 2.19 was determined by the strong kinetic inhibition observed with $[\text{Os}(\text{phen})_3]^{2+}$.

In the pH range 4-6, the rate is independent of pH. Therefore, the rate law for the proposed mechanism is given by

$$\frac{-d[\text{Os(III)}]}{dt} = \frac{k_{\text{et}}k_{\text{re}}[\text{CSA}]_{\text{TOT}}[\text{Os(III)}]}{k_{-\text{et}}[\text{Os(II)}] + k_{\text{re}}} \quad (2.22)$$

For $k_{-\text{et}}[\text{Os(II)}] \gg k_{\text{re}}$, equation 2.22 reduces to equation 2.23

$$\frac{-d[\text{Os(III)}]}{dt} = \frac{k_{\text{et}}k_{\text{re}}[\text{CSA}]_{\text{TOT}}[\text{Os(III)}]}{k_{-\text{et}}[\text{Os(II)}]} \quad (2.23)$$

Comparing the empirical rate-law given in equation 2.16 with the proposed rate-law in equation 2.23,

$$k'_1 = \frac{k_{\text{et}}k_{\text{re}}}{k_{-\text{et}}} \quad (2.24)$$

Substituting values for k_{et} and k'_1 in equation 2.24, $\frac{k_{\text{re}}}{k_{-\text{et}}} = 9.18 \times 10^{-6} \text{ M}$.

The overall reaction is,



Sulfonyl radical ($\text{RSO}_2\cdot$) is a universally accepted intermediate in alkane/aryl sulfinate oxidation by one electron oxidants.^{26,88} $\text{RSO}_2\cdot$ is known to undergo the following equilibrium.⁸⁹



However, the effect of this equilibrium on our reaction seems negligible based on the CSA-based products observed in $^1\text{H-NMR}$.

One possibility for the rearrangement of the cysteinesulfonyl radical is the formation of the corresponding thiyl peroxy radical.

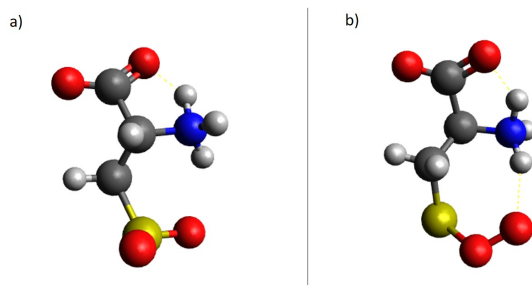


Figure 2.22: Optimized structures of a) cysteinesulfonyl radical, b) cysteine thiyl peroxy radical

It has been reported that thiyl peroxy radicals ($\text{RSOO}\cdot$) are capable of undergoing unimolecular rearrangement to form $\text{RSO}_2\cdot$.^{36,90,91}



From quantum calculations we determined that converting cysteinesulfonyl radical to cysteine thiyl peroxy radical (CysSOO•) requires 159.49 kJ/mol of energy.

Another possible rearrangement the sulfonyl radical could undergo is β hydrogen elimination. The results from the quantum calculations show that for cysteinesulfonyl radical, this reaction may happen in aqueous media at room temperature at a rapid rate. This could correspond to reaction 2.20. However the exact mechanism of how cysteinesulfonate is formed from the β hydrogen eliminated sulfonyl radical is not clear.

2.7 Conclusions

Cysteinesulfinate is oxidation by $[\text{Os}(\text{phen})_3]^{3+}$ proceeds via a rate-limiting outer-sphere electron transfer to form the sulfonyl radical, with first-order kinetic inhibition by the reduced form of oxidant. The electron transfer process does not perturb the coordination sphere of the oxidant. The final cysteine containing product of this reaction is cysteinesulfonate. The kinetics observed in this study show remarkable deviation from kinetics reported for the reaction of CSA with $[\text{IrCl}_6]^{3-}$.³³ This may be due to the differences in charge and the standard reduction potentials of the two oxidants. Also, $[\text{IrCl}_6]^{2-}$ is capable of forming bridges with the reductant, while $[\text{Os}(\text{phen})_3]^{3+}$ is substitution inert.

Chapter 3

Kinetics and mechanism of the oxidation of L-cysteinesulfinic acid by bis(1,4,7-triazacyclononane) nickel (III)

3.1 Introduction

The kinetics described in Chapter 2 on L-cysteinesulfinic acid oxidation by tris(1,10-phenanthroline)osmium(III) strongly contrast with the published rate law for the reaction of L-cysteinesulfinic acid with hexachloroiridate(IV).⁹² To determine the extent of effect of the oxidant on the observed kinetics, the reaction of CSA with stable one-electron

oxidant $[\text{Ni}(\text{tacn})_2](\text{ClO}_4)_3$ was investigated. The charge of the oxidant influences the rate of electron transfer since ΔG is affected by Coulomb energy, as suggested by Marcus Theory.⁶⁷ $[\text{Ni}(\text{tacn})_2](\text{ClO}_4)_3$ was chosen as the oxidant due to its cationic nature similar to $[\text{Os}(\text{phen})_3](\text{CF}_3\text{SO}_3)_3$. The considerably lower self-exchange rate constant of $[\text{Ni}(\text{tacn})_2](\text{ClO}_4)_3$ as well as the higher formal potential compared to $[\text{Os}(\text{phen})_3](\text{CF}_3\text{SO}_3)_3$ predicted interesting kinetic behavior.

$[\text{Ni}(\text{tacn})_2]^{3+}$ is a substitutionally inert transition metal complex. The two ligands coordinated to Ni(III) center are in facial orientation. (Figure 3.1) The metal center has d^7 electron configuration which makes the complex susceptible to Jahn-Teller distortion.⁹³ $[\text{Ni}(\text{III})(\text{tacn})_2]^{3+}$ is not stable in basic media as N-H protons ($\text{p}K_a \approx 9$)⁹⁴ in the ligand tend to deprotonate.

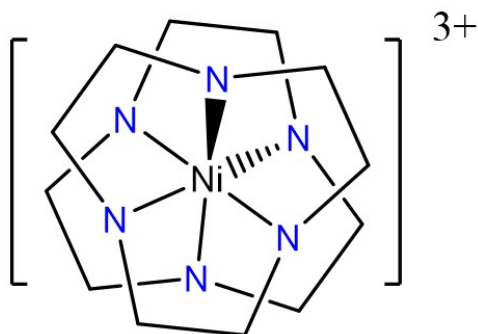


Figure 3.1: Chemical structure of bis(1,4,7-triazacyclononane)Ni(III)

Since bis(1,4,7-triazacyclononane)Ni(III) is coordination saturated, electron-transfer reactions are expected to take place via outer-sphere electron transfer mechanism yielding bis(1,4,7-triazacyclononane)Ni(II), and this has been observed in many studies.^{95–97}



3.2 Reagents and solutions

L-cysteinesulfinic acid monohydrate (CSA, 99% Aldrich), $\text{Ni}(\text{ClO}_4)_2 \cdot 6\text{H}_2\text{O}$ (Alfa Aesar), 1,4,7-triazacyclononane trihydrochloride (tacn, TCI), $\text{Na}_2\text{S}_2\text{O}_8$, L-cysteic acid monohydrate, and CH_3COONa anhydrous (all from Sigma), glacial acetic acid, NaCl, methanol, KBrO_3 , and KBr, (all from Fischer Scientific), D_2O 99.8% isotopic (Alfa Aesar), NaOH pellets, 3-(trimethylsilyl)-1-propanesulfonic acid sodium salt (DSS), Sephadex C-25, and QAE Sephadex (all from Sigma-Aldrich), and methyl orange were used as supplied.

All the aqueous solutions were prepared using purified deionized water from a Barnstead Nanopure Infinity system. Stock solutions of L-cysteinesulfinic acid, glacial acetic acid and CH_3COONa were prepared and stored in the refrigerator. All other solutions were freshly prepared for each experiment. All solutions were purged with argon unless specified otherwise in-order to keep the solutions oxygen free. The sulfonyl radicals formed by one electron oxidation of sulfinates are known to react with oxygen giving rise to a chain reaction.²⁶ Stock solutions of L-cysteinesulfinic acid were standardized using a bromo-metric titration. For this, an aliquot of strongly acidified L-cysteinesulfinic acid solution in the presence of KBr and two drops of methyl orange was titrated with standard $\text{KBrO}_3(\text{aq})$ solution. All solutions were purged with argon. To minimize decomposition all $[\text{Ni}(\text{III})(\text{tacn})_2]^{3+}$ solutions were prepared at pH 3 or lower, and were protected from exposure to light.

3.3 Preparation of bis(1,4,7-triazacyclononane)Ni(II) perchlorate

Bis(1,4,7-triazacyclononane)Ni(II) perchlorate was prepared as described in literature.⁹⁸ 96.8 mg of 1,4,7-triazacyclononane (tacn) was dissolved in 1.2 ml of 1 M NaOH and heated

till tacn was dissolved. Then 73.8 mg of $\text{Ni}(\text{ClO}_4)_2 \cdot 6\text{H}_2\text{O}$ was dissolved in 1.5 ml methanol and added to the tacn solution. The resulting lilac solution was warmed on a steam bath for 7 min. After that the pH of the mixture was adjusted to 5 and the solution was cooled at 0 °C. Lilac crystals were formed within two hours in almost quantitative yield.

3.4 Preparation of bis(1,4,7-triazacyclononane)Ni(III) perchlorate

Bis(1,4,7-triazacyclononane)Ni(III) perchlorate was prepared using a method described in literature.⁹⁹ Bis(1,4,7-triazacyclononane)Ni(II) perchlorate crystals were dissolved in a minimum amount of 1 M HClO_4 . Then a saturated solution of $\text{Na}_2\text{S}_2\text{O}_8$ was added to achieve the ratio of bis(1,4,7 triazacyclononane)Ni(II) perchlorate : $\text{Na}_2\text{S}_2\text{O}_8$ to be 1:0.6. To the resulting dark brown solution, saturated NaClO_4 was added drop-wise until formation of bis(1,4,7-triazacyclononane)Ni(III) precipitate could be detected. After that, the mixture was cooled at 0 °C. The lustrous brown crystals formed overnight were vacuum dried and the yield was approximately 80%.

3.5 Experimental methods

To obtain UV-Vis spectra of the reagents and the product mixtures, examine the photosensitivity of reagents, and for spectrophotometric titrations, an HP-8453 diode array spectrophotometer was used. Solutions were kept in quartz cells with path length 1 mm or 1 cm. To obtain kinetic data, a Hi-Tech SF-51 stopped-flow spectrophotometer with a 1 cm path length configuration with a C-400 circulatory water bath to keep solutions at 25 °C was used. In each run, equal volumes of reactants were mixed. The progress of the reaction was monitored by observing decrease of absorbance at 312 nm. Data were stored

using an OLIS 4300 data acquisition and analysis software and analyzed with GraphPad PRISM 8. To calculate observed rate constant, the average rate constant of at least five reproducible runs were used. All pH measurements were collected at room temperature and pressure using a Corning 450 pH/ion meter equipped with a Mettler Toledo InLab 421 pH electrode filled with 3.0 M NaCl(aq); NaCl was used instead of KCl to avoid precipitation of KClO₄ on the surface of the pH probe. The pH electrode was calibrated using standard buffers before each measurement. ¹H NMR spectra of the reagents and product mixtures were obtained from a Bruker AV 400 MHz spectrometer. For ¹H NMR measurements, anaerobic solutions were prepared in D₂O with 3-(trimethylsilyl)-1-propanesulfonic acid sodium salt (DSS) as the internal standard. Electrochemical analyses of the reagents and product mixtures were done on an electrochemical analyzer equipped with BAS C3 cell stand with a stirring and purging system. The working electrode was a Pt electrode and the reference electrode was a Ag/AgCl electrode containing 3.0 M NaCl. (E° = 0.205 V vs NHE) The counter electrode was a Pt wire. Electrospray mass spectra were recorded with a Waters Q-ToF premier mass spectrometer in the negative mode. The product mixtures were separated using HILIC (Hydrophilic Interaction) chromatography.

3.6 Results

3.6.1 Properties of bis(1,4,7-triazacyclononane)Ni(III)

The UV spectrum of aqueous bis(1,4,7-triazacyclononane)Ni(III) perchlorate was obtained by preparing a 0.6 mM solution of bis(1,4,7-triazacyclononane)Ni(III) perchlorate in 0.1 M HCl. In the UV spectrum, two absorbance maxima are observed at 270 nm and 312 nm, and a shallow minimum is observed at 290 nm (Figure 3.2). $\epsilon = 1.0 \times 10^4 \text{ M}^{-1} \text{ cm}^{-1}$ (312 nm). ϵ reported in literature for bis(1,4,7-triazacyclononane)Ni(III) is comparable to the value we experimentally obtained ($10,100 \text{ M}^{-1} \text{ cm}^{-1}$ at 312 nm).⁹⁸

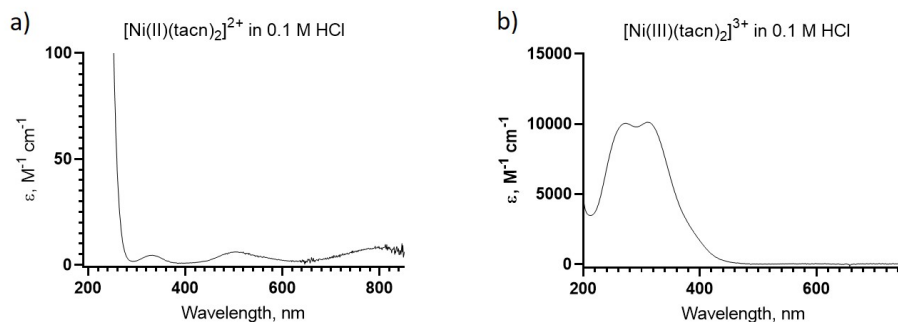


Figure 3.2: The UV-VIS spectra of a) bis(1,4,7-triazacyclononane)Ni(II) perchlorate in 0.1 M HCl b) bis(1,4,7-triazacyclononane)Ni(III) perchlorate in 0.1 M HCl where $\epsilon_{312}\text{Ni(III)} = 1.01 \times 10^4 \text{ M}^{-1} \text{ cm}^{-1}$

1 mM solution of bis(1,4,7-triazacyclononane)Ni(III) perchlorate with 0.1 M NaCl displays a reversible cyclic voltammogram with $E^{\circ'} = 0.94 \text{ V vs NHE}$ (Figure 3.3). The reported $[\text{Ni}(\text{tacn})_2]^{2+/3+}$ $E^{\circ'} = 0.720 \text{ V vs SCE}$ ¹⁰⁰

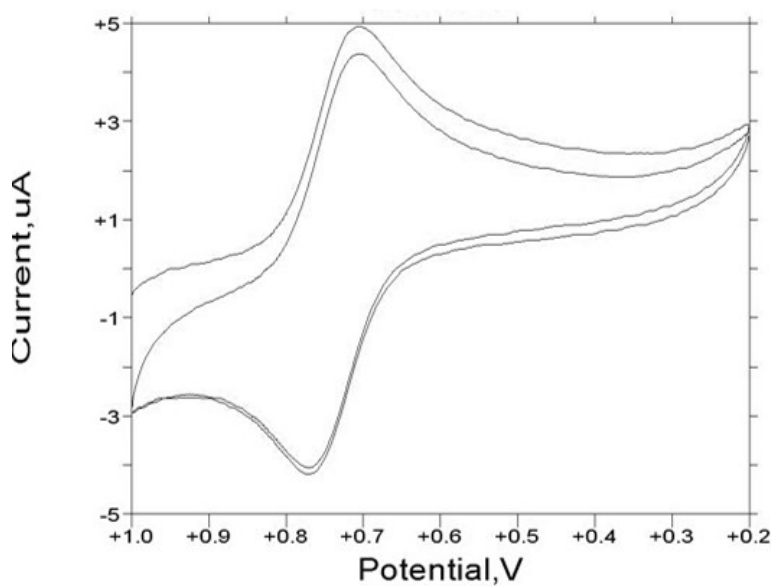


Figure 3.3: The cyclic voltammogram of 0.1 mM bis(1,4,7-triazacyclononane)Ni(III) perchlorate at pH 3. Scan rate = 100 mV s^{-1} .

3.6.2 Photosensitivity of bis(1,4,7-triazacyclononane)Ni(III)

Photosensitivity of the metal complex was studied at 312 nm using a diode-array spectrophotometer with both the UV and visible lamps on. This method allows for the illumination of the sample with a beam of white light. A solution of $[\text{Ni(III)(tacn)}_2]^{3+}$ at pH 3.4 and $\mu = 0.1 \text{ M}$ (NaCl) was put into a quartz sample cell with 1 mm path length and was irradiated for 1 hr with 2 s integration time and 4 s cycle time. The sample showed 90% decrease of absorbance. When the cycle time was increased to 20 s, the decrease of absorbance was approximately 34%. The decay of absorbance at 312 nm with time is shown in Figure 3.4.

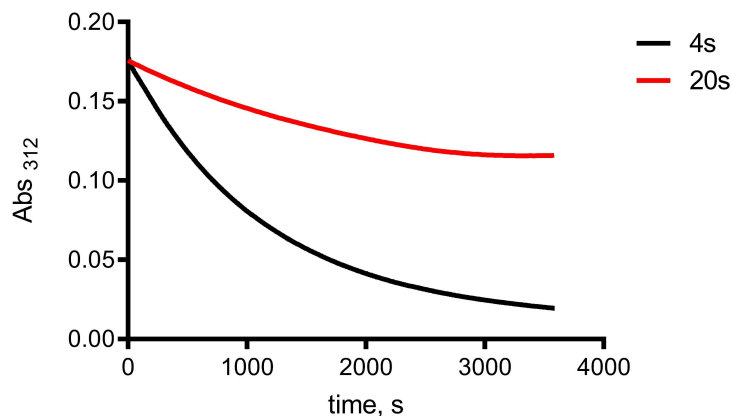


Figure 3.4: Decrease of absorbance at 312 nm when 0.1 mM $[\text{Ni(III)(tacn)}_2]^{3+}$ at pH 3.4 at different cycle times.

3.6.3 Kinetics of the reaction



For the equation above, the rate law can be written as,

$$\frac{-d[[\text{Ni(tacn)}_2]^{3+}]}{dt} = k[\text{CSA}][[\text{Ni(tacn)}_2]^{3+}] \quad (3.3)$$

When $[\text{CSA}] \gg \gg [[\text{Ni(tacn)}_2]^{3+}]$, $\Delta[\text{CSA}] \approx 0$

Therefore, the rate law could be re-written as

$$\frac{-d[[\text{Ni(tacn)}_2]^{3+}]}{dt} = k_{\text{OBS}}[[\text{Ni(tacn)}_2]^{3+}] \quad (3.4)$$

Where $k_{\text{OBS}} = k[\text{CSA}]$

When 0.05 mM $[\text{Ni(III)(tacn)}_2]^{3+}$ and 1 mM CSA are mixed to make a solution at pH 4

and $\mu = 0.1$ M (NaCl) from the decay of absorbance at 312 nm excellent first-order kinetics can be observed. (Figure 3.5)

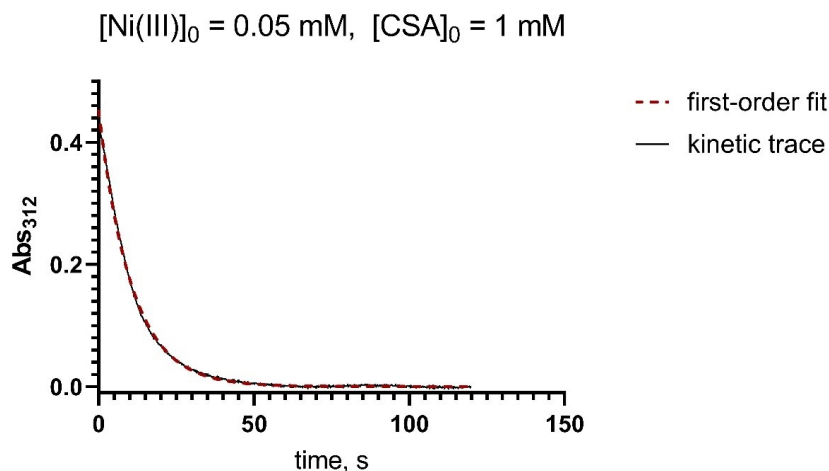


Figure 3.5: Decay of absorbance at 312 nm $[[\text{Ni(III)(tacn)}_2]^{3+}]_0 = 0.05$ mM, $[\text{CSA}]_0 = 1$ mM, $[\text{NaCl}] = 0.1$ M, $T = 25$ °C, $\text{pH} = 2.5$ (dilute HCl), $k_{\text{OBS}} = 0.09$ s⁻¹

3.6.4 Rate dependence on presence of $[\text{Ni(II)(tacn)}_2]^{2+}$

Effect of the reaction product $[\text{Ni(II)(tacn)}_2]^{2+}$ on the reaction rate was studied by adding varying amounts of $[\text{Ni(II)(tacn)}_2]^{2+}$ into the reaction mixture and determining the rate of the reaction using stopped-flow methods. 0.05 mM $[\text{Ni(III)(tacn)}_2]^{3+}$ and 1 mM CSA was reacted at pH 4.5 (10 mM acetate buffer) and $\mu = 0.1$ M (NaCl) without any $[\text{Ni(II)(tacn)}_2]^{2+}$ present, and then with 0.2 mM, 0.4 mM, 0.6 mM, 0.8 mM, 1.0 mM, and 1.2 mM $[\text{Ni(II)(tacn)}_2]^{2+}$ present. The rate of the reaction was found to decrease slightly with increasing $[\text{Ni(II)(tacn)}_2]^{2+}$ concentration. However significant changes in fit were not observed at any Ni(II) concentration used. (Table A.7, Figure 3.6)

[Ni(III)]₀ = 0.05 mM, [CSA]₀ = 1 mM

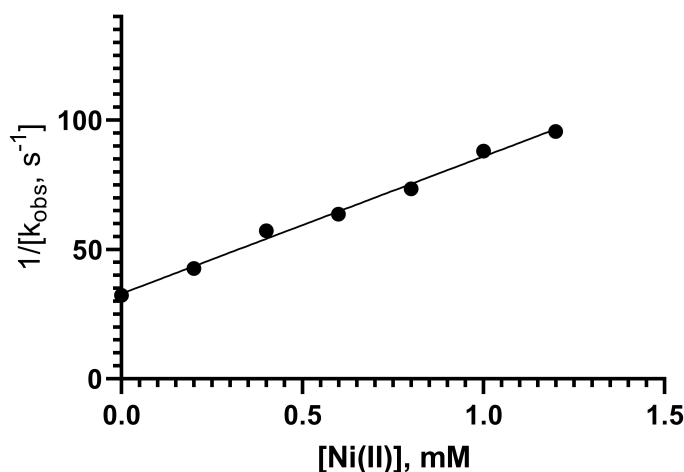


Figure 3.6: The plot of $1/k_{\text{OBS}}$ vs $[\text{Ni(II)}]_0$ at pH 4.5 (acetate buffer); $[\text{Ni(III)}]_0 = 0.05$ mM, $[\text{CSA}]_{\text{TOT}} = 1$ mM, $\mu = 0.1$ M (NaCl), $T = 25$ °C, Straight line fit with slope = $(5.3 \pm 0.2) \times 10^4$ s M^{-1} , Y intercept = $(3.4 \pm 0.1) \times 10$ s.

$$\frac{1}{k_{\text{OBS}}} = k'[\text{Ni(II)}] + k'' \quad k' \text{ and } k'' \text{ are constants} \quad (3.5)$$

Here, $k' = (5.3 \pm 0.2) \times 10^4$ s M^{-1} , $k'' = (3.4 \pm 0.1) \times 10$ s.

3.6.5 Rate dependence on the concentration of CSA

Rate dependence on CSA concentration was determined by carrying out the reaction between $[\text{Ni(III)(tacn)}_2]^{3+}$ and CSA at varying CSA concentrations (1 mM to 25 mM) and determining the rate constant for the reaction at each CSA concentration. CSA solutions of different concentrations were prepared by diluting a standardized CSA solution at 0.02 M in pH 4.6 10 mM acetate buffer. 0.05 mM $[\text{Ni(III)(tacn)}_2]^{3+}$ solutions were used for

these experiments. Kinetics were studied at pH 4.4 – 4.6, $\mu = 0.1$ M (NaCl), and $T = (25 \pm 0.1)$ °C in a dark room. (Table A.8, Figure 3.7)

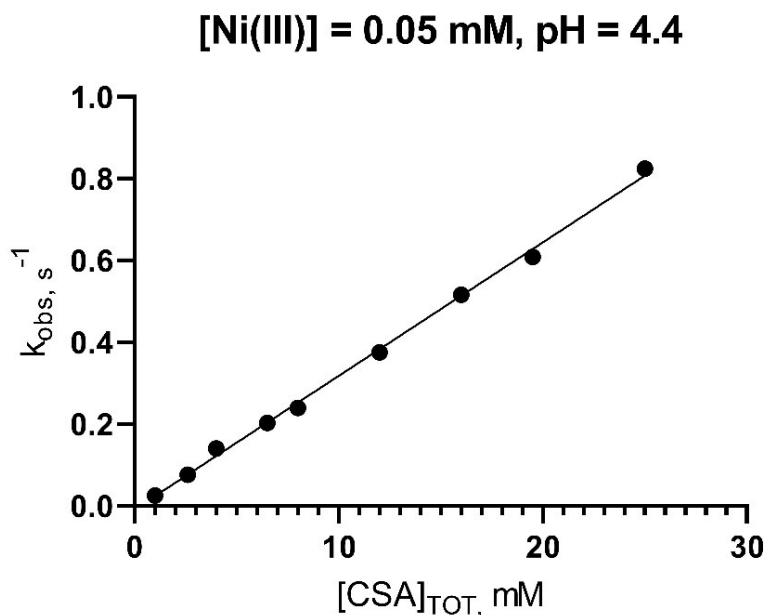


Figure 3.7: k_{OBS} vs $[CSA]_{tot}$ at pH 4.4-4.6 (10 mM acetate buffer) with $[Ni(III)]_0 = 0.05$ mM, and $\mu = 0.1$ M, $T = 25$ °C. Straight line fit with slope = $(3.26 \pm 0.06) \times 10^3 \text{ M}^{-1} \text{ s}^{-1}$ and Y intercept = $(-8.6 \pm 7.4) \times 10^{-3} \text{ s}^{-1}$

3.6.6 pH dependence

pH dependence of the kinetics of the reaction between CSA and $[Ni(III)(tacn)_2]^{3+}$ was examined under anaerobic conditions by carrying out the reaction at different pH media ranging from pH 1 to pH 5.51 with $[CSA]_{TOT} = 1$ mM, $[Ni(III)(tacn)_2]^{3+}_0 = 0.05$ mM, 0.1 M ionic strength (NaCl) and monitoring the decay of absorbance at 312 nm using a stopped-flow instrument equipped with a spectrophotometer. A stock solution of CSA was prepared in pH 4.5 acetate buffer and diluted with different buffers as required to attain the

necessary pH. To prepare reaction media at pH 1-3, dilute HCl was used. For experiments done above pH 3, 10 mM acetate buffers were used to maintain the pH of the reaction mixture. Figure 3.8 shows the dependence of k_{OBS} on the pH of the medium. As discussed in detail in section 2.5.3, CSA has two pK_a 's (1.5 and 2.3) in the pH range the experiments are carried out, and thus CSA exists in 3 different forms.⁷⁷

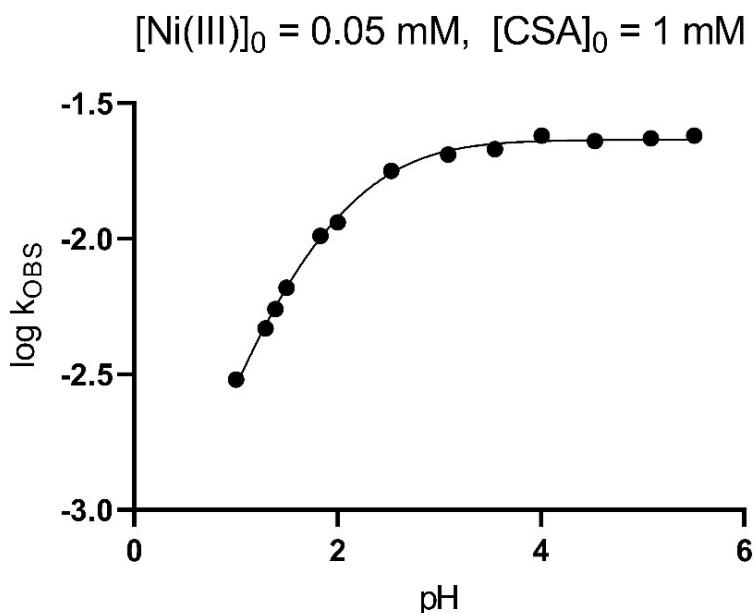


Figure 3.8: The plot of $\log k_{\text{OBS}}$ vs pH with $[\text{CSA}]_{\text{TOT}} = 1 \text{ mM}$, $[\text{Ni(III)}]_0 = 0.05 \text{ mM}$, $\mu = 0.1 \text{ M}$ (NaCl), $T = 25 \text{ }^\circ\text{C}$, data is fit in to equation 2.14. $k_1 = (2.32 \pm 0.07) \times 10 \text{ M}^{-1} \text{ s}^{-1}$, $k_2 = (1.10 \pm 0.05) \times 10 \text{ M}^{-1} \text{ s}^{-1}$.

The reaction was carried out using air saturated solutions and also using solutions with oxygen gas bubbled in. Comparison of the rate constants obtained from the experiments show that presence of oxygen decreases the rate of the reaction.(Table A.10) Also, figure 3.9 shows that the kinetic data obtained using air saturated or O_2 saturated solutions does not fit well into the rate equation 2.14 derived in Chapter 2.

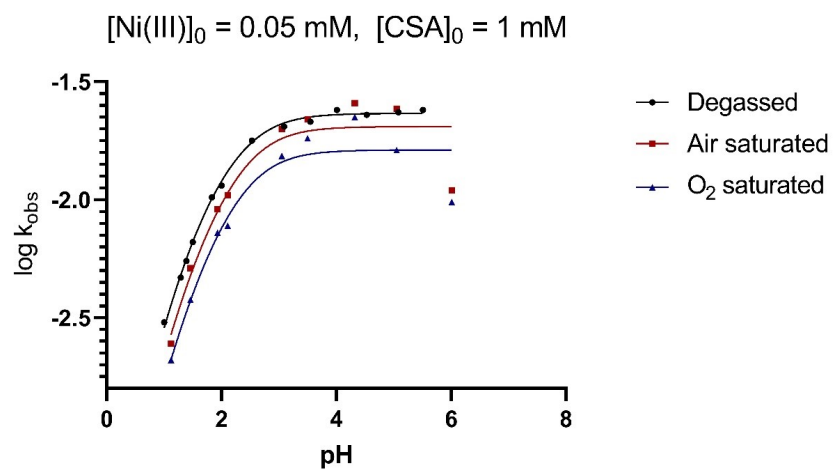


Figure 3.9: The effect of the presence of air and oxygen in the reaction medium with $[\text{CSA}]_{\text{TOT}} = 1 \text{ mM}$, $[\text{Ni(III)}]_0 = 0.05 \text{ mM}$, $\mu = 0.1 \text{ M}$ (NaCl), $T = 25 \text{ }^\circ\text{C}$, data is fit in to equation 2.14.

3.6.7 Product identification and stoichiometry

Product identification

Products containing CSA was identified using $^1\text{H-NMR}$ spectrometry and ESI-MS. For ^1H NMR spectrometry, the test solution consisted of 10 mM $[\text{Ni(III)(tacn)}_2]^{3+}$ and 5 mM CSA with 0.1 mM DSS as internal reference in D_2O . The reactants were allowed to react for 40 min under bubbled argon, protected from light. 3 signals from CSA and 3 signals from cysteic acid can be identified from the spectrum.(Figure 3.10) Peaks at δ 4.3 (d), δ 3.5 (d) and δ 3.3 (dd) arise from cysteic acid. An unidentified multiplet is observed around δ 4.0. When the product mixture is spiked with L-cysteic acid, peaks at δ 4.3 (d), δ 3.5 (d) and δ 3.3 (dd) become more intense. However the intensity of the unknown multiplet remains the same. From the integrals, [Unknown multiplet]: [CysSO₃H] can be calculated as approximately 0.9. Also, $[\text{Ni(III)}]_0$: [CysSO₃H] \approx 2.27.

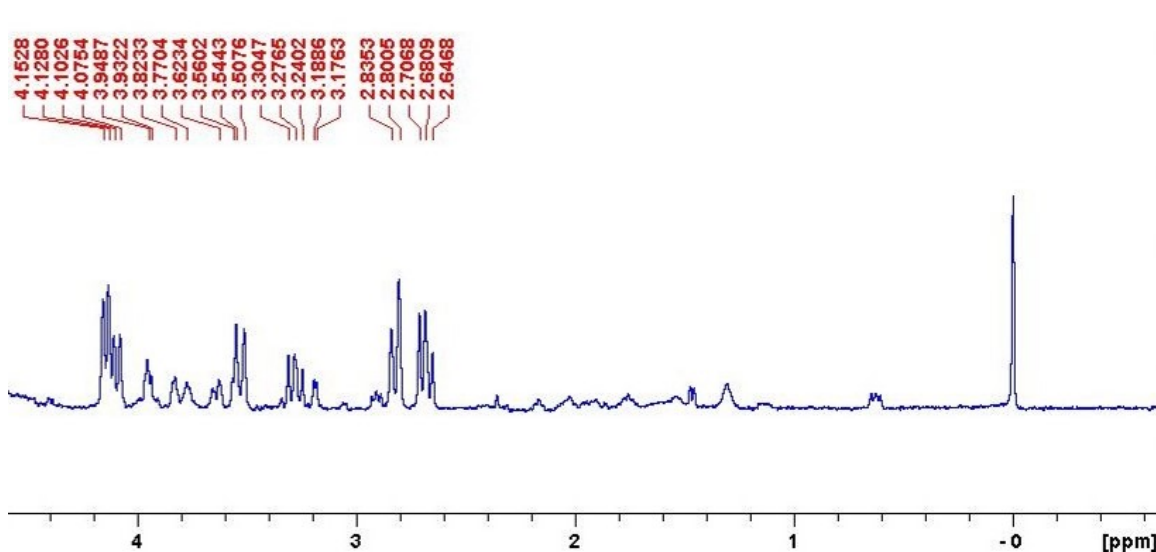


Figure 3.10: $^1\text{H-NMR}$ of the product mixture for the reaction between CSA and $[\text{Ni(III)(tacn)}_2]^{3+}$.

To gain a better understanding about the unknown, the product mixture was passed through a cation-exchange column made of CM-sephadex 25 and taken to dryness by rotary evaporation. The resulting powder was then dissolved in D₂O, and the ¹H-NMR of the solution was collected using DSS as reference. No significant difference was perceived in the resulting spectrum from the spectrum shown above. Then, the product mixture was passed through an anion exchange column QAE-sephadex and the procedure above was repeated to obtain its ¹H-NMR spectrum. It was observed that the unknown species appears in both the cation removed and anion removed spectra. Therefore, it was concluded that the unknown compound is a neutral molecule.

For mass spectrometry, a solution of 10 mM CSA and 5 mM [Ni(III)(tacn)₂]³⁺ at pH 3 was allowed to react for 1 hr and then the cations in the product mixture were removed by passing the mixture through a pre-conditioned cation exchange column prepared with CM-Sephadex C-25. The eluent was concentrated via rotary evaporation and the resultant solution was separated by HILIC (Hydrophilic Interaction Liquid Ion-exchange) chromatography. Then the mass spectrum of the product mixture was obtained. (Figure 3.11) The ESI-MS spectrum of the product mixture resulting from CSA and [Ni(III)(tacn)₂]³⁺ showed peaks for cysteic acid and CSA after being separated using HILIC chromatography.

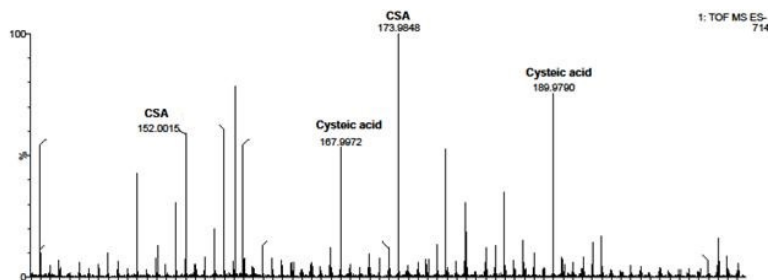


Figure 3.11: ESI-MS ((-ve) mode) of the product mixture after HILIC separation

Ni containing products of the reaction were identified using cyclic voltammetry as well as by spectrophotometric methods. The cyclic voltammogram of a solution with 0.1 mM $[\text{Ni(II)(tacn)}_2]^{2+}$ and 2 mM CSA in $\mu = 0.1 \text{ M (NaCl)}$ was recorded. $E_{1/2} = 680 \text{ mV vs Ag/AgCl(s)}$ ($E_{1/2} = 0.877 \text{ vs normal hydrogen electrode}$)

Next, the cyclic voltammogram of a solution with 0.1 mM $[\text{Ni(III)(tacn)}_2]^{3+}$ and 2 mM CSA in $\mu = 0.1 \text{ M (NaCl)}$ was recorded. $E_{1/2} = 679 \text{ mV vs Ag/AgCl(s)}$ ($E_{1/2} = 0.876 \text{ vs normal hydrogen electrode}$) (Figure 3.12) The reversibility of the oxidation process observed in the cyclic voltammograms in figure 13 show that the electron transfer has taken place at the metal center instead of at the ligand system.

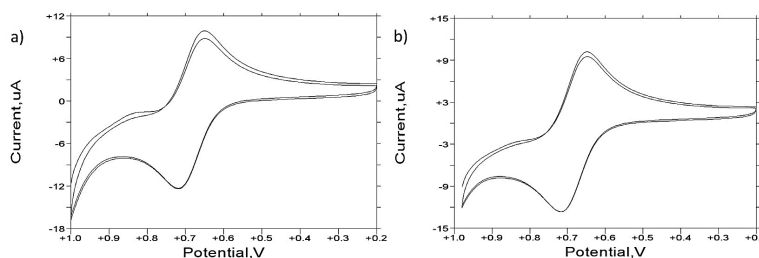


Figure 3.12: a) CV of Ni(II) with CSA; $[\text{CSA}]_{\text{TOT}} = 2 \text{ mM}$, $[\text{Ni(II)}]_0 = 0.1 \text{ mM}$, $\mu = 0.1 \text{ M (NaCl)}$, $T = 25 \text{ }^\circ\text{C}$ b) CV of Ni(III) with CSA; $[\text{CSA}]_{\text{TOT}} = 2 \text{ mM}$, $[\text{Ni(III)}]_0 = 0.1 \text{ mM}$, $\mu = 0.1 \text{ M (NaCl)}$, $T = 25 \text{ }^\circ\text{C}$

To determine yield of Ni(II) from the reaction, the two reactant solutions were prepared as follows. 0.00358 g of bis(1,4,7 triazacyclononane)Ni(III) perchlorate was dissolved in 5 mL of pH 2 HCl, and then diluted 10 fold with pH 2 HCl to prepare a 0.1 mM solution of Ni(III). A 0.32 mM CSA solution was prepared by diluting 10 fold a solution made by dissolving $2.379 \times 10^{-3} \text{ g}$ of CSA monohydrate in 5 mL H_2O . Before the reaction, the UV VIS spectrum of the Ni(III) solution was recorded. Then, 1 ml of CSA solution was added to 8 ml of Ni(III) solution and was allowed to react under argon protected from light for 2 hrs. At the end of the reaction time the UV spectrum of the solution was recorded. Next,

0.1 mg of $\text{Na}_2\text{S}_2\text{O}_8$ was added to the reaction mixture and allowed to react. The final UV spectrum was collected after 0.5 hrs. The observed UV spectra are shown in figure 3.13.

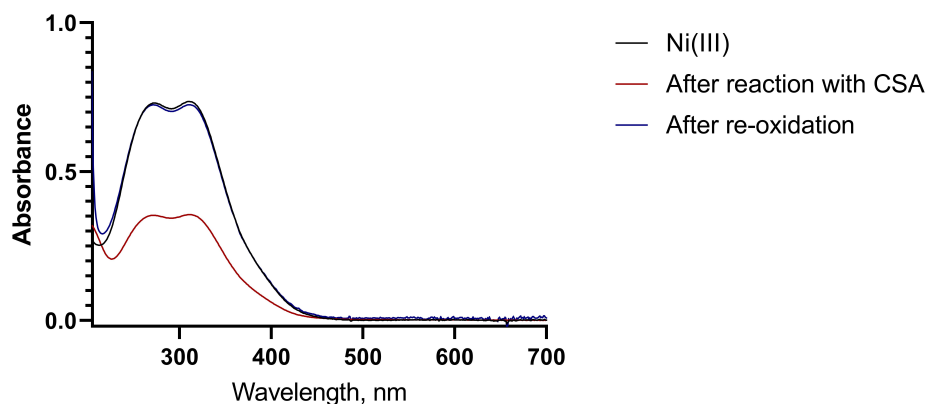


Figure 3.13: UV spectra for determining yield of Ni(II) from the reaction

From the figure above it can be calculated that 97.4% of $[\text{Ni(III)}]_0$ was recovered after $\text{S}_2\text{O}_8^{2-}$ oxidation. This reversibility of the oxidation process further confirms that the electron transfer has taken place at the metal center instead of at the ligand system. Takagi et al have reported difficulties in complete conversion of bis(1,4,7-triazacyclononane)Ni(II) to bis(1,4,7-triazacyclononane)Ni(III).¹⁰¹ Decomposition of Ni(III) during the oxidation process is suggested as the cause for this observation. To avoid possible decomposition of Ni(III) by light, all Ni containing solutions were protected from light in our experiments.

3.6.8 Reaction stoichiometry

A spectrophotometric titration was performed to determine the stoichiometry of the reaction between CSA and $[\text{Ni(III)(tacn)}_2]^{3+}$. For this experiment, first 2 ml of 0.16 mM CSA at pH 3 (dilute HCl) was added into a quartz cuvette and the UV spectrum was recorded. Next, 0.1 ml of 0.8 mM $[\text{Ni(III)(tacn)}_2]^{3+}$ at pH 3 (dilute HCl) was added into

the cuvette and allowed to react for 30 min. While the reaction was taking place, the solution in cuvette was bubbled with argon to remove any O₂ present. When 30 min had passed, the UV spectrum of the reaction mixture was recorded. After that, the procedure was repeated adding 0.1 ml aliquots of [Ni(III)(tacn)₂]³⁺ at 30 min intervals till the total amount of 0.8 mM [Ni(III)(tacn)₂]³⁺ added was 0.7 ml. Figure 3.14 shows the UV spectra of the product mixture after each addition. Absorbance at 312 nm was considered to determine the end point of the titration. Absorbance readings were corrected for dilution.

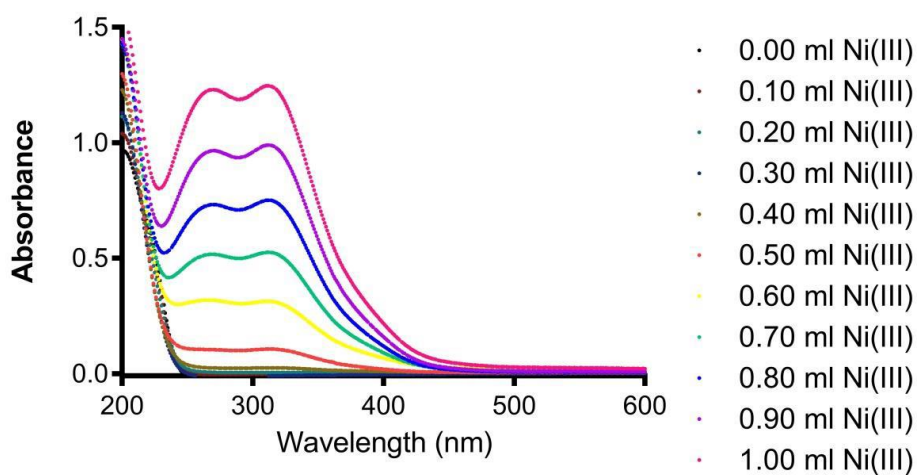


Figure 3.14: Change in UV spectrum after each addition of Ni(III)

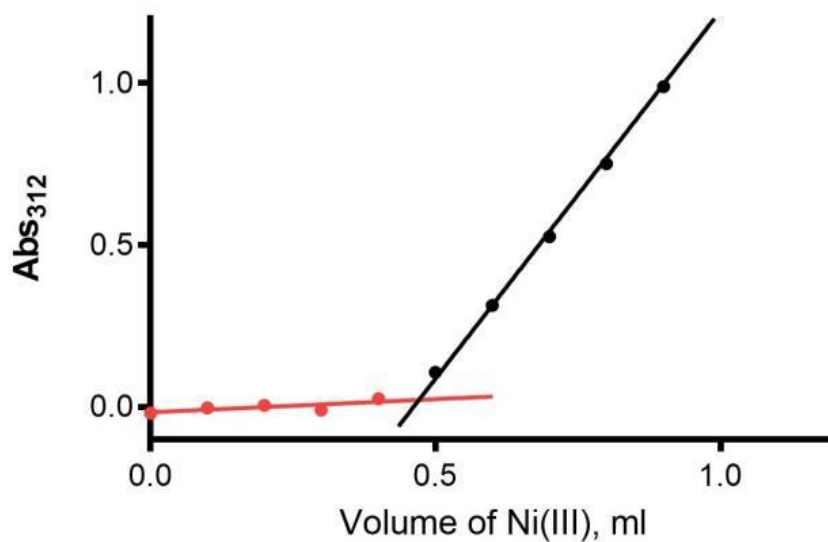


Figure 3.15: Change in absorbance at 312 nm after each addition of Ni(III); $[\text{CSA}]_{\text{TOT}} = 0.16 \text{ mM}$, $[[\text{Ni(III)(tacn)}_2]^{3+}]_0 = 0.8 \text{ mM}$, $\text{pH} = 3.0$, $\mu = 0.1 \text{ M}$ (NaCl). Collection of the ten data points took approximately 4.5 hrs.

Figure 3.15 shows that this titration has a clear end point. From the spectrophotometric titration, the stoichiometric ratio $\Delta[[\text{Ni(III)(tacn)}_2]^{3+}]/\Delta[\text{CSA}]$ can be calculated to be (0.97 ± 0.02) .

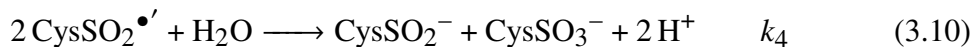
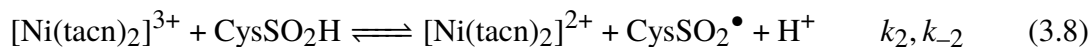
3.7 Discussion

The empirical rate law obtained for the reaction of L-cysteinesulfinic acid with $[\text{Ni(III)(tacn)}_2]^{3+}$ is,

$$\frac{-d[[\text{Ni(tacn)}_2]^{3+}]}{dt} = \frac{K_{a1}[\text{CSA}]_{\text{TOT}}[[\text{Ni(tacn)}_2]^{3+}]}{\left(\frac{1}{(k'_1 K_{a2} + k'_2 [\text{H}^+])} + \frac{k'}{K_{a2}} [[\text{Ni(tacn)}_3]^{2+}]\right)([\text{H}^+]^2 + [\text{H}^+]K_{a1} + K_{a1}K_{a2})} \quad (3.6)$$

Using the data given in the kinetics section of this chapter, values for k'_1 , k'_2 , and k' were determined. $k'_1 = (2.70 \pm 0.08) \times 10 \text{ M}^{-1} \text{ s}^{-1}$, $k'_2 = (9.6 \pm 0.7) \text{ M}^{-1} \text{ s}^{-1}$, and $k' = (4.7 \pm 0.5) \times 10 \text{ s}$.

The following mechanism could be suggested for the reaction of L-cysteinesulfinic acid with $[\text{Ni(III)(tacn)}_2]^{3+}$ in aqueous media.



By applying the steady-state approximation to all radical species, the above mechanism

leads to,

$$\frac{-d[[\text{Ni}(\text{tacn})_2]^{3+}]}{dt} = \frac{K_{a1}[\text{CSA}]_{\text{TOT}}[[\text{Ni}(\text{tacn})_2]^{3+}]}{\left(\frac{1}{(k_1K_{a2}+k_2[\text{H}^+])} + \frac{k_{-1}}{k_3k_1K_{a2}}[[\text{Ni}(\text{tacn})_3]^{2+}]\right)([\text{H}^+]^2 + [\text{H}^+]K_{a1} + K_{a1}K_{a2})} \quad (3.11)$$

Equation 3.11 does not contain the term k_{-2} since $k_{-2} = \frac{k_2k_{-1}}{k_1K_{a2}}$.

Comparing equations 3.6 and 3.11, $k_1 = (2.70 \pm 0.08) \times 10 \text{ M}^{-1} \text{ s}^{-1}$, $k_2 = (9.6 \pm 0.7) \text{ M}^{-1} \text{ s}^{-1}$, and $(k_{-1}/k_3k_1) = (4.7 \pm 0.5) \times 10 \text{ s}$.

According to the $^1\text{H-NMR}$ and ESI-MS results, the major product of this reaction is the sulfonic acid. The two-electron conversion of sulfinic acid to sulfonic acid would require a 2:1 stoichiometry for $[\text{Ni}(\text{III})(\text{tacn})_2]^{3+} : \text{CysSO}_2\text{H}$. However, the stoichiometry observed in the reaction is 1:1. One possibility for this observed stoichiometry is the formation of disulfones. The sulfonyl radicals formed in equation 3.7 may combine to yield cysteine disulfone.



Quantum calculations in gas phase show that reaction 3.12 is energetically favorable with $\Delta G^\circ = -1.44 \times 10^2 \text{ kJ mol}^{-1}$.

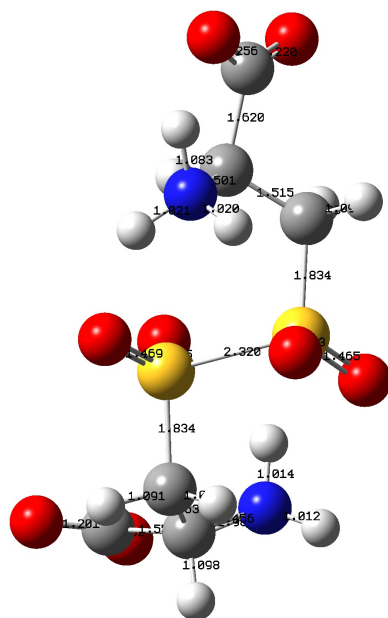
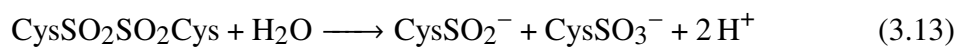


Figure 3.16: Optimized geometry of cysteinedisulfone, The structure is optimized using B3LYP method under 6-311G* basis set.

Disulfones are known to undergo disproportionation to yield sulfinic acids and sulfonic acids.¹⁰² This may be the reason that peaks corresponding to cysteic acids are observed in ¹H-NMR spectra for the reaction products.



3.8 Conclusions

Oxidation of cysteinesulfinate by the one-electron oxidant $[\text{Ni(III)(tacn)}_2]^{3+}$ yields $[\text{Ni(III)(tacn)}_2]^{2+}$ and cysteinesulfonate as major products. The stoichiometric ratio for $[\text{Oxidant}]:[\text{CysSO}_2^-]$ is 1:1 as opposed to the 2:1 stoichiometry observed for $[\text{Os(phen)}_3]^{3+}$ reaction with cysteinesulfinate in Chapter 2. This stoichiometry requires that the formation of sulfonate from the cysteinesulfonyl radical product to be independent of $[\text{Ni(III)(tacn)}_2]^{3+}$. The electron transfer process does not cause any perturbation to the coordination sphere of the oxidant.

Chapter 4

Kinetics and mechanism of methanesulfinate oxidation by bis(1,4,7-triazacyclononane) nickel (III)

4.1 Introduction

The functional groups on the alkanesulfinate dictate its electronic environment. To determine the effect of the functional groups of the alkanesulfinate on the oxidation kinetics, methanesulfinate was chosen because of its structural simplicity. A comparison of the observed kinetics for methanesulfinate oxidation by bis(1,4,7-triazacyclononane)Ni(III), with the kinetics of the reaction of L-cysteinesulfinic acid with the same oxidant discussed in Chapter 2, would clarify the extent to which the electronic environment of the reductant

affects the alkanesulfinate oxidation mechanism. As shown in figure 1.4 in Chapter 1, L-cysteinesulfinate and methanesulfinate have distinctly different electronic environments. Methanesulfinate has been suggested to be a part of the atmospheric sulfur cycle.^{103,104} Dimethyl sulfide (DMS) oxidation in atmosphere has significant environmental significance as it leads to creating sulfate particles which are cloud condensation nuclei.¹⁰⁵ During OH-radical initiated oxidation of DMS in the atmosphere, DMSO is formed.¹⁰⁶ Further oxidation of DMSO yields methanesulfinic acid as a major product. Aerosols in the atmosphere can then easily oxidize methanesulfinic acid into methanesulfonic acid. In the gas-phase, the major oxidation product of methanesulfinic acid is SO₂.¹⁰⁵ To explore the redox reactivity of methanesulfinate (MSA) and to construct mechanisms for the oxidation processes, the one-electron oxidant bis(1,4,7-triazacyclononane)Ni(III) was used in this study.

[Ni(tacn)₂]³⁺ is a substitutionally inert transition metal complex. The preparation and properties of [Ni(tacn)₂]³⁺ and [Ni(tacn)₂]²⁺ are described in detail in Chapter 3.

4.2 Reagents and solutions

Ni(ClO₄)₂·6H₂O (Alfa Aesar), 1,4,7-triazacyclononane trihydrochloride (TCI), glacial acetic acid, Na₂S₂O₈, NaOH pellets (98% Sigma Aldrich), NaCl, 3-(trimethylsilyl)-1-propanesulfonic acid sodium salt (DSS) (Sigma-Aldrich), D₂O 999.8‰ isotopic (Alfa Aesar), sodium methane sulfinate (Alfa Aesar), NaClO₄ (85.0-90.0% Alfa Aesar), KBrO₃, CH₃COONa anhydrous (Sigma), KBr, and methyl orange were used as supplied.

All the aqueous solutions were prepared using purified deionized water from a Barnstead Nanopure Infinity system. Stock solutions of sodium methane sulfinate, glacial acetic acid and CH₃COONa were prepared and stored in the refrigerator. All other solutions were freshly prepared for each experiment. Stock solutions of sodium methanesulfinate were standardized using a bromo-metric titration. For this, an aliquot of strongly acidified

sodium methanesulfinate solution in the presence of KBr and two drops of methyl orange was titrated with standard $\text{KBrO}_3(\text{aq})$ solution. All solutions were purged with Ar. To minimize decomposition all $[\text{Ni}(\text{III})(\text{tacn})_2]^{3+}$ solutions were prepared at pH 3 or lower.

4.3 Experimental methods

To obtain UV-Vis spectra of the reagents and the product mixtures, examine the photosensitivity of reagents, and for spectrophotometric titrations, an HP-8453 diode array spectrophotometer was used. Solutions were kept in quartz cells with path length 1 mm or 1 cm. To obtain kinetic data, a Hi-Tech SF-51 stopped-flow spectrophotometer with a 1 cm path length configuration with a C-400 circulatory water bath to keep solutions at 25 °C was used. In each run, equal volumes of reactants were mixed. The progress of the reaction was monitored by observing decrease of absorbance at 312 nm. Data were stored using an OLIS 4300 data acquisition and analysis software and analyzed with GraphPad PRISM 8. To calculate observed rate constant, the average rate constant of at least five reproducible runs were used. All pH measurements were collected at room temperature and pressure using a Corning 450 pH/ion meter equipped with a Mettler Toledo InLab 421 pH electrode filled with 3.0 M $\text{NaCl}(\text{aq})$; NaCl was used instead of KCl to avoid precipitation of KClO_4 on the surface of the pH probe. The pH electrode was calibrated using standard buffers before each measurement. ^1H NMR spectra of the reagents and product mixtures were obtained from a Bruker AV 400 MHz spectrometer. For ^1H NMR measurements, anaerobic solutions were prepared in D_2O with 3-(trimethylsilyl)-1-propanesulfonic acid sodium salt (DSS) as the internal standard. Electrochemical analyses of the reagents and product mixtures were done on an electrochemical analyzer equipped with BAS C3 cell stand with a stirring and purging system. The working electrode was a Pt electrode and the reference electrode was a Ag/AgCl electrode containing 3.0 M NaCl. ($E^\circ = 0.205$ V vs NHE) The counter electrode was a Pt wire. Electrospray mass spectra were recorded with

a Waters Q-Tof Premier mass spectrometer in the negative mode. The product mixtures were separated using HILIC (Hydrophilic Interaction Liquid Chromatography) technique. HILIC method consists of a hydrophilic stationary phase and a reversed-phase type eluent. Analytes are eluted in descending order of polarity and neutral analytes are retained.

4.4 Computational Methods

Calculations were performed with the Gaussian 16 software package.¹⁰⁷ The molecular structures were optimized in the gas phase at the MP2/aug-cc-pVQZ level with the Frozen Core approximation. For the calculations of the solvated species, PCM (Polarizable Continuum Model) and SMD (Solvation Model based on Density) methods were used. Using the $(\epsilon_0 + G_{\text{corr}})$ values for individual species obtained from the Gaussian output files, reaction Gibbs energies were calculated using the equation given below. Here $(\epsilon_0 + G_{\text{corr}})$ denotes the sum of electronic and thermal free energies.

$$\Delta_r G^{\text{O}}(298\text{K}) = \Sigma(\epsilon_0 + G_{\text{corr}})_{\text{products}} - \Sigma(\epsilon_0 + G_{\text{corr}})_{\text{reactants}} \quad (4.1)$$

4.5 Results

4.5.1 Kinetics of the reaction



For the equation above, the rate law can be written as,

$$\frac{-d[[\text{Ni}(\text{tacn})_2]^{3+}]}{dt} = k[\text{MSA}][[\text{Ni}(\text{tacn})_2]^{3+}] \quad (4.3)$$

When $[\text{MSA}] \gg [\text{Ni}(\text{tacn})_2]^{3+}$, $\Delta[\text{MSA}] \approx 0$

Therefore, the rate law could be re-written as

$$\frac{-d[[\text{Ni}(\text{tacn})_2]^{3+}]}{dt} = k_{\text{OBS}}[[\text{Ni}(\text{tacn})_2]^{3+}] \quad (4.4)$$

Where $k_{\text{OBS}} = k[\text{MSA}]$

When 0.05 mM $[\text{Ni}(\text{III})(\text{tacn})_2]^{3+}$ and 20 mM MSA is mixed to make a solution at pH 4 and $\mu = 0.1$ M (NaCl) from the decay of absorbance at 312 nm first-order kinetics can be observed. (Figure 4.1)

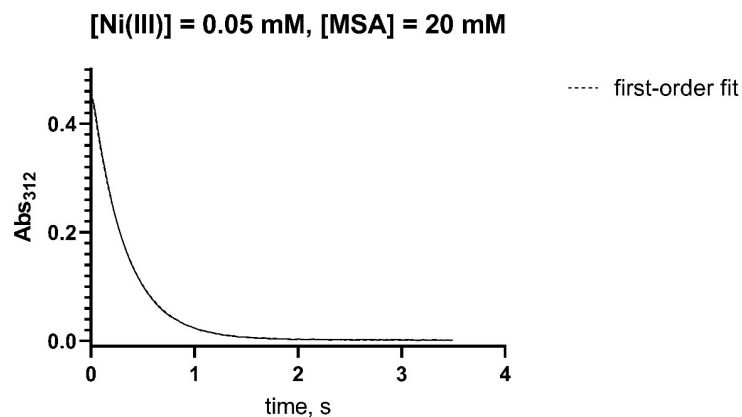


Figure 4.1: Decay of absorbance at 312 nm. $[[\text{Ni}(\text{III})(\text{tacn})_2]^{3+}]_0 = 0.05$ mM, $[\text{MSA}]_{\text{TOT}} = 20$ mM, $[\text{NaCl}] = 0.1$ M, $T = 25$ °C, $\text{pH} = 4$ (10 mM acetate buffer)

4.5.2 Rate dependence on presence of $[\text{Ni}(\text{II})(\text{tacn})_2]^{2+}$

Dependence on the reaction product $[\text{Ni}(\text{II})(\text{tacn})_2]^{2+}$ was studied by adding varying amounts of $[\text{Ni}(\text{II})(\text{tacn})_2]^{2+}$ into the reaction mixture and determining the rate of the reaction using stopped flow methods. 0.05 mM $[\text{Ni}(\text{II})(\text{tacn})_2]^{3+}$ and 1 mM MSA was

reacted at pH 4 (10 mM acetate buffer) and $\mu = 0.1$ M (NaCl) without any $[\text{Ni(II)(tacn)}_2]^{2+}$ present, and with 0.2 mM, 0.4 mM, 0.6 mM, 0.8 mM, 1.0 mM, and 1.2 mM. The rate of the reaction was found to decrease with increasing $[\text{Ni(II)(tacn)}_2]^{2+}$. (Figure 4.2)

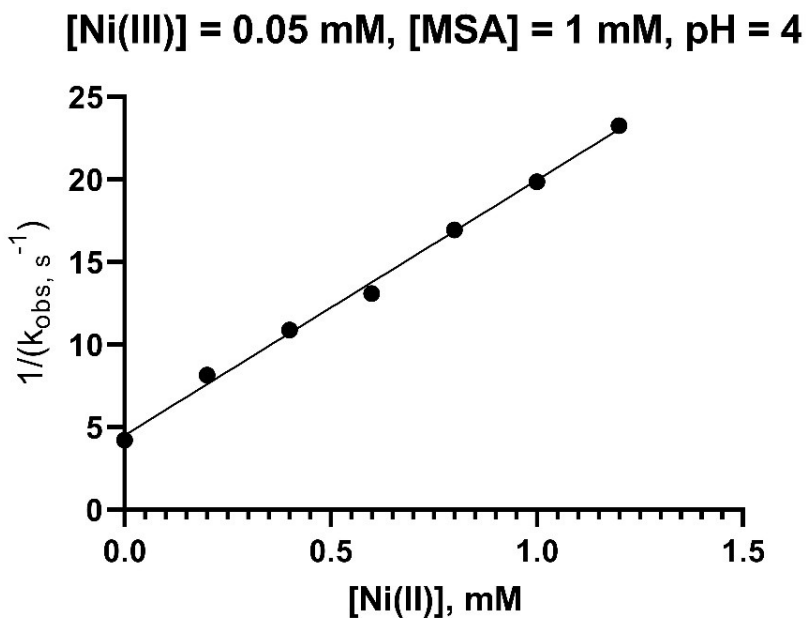


Figure 4.2: The plot of $1/k_{\text{OBS}}$ vs $[\text{Ni(II)}]_0$ at pH 4.5 (acetate buffer); $[\text{Ni(III)}]_0 = 0.05$ mM, $[\text{MSA}]_{\text{TOT}} = 1$ mM, $\mu = 0.1$ M (NaCl), $T = 25$ °C, Straight line fit with slope = $(1.55 \pm 0.04) \times 10^4$ s M⁻¹, Y intercept = (4.5 ± 0.3) s.

$$\frac{1}{k_{\text{OBS}}} = k'[\text{Ni(II)}] + k'' \quad k' \text{ and } k'' \text{ are constants} \quad (4.5)$$

Here, $k' = (1.55 \pm 0.04) \times 10^4$ s M⁻¹, $k'' = (4.5 \pm 0.3)$ s.

4.5.3 Rate dependence on the concentration of MSA

The rate dependence on MSA concentration was determined by carrying out the reaction between $[\text{Ni(III)(tacn)}_2]^{3+}$ and MSA at MSA concentrations 4 mM, 8 mM, 12 mM, 16 mM, and 20 mM and determining the rate constant for the reaction at each MSA concentration. (Table A.12) MSA solutions of different concentrations were prepared by diluting a standardized MSA solution at 0.02 M. 0.05 mM $[\text{Ni(III)(tacn)}_2]^{3+}$ solutions were used for these experiments. Kinetics were studied at pH 4, $\mu = 0.1$ M (NaCl), and $T = (25 \pm 0.1)$ °C in a dark room. (Figure 4.3)

$[\text{Ni(III)}]_0 = 0.05$ mM, pH 3 (HCl), $\mu = 0.1$ M (NaCl)

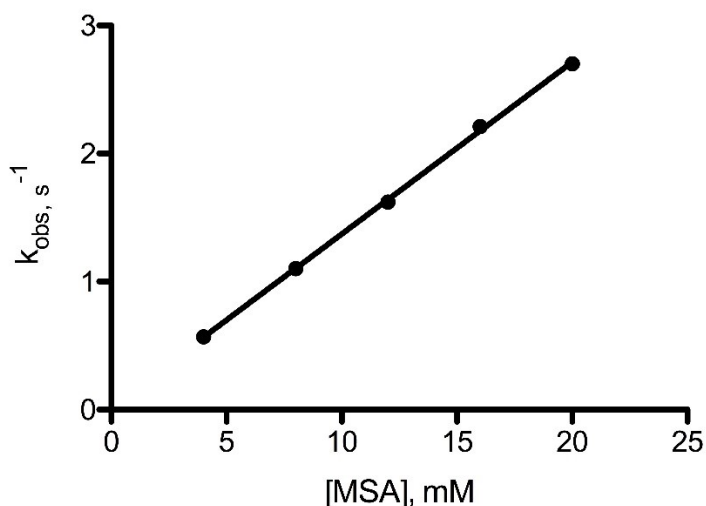
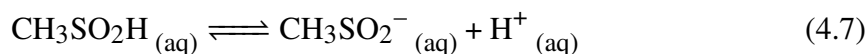
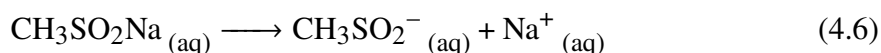


Figure 4.3: k_{OBS} vs $[\text{MSA}]_{\text{tot}}$ at pH 3 (dilute HCl) with $[\text{Ni(III)}]_0 = 0.05$ mM, and $\mu = 0.1$ M, $T = 25$ °C. Straight line fit with slope = $(1.34 \pm 0.02) \times 10^4 \text{ M}^{-1} \text{ s}^{-1}$ and Y intercept = $(2.9 \pm 2.5) \times 10^{-2} \text{ s}^{-1}$

4.5.4 pH dependence

pH dependence of the kinetics of the reaction between MSA and $[\text{Ni(III)(tacn)}_2]^{3+}$ was examined under anaerobic conditions by carrying out the reaction at different pH media ranging from pH 1 to pH 5.5 with $[\text{MSA}]_{\text{TOT}} = 1 \text{ mM}$, $[[\text{Ni(III)(tacn)}_2]^{3+}]_0 = 0.05 \text{ mM}$, 0.1 M ionic strength (NaCl) and monitoring the decay of absorbance at 312 nm using a stopped-flow instrument equipped with a spectrophotometer. A stock solution of MSA was prepared in pH 4.5 acetate buffer and diluted with different buffers as required to attain the necessary pH. To prepare reaction media at pH 1-3, dilute HCl was used. For experiments done above pH 3, 10 mM acetate buffers were used to maintain the pH of the reaction mixture. Figure 4.4 shows the dependence of k_{OBS} on the pH of the medium. MSA has a $\text{p}K_a$ of 2.29.¹⁰⁸ In the pH range the experiments are carried out, MSA can exist in 2 different forms.



$$K_a = \frac{[\text{CH}_3\text{SO}_2^-]_{(\text{aq})}[\text{H}^+]_{(\text{aq})}}{[\text{CH}_3\text{SO}_2\text{H}]_{(\text{aq})}} \quad (4.8)$$

Therefore, the rate constant for the reaction between MSA and $[\text{Ni(III)(tacn)}_2]^{3+}$ is expected to change with pH.

From equation 4.4,

$$\frac{-d[\text{Ni(tacn)}_2]^{3+}}{dt} = k_{\text{OBS}}[[\text{Ni(tacn)}_2]^{3+}] \quad (4.9)$$

Since both $\text{CH}_3\text{SO}_2\text{H}$ and CH_3SO_2^- are present in the media, in the given pH range

we can hypothesize that

$$k_{\text{OBS}} = k_1[\text{CH}_3\text{SO}_2^-]_{(\text{aq})} + k_2[\text{CH}_3\text{SO}_2\text{H}]_{(\text{aq})} \quad (4.10)$$

$$k_{\text{OBS}} = \frac{(k_1 K_a [\text{CH}_3\text{SO}_2\text{H}])}{([\text{H}^+])} + k_2 [\text{CH}_3\text{SO}_2\text{H}] = \frac{((k_1 K_a + k_2 [\text{H}^+]) [\text{CH}_3\text{SO}_2\text{H}])}{([\text{H}^+])} \quad (4.11)$$

$$K_a + [\text{H}^+] = \frac{([\text{CH}_3\text{SO}_2^-][\text{H}^+])}{[\text{CH}_3\text{SO}_2\text{H}]} + [\text{H}^+] = \left(\frac{[\text{CH}_3\text{SO}_2^-]}{[\text{CH}_3\text{SO}_2\text{H}]} + 1 \right) [\text{H}^+] \quad (4.12)$$

$$K_a + [\text{H}^+] = \frac{([\text{CH}_3\text{SO}_2^-] + [\text{CH}_3\text{SO}_2\text{H}])}{[\text{CH}_3\text{SO}_2\text{H}]} [\text{H}^+] = \frac{[\text{MSA}]_{\text{TOT}} [\text{H}^+]}{[\text{CH}_3\text{SO}_2\text{H}]} \quad (4.13)$$

$$[\text{CH}_3\text{SO}_2\text{H}] = \frac{[\text{MSA}]_{\text{TOT}} [\text{H}^+]}{(K_a + [\text{H}^+])} \quad (4.14)$$

$$k_{\text{OBS}} = \frac{(k_1 K_a + k_2 [\text{H}^+])}{[\text{H}^+]} \frac{[\text{MSA}]_{\text{TOT}} [\text{H}^+]}{(K_a + [\text{H}^+])} = \frac{(k_1 K_a + k_2 [\text{H}^+])}{(K_a + [\text{H}^+])} [\text{MSA}]_{\text{TOT}} \quad (4.15)$$

$[\text{Ni(III)}]_0 = 0.05 \text{ mM}$, $[\text{MSA}]_0 = 4 \text{ mM}$, $\mu = 0.1 \text{ M (NaCl)}$

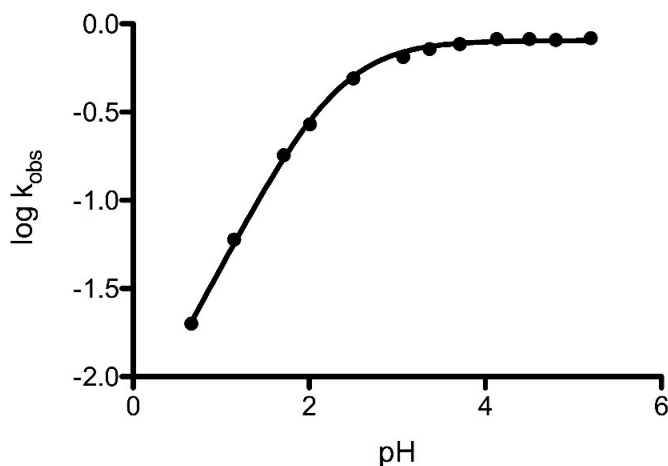


Figure 4.4: The plot of $\log k_{\text{OBS}}$ vs pH with $[\text{MSA}]_{\text{TOT}} = 4 \text{ mM}$, $[\text{Ni(III)}]_0 = 0.05 \text{ mM}$, $\mu = 0.1 \text{ M (NaCl)}$, $T = 25 \text{ }^\circ\text{C}$, data is fit in to equation 4.15. $k_1 = (2.01 \pm 0.02) \times 10^2 \text{ M}^{-1} \text{ s}^{-1}$, $k_2 = (3.90 \pm 2.12) \times 10^{-1} \text{ M}^{-1} \text{ s}^{-1}$.

4.5.5 Product identification and stoichiometry

Product identification

Product identification was done using $^1\text{H-NMR}$ spectrometry and ESI-MS in (-) ve mode. For $^1\text{H-NMR}$ spectrometry, the test solution consisted of 10 mM $[\text{Ni(III)(tacn)}_2]^{3+}$ and 9 mM MSA with 0.1 mM DSS as internal reference in D_2O . Both the MSA and $[\text{Ni(III)(tacn)}_2]^{3+}$ solutions were purged with Ar and protected from light during the reaction time (40 min). In the $^1\text{H-NMR}$ spectrum (Figure 4.5) a singlet arising from methanesulfonic acid can be observed at 2.81 ppm. Using integrals for the peaks in the product $^1\text{H-NMR}$ spectrum, yield of methanesulfonate can be calculated as 93%.

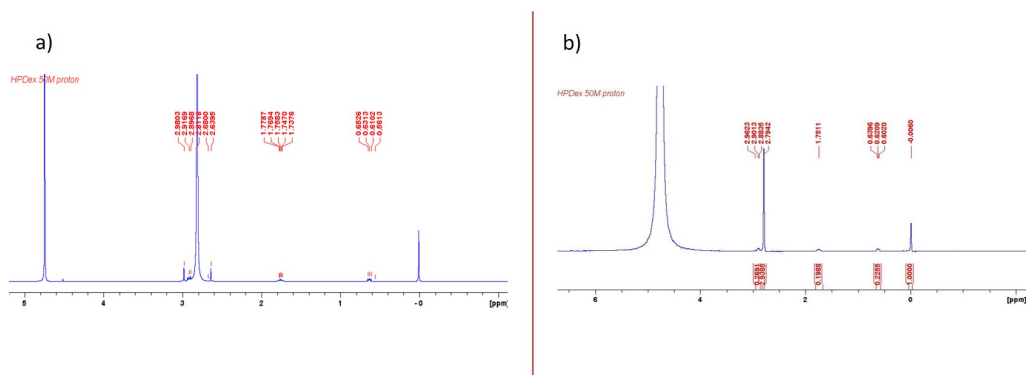


Figure 4.5: $^1\text{H-NMR}$ of a) pure methanesulfonate and b) the product mixture for the reaction between MSA and $[\text{Ni(III)(tacn)}_2]^{3+}$.

For ESI-MS in (-ve) mode, a solution of 10 mM MSA and 5 mM $[\text{Ni(III)(tacn)}_2]^{3+}$ at pH 3 was allowed to react for 1 hr and then the cations in the product mixture were removed by passing the mixture through a pre-conditioned cation exchange column prepared with CM-Sephadex C-25. The eluent was concentrated via rotary evaporation and the resultant solution was separated by HILIC chromatography. Then the mass spectrum of the product mixture was obtained. (Figure 4.6)

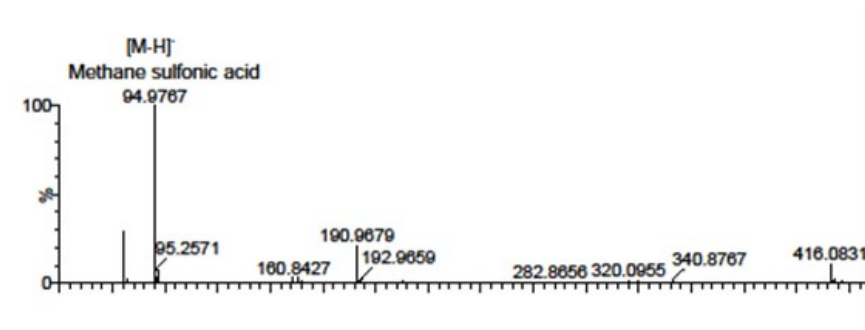


Figure 4.6: ESI-MS spectrum of the product mixture of the reaction between MSA and $[\text{Ni(III)(tacn)}_2]^{3+}$

ESI-MS spectrum shows that the major oxidation product of MSA is methanesulfonic

acid.

Stoichiometry

The stoichiometry of the reaction between MSA and $[\text{Ni}(\text{tacn})_2]^{3+}$ was determined using a spectrophotometric titration. For this experiment, first 2 ml of 0.16 mM MSA at pH 3 was added into a quartz cuvette and the UV spectrum was recorded. Next, 0.1 ml of 0.8 mM $[\text{Ni}(\text{III})(\text{tacn})_2]^{3+}$ at pH 3 was added into the cuvette and allowed to react for 30 min. While the reaction was taking place, the solution in cuvette was bubbled with Ar to remove any O_2 present. When 30 min had passed, the UV spectrum of the reaction mixture was recorded. After that, the procedure was repeated adding 0.1 ml aliquots of $[\text{Ni}(\text{III})(\text{tacn})_2]^{3+}$ at 30 min intervals till the total amount of 0.8 mM $[\text{Ni}(\text{III})(\text{tacn})_2]^{3+}$ added was 0.7 ml. Figure 4.7 shows the UV spectra of the product mixture after each addition. Absorbance at 312 nm was considered to determine the end point of the titration. (Table A.14)

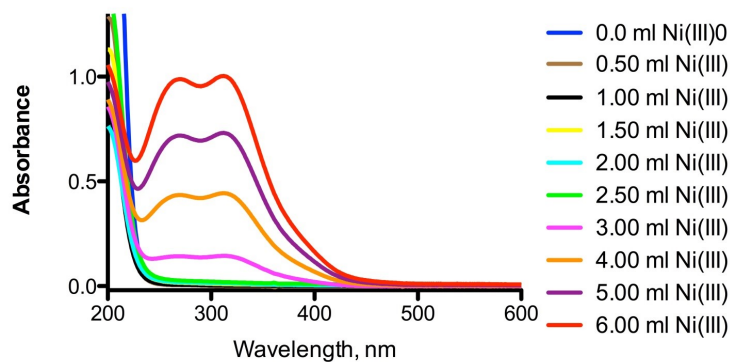


Figure 4.7: Change in UV spectrum after each addition of Ni(III) into MSA solution

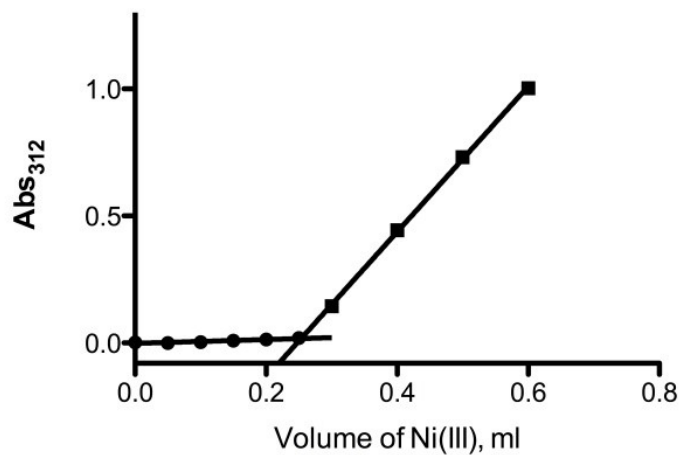


Figure 4.8: Change in absorbance at 312 nm after each addition of Ni(III); $[\text{MSA}]_{\text{TOT}} = 0.16 \text{ mM}$, $[[\text{Ni(III)(tacn)}_2]^{3+}]_0 = 0.8 \text{ mM}$, $\text{pH} = 3.0$, $\mu = 0.1 \text{ M}$ (NaCl)

Figure 4.8 shows that this titration has a clear end point. From the spectrophotometric titration, the stoichiometric ratio $\Delta[\text{Ni(III)(tacn)}_2]^{3+} / \Delta[\text{MSA}]$ can be calculated to be (1.10 ± 0.02)

4.5.6 Yield of Ni(II) from the reaction between MSA and Ni(III)

5.7 mg of bis(1,4,7 triazacyclononane)Ni(III) perchlorate was dissolved in 10 mL of pH 2 HCl, and then diluted 10 fold with pH 2 HCl. A 0.24 mM MSA solution was prepared by diluting 10-fold a solution made by dissolving 2 mg of sodium methanesulfinate in 5 mL H₂O. Before the reaction, the UV VIS spectrum of the Ni(III) solution was recorded. Then, 1 ml of MSA solution was added to 10 ml of Ni(III) solution and was allowed to react under argon protected from light for 2 hrs. At the end of the reaction time the UV spectrum of the solution was recorded. Next, 0.1 mg of Na₂S₂O₈ was added to the reaction mixture and allowed to react. The final UV spectrum was collected after 0.5 hrs. Figure 4.9 shows the observed UV spectra.

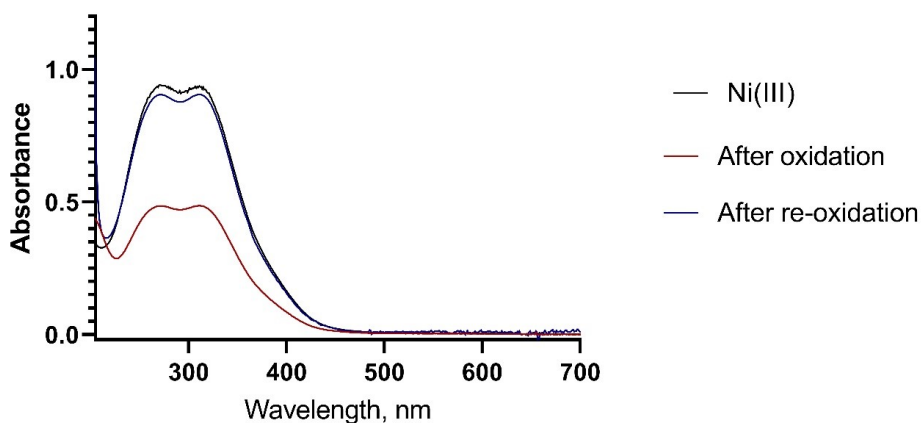


Figure 4.9: UV spectra for determining yield of Ni(II) from the reaction

From the figure above the percentage of Ni(III) recovered after the S₂O₈²⁻ oxidation can be calculated to be 93%. This reversibility of the oxidation process shows that the electron transfer has taken place at the metal center instead of at the ligand system. Takagi et al have reported difficulties in complete conversion of bis(1,4,7-triazacyclononane)Ni(II) to bis(1,4,7 triazacyclononane)Ni(III).¹⁰¹ Decomposition of Ni(III) during the oxidation

process is suggested as the cause for this observation. To avoid possible decomposition of Ni(III) by light, all Ni containing solutions were protected from light in our experiments.

4.6 Structures of CH_3SO_2^- and $\text{CH}_3\text{SO}_2^\bullet$

Structures of CH_3SO_2^- and $\text{CH}_3\text{SO}_2^\bullet$ were optimized in gas phase under B3LYP-aug-cc-pVTZ level using Gaussian 16, in-order to determine the structural changes accompanied with the electron transfer between the two species.

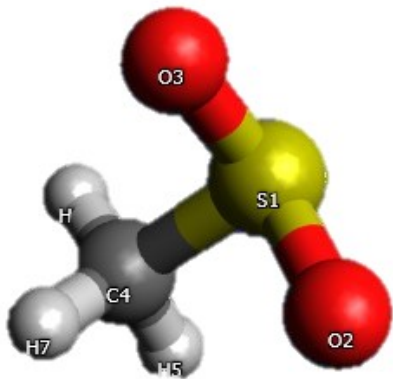


Figure 4.10: Optimized structure of methanesulfinate anion

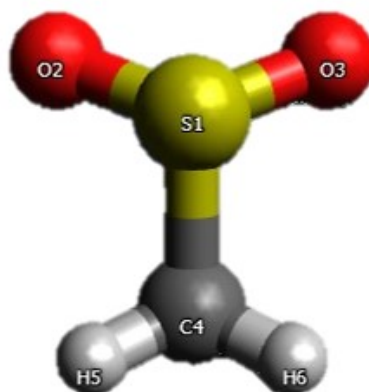


Figure 4.11: Optimized structure of methanesulfonyl radical

Table 4.1: Bond lengths of methanesulfinate anion and methanesulfonyl radical

Bond	Bond length CH_3SO_2^- , Å	Bond length $\text{CH}_3\text{SO}_2^\bullet$, Å
S1-C4	1.877	1.838
S1-O2	1.520	1.474
S1-O3	1.520	1.474
C4-H5	1.091	1.085
C4-H6	1.091	1.085
C4-H7	1.091	1.0858

Table 4.2: Bond angles of methanesulfinate anion and methanesulfonyl radical

Bond angle	Bond angle CH_3SO_2^- , °	Bond angle $\text{CH}_3\text{SO}_2^\bullet$, °
O2-S1-C4	100.786	106.821
O3-S1-C4	100.776	106.821
O2-S1-O3	112.758	120.724
S1-C4-H5	108.980	107.393
S1-C4-H6	108.983	107.393
S1-C4-H7	105.854	106.012
H5-C4-H6	111.099	112.433
H5-C4-H7	110.860	111.607
H6-C4-H7	110.894	111.607

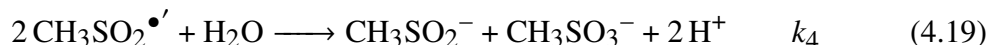
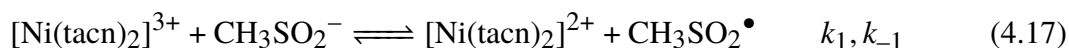
4.7 Discussion

The empirical rate law obtained for the reaction of methanesulfinate with $[\text{Ni(III)(tacn)}_2]^{3+}$ is given below.

$$\frac{-d[[\text{Ni(tacn)}_2]^{3+}]}{dt} = \frac{k'_1 K_a [\text{MSA}]_{\text{TOT}} [[\text{Ni(tacn)}_2]^{3+}]}{(1 + k' [[\text{Ni(tacn)}_2]^{2+}])(K_a + [\text{H}^+])} \quad (4.16)$$

Using the data given in the kinetics section of this chapter, values for k' , and k'_1 were determined. $k'_1 = (1.90 \pm 0.05) \times 10^2 \text{ M}^{-1} \text{ s}^{-1}$, and $k' = (2.7 \pm 0.2) \times 10^3 \text{ M}^{-1}$.

By analogy of a mechanism proposed for the same reaction with $[\text{IrCl}_6]^{2-}$,³³ the following mechanism could be suggested for the reaction of methanesulfinate with $[\text{Ni(III)(tacn)}_2]^{3+}$.



By applying the steady-state approximation to all radical species the above mechanism leads to,

$$\frac{-d[[\text{Ni(tacn)}_2]^{3+}]}{dt} = \frac{k_1 K_a [\text{MSA}]_{\text{TOT}} [[\text{Ni(tacn)}_2]^{3+}]}{(1 + (\frac{k_{-1}}{k_3}) [[\text{Ni(tacn)}_2]^{2+}])(K_a + [\text{H}^+])} \quad (4.20)$$

Comparing equations 4.16 and 4.20, $k_1 = (1.90 \pm 0.05) \times 10^2 \text{ M}^{-1} \text{ s}^{-1}$, and $(\frac{k_{-1}}{k_3}) = (2.7$

$\pm 0.2) \times 10^3 \text{ M}^{-1}$.

One possibility for the rearrangement of the methanesulfonyl radical is the formation of the corresponding thiyl peroxy radical.

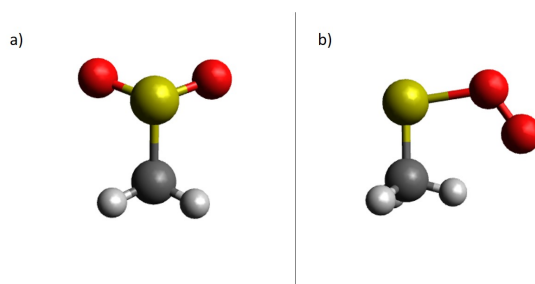


Figure 4.12: Optimized structures of a) methanesulfonyl radical, b) methane thiyl peroxy radical

It has been reported that thiyl peroxy radicals ($\text{RSOO}\cdot$) are capable of undergoing unimolecular rearrangement to form RSO_2 .^{36,90,91} From quantum calculations, the conversion of methanesulfonyl radical to the corresponding thiyl peroxy radical requires 230 kJ/mol.¹⁰⁹

According to the $^1\text{H-NMR}$ and ESI-MS results, the major product of these reactions are sulfonic acids. The two-electron conversion of sulfinic acid to sulfonic acid would require a 2:1 stoichiometry for $[\text{Ni(III)(tacn)}_2]^{3+} : \text{CH}_3\text{SOOH}$. However, the stoichiometry observed in the reaction is 1:1. One possibility for this observed stoichiometry is the formation of disulfones. The sulfonyl radicals formed in equation 4.17 may combine to yield methane disulfone. The rate constant for this reaction has been reported as $1.8 \times 10^9 \text{ M}^{-1} \text{ s}^{-1}$.³⁴

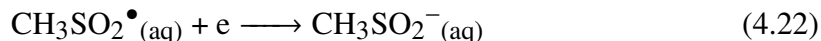


Table 4.3: Free Energies Calculated with Gaussian 16

species	G, a. u.
CH ₃ SO ₂ H(aq) ^a	-588.426880
CH ₃ SO ₂ •(aq) ^a	-587.802023
CH ₃ SO ₂ H(aq) ^b	-588.431720
CH ₃ SO ₂ •(aq) ^b	-587.804352
H ₂ (g)	-1.167917
CH ₄ (g)	-40.399304
SO ₂ (g)	-548.048728

a = PCM method, b = SMD method.

To determine E^O of the electron transfer half-reaction 4.22, quantum calculations were carried out.



First, the values for the sum of electronic and thermal free energies of the species CH₃SO₂•(aq), H₂(g), CH₄(g), SO₂(g), and CH₃SO₂H(aq) were calculated. From these energies, $\Delta_r G^\circ$ for the reaction CH₃SO₂H(aq) \longrightarrow CH₃SO₂•(aq) + $\frac{1}{2}$ H₂(g) was determined. From this reaction Gibbs free energy, $E^O((\text{CH}_3\text{SO}_2\bullet_{(\text{aq})} + \text{H}_{(\text{aq})}^+)/(\text{CH}_3\text{SO}_2\text{H}_{(\text{aq})}))$ was calculated to be -1.36 V (SMD method). Next, by calculating the Gibbs free energy of the reaction CH₃SO₂H(aq) \longrightarrow CH₄(g) + SO₂(g), and combining this result with NBS data¹¹⁰ for $\Delta_f G^\circ$ of CH₄(g) and SO₂(g), a value of -301.65 kJ/mol was calculated for $\Delta_f G^\circ \text{CH}_3\text{SO}_2\text{H}_{(\text{aq})}$ with SMD method. Using this result along with $E^O((\text{CH}_3\text{SO}_2\bullet_{(\text{aq})} + \text{H}_{(\text{aq})}^+)/(\text{CH}_3\text{SO}_2\text{H}_{(\text{aq})}))$ calculated above, a value of -170.521 kJ/mol was calculated for

$\Delta_f G^\circ \text{CH}_3\text{SO}_2^\bullet(\text{aq})$. Then, using the value of pK_a for $\text{CH}_3\text{SO}_2\text{H}$ along with the results calculated above,

$E^\circ(\text{CH}_3\text{SO}_2^\bullet(\text{aq})/\text{CH}_3\text{SO}_2^-(\text{aq}))$ was determined to be +1.224 V. With PCM method, the same calculation leads to $E^\circ(\text{CH}_3\text{SO}_2^\bullet(\text{aq})/\text{CH}_3\text{SO}_2^-(\text{aq})) = 0.978\text{V}$.

Table 4.4: Free energies of formation for selected species

Species	$\Delta_f G^\circ$, kJ/mol
$\text{CH}_3\text{SO}_2\text{H}(\text{aq})^a$	-295.395
$\text{CH}_3\text{SO}_2^\bullet(\text{aq})^a$	-188.016
$\text{CH}_3\text{SO}_2\text{H}(\text{aq})^b$	-301.654
$\text{CH}_3\text{SO}_2^\bullet(\text{aq})^b$	-170.521
$\text{CH}_3\text{SO}_2\text{H}(\text{g})$	-254.650
$\text{CH}_3\text{SO}_2^\bullet(\text{g})$	-134.737

a = PCM method, b = SMD method.

From the reported standard reduction potential for Ni(III)/Ni(II) redox couple and the standard reduction potential calculated for $\text{CH}_3\text{SO}_2^\bullet/\text{CH}_3\text{SO}_2^-$ redox couple using SMD results, $K_1 = 1.58 \times 10^{-5}$. Therefore, $k_{-1} = 1.20 \times 10^5 \text{ M}^{-1} \text{ s}^{-1}$, and $k_3 = 44.3 \text{ s}^{-1}$. Using results obtained from PCM method, $K_1 = 0.228$. Therefore, $k_{-1} = 8.81 \times 10^2 \text{ M}^{-1} \text{ s}^{-1}$, and $k_3 = 0.32 \text{ s}^{-1}$.

Application of Marcus cross correlation (eq: 5.23) yields an estimate for the self-exchange rate constant for the $\text{CH}_3\text{SO}_2^\bullet/\text{CH}_3\text{SO}_2^-$ redox couple.

$$k_{12} = (k_{11}k_{22}K_{12}f_{12})^{1/2}W_{12} \quad (4.23)$$

where k_{12} is the second-order electron transfer rate constant, k_{11} and k_{22} are the self-exchange rate constants for the Ni(III)/Ni(II) and $\text{CH}_3\text{SO}_2^\bullet/\text{CH}_3\text{SO}_2^-$ redox couples. W_{12} term is included to account for the substantial electrostatic effects. Chapter 1 describes how W_{12} is determined.

Using values $k_{11} = 6 \times 10^3 \text{ M}^{-1} \text{ s}^{-1}$, $K_{12} = 1.58 \times 10^{-5}$ (SMD solvation model), and the radii of $[\text{Ni}(\text{tacn})_2]^{3+}$ and CH_3SO_2^- as 3.8 and 2.42 Å respectively, k_{22} was determined to be $0.185 \text{ M}^{-1} \text{ s}^{-1}$.⁹⁵ The significant structural and solvent reorganization involved provides a rationale for a low k_{22} value. The value of k_{22} for $\text{SO}_3^-/\text{SO}_3^{2-}$ redox couple is comparable to the k_{22} for $\text{CH}_3\text{SO}_2^\bullet/\text{CH}_3\text{SO}_2^-$.¹¹¹ PCM results yield a value of $3.01 \times 10^{-6} \text{ M}^{-1} \text{ s}^{-1}$ for k_{22} .

4.8 Conclusions

Oxidation of methanesulfinate by the one-electron oxidant $[\text{Ni}(\text{III})(\text{tacn})_2]^{3+}$ in aqueous media yields methanesulfonate and $[\text{Ni}(\text{III})(\text{tacn})_2]^{2+}$ as major products. Similar to the reaction of $[\text{Ni}(\text{III})(\text{tacn})_2]^{3+}$ with CSA described in Chapter 3, mild kinetic inhibition by $[\text{Ni}(\text{III})(\text{tacn})_2]^{2+}$ is observed. However excellent pseudo-first-order fits can be obtained without addition of spin-traps.

Chapter 5

Kinetics and mechanism of methanesulfinate oxidation by tris(1,10-phenanthroline) osmium(III)

5.1 Introduction

Chapter 2 outlined possible β hydrogen elimination reactions taking place during the oxidation of L-cysteinesulfinic acid by tris(1,10-phenanthroline)osmium(III). To determine how the oxidation mechanisms changes when the sulfinate does not possess any β hydrogen atoms, methanesulfinate oxidation was studied with the same oxidant.

One electron oxidation of MSA has been studied with several oxidants. For the reaction of $\text{OH}\cdot$ with MSA, a rate constant $1.2 \times 10^{10} \text{ M}^{-1} \text{ s}^{-1}$ is reported at room temperature.²⁹ For

the same reaction, a rate constant of $6 \times 10^9 \text{ M}^{-1} \text{ s}^{-1}$ have been observed for the formation of methanesulfonyl radical.³⁸ The formed radical then disappears via a second order self-reaction with a rate of $1 \times 10^9 \text{ M}^{-1} \text{ s}^{-1}$. Also, methanesulfonyl radical disappearance has been found to be independent of ionic strength up to 1 M. Methanesulfonyl radical has an absorption feature at 325 nm with $(900 \pm 100) \text{ M}^{-1} \text{ cm}^{-1}$.

In another study on $\text{OH}\cdot$ and $\text{N}_3\cdot$ reaction with MSA in aqueous phase, reactions were found to proceed by forming short lived adducts with MSA which dissociate to give methanesulfonyl radical which is strongly oxidizing.³⁴

5.2 Reagents, solutions, and methods

5.2.1 Reagents

Sodium methanesulfinatate (95% Alfa Aesar), sodium methanesulfonate (Alfa Aesar), glacial acetic acid (Fischer Scientific), NaOH pellets (98% Sigma Aldrich), NaCl (Fischer Scientific), NaBr (J.T. Baker), 3-(trimethylsilyl)-1-propanesulfonic acid sodium salt (DSS) (Sigma-Aldrich), D_2O 99.8% isotopic (Alfa Aesar), Br_2 (Alfa Aesar), CH_3COONa anhydrous (Sigma), NaCF_3SO_3 (Alfa Aesar), CH_3CN (Fisher), 1,10-phenanthroline monohydrate (Sigma-Aldrich), diethyl ether (J.T. Baker), ethyl acetate (Fischer Scientific), ethylene glycol (J.T. Baker), acetonitrile (Fischer Scientific), acetone (VWR), isopropyl alcohol (VWR) were used as supplied.

All the aqueous solutions were prepared using purified deionized water from a Barnstead Nanopure Infinity system. Stock solutions of sodium methanesulfinatate, glacial acetic acid and CH_3COONa were prepared and stored in the refrigerator. All other solutions were freshly prepared for each experiment. All solutions were purged with Ar.

$[\text{Os}(\text{phen})_3](\text{CF}_3\text{SO}_3)_2$ was synthesized starting from $(\text{NH}_4)_2\text{OsCl}_6$ available from a prior study⁷⁴ using a modified procedure from literature.⁷⁴⁻⁷⁶ 0.177 g of $(\text{NH}_4)_2\text{OsCl}_6$

and 0.232 g of 1,10-phenanthroline monohydrate were dissolved in 30 ml of ethylene glycol in a round bottom flask. The mixture was refluxed at 200 °C for 12 hrs. The resulting dark solution was extracted first using 4:1 diethyl ether:acetone mixture and then after dilution of the resulting solution by adding H₂O (approximately 10% by volume), the resulting solution was extracted with ethyl acetate to remove excess ethylene glycol. The H₂O was evaporated off using the rotary evaporator, and [Os(phen)₃](CF₃SO₃)₃ was precipitated by addition of saturated CF₃SO₃Na. The crude product was recrystallized by dissolving in a minimum of H₂O at 60 °C and precipitating by drop-wise addition of a saturated aqueous solution of CF₃SO₃Na.

5.2.2 Preparation of solutions

[Os(phen)₃]³⁺ is unstable in aqueous solutions for prolonged periods of time. Therefore [Os(phen)₃]³⁺ solutions were generated just prior to experiments by adding a deficiency of 5 mM Br₂/CH₃CN drop-wise to solutions of [Os(phen)₃]²⁺. MSA stock solutions were standardized by titrating with KBrO₃ in the presence of bromide in acidic medium; the end point was determined using methyl red indicator.

Both the [Os(phen)₃]³⁺ and MSA solutions were purged with argon prior to experiments. In solutions with pH higher than 3, Os(III) reaction with water to give Os(II) is significant. Therefore, the Os(II)/Os(III) solutions were all kept at or below pH 3. All osmium-containing solutions were protected from light.

5.2.3 Analytical instrumentation and methods

All UV-Vis data were obtained with an HP-8453 diode array spectrophotometer. The progress of kinetic experiments was monitored by observing the increase of absorbance at 610 nm using a Hi-Tech SF-51 stopped-flow spectrophotometer equipped with OLIS 4300 data acquisition and analysis software along with a 590 nm optical cut-off filter. To

analyze kinetic data GraphPad Prism version 8.3.1 was used. A Corning 450 pH/ion meter with a Mettler Toledo Inlab 421 pH electrode was used to obtain pH measurements. Electrochemical measurements were collected using a BAS 100B/W Electrochemical Analyzer, using a Ag/AgCl reference electrode, a glassy carbon working electrode, and a platinum wire auxiliary electrode; measurements were obtained at room temperature under N₂.

5.2.4 Computational Studies

Calculations were performed with the Gaussian 16 software package.¹⁰⁷ Molecular structures were optimized using MP2/aug-cc-pVQZ level with the Frozen Core approximation. For the calculations of the solvated species, PCM method was used.

5.3 Results

Characterization of [Os(phen)₃](CF₃SO₃)₂ is described in detail in Chapter 2.

5.3.1 Kinetics of the reaction



For the equation above, the rate law can be written as,

$$\frac{-d[[\text{Os}(\text{phen})_3]^{3+}]}{dt} = k[\text{MSA}][[\text{Os}(\text{phen})_3]^{3+}] \quad (5.2)$$

When [MSA] >>> [[Os(phen)₃]³⁺], Δ[MSA] ≈ 0

Therefore, the rate law could be re-written as

$$\frac{-d[[\text{Os}(\text{phen})_3]^{3+}]}{dt} = k_{\text{OBS}}[[\text{Os}(\text{phen})_3]^{3+}] \quad (5.3)$$

Where $k_{\text{OBS}} = k[\text{MSA}]$

When 0.01 mM $[\text{Os}(\text{phen})_3]^{3+}$ and 12 mM MSA is mixed to make a solution at pH 4.5 and $\mu = 0.1$ M (NaCl). The first-order fit obtained from the kinetic trace at 610 nm is not very good. (Figure 5.1)

$[\text{Os}(\text{III})]_0 = 0.01$ mM, $[\text{Os}(\text{II})]_0 = 0.1$ mM, $[\text{MSA}]_0 = 12$ mM

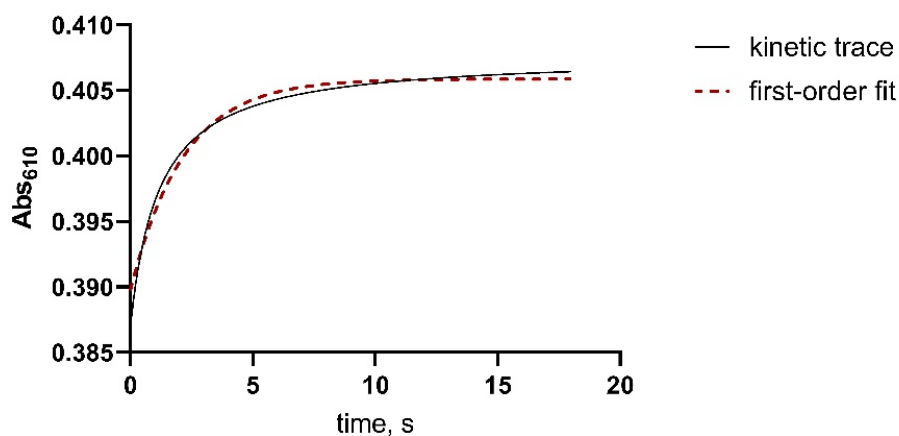


Figure 5.1: Kinetic trace of the oxidation of MSA by $[\text{Os}(\text{phen})_3]^{3+}$. $[[\text{Os}(\text{phen})_3]^{3+}]_0 = 0.01$ mM, $[[\text{Os}(\text{phen})_3]^{2+}]_0 = 0.1$ mM, $[\text{MSA}]_{\text{TOT}} = 12$ mM, $\mu = 0.1$ M (NaCl), $T = 25$ °C, pH = 4.5 (acetate buffer), monitored at 610 nm, $k_{\text{OBS}} = 0.51$ s⁻¹

5.3.2 Second-order fits of kinetic experiments

It was found that the pseudo-second-order fits (equation 5.10) are significantly better than pseudo-first-order fits for the kinetics between MSA and $[\text{Os}(\text{phen})_3]^{3+}$ in the presence of excess $[\text{Os}(\text{phen})_3]^{2+}$. An example is shown below in figure 5.2. Here, $\Delta\varepsilon_{610} = (\varepsilon_{610, \text{Os(II)}} - \varepsilon_{610, \text{Os(III)}}) = 3.46 \times 10^3 \text{ M}^{-1} \text{ cm}^{-1}$

$$\frac{-d[\text{Os(III)}]}{dt} = k[\text{Os(III)}]^2 \quad (5.4)$$

$$\frac{1}{[\text{Os(III)}]_t} = \frac{1}{[\text{Os(III)}]_0} + kt \quad (5.5)$$

$$\frac{\Delta\varepsilon_{610}}{(A_{610,\text{inf}} - A_{610,t})} = \frac{\Delta\varepsilon_{610}}{(A_{610,\text{inf}} - A_{610,0})} + kt \quad (5.6)$$

$$\frac{1}{(A_{610,\text{inf}} - A_{610,t})} = \frac{1}{(A_{610,\text{inf}} - A_{610,0})} + k't \quad \text{where } k' = \frac{k}{\Delta\varepsilon_{610}} \quad (5.7)$$

$$A_{610,\text{inf}} - A_{610,t} = \frac{(A_{610,\text{inf}} - A_{610,0})}{(1 + (A_{610,\text{inf}} - A_{610,t})k't)} \quad (5.8)$$

$$A_{610,\text{inf}} - A_{610,t} = \frac{(A_{610,\text{inf}} - A_{610,0})}{(1 + \frac{(A_{610,\text{inf}} - A_{610,t})kt}{\Delta\varepsilon_{610}})} \quad (5.9)$$

$$Y = A_{610,t} = A_{610,\text{inf}} - \frac{(A_{610,\text{inf}} - A_{610,0})}{(1 + \frac{(A_{610,\text{inf}} - A_{610,t})kX}{\Delta\varepsilon_{610}})} \quad (5.10)$$

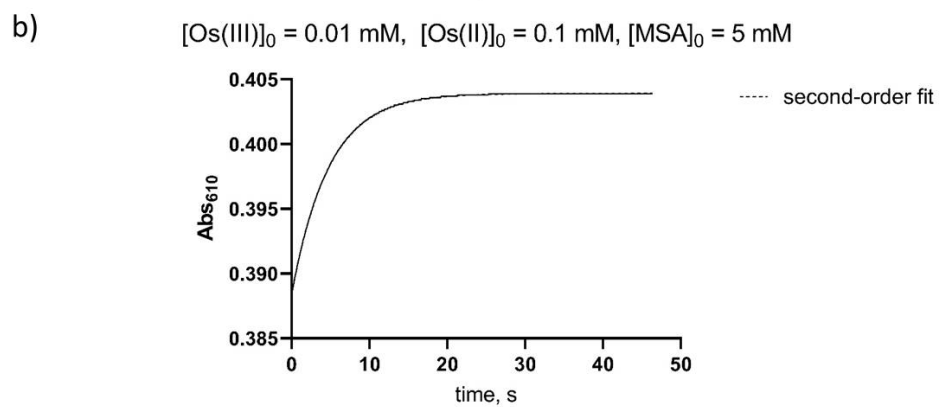
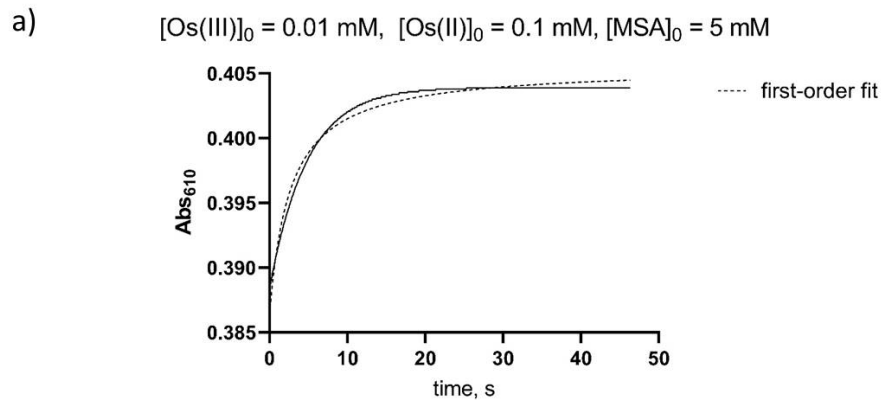


Figure 5.2: Kinetic trace between MSA and Os(III) in the presence of excess Os(II) at pH 3.71 (10 mM acetate buffer) with a) first-order fit, b) second-order fit.

Rate dependence on $[\text{Os}(\text{phen})_3]^{2+}$

Rate dependence on the reaction product $[\text{Os}(\text{phen})_3]^{2+}$ was monitored by adding varying amounts of $[\text{Os}(\text{phen})_3]^{2+}$ into the reaction mixture and determining the rate of the reaction using stopped-flow methods. The reaction mixture contained 0.01 mM $[\text{Os}(\text{phen})_3]^{3+}$ and 20 mM MSA at pH 5 and $\mu = 0.1$ M (NaCl) with 0.09 mM, 0.135 mM, 0.18 mM, 0.225 mM, and 0.27 mM concentrations of $[\text{Os}(\text{phen})_3]^{2+}$ present. The rate of the reaction was found to decrease with increasing $[\text{Os}(\text{phen})_3]^{2+}$ concentration. (Table A.15, Figure 5.3)

$$\frac{1}{k_{\text{OBS}}} = k'[\text{Os}(\text{II})] \quad \text{where } k' \text{ is a constant} \quad (5.11)$$

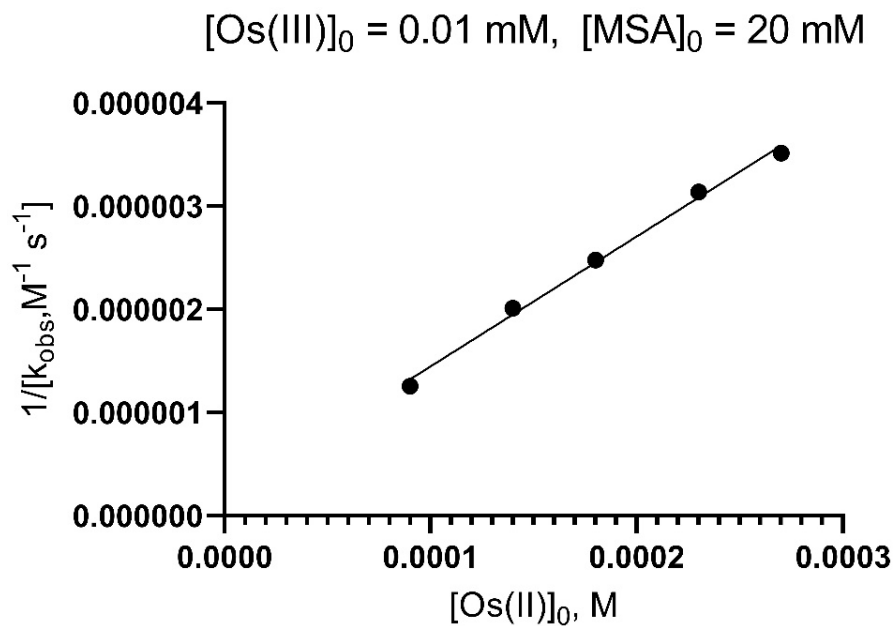


Figure 5.3: The plot of $1/k_{\text{OBS}}$ vs $[[\text{Os(phen)}_3]^{2+}]$ at pH 4.5 (acetate buffer), $\mu = 0.1 \text{ M}$ (NaCl), $T = 25 \text{ }^\circ\text{C}$. Straight line fit with slope = $(1.26 \pm 0.05) \times 10^{-2} \text{ s}$, Y intercept = $(1.9 \pm 1.0) \times 10^{-7} \text{ M s}$.

When data points in Figure 5.3 are fit into equation 5.11, $k' = (1.26 \pm 0.05) \times 10^{-2} \text{ s}$.

Rate dependence on MSA concentration

Rate dependence on MSA concentration was determined by reacting 0.01 mM $[\text{Os}(\text{phen})_3]^{3+}$ and 0.1 mM $[\text{Os}(\text{phen})_3]^{2+}$ at pH 4.4-4.5 with solutions of varying MSA concentrations.

(Table A.16, Figure 5.4)

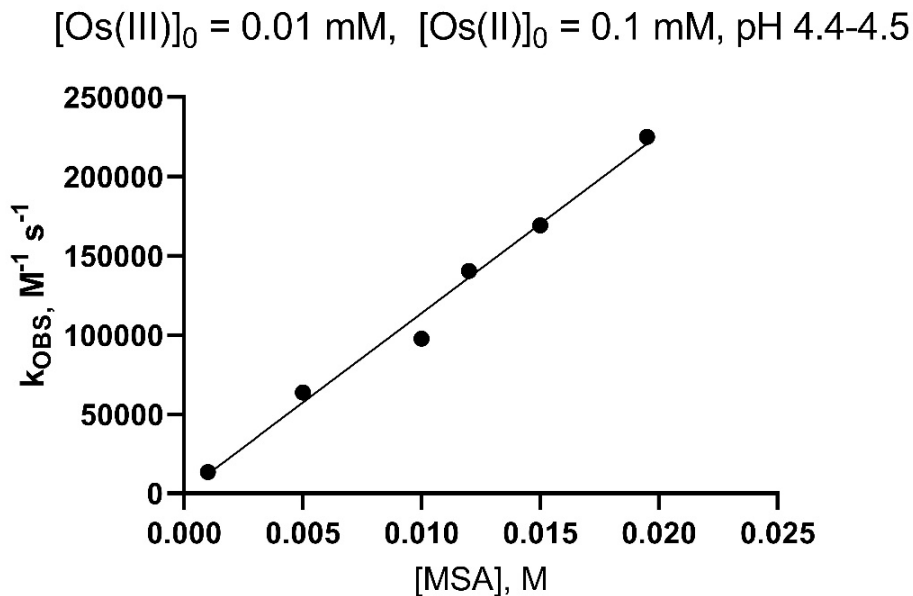


Figure 5.4: The plot of k_{OBS} vs $[\text{MSA}]_{\text{TOT}}$ at pH 4.4-4.6 (acetate buffer) with $[[\text{Os}(\text{phen})_3]^{3+}]_0 = 0.01 \text{ mM}$ and $[[\text{Os}(\text{phen})_3]^{2+}]_0 = 0.1 \text{ mM}$, $\mu = 0.1 \text{ M}$, $T = 25 \text{ }^\circ\text{C}$. Straight line fit with slope = $(1.13 \pm 0.06) \times 10^7 \text{ M}^{-2} \text{ s}^{-1}$ and Y intercept = $(7.9 \pm 7.4) \times 10^2 \text{ M}^{-1} \text{ s}^{-1}$

Second-order rate constants for pH dependence

pH dependence of the kinetics of the reaction between MSA and $[\text{Os}(\text{phen})_3]^{3+}$ was examined under anaerobic conditions by carrying out the reaction at different pH media ranging from pH 1 to pH 5.5 with $[\text{MSA}]_{\text{TOT}} = 4 \text{ mM}$, $[[\text{Os}(\text{phen})_3]^{3+}]_0 = 0.01 \text{ mM}$, $[[\text{Os}(\text{phen})_3]^{2+}]_0 = 0.1 \text{ mM}$, 0.1 M ionic strength (NaCl) and monitoring the increase of absorbance at 610 nm using a stopped flow instrument equipped with a spectrophotometer. A stock solution of MSA was prepared in pH 3.6 acetate buffer and diluted with different buffers as required to attain the necessary pH. To prepare reaction media at pH 1-1.78, dilute HCl was used. Reaction media with pH 1.8-3.36 were prepared using 10 mM chloroacetate buffer. For experiments done above pH 3.6, 10 mM acetate buffers were used to maintain the pH of the reaction mixture. Figure 5.5 shows the dependence of second-order k_{OBS} on the pH of the medium.

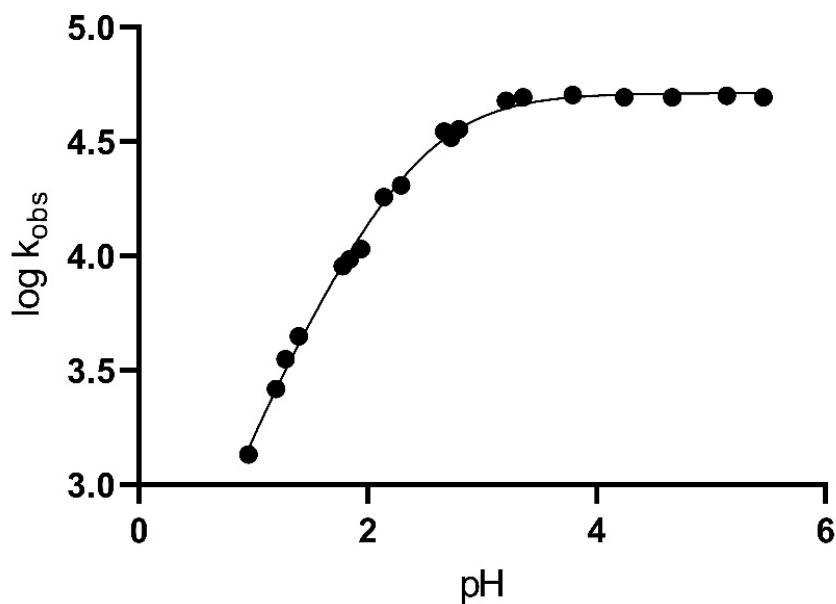


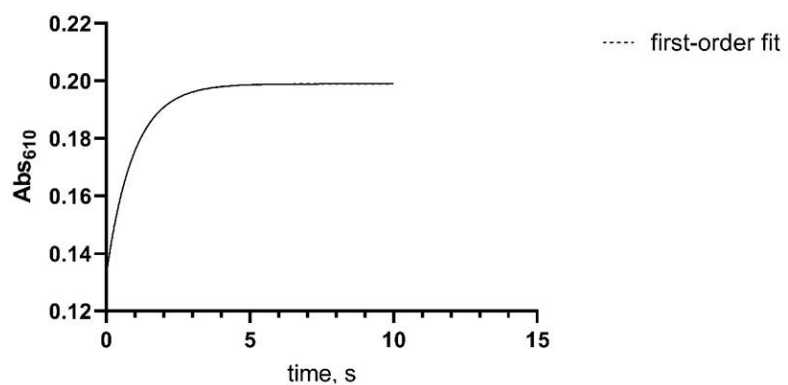
Figure 5.5: The plot of $\log k_{OBS}$ vs pH with $[MSA]_{TOT} = 4 \text{ mM}$, $[Os(III)]_0 = 0.01 \text{ mM}$, $[Os(II)]_0 = 0.1 \text{ mM}$, $\mu = 0.1 \text{ M (NaCl)}$, $T = 25 \text{ }^\circ\text{C}$, data is fit in to equation 4.15. $k_1 = (1.30 \pm 0.07) \times 10^7 \text{ M}^{-2} \text{ s}^{-1}$, $k_2 = (-6.0 \pm 7.0) \times 10^4 \text{ M}^{-2} \text{ s}^{-1}$, $K_a = (3.7 \pm 0.9) \times 10^{-3} \text{ M}$.

The results show that the $\text{CH}_3\text{SO}_2\text{H}$ species is not reactive and that CH_3SO_2^- is the reactive species. Also, when K_a is used as a fitted parameter, a $\text{p}K_a$ range of 2.34 – 2.55 is obtained. Wudl et al reported 2.29 as the $\text{p}K_a$ of methanesulfinic acid.¹⁰⁸

5.3.3 Kinetic traces with PBN

Spin traps are used in experiments to scavenge free radicals that form as the reaction progresses. In these experiments a spin trap may scavenge $\text{CH}_3\text{SO}_2\cdot$ formed thus eliminating the effect of Os(II) on the reaction rate. A series of experiments were carried out to determine the effect of the spin trap N-tert butyl α -phenylnitrone (PBN) on reaction rate. It was confirmed by $^1\text{H-NMR}$ that MSA does not react with PBN. For all the experiments with PBN, Os(II) is fully oxidized to Os(III) in the beginning using excess 5 mM $\text{Br}_2/\text{CH}_3\text{CN}$, and then the excess Br_2 was removed by argon purging. Figure 5.6 shows the typical kinetic trace for the reaction when PBN is present.

a) [PBN] = 1.25 mM, [Os(III)] = 0.13 mM, [MSA] = 4.88 mM



b) [PBN] = 1.25 mM, [Os(III)] = 0.13 mM, [MSA] = 4.88 mM

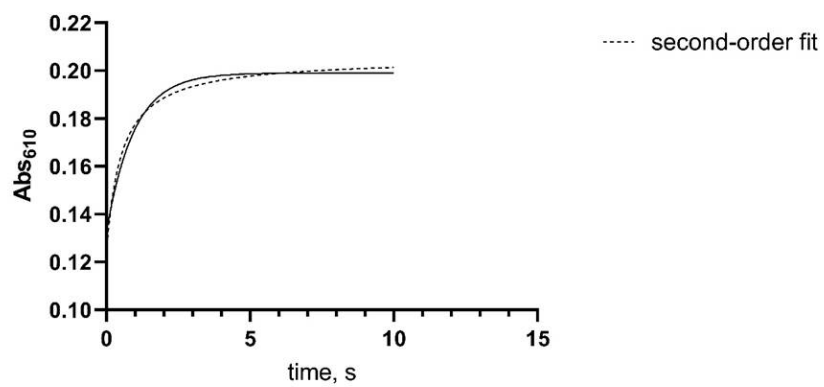


Figure 5.6: Kinetic traces in the presence of PBN with a) first-order fit b) second-order fit, pH = 4.4 (acetate buffer)

Optimum PBN concentration

To determine the range of PBN concentrations where the reaction rate is independent of [PBN], a series of kinetic experiments were carried out with varying concentrations of PBN. (Table A.17, Figure 5.7)

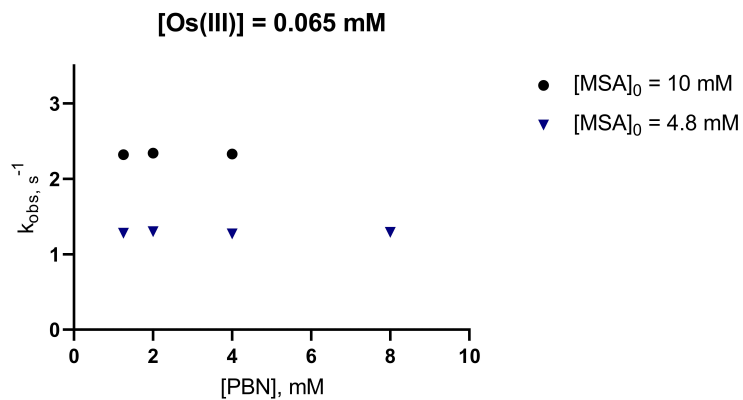


Figure 5.7: Rate dependence on PBN concentration

From the results above it was determined that in the PBN concentration range 1.3 mM to 4 mM at 0.065 mM Os(III) and 10 mM MSA concentrations, the deviation in reaction rate is negligible.

pH dependence in the presence of PBN

pH dependence of the kinetics of the reaction between MSA and $[\text{Os}(\text{phen})_3]^{3+}$ in the presence of PBN was examined under anaerobic conditions by carrying out the reaction at different pH media ranging from pH 1 to pH 5.5 with $[\text{MSA}]_{\text{TOT}} = 10$ mM, $[[\text{Os}(\text{phen})_3]^{3+}]_0 = 0.133$ mM, and 0.1 M ionic strength (NaCl) and monitoring the decay of absorbance at 610 nm using a stopped-flow instrument equipped with a spectrophotometer. All Os(II) in solution was converted to Os(III) and bubbled with argon before each experiment. A stock solution of MSA was prepared in a pH 3.6 acetate buffer and diluted with different buffers as required to attain the necessary MSA concentrations. To prepare reaction media at pH 1-3, dilute HCl was used. For experiments done above pH 3, 10 mM acetate buffers were used to maintain the pH of the reaction mixture. Figure 5.8 shows the dependence of k_{OBS} on the pH of the medium.

[Os(III)] = 0.133 mM , [MSA] = 10 mM, [PBN] = 1.25 mM

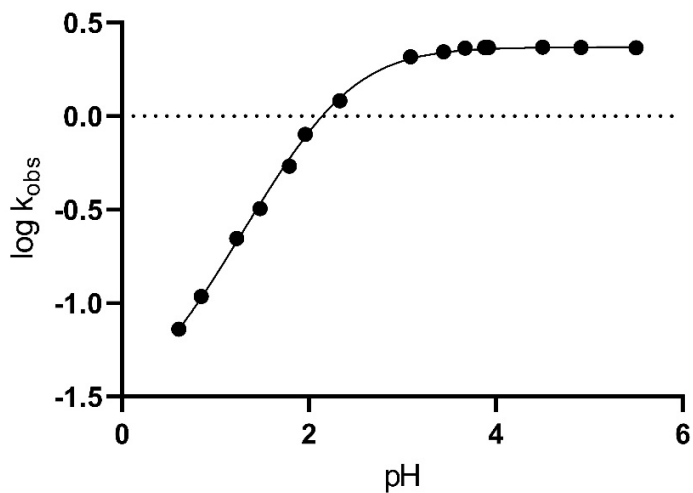


Figure 5.8: The plot of $\log k_{\text{OBS}}$ vs pH with $[\text{MSA}]_{\text{TOT}} = 10 \text{ mM}$, $[[\text{Os}(\text{phen})_3]^{3+}]_0 = 0.133 \text{ mM}$, Os(II) is not present in the medium at $t = 0$, $\mu = 0.1 \text{ M}$ (NaCl), $T = 25 \text{ }^\circ\text{C}$, data is fit in to equation 4.15. $k_1 = (2.34 \pm 0.05) \times 10^2 \text{ M}^{-1} \text{ s}^{-1}$, $k_2 = (2.4 \pm 0.5) \text{ M}^{-1} \text{ s}^{-1}$.

Rate dependence on MSA concentration

Rate dependence on MSA concentration was determined by reacting 0.065 mM $[\text{Os}(\text{phen})_3]^{3+}$ and 1.25 mM PBN at pH 4.4-4.5 with solutions of varying MSA concentrations. All Os(II) in solution was converted to Os(III) and bubbled with argon before each experiment. (Table A.20, Figure 5.9)

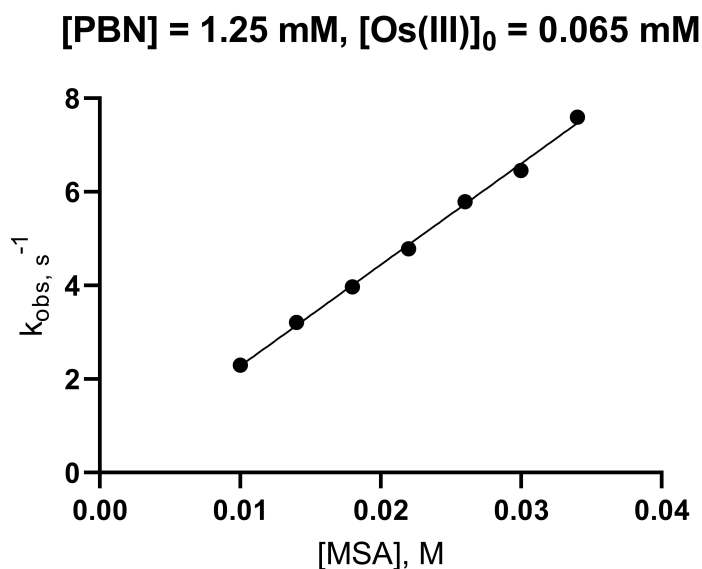


Figure 5.9: The plot of k_{OBS} vs $[\text{MSA}]_{\text{tot}}$ at pH 4.4-4.5 (acetate buffer) with $[[\text{Os}(\text{phen})_3]^{3+}]_0 = 0.065$ mM and $[\text{PBN}] = 0.1$ mM, $\mu = 0.1$ M, $T = 25$ °C. Os(II) is not present in the medium at $t = 0$. Straight line fit with slope = $(2.16 \pm 0.05) \times 10^2 \text{ M}^{-1} \text{ s}^{-1}$ and Y intercept = $(1.15 \pm 1.18) \times 10^{-1} \text{ s}^{-1}$.

5.3.4 Stoichiometry of the reaction in the presence of PBN

0.008 g of $[\text{Os}(\text{phen})_3](\text{CF}_3\text{SO}_3)_2$ was dissolved in 10 ml pH 3 HCl and the absorbance of the solution was recorded. Next, 2 ml Br_2 in CH_3CN was added to the solution to convert all Os(II) to Os(III), and then bubbled with argon to remove excess Br_2 . After that, 5 ml of degassed 0.6 mM MSA with 1 mM PBN was added to the Os(III) solution and allowed to react under argon for 1 hr. The spectrum of the resulting solution was recorded to determine the amount of Os(III) converted back to Os(II) by reaction with MSA. At 610 nm, molar absorption coefficients of Os(II) and Os(III) are $4.32 \times 10^3 \text{ M}^{-1} \text{ cm}^{-1}$ and $8.6 \times 10^2 \text{ M}^{-1} \text{ cm}^{-1}$ respectively. PBN does not absorb at 610 nm.

Moles of MSA added = 3×10^{-6} mol

Moles of Os(II) formed = 2.77×10^{-6} mol

n Os(III): n MSA = 0.92:1

5.3.5 Stoichiometry of the reaction without PBN

0.00881 g of Os(phen)₃](CF₃SO₃)₂ was dissolved in 10 ml pH 3 HCl and the absorbance of the solution was recorded. Next, 2 ml Br₂ in CH₃CN was added to the solution to convert all Os(II) to Os(III), and then bubbled with argon to remove excess Br₂. After that, 5 ml of degassed 0.6 mM MSA was added to the Os(III) solution and allowed to react under argon for 30 min. The spectrum of the resulting solution was recorded to determine the amount of Os(III) converted back to Os(II) by reaction with MSA. At 610 nm, molar absorption coefficients of Os(II) and Os(III) are $4.32 \times 10^3 \text{ M}^{-1} \text{ cm}^{-1}$ and $8.6 \times 10^2 \text{ M}^{-1} \text{ cm}^{-1}$ respectively.

Moles of MSA added = 3×10^{-6} mol

Moles of Os(II) formed = 5.9×10^{-6} mol

n Os(III) : n MSA = 1.97:1

5.3.6 Yield of osmium containing product

The yield of osmium containing product was determined using a diode array UV-VIS spectrophotometer. First a solution of 4×10^{-5} M $[\text{Os}(\text{phen})_3]^{2+}$ at pH 2 and 0.1 M ionic strength was prepared, and its UV-VIS spectrum was recorded. Next, all $[\text{Os}(\text{phen})_3]^{2+}$ was oxidized to $[\text{Os}(\text{phen})_3]^{3+}$ using an excess of $\text{Br}_2/\text{CH}_3\text{Cl}$ and bubbled with argon, and the UV-VIS spectrum of $[\text{Os}(\text{phen})_3]^{3+}$ was recorded. After that, 0.003 g of MSA was added to the $[\text{Os}(\text{phen})_3]^{3+}$ solution, and the reactants were allowed to react under argon for 30 minutes. Finally, the UV-VIS spectrum of the product mixture was recorded. According to figure 5.10, all of the $[\text{Os}(\text{phen})_3]^{3+}$ is reduced to $[\text{Os}(\text{phen})_3]^{2+}$ by the excess of MSA added. This confirms that the electron transfer takes place at the metal center during the oxidation of MSA, and not at the ligands of the oxidant.

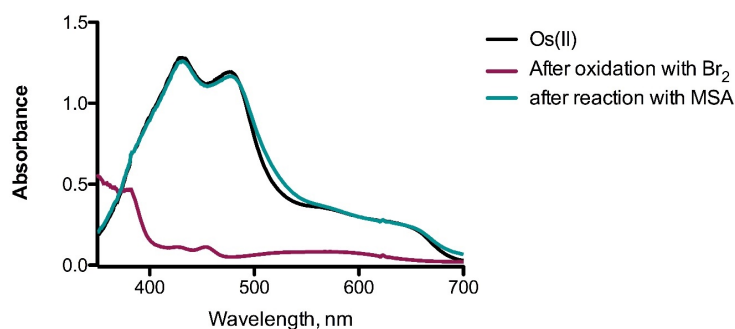


Figure 5.10: UV-VIS spectra for determination of Os(II) yield.

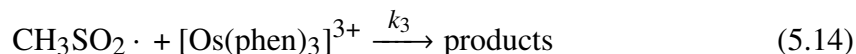
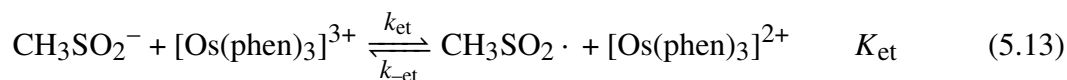
5.4 Discussion

In the absence of the spin trap PBN, the overall empirical rate law for the reaction is

$$\frac{-d[[\text{Os}(\text{phen})_3]^{3+}]}{dt} = \frac{k_1'' K_a [\text{MSA}]_{\text{TOT}} [[\text{Os}(\text{phen})_3]^{3+}]^2}{(K_a + [\text{H}^+]) [[\text{Os}(\text{phen})_3]^{2+}]} \quad (5.12)$$

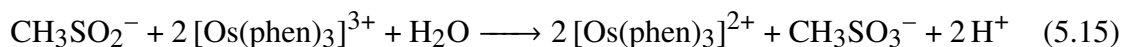
where $k_1'' = (1.09 \pm 0.07) \times 10^3 \text{ M}^{-1} \text{ s}^{-1}$.

The following two-step mechanism is proposed for the oxidation reaction of MSA by $[\text{Os}(\text{phen})_3]^{3+}$.



The first step of the mechanism is a reversible electron transfer process. Evidence for the reversibility of this step is obtained by the strong kinetic inhibition by $[\text{Os}(\text{phen})_3]^{2+}$.

Therefore, the overall reaction in the absence of PBN can be written as,



The mechanism leads to the rate-law

$$\frac{-d[[\text{Os}(\text{phen})_3]^{3+}]}{dt} = 2K_{et}k_3K_a \frac{[[\text{Os}(\text{phen})_3]^{3+}]^2 [\text{MSA}]_{\text{TOT}}}{(K_a + [\text{H}^+]) [[\text{Os}(\text{phen})_3]^{2+}]} \quad (5.16)$$

Comparing equations 5.12 and 5.16, the two equations are equivalent when the

empirical rate constant k_1'' is equal to $2K_{et}k_3$.

In the presence of PBN, the first step of the mechanism is irreversible due to scavenging of $\text{CH}_3\text{SO}_2\cdot$ by PBN. The overall experimental rate-law for the reaction in the presence of PBN is

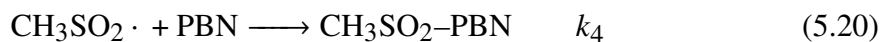
$$\frac{-d[[\text{Os}(\text{phen})_3]^{3+}]}{dt} = \frac{k_1'K_a[\text{MSA}]_{\text{TOT}}[[\text{Os}(\text{phen})_3]^{3+}]}{(K_a + [\text{H}^+])} \quad (5.17)$$

Here, $k_1' = (2.38 \pm 0.05) \times 10^2 \text{ M}^{-1} \text{ s}^{-1}$.

The overall reaction is,



The proposed mechanism is,



The above mechanism leads to the rate-law,

$$\frac{-d[[\text{Os}(\text{phen})_3]^{3+}]}{dt} = k_{et}K_a \frac{[\text{MSA}]_{\text{TOT}}[[\text{Os}(\text{phen})_3]^{3+}]}{(K_a + [\text{H}^+])} \quad (5.21)$$

Comparing equations 5.17 and 5.21, $k_{et} = k_1'$

Substituting k_{et} in 5.16,

$$\frac{k_3}{k_{-et}} = \frac{k_1''}{2k_1'} \quad (5.22)$$

In Chapter 4, $E^\circ(\text{CH}_3\text{SO}_2^\bullet(\text{aq})/\text{CH}_3\text{SO}_2^-(\text{aq}))$ was determined to be 1.224 V (SMD solvation model). This value corresponds to $K_{et} = 3.22 \times 10^{-7}$. Combining this with the value for k_{et} and the ratio of $\frac{k_3}{k_{-et}}$ calculated above, $k_{-et} = 7.4 \times 10^8 \text{ M}^{-1} \text{ s}^{-1}$ and $k_3 = 1.7 \times 10^9 \text{ M}^{-1} \text{ s}^{-1}$.

Application of Marcus cross correlation (eq: 5.23) yields an estimate for the self-exchange rate constant for the $\text{CH}_3\text{SO}_2^\bullet/\text{CH}_3\text{SO}_2^-$ redox couple.

$$k_{12} = (k_{11}k_{22}K_{12}f_{12})^{1/2}W_{12} \quad (5.23)$$

where k_{12} is the second-order electron transfer rate constant, k_{11} and k_{22} are the self-exchange rate constants for the Os(III)/Os(II) and $\text{CH}_3\text{SO}_2^\bullet/\text{CH}_3\text{SO}_2^-$ redox couples. W_{12} is the electrostatic work term. Chapter 1 describes how W_{12} is determined.

Using $k_{11} = 3.09 \times 10^8 \text{ M}^{-1} \text{ s}^{-1}$, $K_{12} = 3.22 \times 10^{-7}$, and the radii of $[\text{Os}(\text{phen})_3]^{3+}$ and CH_3SO_2^- as 6.7 and 2.42 Å respectively, k_{22} was determined to be $0.125 \text{ M}^{-1} \text{ s}^{-1}$.⁷⁴ The significant structural and solvent reorganization involved suggests that k_{22} value would be small. Furthermore, the self-exchange rate constant for $\text{CH}_3\text{SO}_2^\bullet/\text{CH}_3\text{SO}_2^-$ calculated in Chapter 4 is in excellent agreement with the value of k_{22} for $\text{CH}_3\text{SO}_2^\bullet/\text{CH}_3\text{SO}_2^-$ determined here. When the free energy results obtained from PCM solvation model are used, the same calculations yield a value of $7.6 \times 10^{-7} \text{ M}^{-1} \text{ s}^{-1}$ for k_{22} .

5.5 Conclusions

Oxidation of methanesulfinate by $[\text{Os}(\text{phen})_3]^{3+}$ in aqueous media yields methanesulfonate and $[\text{Os}(\text{phen})_3]^{2+}$ as major products. In the absence of the spin-trap PBN, a rate-law

second-order in oxidant concentration was observed with strong kinetic inhibition by M_{red} . Scavenging of RSO_2^\bullet by spin trap PBN is rapid enough to compete with reverse reaction and eliminate $[\text{Os}(\text{phen})_3]^{2+}$ inhibition kinetics. For the reaction of $[\text{IrCl}_6]^{2-}$ with CSA, effects of PBN on the kinetics are not observed.³³ This may be because of the relatively slow reaction rates of $[\text{Os}(\text{phen})_3]^{3+}$ reaction compared to the reaction of $[\text{IrCl}_6]^{2-}$ with CSA, allowing PBN to react with the generated alkanesulfonyl radicals. The reason for rapid reaction rates of $[\text{IrCl}_6]^{2-}$ is its capability of undergoing rapid inner-sphere electron transfer with cysteinesulfonyl radical to form a bridged complex. $[\text{Os}(\text{phen})_3]^{3+}$ is a coordination saturated complex and does not possess ligands capable of bridging.

Chapter 6

Kinetics and mechanism of the two-electron oxidation of methanesulfinic acid by aqueous tri-iodide

This chapter is based on the following paper and reprints were made with permission from the American Chemical Society. The crystallographic data in this chapter were obtained and analyzed by Dr. John D. Gorden.

Rajakaruna, P.; Gorden, J. D.; Stanbury, D. M. Methanesulfonyl Iodide. *Inorg. Chem.* **2019**, 58 (21), 14752–14759.

6.1 Introduction

Compounds having covalent sulfur-halogen bonds have a long history^{112–115} and some, such as SF₆, are impressively stable. Their stability tends to decrease down the halogen group, and the stable compounds with sulfur-iodine bonds are mostly limited to organo-sulphenyl and -sulfonyl iodides. The organo-sulfonyl iodides are almost entirely limited to arylsulfonyl iodides (ArSO₂I). A few alkane sulfonyl iodides (RSO₂I) have been reported and have received some use, but they have not been well characterized.¹¹² Methanesulfonyl iodide is probably the best known of these,¹¹⁶ having received significant use as a reagent in organic synthesis.¹¹⁷ However, the solid form is reported to decompose on isolation¹¹⁸ and its exact composition has not been determined. ³³S and ¹⁷O NMR spectra have been reported for a species believed to be CH₃SO₂I in benzene solution, but no evidence was provided to support this belief.¹¹⁹ To our knowledge there are no examples of alkane sulfonyl iodides that have been characterized structurally or energetically. Herein we report the crystal structures of two compounds containing methanesulfonyl iodide, the equilibrium constant for its formation from triiodide and methanesulfinate in aqueous solution, and the kinetics of its formation and decomposition to methanesulfonate. An unanticipated outcome of our efforts to crystallize methanesulfonyl iodide was its isolation as inclusion compounds in alkali metal polyiodide hosts. The crystal structures of these compounds reveal some unusual polyiodide interactions and provide a rationale for the high iodine content and stability of these substances.

6.2 Reagents and solutions

Sodium methanesulfinate (MSA, 95% Alfa Aesar), sodium methanesulfonate (Alfa Aesar), RbI (TCI), NaClO₄, Na₂C₂O₄, Na₂HPO₄·2H₂O, NaH₂PO₄·H₂O, Na₂HPO₄, NaI,

KI, HClO₄, KBr, KBrO₃, HCl, 3-(trimethylsilyl)-1-propanesulfonic acid sodium salt (DSS) (Sigma-Aldrich), and D₂O 99.8% isotopic (Alfa Aesar) were used as supplied. I₂ was purified by sublimation. All the aqueous solutions were prepared using purified deionized water from Barnstead Nanopure Infinity system. Iodine and iodide stock solutions were protected from light. All other solutions were freshly prepared for each experiment. Iodide concentrations of the solutions were adjusted using a stock solution of sodium iodide. To prepare the stock solution of iodine, potassium iodide was used. Stock solutions of methanesulfinate (MSA) was prepared and stored in the refrigerator. Fresh stock solutions of MSA were prepared weekly, standardized by titration with potassium bromate in the presence of potassium bromide in strongly acidic media with methyl orange as indicator, and diluted to prepare the MSA solutions of known concentrations required for equilibrium and kinetic experiments.

6.3 Instrumentation and methods

To obtain UV-VIS spectra, an HP-8453 diode array spectrophotometer using a quartz cuvette with 1 cm path length was used. ¹H-NMR spectra of the reactants and products were collected using D₂O as solvent and DSS as the reference on a Bruker AV 400 MHz spectrometer. The progress of kinetic experiments was monitored by observing the change in absorbance at 352 nm. A Hi-Tech SF-51 stopped-flow spectrophotometer in the 1-cm pathlength configuration and with a 312 nm optical filter was used to monitor kinetics. Data were acquired and analyzed with OLIS 4300 software. A Thermo Scientific Nicolet iS50 FT-IR instrument was used to obtain infrared spectra. A Corning 450 pH/ion meter with a Mettler Toledo Inlab 421 pH electrode was used to obtain pH measurements. To collect X-ray crystallographic data, Bruker D8 VENTURE χ -geometry diffractometer system with Mo for irradiation at 100 K was employed. Bruker SAINT software package was used to combine frames and Bruker SHELXTL Software Package was used to refine the structure.

6.3.1 Solution-phase studies

Solution-phase studies of the reaction of MSA with I_3^- were performed with NaI instead of KI or RbI in order to prevent precipitation of the product. The equilibrium constant for formation of CH_3SO_2I was determined by fitting the equilibrium I_3^- concentrations to eq 6.7 with Datafit 9.1.¹²⁰ Kinetic studies on the hydrolysis of CH_3SO_2I were performed by pH measurement; the pH values were converted to $[H^+]$ in the pH-dependent experiments, while the production of H^+ in the iodide-dependent experiments was calculated from the conversion of HPO_4^{2-} to $H_2PO_4^-$ as determined by the pH.

6.3.2 Computational studies

Calculations were performed with the Gaussian 16 software package.¹⁰⁷ Molecular structures were optimized in the gas phase at the MP2/aug-cc-pVQZ level with the Frozen Core approximation. Effective Core Potentials were used for calculations on iodine-containing molecules. Solvated species were calculated by using the PCM method.

6.4 Synthesis of $(CH_3SO_2I)_4 \cdot KI_3 \cdot 2I_2$

This compound was prepared as described by Field et al. for the synthesis of "methanesulfonyl iodide".¹¹⁶ A solution of sodium methanesulfinate (MSA) was prepared in an ignition tube by dissolving 0.5 g of MSA in 2 ml of deionized water. Next a solution of triiodide was prepared by mixing 1.3 g of KI and 0.685 g of solid I_2 in 2 ml of deionized water. Then, the triiodide solution was slowly added down the wall of the ignition tube and into the sodium methanesulfinate solution. Lustrous brown/green dichroic needles suitable for single crystal X-ray diffraction formed immediately. The tube was covered with aluminum foil to protect the crystals from light, and stored in a refrigerator. About

4 hours after isolation from the mother liquor and exposure to air the needles became less defined. Due to their decomposition when drying, except for their IR spectrum, Field et al. and also others who have followed the same synthetic procedure have not analyzed the crystals to confirm their identity.¹¹⁸ Crystals were preserved for X-ray analysis by coating them in Paratone.

6.5 Synthesis of $(\text{CH}_3\text{SO}_2\text{I})_2 \cdot \text{RbI}_3$

This compound was prepared similarly to $(\text{CH}_3\text{SO}_2\text{I})_4 \cdot \text{KI}_3 \cdot 2\text{I}_2$ except that RbI was used instead of KI. A solution of MSA was prepared in an ignition tube by dissolving 0.25 g of MSA in 1 ml of deionized water. Next a solution of triiodide was prepared by mixing 0.828 g of RbI and 0.3425 g of solid I_2 in 1 ml of deionized water. Then, the triiodide solution was slowly added through down the wall of the ignition tube into the sodium methanesulfinate solution. Lustrous long brown/green dichroic needles suitable for single crystal X-ray diffraction were instantly formed. The tube was covered with aluminum foil to protect the crystals from light, and stored in a refrigerator. Decomposition of the crystals occurred a few days after isolation and exposure to air. X-ray analysis was performed on crystals coated with Paratone.

6.6 Results

Crystals containing methanesulfonyl iodide (MSI, $\text{CH}_3\text{SO}_2\text{I}$) were obtained upon mixing concentrated aqueous solutions of MSA and RbI/ I_2 or KI/ I_2 . X-ray crystallography revealed that these crystals were inclusion compounds of MSI in matrices of alkali metal polyiodide salts. Selected crystallographic data for the two compounds are presented in Table 6.1, and structural diagrams are shown in Figures 6.1 and 6.2. In an effort to obtain an analogous Ca^{2+} compound, crystals of $\text{Ca}_2(\text{CH}_3\text{SO}_2)_2(\text{CH}_3\text{SO}_3)(\text{I}_3)(\text{H}_2\text{O})_3$

were obtained. This compound is an interesting mixed sulfinate/sulfonate with polyiodide sheets, but it contains no sulfonyl iodide; crystallographic data on this compound are presented in Appendix B.

Table 6.1: Selected crystallographic data for the MSI containing crystals

Formula	$(\text{CH}_3\text{SO}_2\text{I})_2 \cdot \text{RbI}_3$	$(\text{CH}_3\text{SO}_2\text{I})_4 \cdot \text{KI}_3 \cdot 2\text{I}_2$
Crystal system	monoclinic	monoclinic
Space group	P 21/m	P 21/c
a (Å)	9.4977(5)	14.6211(6)
b (Å)	14.7549(8)	26.1593(9)
c (Å)	12.3947(7)	9.5131(3)
β (deg)	94.818(2)	108.9673(11)
V (Å ³)	1730.83	3440.99
Z	8	4
R factor %	2.45	3.33

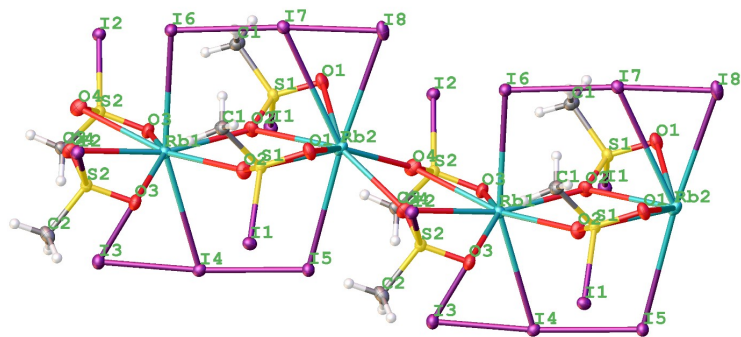


Figure 6.1: The crystal structure of $(\text{CH}_3\text{SO}_2)_2 \cdot \text{RbI}_3$ showing the infinite chain that extends along the a -axis and the two different coordination modes of I_3^-

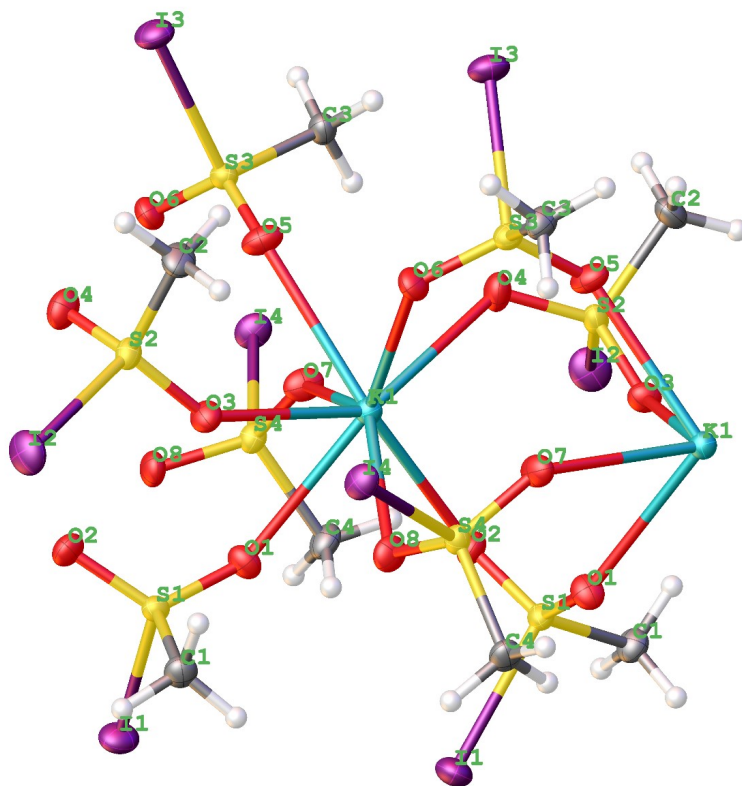


Figure 6.2: The crystal structure of $(\text{CH}_3\text{SO}_2\text{I})_4 \cdot \text{KI}_3 \cdot 2\text{I}_2$ excluding the I_3^- and I_2 components.

Both of the sulfonyl iodide compounds contain alkali metal cations coordinated to the oxygen atoms of the MSI molecules. However, despite their crystallization under very similar conditions they are fundamentally different in that the ratio of M^+/MSI differs and as does the iodine content.

6.6.1 $(\text{CH}_3\text{SO}_2)_2 \cdot \text{RbI}_3$

The rubidium compound consists of two crystallographically independent molecules of MSI, two independent nearly-linear I_3^- ions, and two independent Rb^+ ions. These

components are arranged with MSI and I_3^- ligands bridging adjacent Rb^+ cations to form infinite chains that extend along the a -axis. Within the two MSI molecules the S–I bond lengths are almost identical (2.44 Å), as are the S–O (1.44 - 1.45 Å) and S–C bonds (1.76 Å). The I_3^- ions are asymmetric, having short and long bonds (2.84 and 3.05 Å in one of the I_3^- ions, 2.78 and 3.15 Å in the other). They have long I_3^- – I_3^- contacts (3.8 Å) forming approximately linear chains, and these chains are aligned parallel to the a -axis of the unit cell. The observed dichroism of the crystals can be attributed to this I_3^- alignment. Somewhat surprisingly, there are rather short I–I contacts between the iodine atoms of the MSI molecules and the I_3^- ions (3.38 and 3.43 Å). Similar weak interactions between covalently-bound I and polyiodide anions have been reported elsewhere¹²¹ The two Rb^+ ions reside on a mirror plane. They have approximate hexagonal bipyramidal coordination with six equatorial MSI oxygen atoms, one axial I_3^- iodine atom and an axial I_3^- - η^2 bonded. The Rb(2)-O distances range from 2.83 to 3.09 Å and thus are comparable to the Rb-O distances in $Rb_2S_2O_6$.¹²² As is shown in Table 6.2, the solid-state IR spectrum of $(CH_3SO_2I)_2 \cdot RbI_3$ has features quite similar to those reported for the other methane sulfonyl halides.¹²³

Table 6.2: Comparison of Vibrational Frequencies Obtained for $(\text{CH}_3\text{SO}_2\text{I})_2 \cdot \text{RbI}_3$ Crystals with Published Vibrational Assignments for Methanesulfonyl Halides

Vibrational assignment	$\text{CH}_3\text{SO}_2\text{F}^{\text{a}}$	$\text{CH}_3\text{SO}_2\text{Cl}^{\text{a}}$	$\text{CH}_3\text{SO}_2\text{Br}^{\text{a}}$	$(\text{CH}_3\text{SO}_2\text{I})_2 \cdot \text{RbI}_3^{\text{b}}$
	cm^{-1}			
CSO_2 , b	493	493	480	456
CSO_2 , b	534	540	525	518
C-S, st	733	755	749	720
CH_3 , r	985	970	974	943
SO_2 , st	1177	1175	1170	1104
CH_3 , d	1324	1324	1326	1269
SO_2 , st	1367	1375	1369	1300
CH_3 , d	1425	1411	1411	1392
CH_3 , st	2955	2938	2932	2905
CH_3 , st	3045	3045	3043	3023

^aReference.¹²³ ^bThis work

6.6.2 $(\text{CH}_3\text{SO}_2\text{I})_4 \cdot \text{KI}_3 \cdot 2\text{I}_2$

In this compound all the K^+ ions are equivalent. There are four symmetry independent MSI molecules, three symmetry independent I_2 molecules, and one unique I_3^- ion. The MSI molecules are coordinated to the K^+ ions through their O atoms in a bridging mode, resulting in $(\text{K}(\text{CH}_3\text{SO}_2\text{I})_4^+)_{\infty}$ chains running parallel to the c axis. These chains are

sandwiched between pleated sheets of $(\text{I}_7^-)_\infty$ as shown in Figure 6.3.

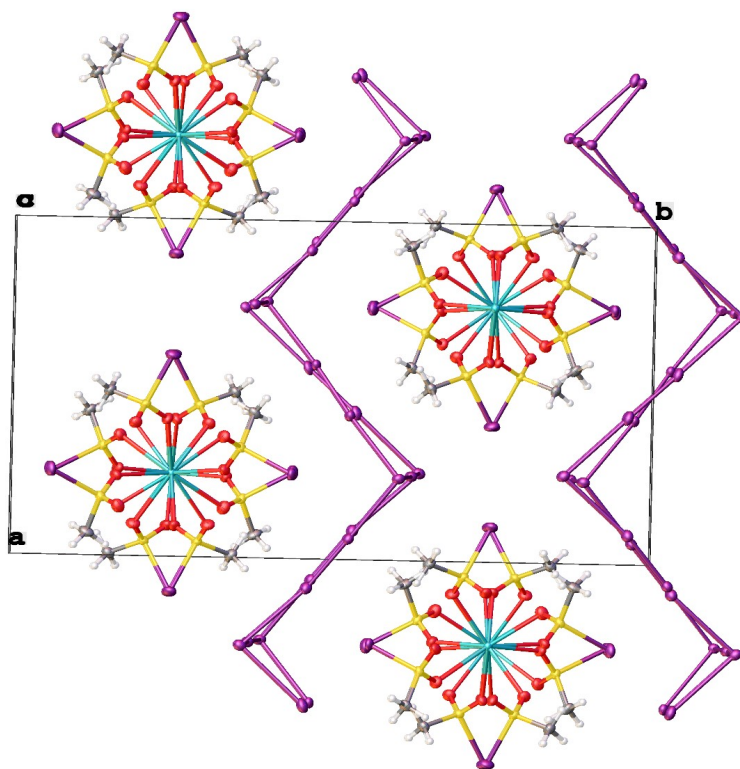


Figure 6.3: Packing diagram of $(\text{CH}_3\text{SO}_2\text{I})_4 \cdot \text{KI}_3 \cdot 2\text{I}_2$ viewed down the c axis illustrating the $(\text{I}_7^-)_\infty$ pleated sheets and $(\text{K}(\text{CH}_3\text{SO}_2\text{I})_4^+)_\infty$ chains

The MSI S–I bond lengths are quite similar at 2.440, 2.442, 2.447, and 2.440 Å, and they are essentially identical to those in the rubidium compound. Likewise the S–O bond lengths are very similar (between 1.43 and 1.44 Å), as are the S–C bond lengths (1.76 – 1.77 Å), and they are also essentially identical to those in the rubidium compound. The $(\text{I}_7^-)_\infty$ sheets can be regarded as consisting of I_2 and I_3^- subunits. The I_2 subunits have I–I bond lengths ranging from 2.73 to 2.74 Å, which is somewhat longer than the I–I bond length in the free molecule (2.67 Å).¹²⁴ The I_3^- ions are nearly linear (176°) and almost symmetric with I–I bond lengths of 2.917 and 2.934 Å; these are typical I_3^- bond

lengths Longer I–I contacts (3.35 - 3.5 Å) form the sheets. Layered (I_7^-) networks have been reported previously.¹²¹ The oriented polyiodide structure provides a rationale for the compound's dichroism. Additional I–I contacts can be found between the sulfonyl iodide and polyiodide atoms in the range of 3.70 to 3.79 Å, which could provide some additional stabilization to the compound. The K^+ ions are octacoordinate, being bonded to one O atom from each of 8 MSI molecules. The K–O bond lengths range from 2.73 to 2.80 Å, which are similar to those in $K_2S_2O_6$ (2.75 - 2.97 Å).¹²⁵ We infer that the compound first reported by Field et al. as CH_3SO_2I is actually $(CH_3SO_2I)_4 \cdot KI_3 \cdot 2I_2$.¹¹⁶ This inference is based on the fact that our crystals of $(CH_3SO_2I)_4 \cdot KI_3 \cdot 2I_2$ were obtained under the same conditions as were used to obtain " CH_3SO_2I ". Additional supporting evidence is that the IR spectrum reported by Field et al. had strong bands at 1300, 1150, 960, and 730 cm^{-1} , which are similar to those reported here for $(CH_3SO_2I)_2 \cdot RbI_3$. In addition, similarly to the prior workers we find that the compound has a dark green/brown color and is unstable when removed from its mother liquor.

6.6.3 Quantum Structure, Polarity, and Energetics of CH_3SO_2I

Structural optimization in the gas phase leads to a CH_3SO_2I molecule with C_s symmetry in the staggered configuration. Tables 6.3 and 6.4 compare the structural parameters of this molecule as calculated for the gas phase and as found in the two crystal structures.

Table 6.3: Comparison of the Bond Lengths Obtained from the Crystal Structures with the Values Calculated

Bond length	(CH ₃ SO ₂ I) ₂ ·RbI ₃ , Å	(CH ₃ SO ₂ I) ₄ ·KI ₃ ·2I ₂ , Å	CH ₃ SO ₂ I(Gaussian), Å
S-I	2.44	2.44	2.4404
S-O	1.448, 1.45	1.43	1.4383
C-H	(0.98)	(0.98)	1.0844, 1.0884
C-S	1.77	1.757, 1.77	1.7709
Parentetical values imposed in the crystallography			

Table 6.4: Comparison of the Bond Angles Obtained from the Crystal Structures with the Values Calculated

Bond angle	(CH ₃ SO ₂ I) ₂ ·RbI ₃ , °	(CH ₃ SO ₂ I) ₄ ·KI ₃ ·2I ₂ , °	CH ₃ SO ₂ I (Gaussian), °
H-C-H	(109.4)	(109.4)	111.480, 112.287
H-C-S	(109.5)	(109.5)	105.290, 107.965
C-S-O	108.6	109.2, 109.3	109.002
O-S-I	108.3, 109.7	105.6, 107.8	107.493
O-S-O	116.0	118.9, 119.0	121.518
I-S-C	103.4	104.7	100.221
Parentetical values imposed in the crystallography			

These comparisons show that the gas-phase and solid-state crystal structures of $\text{CH}_3\text{SO}_2\text{I}$ are very similar. The gas-phase molecule has a calculated dipole moment of 4.48 D with the oxygen atoms having a significant accumulation of negative charge and the iodine atom having some positive charge. Figure 6.4 displays the calculated charge distribution. This charge distribution leads to a charge-dipole interaction between the metal cations and the oxygen atoms that provides a stabilizing force for the crystals.

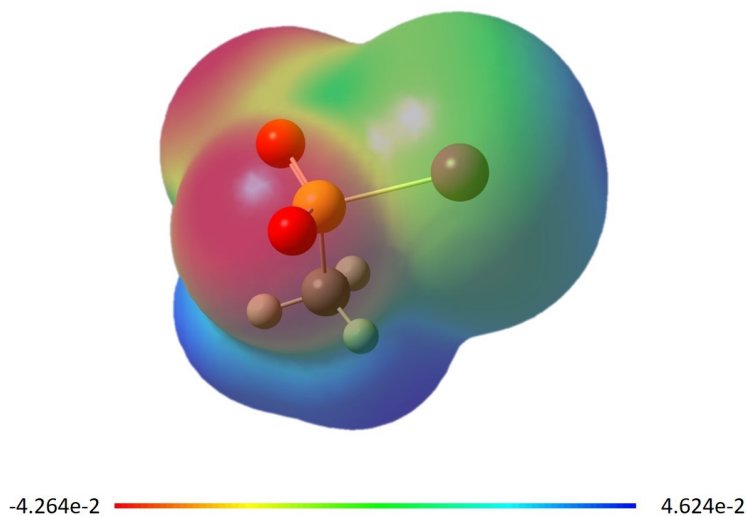


Figure 6.4: Calculated charge distribution in $\text{CH}_3\text{SO}_2\text{I}$

Calculations were also performed on $\text{CH}_3\text{SO}_2\text{H}$, I_2 , and HI . The optimized structure for $\text{CH}_3\text{SO}_2\text{H}(\text{g})$ has a H-O-S-O dihedral angle of 169° , which corresponds to the species MSIA1 calculated by Carvalho et al.¹²⁶ Gibbs energies calculated for the various species are summarized in Table 6.5.

Table 6.5: Gibbs Energies Calculated with Gaussian 16

species	G , a. u.
CH ₃ SO ₂ H(g)	-588.416161
CH ₃ SO ₂ H(aq)	-588.426880
CH ₃ SO ₂ I(g)	-882.803081
CH ₃ SO ₂ I(aq)	-882.811792
I ₂ (g)	-589.953578
HI(g)	-295.566281

From the data in Table 6.5 the Gibbs energy change for reaction 6.1 is calculated to be $\Delta G^\circ = 6.26 \text{ kJ mol}^{-1}$. Combining this result with NBS data¹¹⁰ for $\Delta_f G^\circ$ of I₂(g) and HI(g) leads to $\Delta_f G^\circ(\text{CH}_3\text{SO}_2\text{I}(\text{aq})) - \Delta_f G^\circ(\text{CH}_3\text{SO}_2\text{H}(\text{aq})) = 23.89 \text{ kJ mol}^{-1}$. From this Gibbs energy difference and NBS $\Delta_f G^\circ$ data for I₃⁻(aq), H⁺(aq), and I⁻ a value of $\Delta G^\circ = -27.9 \text{ kJ mol}^{-1}$ is calculated for eq 6.2. With use of the reported pK_a of CH₃SO₂H(aq) = 2.28,¹⁰⁸ a value of $\Delta G^\circ = -40.9 \text{ kJ mol}^{-1}$ is then calculated for eq 6.3. In view of the challenges in calculations of iodine-containing molecules and of hydration energies, we suggest an uncertainty of $\pm 40 \text{ kJ mol}^{-1}$ for this last result (ΔG° , eq 6.3).



6.6.4 CH₃SO₂I Formation in Solution.

When dilute solutions of MSA are mixed with triiodide solutions no precipitation occurs, but a reaction does occur as indicated by an immediate loss of color intensity. Stopped-flow experiments show that the absorbance due to I₃⁻ decreases immediately within the dead time (≈ 2 ms) of the instrument. For example, upon mixing a solution of 4 mM MSA, 20 μM I₂ and 0.01 M I⁻ the initial absorbance is 0.017 at 352 nm. In such solutions the I₂ reacts extensively with I⁻ to form I₃⁻ ($K_{I_3^-} = 721 \text{ M}^{-1}$).¹²⁷



I₃⁻ has been reported to have $\epsilon_{352} = 2.7 \times 10^4 \text{ M}^{-1} \text{ cm}^{-1}$,¹²⁷ and we find $\epsilon_{352} = 2.5 \times 10^4 \text{ M}^{-1} \text{ cm}^{-1}$. Under the conditions mentioned above and if no reaction with MSA had occurred the equilibrium concentration of I₃⁻ should have been 18 μM and the absorbance should have been 0.48. It is clear that most of the I₃⁻ was consumed by the MSA.

The UV/vis spectra of I₃⁻, MSA, and I⁻ are shown in Figure 6.5. From these spectra it can be seen that I₃⁻ has two characteristic absorption peaks at 288 and 352 nm, while neither MSA nor I⁻ absorbs significantly at wavelengths longer than 250 nm.

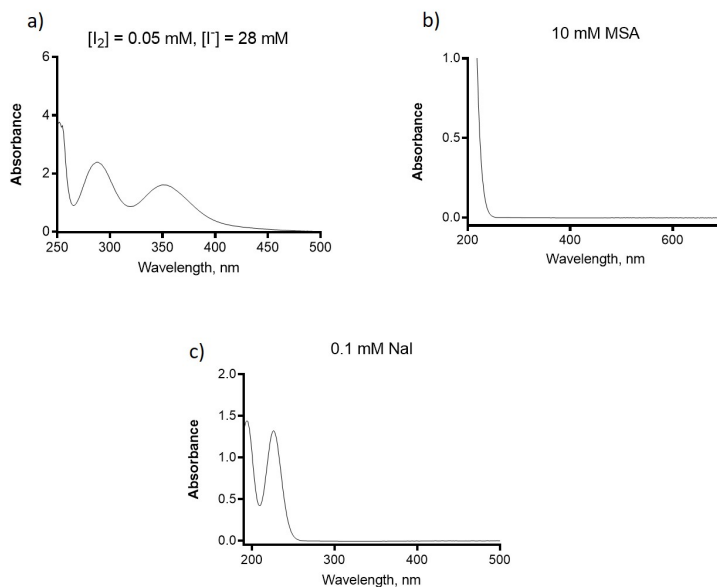


Figure 6.5: UV-VIS spectra of a) triiodide, b) MSA, and c) 0.1 mM iodide in H₂O

Spectra of product mixtures at various MSA concentrations are shown in Figure 6.6.

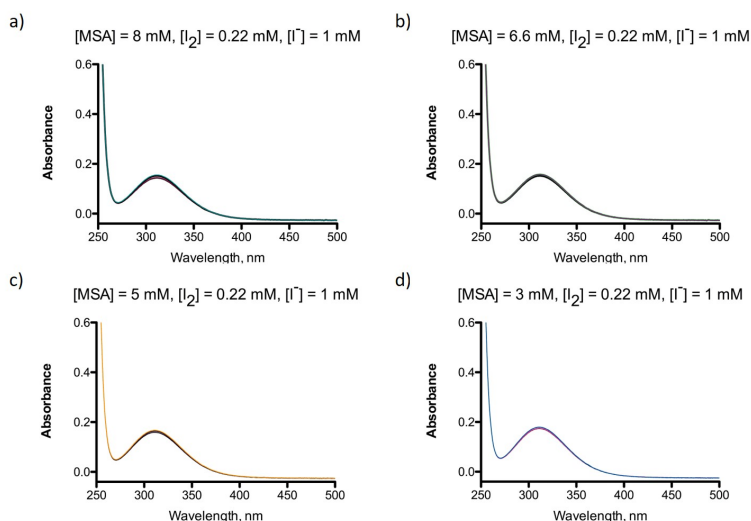


Figure 6.6: UV-VIS spectra of the product mixtures at various [MSA]; $[I_2]_0 = 0.22 \text{ mM}$ and $[I^-] = 1 \text{ mM}$. All solutions were unbuffered. a) $[MSA] = 8 \text{ mM}$, b) $[MSA] = 6.6 \text{ mM}$, c) $[MSA] = 5 \text{ mM}$, d) $[MSA] = 3 \text{ mM}$.

These spectra show that at low I^- concentrations the characteristic 2-peak spectrum of I_3^- is entirely depleted and replaced by a weaker feature with a single absorption peak having λ_{max} at 309 nm. This new absorption feature is ascribed to MSI. Similar results are obtained at 5.3 mM MSA with 66 μM I_2 and 0.33 mM I^- , from which we calculate $\epsilon_{309} = 667 \text{ M}^{-1} \text{ cm}^{-1}$ and $\epsilon_{352} = 197 \text{ M}^{-1} \text{ cm}^{-1}$. This spectrum is remarkably similar to that reported for SO_3I^- ($\epsilon_{300} = 500 \text{ M}^{-1} \text{ cm}^{-1}$).¹²⁸

As noted above, under certain conditions the I_3^- is only partially consumed. A series of experiments was performed to explore the degree of consumption as a function of the initial concentrations of I^- and MSA. Determination of the equilibrium constant for formation of CH_3SO_2I was performed by mixing solutions of I_3^- and $CH_3SO_2^-$ in the stopped-flow instrument and measuring the absorbance at 352 nm a few ms after the formation of CH_3SO_2I was complete. These absorbance values were then corrected for a minor

contribution from $\text{CH}_3\text{SO}_2\text{I}$ and then converted to values of $[\text{I}_3^-]_{\text{eq}}$ by use of the molar absorptivity of I_3^- . The correction for $\text{CH}_3\text{SO}_2\text{I}$ absorbance was performed by the method of successive approximations in fitting the data with equation. These experiments were performed at $25.0\text{ }^\circ\text{C}$ and $\mu = 0.1\text{ M}$ (NaClO_4). The results are reported in table A.21 as the absorbance at 352 nm immediately after mixing in the stopped-flow instrument and the corresponding I_3^- concentration after correction for the absorbance of MSI. Figure 6.7 shows a linear relationship between $[\text{I}_3^-]_{\text{eq}}$ and $[\text{MSA}]$ with a nonzero intercept, while Figure 6.8 shows a linear dependence of $1/[\text{I}_3^-]_{\text{eq}}$ on $1/[\text{I}^-]_2$ with a marginally significant intercept.

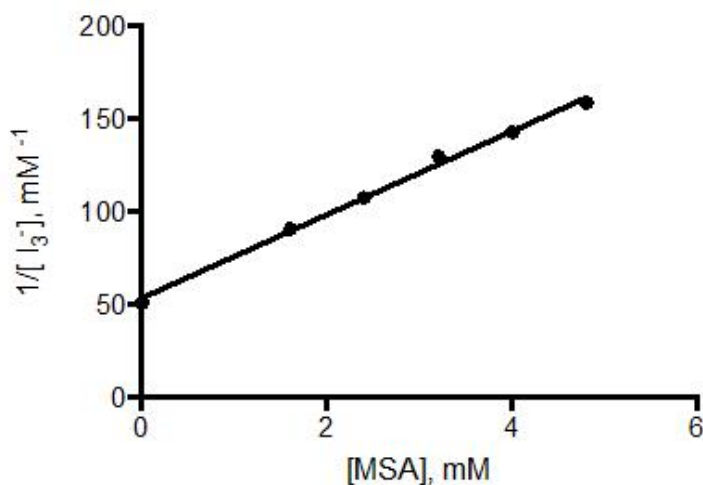


Figure 6.7: MSA dependence of $[\text{I}_3^-]_{\text{eq}}$, $[\text{I}_2]_0 = 0.02\text{ mM}$, $[\text{I}^-]_0 = 48\text{ mM}$. Slope = $(22.5 \pm 0.8) \times 10^6\text{ M}^{-2}$; y intercept = $(54 \pm 2) \times 10^3\text{ M}^{-1}$

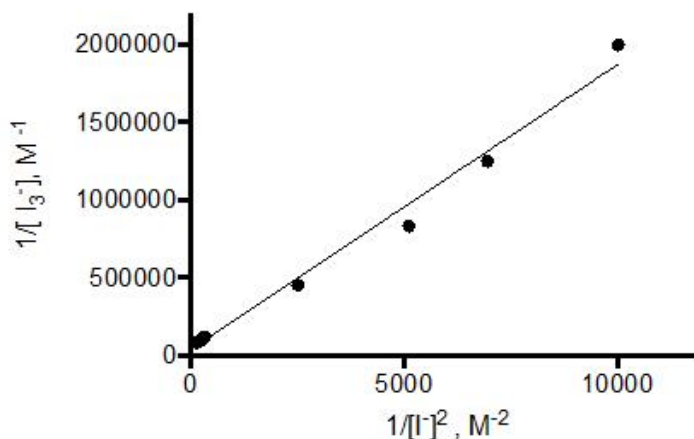
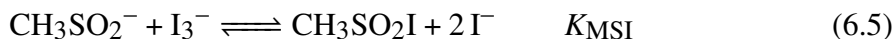


Figure 6.8: $[I^-]$ dependence of $[I_3^-]_{eq}$. $[I_2]_0 = 0.02$ mM, $[MSA]_0 = 4.05$ mM. Slope = (178 ± 5) M, y intercept = $(4.4 \pm 2.0) \times 10^4$ M^{-1}

These two linear dependences are consistent with formation of MSI in an equilibrium shown in equation 6.5.



Under the conditions of Figs 6.7 and 6.8 the triiodide equilibrium (eq 6.4) lies well to the right, so we approximate that $[I_3^-] = [I_2] + [I_3^-]$ so $[I_3^-]_0 = [I_2]_0$. Also, the concentrations of I^- and MSA are in large excess over the $[I_2]_0$. With these approximations the corresponding equilibrium relationship is

$$K_{MSI} = \frac{([I_3^-]_0 - [I_3^-])[I^-]^2}{[I_3^-][CH_3SO_2^-]} \quad (6.6)$$

$$[I_3^-] = \frac{[I_3^-]_0 [I^-]^2}{(K_{MSI}[CH_3SO_2^-] + [I^-]^2)} \quad (6.7)$$

A fit of the data with eq 6.7 yields $K_{MSI} = (1.07 \pm 0.01)$ M. Experiments in 2

mM phosphate buffers at pH 5.8, 6.5 and 6.9 showed that the position of equilibrium is independent of pH in this range. The magnitude of K_{MSI} determined here is comparable to the ab initio value obtained above, given the large uncertainties in the latter.

Equilibria involving I_3^- analogous to eq 6.5 have been reported for other nucleophiles, including SCN^- ,¹²⁹ $\text{S}_2\text{O}_3^{2-}$,¹³⁰ H_2O ,¹³¹ HCN ,¹³² and Br^- .¹²⁷ In all cases the reactions proceed to equilibrium extremely rapidly, as we have also found for MSA. Reaction to form an I_2 addition species (I_2Nu^-) instead of NuI is also reported as in eq 6.8 for various nucleophiles.^{133,134} but the linear dependence on $1/[\text{I}^-]^2$ in Figure 6.11 shows that formal net I^+ transfer as in eq 6.7 is the observed process with MSA.



We note that eqs 6.5 and 6.8 represent the equilibria in terms of I_3^- as the major species, but the solutions also contain minor amounts of I_2 . It is possible that the actual mechanism of formation of MSI entails I_2 rather than I_3^- as the species that reacts with MSA. To identify which of these two species is the actual reactant would require kinetic data on the reaction. Such data are lacking because the equilibrium is established within the dead time of the stopped-flow instrument.

6.7 $\text{CH}_3\text{SO}_2\text{I}$ Decomposition in Solution.

As Figures 6.6 - 6.8 demonstrate, mixtures of I_3^- and MSA immediately generate MSI. However, on a longer time scale methanesulfonate: CH_3SO_3^- is formed as the ultimate product. ^1H NMR spectra conclusively identify this species as the major product by comparison with an authentic sample of CH_3SO_3^- and its appearance as a singlet at δ 2.81 ppm. The overall reaction is thus



Further evidence for this stoichiometry is obtained by pH measurements, which indicate nearly quantitative yield of H^+ for initial conditions of 2 mM MSA, 0.2 mM I_2 , 10 mM I^- and pH 2.35, 3.53 and pH 4.7 (HClO_4). The time dependence of the pH in the above three experiments led to pseudo-first-order kinetics with half lives of several hours. Values of k_{OBS} are given in table 6.6. These results indicate that the rates are accelerated at low pH but are independent of pH above pH 3.5. Additional pH measurements in phosphate buffer were performed to determine the dependence on $[\text{I}^-]$. These results are shown in Figure 6.9 as a linear plot of $1/k_{\text{OBS}}$ vs $[\text{I}^-]^2$.

Table 6.6: Kinetics of $\text{CH}_3\text{SO}_2\text{I}$ Hydrolysis^a

pH ₀	$[\text{I}^-]$, M	k_{OBS} , hr ⁻¹
2.35	0.010	0.22
3.53	0.010	0.035
4.7	0.010	0.037
6.9	0.010	0.326 ^b
6.9	0.020	0.229 ^b
6.9	0.030	0.158 ^b
6.9	0.040	0.110 ^b

^a[MSA] = 2 mM, $[\text{I}_2]_{\text{TOT}} = 0.2 \text{ mM}$, $\mu = 0.1 \text{ M}$ (NaClO_4)
^b2 mM phosphate buffer

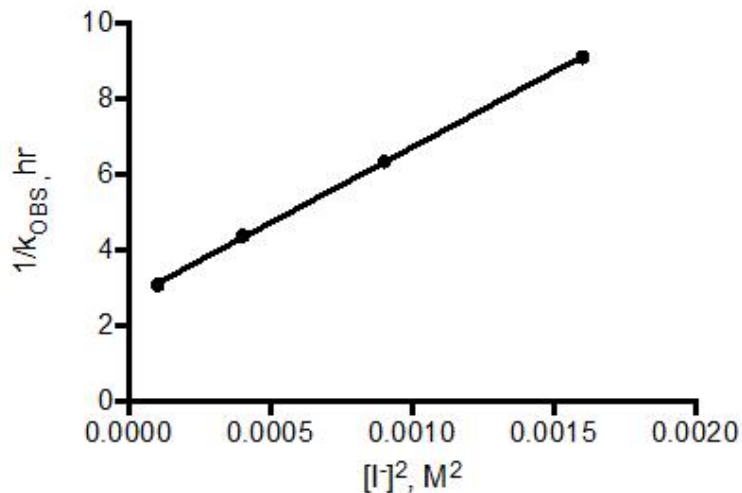
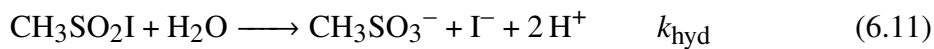
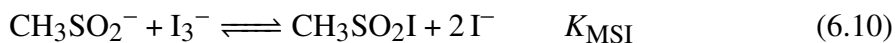


Figure 6.9: Kinetics of H^+ production during hydrolysis of $\text{CH}_3\text{SO}_2\text{I}$. $[\text{MSA}] = 2 \text{ mM}$, $[\text{I}_2]_{\text{TOT}} = 0.2 \text{ mM}$, 2 mM phosphate buffer, $\mu = 0.1 \text{ M}$ (NaClO_4). $1/k_{\text{OBS}}$ vs $[\text{I}^-]^2$. Linear fit with slope = $(4.00 \pm 0.05) \times 10^3 \text{ hr M}^{-2}$ and intercept = $(2.71 \pm 0.05) \text{ hr}$.

This rate law is consistent with a simple two-step mechanism:



As mentioned above, the first step (eq 6.10) may actually proceed through reaction of I_2 instead of I_3^- , but we show it here in terms of I_3^- because I_3^- is the major species and our data do not distinguish between the two pathways.

$$K_{\text{MSI}} = \frac{[\text{MSI}][\text{I}^-]^2}{[\text{MSA}][\text{I}_3^-]} \quad (6.12)$$

$$[I_2]_{TOT} = [I_3]^- + [MSI] \quad \text{or} \quad (6.13)$$

$$[MSI] = [I_2]_{TOT} - [I_3]^- \quad (6.14)$$

$$K_{MSI} = \frac{([I_2]_{TOT} - [I_3]^-)[I^-]^2}{[MSA][I_3]^-} \quad (6.15)$$

$$[I_2]_{TOT} - [I_3]^- = \frac{[I_2]_{TOT}[MSA]}{([I^-]^2 + K_{MSI}[MSA])} \quad (6.16)$$

$$\frac{d[H^+]}{dt} = 2k_{hyd}[MSI] = 2k_{hyd}([I_2]_{TOT} - [I_3]^-) = -2\frac{d[I_2]_{TOT}}{dt} \quad (6.17)$$

$$\frac{d[H^+]}{dt} = \frac{2k_{hyd}[I_2]_{TOT}K_{MSI}[MSA]}{[I^-]^2 + K_{MSI}[MSA]} \quad (6.18)$$

$$\frac{d[I_2]_{TOT}}{dt} = \frac{k_{hyd}[I_2]_{TOT}K_{MSI}[MSA]}{([I^-]^2 + K_{MSI}[MSA])} \quad (6.19)$$

$$k_{OBS} = \frac{k_{hyd}K_{MSI}[MSA]}{([I^-]^2 + K_{MSI}[MSA])} \quad \text{or} \quad (6.20)$$

$$\frac{1}{k_{OBS}} = \frac{[I^-]^2}{k_{hyd}K_{MSI}[MSA]} + \frac{1}{k_{hyd}} \quad (6.21)$$

From the linear fit in Figure 6.9 the data yield $k_{hyd} = 1.0 \times 10^{-4} \text{ s}^{-1}$ and $K_{MSI} = 0.34 \text{ M}$. The minor deviation of this value for K_{MSI} from that derived from the equilibrium stopped-flow data is attributed to the phosphate buffer. The value of k_{OBS} at 10 mM

I^- is about 9 times greater in phosphate buffer than the corresponding value at pH 4.7 without phosphate buffer; this difference may be due to phosphate buffer catalysis, which has also been reported for the hydrolysis of IBr ¹²⁷ and $ISCN$.¹²⁹ The rate constant for hydrolysis of MSI reported above is quite small and similar to that reported for hydrolysis of CH_3SO_2Cl ¹³⁵ Nevertheless, solutions of MSI are much more labile and complex because they require significant concentrations of I_3^- to prevent the rapid dehalogenative conversion to $CH_3SO_2^-$ as in eq 6.10. The analogous dehalogenation of CH_3SO_2Cl does not occur, making solutions of CH_3SO_2Cl relatively persistent.

6.8 Conclusions

Here we report the first characterization of an alkanesulfonyl iodide, CH_3SO_2I . It can be precipitated from aqueous mixtures of $CH_3SO_2^-$, KI and I_2 as a KI_3/I_2 inclusion compound or from RbI as a RbI_3 inclusion compound. In both compounds the cations are coordinated to sulfonyl oxygens, but additional stabilization is achieved through weak interactions with the polyiodide anions. The material previously claimed to be CH_3SO_2I is actually the KI_3/I_2 inclusion compound. In NaI/I_2 solutions CH_3SO_2I does not precipitate and is formed very rapidly (ms) in an equilibrium. To our knowledge, measurement of this equilibrium constant provides the first report on the thermodynamic properties of the S–I bond in aqueous solution. CH_3SO_2I solutions hydrolyze to $CH_3SO_3^-$ over several hours, similarly to CH_3SO_2Cl solutions, although the hydrolysis of CH_3SO_2I is made more complex by the concurrent equilibrium with I_3^- .

References

- (1) Hand, C. E.; Honek, J. F. *J. Nat. Prod.* **2005**, *68*, 293–308.
- (2) Pickering, I. J.; George, G. N.; Yu, E. Y.; Brune, D. C.; Tuschak, C.; Overmann, J.; Beatty, J. T.; Prince, R. C. *Biochemistry* **2001**, *40*, 8138–8145.
- (3) Moriarty-Craige, S. E.; Jones, D. P. *Annu. Rev. Nutr.* **2004**, *24*, 481–509.
- (4) Cooper, A. J. L. *Annu. Rev. Biochem.* **1983**, *52*, 187–222.
- (5) Jacob, C.; Giles, G. I.; Giles, N. M.; Sies, H. *Angew. Chemie Int. Ed.* **2003**, *42*, 4742–4758.
- (6) Walsh, C. T. In *Chemical Biology of Sulfur*; 12; Royal Society of Chemistry: 2020, pp 5–22.
- (7) Jacob, C.; Knight, I.; Winyard, P. G. *Biol. Chem.* **2006**, *387*, 1385–1397.
- (8) Benson, S. W. *Chem. Rev.* **1978**, *78*, 23–35.
- (9) Iwaoka, M.; Isozumi, N. *Molecules* **2012**, *17*, 7266–7283.
- (10) Arduengo, A. J.; Burgess, E. M. *J. Am. Chem. Soc.* **1977**, *99*, 2376–2378.
- (11) Nakamura, T.; Yamamoto, T.; Abe, M.; Matsumura, H.; Hagihara, Y.; Goto, T.; Yamaguchi, T.; Inoue, T. *Proc. Natl. Acad. Sci.* **2008**, *105*, 6238–6242.
- (12) Schindler, M. *J. Chem. Phys.* **1988**, *88*, 7638–7649.

- (13) Urmey, A. R.; Zondlo, N. J. *Free Radic. Biol. Med.* **2020**, *148*, 96–107.
- (14) Lo Conte, M.; Carroll, K. S. *J. Biol. Chem.* **2013**, *288*, 26480–26488.
- (15) Paulsen, C. E.; Carroll, K. S. *Chem. Rev.* **2013**, *113*, 4633–4679.
- (16) Mumbengegwi, D. R.; Li, Q.; Li, C.; Bear, C. E.; Engelhardt, J. F. *Mol. Cell. Biol.* **2008**, *28*, 3700–3712.
- (17) Bienert, G. P.; Schjoerring, J. K.; Jahn, T. P. *Biochim. Biophys. Acta - Biomembr.* **2006**, *1758*, 994–1003.
- (18) Murthy, S. N.; Madhav, B.; Reddy, V. P.; Rao, K. R.; Nageswar, Y. V. D. *Tetrahedron Lett.* **2009**, *50*, 5009–5011.
- (19) Hurd, T. R.; Murphy, M. P. In *Redox Signaling and Regulation in Biology and Medicine*, Jacob C.; Winyard, P. G, Ed.; Wiley-VCH: Weinheim, 2009, pp 13–43.
- (20) Dupre, S.; Spirito, A.; Pinnen, F.; Sugahara, K.; Kodama, H. *Amino Acids* **1998**, *15*, 363–372.
- (21) Kice, J. L.; Bowers, K. W. *J. Am. Chem. Soc.* **1962**, *84*, 605–610.
- (22) Forrest, T. P.; Ryan, D. E. *Can. J. Chem.* **1958**, *36*, 1674–1679.
- (23) Wetzell, D. L.; Meloan, C. E. *Anal. Chem.* **1964**, *36*, 2474–2477.
- (24) De Marco, C.; Mosti, R.; Cavallini, D. *J. Chromatogr. A* **1965**, *18*, 492–497.
- (25) Deruer, E.; Hamel, V.; Blais, S.; Canesi, S. *Beilstein J. Org. Chem.* **2018**, *14*, 1203–1207.
- (26) Fontana, M.; Duprè, S.; Pecci, L. In *Taur. 6; 1*; Springer US: 2005; Vol. 389, pp 15–24.
- (27) Baseggio Conrado, A.; D’Angelantonio, M.; D’Erme, M.; Pecci, L.; Fontana, M. In *Taurine 10*, 2017; Vol. 975, pp 573–583.

- (28) Scaduto, R. C. *Free Radic. Biol. Med.* **1995**, *18*, 271–277.
- (29) Bardouki, H.; da Rosa, M.; Mihalopoulos, N.; Palm, W.-U.; Zetzsch, C. *Atmos. Environ.* **2002**, *36*, 4627–4634.
- (30) Baseggio Conrado, A.; D’Angelantonio, M.; Torreggiani, A.; Pecci, L.; Fontana, M. *Free Radical Res.* **2014**, *48*, 1300–1310.
- (31) Baseggio Conrado, A.; Maina, S.; Moseley, H.; Francioso, A.; Mosca, L.; Capuozzo, E.; Fontana, M. In *Taurine 10*, Lee, D.-H., Schaffer, S. W., Park, E., Kim, H. W., Eds.; Springer Netherlands: Dordrecht, 2017; Vol. 975, pp 551–561.
- (32) Fontana, M.; Giovannitti, F.; Pecci, L. *Free Radical Res.* **2008**, *42*, 320–330.
- (33) Bhattarai, N.; Stanbury, D. M. *J. Phys. Chem. B* **2014**, *118*, 1097–1101.
- (34) Flyunt, R.; Makogon, O.; Schuchmann, M. N.; Asmus, K.-D.; von Sonntag, C. *J. Chem. Soc. Perkin Trans. 2* **2001**, 787–792.
- (35) Chatgililoglu, C.; Griller, D.; Guerra, M. *J. Phys. Chem.* **1987**, *91*, 3747–3750.
- (36) Sevilla, M. D.; Yan, M.; Becker, D. *Biochem. Biophys. Res. Commun.* **1988**, *155*, 405–410.
- (37) Chatgililoglu, C.; Griller, D.; Kanabus-Kaminska, J. M.; Lossing, F. P. *J. Chem. Soc., Perkin Trans. 2* **1994**, 357–360.
- (38) Sehested, K.; Holcman, J. *Radiat. Phys. Chem.* **1996**, *47*, 357–360.
- (39) Sumizu, K. *Anal. Biochem.* **1962**, *4*, 378–383.
- (40) Leonard, S. E.; Carroll, K. S. *Curr. Opin. Chem. Biol.* **2011**, *15*, 88–102.
- (41) Jacob, C.; Holme, A. L.; Fry, F. H. *Org. Biomol. Chem.* **2004**, *2*, 1953–1956.
- (42) Reddie, K. G.; Carroll, K. S. *Curr. Opin. Chem. Biol.* **2008**, *12*, 746–754.
- (43) Marino, S. M.; Gladyshev, V. N. *J. Biol. Chem.* **2012**, *287*, 4419–4425.

- (44) Suliman, M. E.; Anderstam, B.; Bergström, J. *Kidney Int.* **1996**, *50*, 1713–1717.
- (45) Stipanuk, M. H.; Ueki, I.; Dominy, J. E.; Simmons, C. R.; Hirschberger, L. L. *Amino Acids* **2009**, *37*, 55–63.
- (46) Alcock, L. J.; Perkins, M. V.; Chalker, J. M. *Chem. Soc. Rev.* **2018**, *47*, 231–268.
- (47) Rosado, J. O.; Salvador, M.; Bonatto, D. *Mol. Cell. Biochem.* **2007**, *301*, 1–12.
- (48) Blackinton, J.; Lakshminarasimhan, M.; Thomas, K. J.; Ahmad, R.; Greggio, E.; Raza, A. S.; Cookson, M. R.; Wilson, M. A. *J. Biol. Chem.* **2009**, *284*, 6476–6485.
- (49) Murakami, T.; Nojiri, M.; Nakayama, H.; Dohmae, N.; Takio, K.; Odaka, M.; Endo, I.; Nagamune, T.; Yohda, M. *Protein Sci.* **2000**, *9*, 1024–1030.
- (50) Keller, M. D. *Biol. Oceanogr.* **1988**, *6*, 375–382.
- (51) Bullock, H. A.; Luo, H.; Whitman, W. B. *Front. Microbiol.* **2017**, *8*, 1–17.
- (52) Sorensen, S.; Falbe-Hansen, H.; Mangoni, M.; Hjorth, J.; Jensen, N. *J. Atmos. Chem.* **1996**, *24*, 299–315.
- (53) Chen, Q.; Sherwen, T.; Evans, M.; Alexander, B. *Atmos. Chem. Phys.* **2018**, *18*, 13617–13637.
- (54) Zhu, L.; Nicovich, J. M.; Wine, P. H. *J. Phys. Chem. A* **2005**, *109*, 3903–3911.
- (55) Green, T. R.; Fellman, J. H.; Eicher, A. L.; Pratt, K. L. *Biochim. Biophys. Acta - Gen. Subj.* **1991**, *1073*, 91–97.
- (56) Learn, D. B.; Fried, V. A.; Thomas, E. L. *J. Leukocyte Biol.* **1990**, *48*, 174–182.
- (57) Jacobsen, J. G.; Smith, L. H. *Physiol. Rev.* **1968**, *48*, 424–511.
- (58) Fontana, M.; Pecci, L.; Duprè, S.; Cavallini, D. *Neurochem. Res.* **2004**, *29*, 111–116.
- (59) Cavallini, D.; De Marco, C.; Mondovì, B.; Stirpe, F. *Biochim. Biophys. Acta* **1954**, *15*, 301–303.

- (60) Fellman, J. H.; Green, T. R.; Eicher, A. L. In *The Biology of Taurine. Advances in Experimental Medicine and Biology*; 9; Springer, Boston, MA.: 1987; Vol. 217, pp 39–48.
- (61) Dupré S., Spirito A., Sugahara K., K. H., *Taurine 3. Advances in Experimental Medicine and Biology*; Springer, Boston, MA.: 1998, pp 3–8.
- (62) Sharma, D. K. S.; Kebarle, P. *J. Am. Chem. Soc.* **1982**, *104*, 19–24.
- (63) Hückel, E *Zeitschrift für Phys.* **1925**, *26*, 93–147.
- (64) Pyun, C. W. *J. Chem. Educ.* **1971**, *48*, 194.
- (65) Taube, H. *J. Chem. Educ.* **1968**, *45*, 452.
- (66) Taube, H.; Myers, H. *J. Am. Chem. Soc.* **1954**, *76*, 2103–2111.
- (67) Marcus, R. A. *J. Chem. Phys.* **1956**, *24*, 966–978.
- (68) Ratner, M. A.; Levine, R. D. *J. Am. Chem. Soc.* **1980**, *102*, 4898–4900.
- (69) Libby, W. F. *J. Phys. Chem.* **1952**, *56*, 863–868.
- (70) Rhee, S.; Jeong, W.; Chang, T.-S.; Woo, H. *Kidney Int.* **2007**, *72*, S3–S8.
- (71) Danielson, S. R.; Andersen, J. K. *Free Radic. Biol. Med.* **2008**, *44*, 1787–1794.
- (72) Irvine, G. B.; El-Agnaf, O. M.; Shankar, G. M.; Walsh, D. M. *Mol. Med.* **2008**, *14*, 451–464.
- (73) Pimentel, C.; Batista-Nascimento, L.; Rodrigues-Pousada, C.; Menezes, R. A. *Oxidative Med. Cell. Longev.* **2012**, *2012*, 1–9.
- (74) Hung, M.; Stanbury, D. M. *Inorg. Chem.* **2005**, *44*, 9952–9960.
- (75) Song, N.; Stanbury, D. M. *Inorg. Chem.* **2012**, *51*, 4909–4911.
- (76) Sarala, R.; Rabin, S. B.; Stanbury, D. M. *Inorg. Chem.* **1991**, *30*, 3999–4007.

- (77) Palmieri, F.; Stipani, I.; Iacobazzi, V. *Biochim. Biophys. Acta - Biomembr.* **1979**, 555, 531–546.
- (78) Potapenko, D. I.; Bagryanskaya, E. G.; Reznikov, V. V.; Clanton, T. L.; Khramtsov, V. V. *Magn. Reson. Chem.* **2003**, 41, 603–608.
- (79) Potapenko, D. I.; Clanton, T. L.; Bagryanskaya, E. G.; Gritsan, N. P.; Reznikov, V. A.; Khramtsov, V. V. *Free Radic. Biol. Med.* **2003**, 34, 196–206.
- (80) Potapenko, D. I.; Bagryanskaya, E. G.; Tsentalovich, Y. P.; Reznikov, V. A.; Clanton, T. L.; Khramtsov, V. V. *J. Phys. Chem. B* **2004**, 108, 9315–9324.
- (81) Hanna, P. M.; Chamulitrat, W.; Mason, R. P. *Arch. Biochem. Biophys.* **1992**, 296, 640–644.
- (82) Makino, K.; Hagiwara, T.; Hagi, A.; Nishi, M.; Murakami, A. *Biochem. Biophys. Res. Commun.* **1990**, 172, 1073–1080.
- (83) Alberti, A.; Carloni, P.; Ebersson, L.; Greci, L.; Stipa, P. *J. Chem. Soc. Perkin Trans. 2* **1997**, 887–892.
- (84) Forrester, A. R.; Hepburn, S. P. *J. Chem. Soc. C Org.* **1971**, M, 701.
- (85) Volman, D. H.; Chen, J. C. *J. Am. Chem. Soc.* **1959**, 81, 4141–4144.
- (86) Volman, D. H.; Swanson, L. W. *J. Am. Chem. Soc.* **1960**, 82, 4141–4144.
- (87) Nauser, T.; Koppenol, W. H.; Schöneich, C. *J. Phys. Chem. B* **2012**, 116, 5329–5341.
- (88) Harman, L. S.; Mottley, C.; Mason, R. P. *J. Biol. Chem.* **1984**, 259, 5606–5611.
- (89) Thoi, H. H.; Iino, M.; Matsuda, M. *J. Org. Chem.* **1980**, 45, 3626–3630.
- (90) Razskazovskii, Y.; Colson, A.-O.; Sevilla, M. D. *J. Phys. Chem.* **1995**, 99, 7993–8001.

- (91) Sevilla, M.; Becker, D.; Yan, M. *Int. J. Radiat. Biol.* **1990**, *57*, 65–81.
- (92) Bhattarai, N.; Stanbury, D. M. *Inorg. Chem.* **2012**, *51*, 13303–13311.
- (93) Itoh, S.; Koshino, N.; Katsuki, M.; Noda, T.; Ishihara, K.; Inamo, M.; Takagi, H. D. *Dalton Trans.* **2004**, 1862–1866.
- (94) Sonnberger, B.; Hühn, P.; Waßerburger, A.; Wasgestian, F. *Inorg. Chim. Acta* **1992**, *196*, 65–71.
- (95) Hung, M.-L.; Stanbury, D. M. *Inorg. Chem.* **1994**, *33*, 4062–4069.
- (96) Sarala, R.; Stanbury, D. M. *Inorg. Chem.* **1992**, *31*, 2771–2777.
- (97) McAuley, A.; Spencer, L.; West, P. R. *Can. J. Chem.* **1985**, *63*, 1198–1203.
- (98) McAuley, A.; Norman, P. R.; Olubuyide, O. *Inorg. Chem.* **1984**, *23*, 1938–1943.
- (99) DeMaine, M. M.; Stanbury, D. M. *Inorg. Chem.* **1991**, *30*, 2104–2109.
- (100) Crawford, P. W.; Schultz, F. A. *Inorg. Chem.* **1994**, *33*, 4344–4350.
- (101) Koshino, N.; Funahashi, S.; Takagi, H. D. *Dalton Trans.* **1997**, 4175–4180.
- (102) Patai, S.; Rappoport, Z., *Sulphonic Acids, Esters and their Derivatives (1991)*, 1st ed.; John Wiley & Sons, Ltd: Chichester, UK, 1991, pp 2–3.
- (103) Zhu, L.; Nenes, A.; Wine, P. H.; Nicovich, J. M. *J. Geophys. Res.* **2006**, *111*, D05316.
- (104) Johansen, A. M.; Key, J. M. *Geophys. Res. Lett.* **2006**, *33*, L14818.
- (105) Kukui, A.; Borissenko, D.; Laverdet, G.; Le Bras, G. *J. Phys. Chem. A* **2003**, *107*, 5732–5742.
- (106) Arsene, C.; Barnes, I.; Becker, K. H.; Schneider, W. F.; Wallington, T. T.; Mihalopoulos, N.; Patroescu-Klotz, I. V. *Environ. Sci. Technol.* **2002**, *36*, 5155–5163.
- (107) Frisch, M. J. et al., *Gaussian 16*; Gaussian, Inc., Wallingford CT: 2016.

- (108) Wudl, F.; Lightner, D. A.; Cram, D. J. *J. Am. Chem. Soc.* **1967**, *89*, 4099–4101.
- (109) McKee, M. L. *Chem. Phys. Lett.* **1993**, *211*, 643–648.
- (110) Wagman, D. D.; Evans, W. H.; Parker, V. B.; Schumm, R. H.; Halow, I.; Bailey, S. M.; Churney, K. L.; Nuttall, R. L. *J. Phys. Chem. Ref. Data* **1989**, *18*, 1807–1812.
- (111) Sarala, R.; Stanbury, D. M. *Inorg. Chem.* **1990**, *29*, 3456–3460.
- (112) Danehy, J. P., "The Sulfur-Iodine Bond" in *Sulfur in Organic and Inorganic Chemistry; vol 1*; Senning, A., Ed.; Marcel Dekker, Inc.: New York: 1971, pp 327–339.
- (113) Von Halasz, S. P.; Glemser, O., "The Sulfur-Fluorine Bond" in *Sulfur in Organic and Inorganic Chemistry; vol 1*; Senning, A, Ed.; Marcel Dekker, Inc.: New York: 1971, pp 209–237.
- (114) Russ, C. R.; Douglass, I. B., "The Sulfur-Chlorine Bond" in *Sulfur in Organic and Inorganic Chemistry*; Senning, A, Ed.; Marcel Dekker, Inc.: New York: 1971, pp 239–259.
- (115) Magee, P. S., "The Sulfur-Bromine Bond" in *Sulfur in Organic and Inorganic Chemistry*; Senning, A, Ed.; Marcel Dekker, Inc.: New York: 1971, pp 262–326.
- (116) Field, L.; Parsons, T. F.; Crenshaw, R. R. *J. Org. Chem.* **1964**, *29*, 918–921.
- (117) Truce, W. E.; Heuring, D. L.; Wolf, G. C. *J. Org. Chem.* **1974**, *39*, 238–244.
- (118) Truce, W. E.; Wolf, G. C. *J. Org. Chem.* **1971**, *36*, 1727–1732.
- (119) Barbarella, G.; Chatgililoglu, C.; Tugnoli, V. *J. Magn. Reson.* **1990**, *88*, 277–283.
- (120) Gilmore, J, *Datafit 9.1*; Oakdale Engineering, Oakdale, PA: 2014.
- (121) Svensson, P. H.; Kloo, L. *Chem. Rev.* **2003**, *103*, 1649–1684.
- (122) Barnes, W. H.; Wendling, V. *Zeitschrift für Krist. - Cryst. Mater.* **1938**, *99*, 153–179.

- (123) Geiseler, G.; Kuschmiers, R. *Chem. Ber.* **1960**, *93*, 2041–2047.
- (124) Huber, K. P.; Herzberg, G., *Constants of Diatomic Molecules*; Van Nostrand Reinhold Co.: New York: 1979, p 332.
- (125) Gomes, E. d. M.; Ortega, J.; Etxebarria, J.; Zúñiga, F. J.; Breczewski, T. *J. Phys.: Condens. Matter* **1996**, *8*, 2063–2071.
- (126) Carvalho, N. F.; Silva, S. P.; Resende, S. M. *J. Braz. Chem. Soc.* **2011**, *22*, 950–954.
- (127) Troy, R. C.; Kelley, M. D.; Nagy, J. C.; Margerum, D. W. *Inorg. Chem.* **1991**, *30*, 4838–4845.
- (128) Yiin, B. S.; Margerum, D. W. *Inorg. Chem.* **1990**, *29*, 1559–1564.
- (129) Briot, G.; Smith, R. *Aust. J. Chem.* **1973**, *26*, 1863.
- (130) Scheper, W. M.; Margerum, D. W. *Inorg. Chem.* **1992**, *31*, 5466–5473.
- (131) Eigen, M.; Kustin, K. *J. Am. Chem. Soc.* **1962**, *84*, 1355–1361.
- (132) Smith, R. *Aust. J. Chem.* **1970**, *23*, 431.
- (133) Liu, R. M.; McDonald, M. R.; Margerum, D. W. *Inorg. Chem.* **1995**, *34*, 6093–6099.
- (134) Liu, R. M.; Margerum, D. W. *Inorg. Chem.* **1998**, *37*, 2531–2537.
- (135) Hall, H. K. *J. Am. Chem. Soc.* **1956**, *78*, 1450–1454.
- (136) Rajakaruna, P.; Gorden, J. D.; Stanbury, D. M. *Inorg. Chem.* **2019**, *58*, 14752–14759.

Appendix A

Further experimental details related to Chapters 2-6

A.1 Kinetic data tables for Chapter 2

Table A.1: $[\text{Os}(\text{phen})_3]^{2+}$ concentration dependence of k_{OBS}

Exp.No.	$[\text{Os}(\text{phen})_3]^{2+}$ concentration, mM	rate constant, s^{-1}
1	0.09	1.74
2	0.23	0.68
3	0.29	0.55
4	0.34	0.46
5	0.35	0.45

$[\text{Os}(\text{III})]_0 = 0.01 \text{ mM}$, $[\text{CSA}]_{\text{TOT}} = 20 \text{ mM}$, $T = (25.0 \pm 0.1) \text{ }^\circ\text{C}$
pH = 5 (10 mM acetate buffer, $\mu = 0.1 \text{ M}$ (NaCl))

Table A.2: pH dependence of k_{OBS}

Exp.No.	pH	rate constant, s^{-1}
1	1.13	0.015
2	1.30	0.024
3	1.49	0.030
4	1.88	0.054
5	2.19	0.095
6	2.43	0.146
7	2.97	0.207
8	3.04	0.215
9	3.78	0.250
10	4.35	0.251
11	4.55	0.250
12	5.10	0.261
13	5.70	0.262

$[\text{Os(III)}]_0 = 0.01 \text{ mM}$, $[\text{Os(II)}]_0 = 0.1 \text{ mM}$, $[\text{CSA}]_{\text{TOT}} = 3.75 \text{ mM}$, $T = (25.0 \pm 0.1) \text{ }^\circ\text{C}$

$\mu = 0.1 \text{ M (NaCl)}$, For pH 1-3, dilute HCl was used to adjust the pH.

For experiments done above pH 3, 10 mM acetate buffers were used.

Table A.3: The table of $[\text{CSA}]_{\text{TOT}}$, and corresponding k_{OBS}

Exp.No.	$[\text{CSA}]_{\text{TOT}}$, mM	rate constant, s^{-1}
1	1.00	0.076
2	3.75	0.260
3	6.00	0.460
4	10.0	0.720
5	14.0	0.985
6	17.0	1.256
7	20.0	1.514
8	25.0	1.863

$[\text{Os(III)}]_0 = 0.01 \text{ mM}$, $[\text{Os(II)}]_0 = 0.1 \text{ mM}$, $T = (25.0 \pm 0.1) \text{ }^\circ\text{C}$
 $\mu = 0.1 \text{ M (NaCl)}$, $\text{pH} = 4.4\text{-}4.6$ (10 mM acetate buffer).

Table A.4: Effect of slit width of the spectrophotometer on k_{OBS}

Exp.No.	slit width, mm	rate constant, s^{-1}
1	1.0	0.44
2	1.5	0.45
3	2.0	0.46
4	3.0	0.47

$[\text{Os(III)}]_0 = 0.01 \text{ mM}$, $[\text{Os(II)}]_0 = 0.1 \text{ mM}$, $[\text{CSA}]_{\text{TOT}} = 6 \text{ mM}$, $T = (25.0 \pm 0.1) \text{ }^\circ\text{C}$
 $\mu = 0.1 \text{ M (NaCl)}$, $\text{pH} = 5$ (10 mM acetate buffer).

Table A.5: k_{OBS} dependence on [PBN]

Exp.No.	[PBN],mM	rate constant, s ⁻¹
1	0.1	2.01
2	0.2	2.10
3	0.5	2.37
4	1.0	3.56
5	2.0	3.89
6	5.0	4.58
7	10.0	5.95

[Os(III)]₀ = 0.01 mM, [CSA]_{TOT} = 4 mM, T = (25.0 ± 0.1) °C
 μ = 0.1 M (NaCl), pH = 4.5 (10 mM acetate buffer).

Table A.6: k_{OBS} dependence on [allyl alcohol]

Exp.No.	$[\text{CH}_2\text{CHCH}_2\text{OH}]_0$, mM	k_{OBS} (de- gassed), s^{-1}	k_{OBS} (O_2 saturated), s^{-1}
1	10	0.38	2.39
2	20	0.50	2.32
3	50	0.43	2.33

$[\text{Os(III)}]_0 = 0.01 \text{ mM}$, $[\text{Os(II)}]_0 = 0.1 \text{ mM}$, $[\text{CSA}]_{\text{TOT}} = 4 \text{ mM}$
 $\mu = 0.1 \text{ M}$ (NaCl), pH = 4.5 (10 mM acetate buffer)
 $T = (25.0 \pm 0.1) \text{ }^\circ\text{C}$.

A.2 Kinetic data tables for Chapter 3

Table A.7: Effect of Ni(II) concentration of reaction rate

Exp.No.	[Ni(tacn) ₂] ²⁺ concentration, mM	rate constant × 10 ⁻² , s ⁻¹
1	0.0	3.10
2	0.2	2.35
3	0.4	1.73
4	0.6	1.57
5	0.8	1.36
6	1.0	1.13
7	1.2	1.05

[Ni(III)]₀ = 0.05 mM, [CSA]_{TOT} = 1 mM, T = (25.0 ± 0.1) °C ,
μ = 0.1 M (NaCl)

Table A.8: The table of $[\text{CSA}]_{\text{TOT}}$, and corresponding k_{OBS}

Exp.No.	$[\text{CSA}]_{\text{TOT}}$,mM	rate constant, s ⁻¹
1	1.0	0.025
2	2.6	0.076
3	4.0	0.140
4	6.5	0.203
5	8.0	0.240
6	12.0	0.375
7	16.0	0.517
8	19.5	0.609
9	25.0	0.825

$[\text{Ni(III)}]_0 = 0.05 \text{ mM}$, pH = 4.4 – 4.6 (10 mM acetate buffer),
 $\mu = 0.1 \text{ M}$ (NaCl), T = 25 °C

Table A.9: pH dependence on rate of the reaction between CSA and Ni(III)

Exp. No	pH	$k_{\text{OBS}}, \times 10^{-2} \text{ s}^{-1}$
1	1.05	0.30
2	1.29	0.47
3	1.39	0.55
4	1.50	0.66
5	1.83	1.03
6	2.02	1.15
7	2.53	1.78
8	3.09	2.04
9	3.55	2.14
10	4.01	2.45
11	4.53	2.45
12	5.08	2.48
13	5.51	2.44

[CSA]_{TOT} = 1 mM, [Ni(III)]₀ = 0.05 mM, μ = 0.1 M (NaCl), T = 25 °C,
 Reaction media = dilute HCl (pH 1-3), 10 mM acetate buffers (above pH 3)

Table A.10: Effect of the presence of O₂ and air on rate constant at different pH

Exp.No.	pH	Air saturated $k_{\text{OBS}}, \text{s}^{-1}$	O ₂ saturated, $k_{\text{OBS}}, \text{s}^{-1}$
1	1.12	0.25	0.21
2	1.46	0.51	0.38
3	1.93	0.91	0.72
4	2.11	1.05	0.78
5	3.05	2.00	1.53
6	3.50	2.19	1.82
7	4.32	2.57	2.24
8	5.05	2.43	1.62
9	6.01	1.10	0.98

[CSA]_{TOT} = 1 mM, [Ni(III)]₀ = 0.05 mM, μ = 0.1 M (NaCl),
T = 25 °C, Reaction media = dilute HCl (pH 1-3),
10 mM acetate buffers (above pH 3)

A.3 Kinetic data tables for Chapter 4

Table A.11: Effect of Ni(II) concentration of reaction rate

Exp.No.	[Ni(tacn) ₂] ²⁺ concentration, mM	rate constant × 10 ⁻¹ , s ⁻¹
1	0.0	2.37
2	0.2	1.23
3	0.4	0.92
4	0.6	0.76
5	0.8	0.59
6	1.0	0.50
7	1.2	0.43

[Ni(III)]₀ = 0.05 mM, [MSA]_{TOT} = 1 mM, T = (25.0 ± 0.1) °C ,
μ = 0.1 M (NaCl)

Table A.12: The table of $[\text{MSA}]_{\text{TOT}}$, and corresponding k_{OBS}

Exp.No.	$[\text{MSA}]_{\text{TOT},\text{mM}}$	rate constant, s^{-1}
1	4.0	0.57
2	8.0	1.10
3	12.0	1.62
4	16.0	2.21
5	20.0	2.70

$[\text{Ni(III)}]_0 = 0.05 \text{ mM}$, $\text{pH} = 3$ (HCl)

$\mu = 0.1 \text{ M}$ (NaCl), $T = 25 \text{ }^\circ\text{C}$

Table A.13: pH dependence on rate of the reaction between MSA and Ni(III)

Exp. No	pH	$k_{\text{OBS}}, \text{s}^{-1}$
1	0.66	0.02
2	1.15	0.06
3	1.71	0.18
4	2.01	0.27
5	2.50	0.49
6	3.07	0.65
7	3.37	0.72
8	3.71	0.77
9	4.13	0.82
10	4.5	0.82
11	4.81	0.81
12	5.2	0.83

[MSA]_{TOT} = 4 mM, [Ni(III)]₀ = 0.05 mM, μ = 0.1 M (NaCl), T = 25 °C,
 Reaction media = dilute HCl (pH 1-3), 10 mM acetate buffers (above pH 3)

Table A.14: Absorbance of the product mixture at 312 nm after each addition of Ni(III)

Addition no.	Volume of Ni(III), ml	Absorbance at 312 nm
1	0	0
2	0.05	0
3	0.1	0
4	0.15	0
5	0.2	0.01
6	0.25	0.01
7	0.3	0.14
8	0.4	0.44
9	0.5	0.75
10	0.6	0.99

[MSA]_{TOT} = 0.16 mM, [Ni(III)]₀ = 0.8 mM, μ = 0.1 M (NaCl)
T = 25 °C, pH 3

A.4 Kinetic data tables for Chapter 5

Table A.15: $[\text{Os}(\text{phen})_3]^{2+}$ concentration dependence of k_{OBS}

Exp.No.	$[\text{Os}(\text{phen})_3]^{2+}$ concentration, mM	rate constant $\times 10^5, \text{M}^{-1}$ s^{-1}
1	0.09	7.97
2	0.14	4.98
3	0.18	4.04
4	0.23	3.19
5	0.27	2.84

$[\text{Os}(\text{III})]_0 = 0.01 \text{ mM}$, $[\text{MSA}]_{\text{TOT}} = 20 \text{ mM}$, $T = (25.0 \pm 0.1) \text{ }^\circ\text{C}$

$\text{pH} = 4.5$ (10 mM acetate buffer, $\mu = 0.1 \text{ M}$ (NaCl))

Table A.16: The table of $[\text{MSA}]_{\text{TOT}}$, and corresponding k_{OBS}

Exp.No.	$[\text{MSA}]_{\text{TOT}}$, mM	rate constant, $\text{M}^{-1} \text{s}^{-1}$
1	1	1.35×10^4
2	5	6.37×10^4
3	10	9.76×10^4
4	12	1.40×10^5
5	15	1.69×10^5
6	19.5	2.25×10^5

$[\text{Os(III)}]_0 = 0.01 \text{ mM}$, $[\text{Os(II)}]_0 = 0.1 \text{ mM}$, $T = (25.0 \pm 0.1) \text{ }^\circ\text{C}$
 $\mu = 0.1 \text{ M (NaCl)}$, $\text{pH} = 4.4\text{-}4.6$ (10 mM acetate buffer).

Table A.18: pH dependence of k_{OBS}

Exp.No.	pH	rate constant, $\times 10^4 \text{ M}^{-1} \text{ s}^{-1}$
1	1.03	0.136
2	1.20	0.263
3	1.28	0.355
4	1.40	0.447
5	1.78	0.904
6	1.84	0.968
7	1.94	1.072
8	2.14	1.813
9	2.29	2.042
10	2.67	3.499
11	2.73	3.291
12	2.80	3.589
13	3.21	4.771
14	3.36	4.939
15	3.79	5.066
16	4.24	4.950
17	4.66	4.938
18	5.14	5.023
19	5.46	4.953

$[\text{Os(III)}]_0 = 0.01 \text{ mM}$, $[\text{Os(II)}]_0 = 0.1 \text{ mM}$, $[\text{MSA}]_{\text{TOT}} = 4 \text{ mM}$, $T = (25.0 \pm 0.1) \text{ }^\circ\text{C}$
 $\mu = 0.1 \text{ M (NaCl)}$, For pH 1-3 dilute HCl, for pH 1.8-3.36 10 mM chloroacetate buffers,
and above pH 3.6 10 mM acetate buffers were used to adjust the pH.

Table A.17: The table of $[\text{PBN}]_{\text{TOT}}$, and corresponding k_{OBS}

Exp.No.	$[\text{PBN}]_0$, mM	$[\text{MSA}]_{\text{TOT}}$, mM	$[\text{Os(III)}]_0$, mM	k_{OBS} , s ⁻¹
1	1.3	10	0.065	2.32
2	2.0	10	0.065	2.34
3	4.0	10	0.065	2.32
4	1.3	4.8	0.133	1.28
5	2.0	4.8	0.133	1.30
6	4.0	4.8	0.133	1.28
7	6.0	4.8	0.133	1.29
8	8.0	4.8	0.133	1.28

$[\text{Os(II)}]_0$ is not present in the medium, $T = (25.0 \pm 0.1) \text{ }^\circ\text{C}$

$\mu = 0.1 \text{ M (NaCl)}$, $\text{pH} = 4.4$ (10 mM acetate buffer).

Table A.19: pH dependence of k_{OBS} with PBN present

Exp.No.	pH	rate constant, s ⁻¹
1	0.61	0.07
2	0.85	0.11
3	1.23	0.22
4	1.48	0.32
5	1.79	0.54
6	1.96	0.80
7	2.33	1.21
8	3.09	2.08
9	3.44	2.21
10	3.67	2.31
11	3.88	2.33
12	3.92	2.33
13	4.50	2.33
14	4.91	2.34

$[\text{Os(III)}]_0 = 0.133 \text{ mM}$, $[\text{PBN}]_0 = 1.25 \text{ mM}$, $[\text{MSA}]_{\text{TOT}} = 10 \text{ mM}$, $T = (25.0 \pm 0.1) \text{ }^\circ\text{C}$

$\mu = 0.1 \text{ M (NaCl)}$, For pH 1-3, dilute HCl was used to adjust the pH.

For experiments done above pH 3, 10 mM acetate buffers were used.

Os(II) is not present in the medium at $t = 0$.

Table A.20: The table of $[\text{MSA}]_{\text{TOT}}$, and corresponding k_{OBS} with PBN present

Exp.No.	$[\text{MSA}]_{\text{TOT}}$, mM	rate constant, s^{-1}
1	10	2.30
2	14	3.21
3	18	3.97
4	22	4.78
5	26	5.79
6	30	6.46
7	34	7.60

$[\text{Os(III)}]_0 = 0.065 \text{ mM}$, $[\text{PBN}]_0 = 1.25 \text{ mM}$, $T = (25.0 \pm 0.1) \text{ }^\circ\text{C}$
 $\mu = 0.1 \text{ M}$ (NaCl), $\text{pH} = 4.4\text{-}4.6$ (10 mM acetate buffer).
 Os(II) is not present in the medium at $t = 0$.

A.5 Kinetic tables for Chapter 6

Table A.21: Corrected Values for $[\text{I}_3^-]_{\text{eq}}$ for the equilibrium reaction

$[\text{MSA}]$,mM	$[\text{I}^-]$, mM	Abs ₃₅₂	$[\text{I}_3^-]_{\text{eq}} \times 10^{-5}$, M
0.0040	0.010	0.017	0.05
0.0040	0.012	0.024	0.08
0.0040	0.014	0.034	0.12
0.0040	0.020	0.060	0.23
0.0040	0.056	0.213	0.84

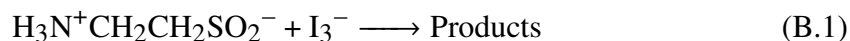
0.0040	0.060	0.233	0.92
0.0040	0.066	0.249	0.99
0.0040	0.070	0.273	1.08
0.0040	0.076	0.287	1.14
0.0040	0.080	0.304	1.21
0.0040	0.086	0.311	1.24
0.0040	0.048	0.075	0.29
0.0040	0.048	0.240	0.94
0.0040	0.048	0.340	1.34
0.0040	0.048	0.430	1.69
0.0040	0.048	0.530	2.09
0.0016	0.048	0.277	1.10
0.0024	0.048	0.235	0.93
0.0032	0.048	0.195	0.77
0.0040	0.048	0.177	0.70
0.0048	0.048	0.161	0.63
0.0016	0.066	0.353	1.40
0.0024	0.066	0.312	1.24
0.0032	0.066	0.275	1.09
0.0048	0.066	0.226	0.89

$[I_2]_0 = 0.02 \text{ mM}$, $T = (25.0 \pm 0.1) ^\circ\text{C}$, unbuffered

$\mu = 0.1 \text{ M (NaCl)}$

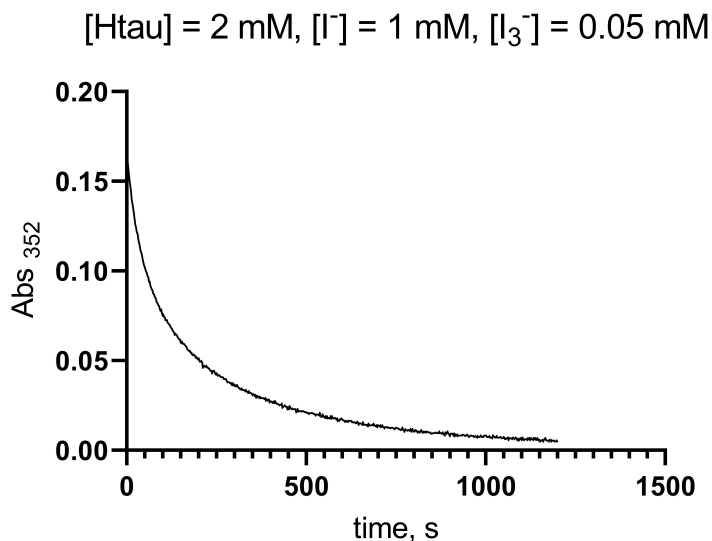
Appendix B

Preliminary results on the two-electron oxidation reaction of hypotaurine by tri-iodide



Kinetics of the reaction B.1 were monitored at 352 nm ($\epsilon_{352}(\text{I}_3^-) = 25060 \text{ M}^{-1} \text{ cm}^{-1}$ (experimentally determined)). The reaction appears to be composed of a very fast equilibrium consuming I_3^- , and then a gradual decrease of I_3^- concentration. The initial very rapid portion of the reaction could not be followed using the stopped flow instrument. However, the sudden drop in tri-iodide absorbance from its starting absorbance indicates that within the dead time of stopped flow, triiodide has reacted with hypotaurine (Htau). Unlike the kinetic trace of tri-iodide reaction with MSA discussed in Chapter 6, where a slower rise in I_3^- concentration follows a very fast equilibrium consuming I_3^- , this reaction

only shows a decrease in absorbance at 352 nm. (Figure B.1)



Expected Abs_{(t=0), 352 nm} = 0.62
Observed Abs_{(t=0), 352 nm} = 0.19

Figure B.1: Typical kinetic trace of the reaction between Htau and tri-iodide when [Htau]_{TOT} = 2 mM, [I⁻]₀ = 1 mM, [I₃⁻] = 0.05 mM; Expected Abs_{(t=0), 352 nm} = 0.62, observed Abs_{(t=0), 352 nm} = 0.19

B.1 Equilibrium between I₃⁻, Htau, HtauI, and I⁻

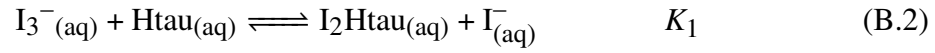
To determine the equilibrium constant of the fast reaction between Htau and I₃⁻ a series of stopped flow experiments were carried out. Here, [I₃⁻] is determined by monitoring absorbance at 352 nm at t = 0 s ($\epsilon_{352}(\text{I}_3^-) = 25,060 \text{ M}^{-1} \text{ cm}^{-1}$)

Table B.1: Concentrations of Htau, Γ , and I_2 used

Exp no.	$10^3[\text{Htau}]_{\text{TOT}}$, M	$10^3[I_2]_0$, M	$10^3[\Gamma]_0$, M	$10^5[I_3^-]_{\text{eq}}$, M
1	0.25	0.05	1.00	3.75
2	0.75	0.05	1.00	2.67
3	1.00	0.05	1.00	2.35
4	1.25	0.05	1.00	2.08
5	1.50	0.05	1.00	1.84
6	0.00	0.05	1.00	4.89
7	0.00	0.05	0.25	3.38
8	0.25	0.05	0.25	2.35
9	0.50	0.05	0.25	1.74
10	0.75	0.05	0.25	1.39
11	1.00	0.05	0.25	1.15
12	0.50	0.10	12.0	7.18
13	0.50	0.10	10.0	7.12
14	0.50	0.10	8.00	7.03
15	0.50	0.10	6.00	6.77
16	0.50	0.10	5.00	6.50
17	0.50	0.10	4.00	6.22
18	0.50	0.10	3.00	5.46

$\mu = 0.1 \text{ M (NaCl)}, T = 25 \text{ }^\circ\text{C}$

Hypothesized equilibrium I



$$K_1 = \frac{[\text{I}_2\text{Htau}][\text{I}^-]}{[\text{I}_3^-][\text{Htau}]} \quad (\text{B.3})$$

$$[\text{I}_3^-] = [\text{I}_3^-]_0 + [\text{I}_2\text{Htau}] \quad (\text{B.4})$$

Substituting (B.4) in (B.3),

$$K_1 = \frac{([\text{I}_3^-] - [\text{I}_3^-]_0)[\text{I}^-]}{[\text{I}_3^-][\text{Htau}]} \quad (\text{B.5})$$

Linearizing (B.5)

$$\frac{1}{[\text{I}_3^-]} = \frac{1}{[\text{I}_3^-]_0} + \frac{K_1[\text{Htau}]}{[\text{I}_3^-]_0[\text{I}^-]} \quad (\text{B.6})$$

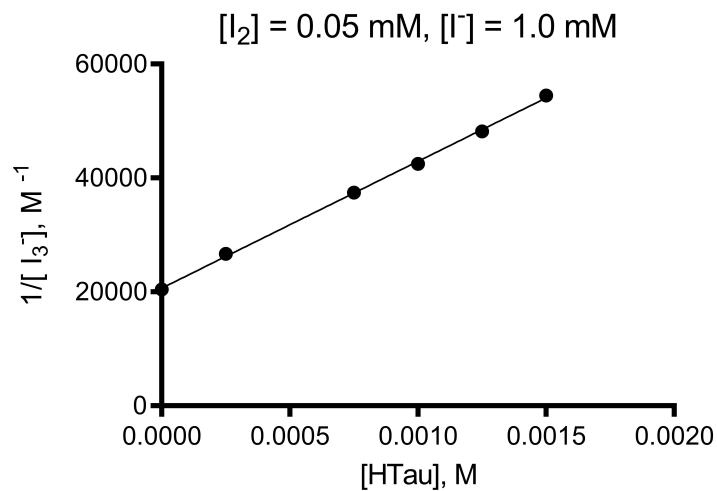


Figure B.2: Htau dependence on $[I_3^-]_{eq}$, $[I_2]_0 = 50 \mu\text{M}$, $[I^-]_0 = 1 \text{ mM}$, data fit in to equation (B.6), slope = $(2.23 \pm 0.03) \times 10^7 \text{ M}^{-2}$, Y-intercept = $(2.06 \pm 0.03) \times 10^4 \text{ M}^4$

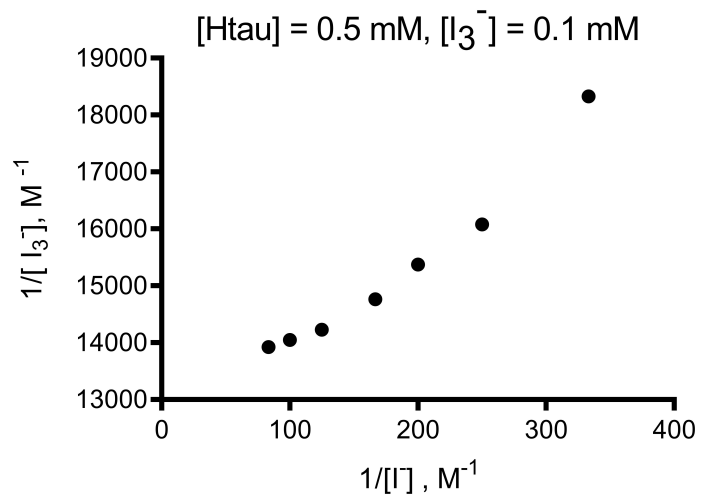
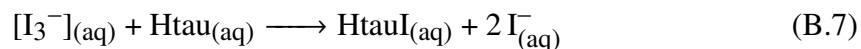


Figure B.3: Dependence of iodide concentration on equilibrium tri-iodide concentration, $[I_2]_0 = 0.1 \text{ mM}$, $[H\tau]_0 = 0.5 \text{ mM}$

Data points in Figure B.3 do not exhibit a linear behavior. Therefore, this reaction equilibrium may be ruled out.

Alternative equilibrium reaction.



$$K_2 = \frac{[\text{HtauI}][\text{I}^-]^2}{[\text{I}_3^-][\text{Htau}]} \quad (\text{B.8})$$

$$[\text{I}_3^-] = [\text{I}_3^-]_0 + [\text{HtauI}] \quad (\text{B.9})$$

Substituting (B.9) in (B.8)

$$K_2 = \frac{([\text{I}_3^-] - [\text{I}_3^-]_0)[\text{I}^-]^2}{[\text{I}_3^-][\text{Htau}]} \quad (\text{B.10})$$

Solving (B.10) for I_3^- ,

$$\frac{1}{[\text{I}_3^-]} = \frac{1}{[\text{I}_3^-]_0} + \frac{K_2[\text{Htau}]}{[\text{I}_3^-]_0[\text{I}^-]^2} \quad (\text{B.11})$$

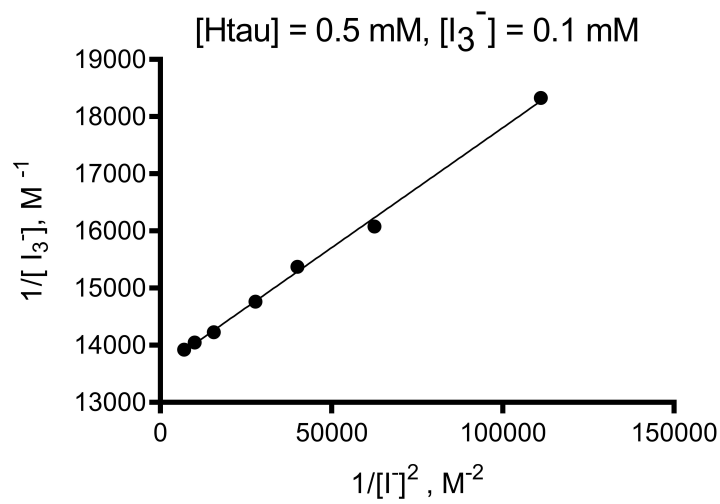


Figure B.4: $1/[I^-]^2$ dependence on $[I_3^-]_{eq}$, $[I_2]_0 = 0.1$ mM, $[HTau]_{TOT} = 0.5$ mM, Slope = $(4.20 \pm 0.09) \times 10^{-2}$ M, Y-intercept = $(1.360 \pm .005) \times 10^4$ M⁻¹

Data in figures B.2 and B.4 show a good fit to the equation B.11. A value of 3.09×10^{-3} M is calculated for K_2 , the formation constant for hypotaurine iodide, from figure B.4. Figure B.2 gives a value of 1.08×10^{-3} M for K_2 . For comparison, formation constant for methanesulfonyl iodide is 1.07 M.¹³⁶

B.2 DFT calculations

The geometry of hypotaurine iodide was optimized using Gaussian 16 software package, and visualized using GausView 6. The calculations were done in B3LYP method under 6-311G* basis set in implicit water.

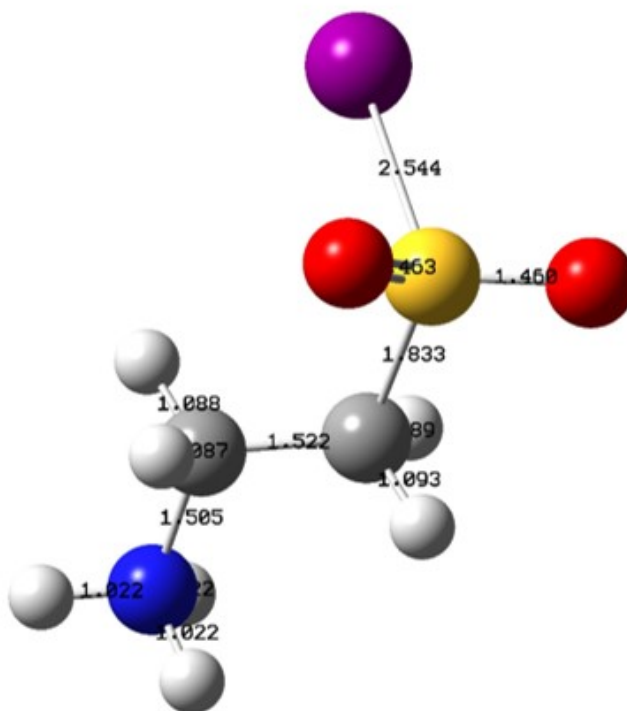


Figure B.5: Optimized geometry of hypotaurine iodide

The S-I bond for hypotaurine iodide is 2.544 Å. For methanesulfonyl iodide, the calculated bond length for S-I was 2.44 Å. The crystal structures of $(\text{CH}_3\text{SO}_2\text{I})_2 \cdot \text{RbI}_3$ and $(\text{CH}_3\text{SO}_2\text{I})_4 \cdot \text{KI}_3 \cdot 2\text{I}_2$ also displayed 2.44 Å bond lengths.¹³⁶ The longer S-I bond

length obtained for hypotaurine iodide may be caused by the steric effects due to the bulky substituent on sulfur atom compared to methanesulfonyl iodide.

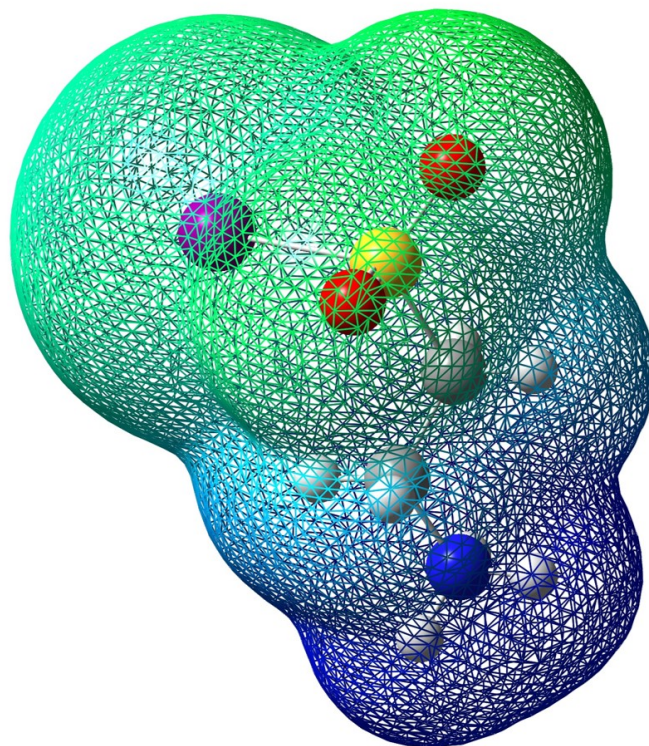


Figure B.6: Charge distribution of hypotaurine iodide; red correlates to the highest negative charge and blue correlates to the highest positive charge

Appendix C

Crystallographic figures and tables

This section is based on the Supporting Information of the following paper and reprints were made with permission from American Chemical Society. Crystallographic data in this chapter were analyzed by Dr. John D. Gorden.

Rajakaruna, P.; Gorden, J. D.; Stanbury, D. M. Methanesulfonyl Iodide. *Inorg. Chem.* **2019**, 58 (21), 14752–14759.

C.1 Crystallographic data for $(\text{CH}_3\text{SO}_2\text{I})_2\cdot\text{RbI}_3$

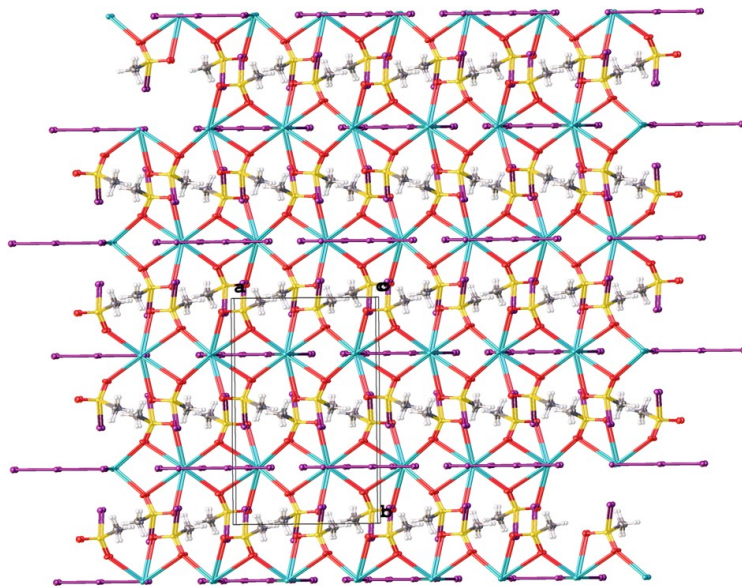


Figure C.1: Molecular packing diagram of $(\text{CH}_3\text{SO}_2\text{I})_2\cdot\text{RbI}_3$ viewed along the ab plane

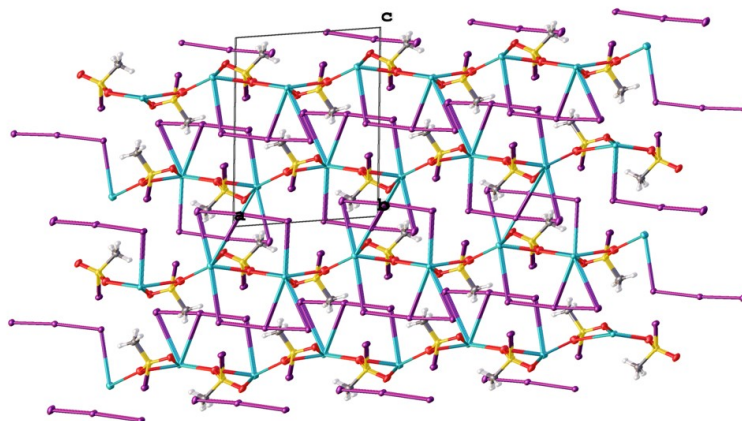


Figure C.2: Molecular packing diagram of $(\text{CH}_3\text{SO}_2\text{I})_2\cdot\text{RbI}_3$ viewed along the ac plane showing two different coordination modes of I_3^- with Rb.

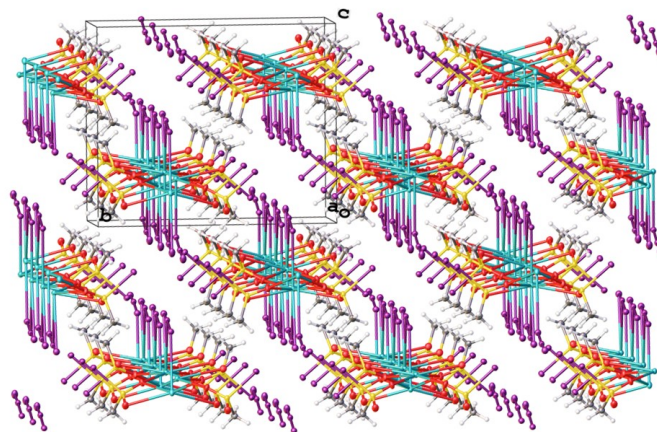


Figure C.3: Molecular packing diagram of $(\text{CH}_3\text{SO}_2\text{I})_2 \cdot \text{RbI}_3$ viewed along the bc plane showing two different coordination modes of I_3^- with Rb.

C.1.1 Sample and crystal data for $(\text{CH}_3\text{SO}_2\text{I})_2 \cdot \text{RbI}_3$

Identification code	DS090518b
Chemical formula	$\text{C}_2\text{H}_6\text{I}_5\text{O}_4\text{RbS}_2$
Formula weight	878.16 g/mol
Temperature	100(2) K
Crystal size	0.095 x 0.110 x 0.215 mm
Crystal habit	clear dark brown block
Crystal system	monoclinic
Space group	P21/m
Unit cell dimensions	$a = 9.4977(5) \text{ \AA}$, $\alpha = 90^\circ$ $b = 14.7549(8) \text{ \AA}$, $\beta = 94.818(2)^\circ$ $c = 12.3947(7) \text{ \AA}$, $\gamma = 90^\circ$
Volume	$1730.83(16) \text{ \AA}^3$
Z	4
Density (calculated)	3.370 g/cm^3
Absorption coefficient	12.011 mm^{-1}
F(000)	1536
Diffractometer	Bruker D8 VENTURE α -geometry diffractometer
Radiation source	Incoatec I μ S 3.0 microfocus sealed tube (Mo K α , $\lambda = 0.71073 \text{ \AA}$)
Theta range for data collection	2.15 to 36.39°
Reflections collected	8638
Independent reflections	8638 [R(int) = 0.0241]

Absorption correction	Multi-Scan
Max. and min. transmission	0.3950 and 0.1820
Structure solution technique	direct methods
Structure solution program	SHELXT 2014/5 (Sheldrick, 2014)
Refinement method	Full-matrix least-squares on F^2
Refinement program	SHELXL-2017/1 (Sheldrick, 2017)
Function minimized	$\Sigma w(F_o^2 - F_c^2)^2$
Data / restraints / parameters	8638 / 0 / 142
Goodness-of-fit on F^2	1.210
Final R indices	8536 data; $I > 2\sigma(I)$, $R1 = 0.0241$, $wR2 = 0.0681$ all data, $R1 = 0.0245$, $wR2 = 0.0682$
Largest diff. peak and hole	1.365 and -1.881 $e\text{\AA}^{-3}$
R.M.S. deviation from mean	0.213 $e\text{\AA}^{-3}$

C.1.2 Atomic coordinates and equivalent isotropic atomic displacement parameters (\AA^2) for $(\text{CH}_3\text{SO}_2\text{I})_2 \cdot \text{RbI}_3$

$U(\text{eq})$ is defined as one third of the trace of the orthogonalized U_{ij} tensor.

	x/a	y/b	z/c	U(eq)
I1	9269.7(2)	5679.5(2)	6761.9(2)	16.78(4)
I2	3972.6(2)	5727.8(2)	8217.1(2)	15.97(4)
I3	15301.2(3)	7500	5740.9(2)	17.87(5)
I4	12305.2(3)	7500	5507.4(2)	15.22(4)
I5	9097.6(3)	7500	5036.6(2)	16.09(4)
I6	3750.7(2)	7500	9925.6(2)	15.10(4)
I7	447.1(3)	7500	9377.7(2)	15.33(4)
I8	-2486.3(3)	7500	9037.5(3)	22.36(5)
Rb1	6379.8(4)	2500	7149.9(3)	13.72(6)
Rb2	1545.2(4)	2500	7991.6(3)	17.06(6)
S1	9330.3(7)	4448.8(4)	8084.4(5)	13.97(10)
S2	4249.8(7)	4502.7(4)	6925.2(5)	13.85(9)
O1	10730(2)	4407.1(15)	8635(2)	20.7(4)
O2	8809(2)	3626.8(14)	7556.1(18)	19.6(4)
O3	5722(2)	4462.9(15)	6707.8(18)	18.7(3)
O4	3659(3)	3673.8(14)	7317(2)	21.5(4)
C1	8119(3)	4808(2)	9002(2)	19.3(4)
C2	3239(3)	4847(2)	5739(2)	21.2(5)

C.1.3 Bond lengths (Å) for (CH₃SO₂I)₂·RbI₃

I1 S1	2.4437(7)	Rb1 S2	3.5787(7)
I2 S2	2.4438(7)	Rb1 S2 ⁵	3.5787(7)
I3 I4	2.8359(4)	Rb1 Rb2	4.7935(5)
I3 Rb1 ¹	3.7982(5)	Rb2 O4 ⁵	2.830(2)
I4 I5	3.0534(4)	Rb2 O4	2.830(2)
I4 Rb1 ¹	3.6193(5)	Rb2 O1 ⁶	3.043(2)
I5 Rb2 ²	3.7518(5)	Rb2 O1 ⁷	3.043(2)
I6 I7	3.1541(4)	Rb2 O2 ⁷	3.094(2)
I6 Rb1 ³	3.6373(5)	Rb2 O2 ⁶	3.094(2)
I7 I8	2.7825(4)	Rb2 S1 ⁷	3.5703(7)
I7 Rb2 ⁴	3.9049(5)	Rb2 S1 ⁶	3.5703(7)
I8 Rb2 ⁴	3.7155(6)	S1 O1	1.444(2)
Rb1 O2	2.854(2)	S1 O2	1.446(2)
Rb1 O2 ⁵	2.854(2)	S1 C1	1.765(3)
Rb1 O3	3.003(2)	S2 O4	1.447(2)
Rb1 O3 ⁵	3.004(2)	S2 O3	1.447(2)
Rb1 O4	3.132(2)	S2 C2	1.762(3)
Rb1 O4 ⁵	3.132(2)		

¹2-X,1-Y,1-Z; ²1-X,1-Y,1-Z; ³1-X,1-Y,2-Z; ⁴-X,1-Y,2-Z; ⁵+X,1/2-Y,+Z; ⁶-1+X,+Y,+Z;

⁷-1+X,1/2-Y,+Z

C.1.4 Bond angles (°) for (CH₃SO₂I)₂·RbI₃

I3I4Rb1 ¹	70.906(9)	O4Rb2O2 ⁶	103.05(6)
I5I4Rb1 ¹	103.951(10)	O1 ⁶ Rb2O2 ⁶	47.18(5)
I4I5Rb2 ²	105.494(10)	O1 ⁷ Rb2O2 ⁶	108.31(6)
I7I6Rb1 ³	95.625(9)	O2 ⁷ Rb2 O2 ⁶	65.01(8)
I8I7I6	176.297(12)	O4 ⁵ Rb2S1 ⁷	87.20(5)
I8I7Rb2 ⁴	64.995(11)	O4Rb2S1 ⁷	159.52(5)
I6I7Rb2 ⁴	111.302(10)	O1 ⁶ Rb2 S1 ⁷	124.95(5)
I7I8 Rb2 ⁴	72.263(10)	O1 ⁷ Rb2 S1 ⁷	23.53(4)
O2Rb1O2 ⁵	71.26(9)	O2 ⁷ Rb2 S1 ⁷	23.70(4)
O2Rb1O3	67.86(6)	O2 ⁶ Rb2S1 ⁷	87.13(4)
O2 ⁵ Rb1O3	138.29(6)	O4 ⁵ Rb2S1 ⁶	159.52(5)
O2Rb1O3 ⁵	138.29(6)	O4Rb2S1 ⁶	87.20(5)
O2 ⁵ Rb1O3 ⁵	67.86(6)	O1 ⁶ Rb2S1 ⁶	23.53(4)
O3Rb1O3 ⁵	149.28(9)	O1 ⁷ Rb2 S1 ⁶	124.95(5)
O2Rb1O4	108.99(6)	O2 ⁷ Rb2S1 ⁶	87.13(4)
O2 ⁵ Rb1O4	165.85(6)	O2 ⁶ Rb2S1 ⁶	23.70(4)
O3Rb1O4	47.06(5)	S1 ⁷ Rb2S1 ⁶	107.29(2)
O3 ⁵ Rb1O4	112.66(6)	O4 ⁵ Rb2I8 ⁴	100.08(5)
O2Rb1O4 ⁵	165.85(6)	O4Rb2I8 ⁴	100.08(5)
O2 ⁵ Rb1O4 ⁵	108.99(6)	O1 ⁶ Rb2I8 ⁴	77.61(4)
O3Rb1O4 ⁵	112.66(6)	O1 ⁷ Rb2I8 ⁴	77.61(4)

O3 ⁵ Rb1O4 ⁵	47.06(5)	O2 ⁷ Rb2I8 ⁴	107.55(4)
O4Rb1O4 ⁵	67.14(8)	O2 ⁶ Rb2 I8 ⁴	107.55(4)
O2Rb1S2	88.63(5)	S1 ⁷ Rb2I8 ⁴	93.524(13)
O2 ⁵ Rb1S2	159.72(5)	S1 ⁶ Rb2I8 ⁴	93.523(13)
O3Rb1S2	23.37(4)	O4 ⁵ Rb2I5 ²	76.37(5)
O3 ⁵ Rb1S2	132.41(4)	O4Rb2I5 ²	76.37(5)
O4Rb1S2	23.72(4)	O1 ⁶ Rb2I5 ²	103.81(5)
O4 ⁵ Rb1S2	89.86(4)	O1 ⁷ Rb2I5 ²	103.81(5)
O2Rb1S2 ⁵	159.72(5)	O2 ⁷ Rb2I5 ²	76.22(4)
O2 ⁵ Rb1S2 ⁵	88.63(5)	O2 ⁶ Rb2I5 ²	76.22(4)
O3 Rb1S2 ⁵	132.41(4)	S1 ⁷ Rb2I5 ²	89.162(13)
O3 ⁵ Rb1S2 ⁵	23.37(4)	S1 ⁶ Rb2I5 ²	89.162(13)
O4 Rb1S2 ⁵	89.86(4)	I8 ⁴ Rb2I5 ²	175.462(13)
O4 ⁵ Rb1S2 ⁵	23.72(4)	O4 ⁵ Rb2I7 ⁴	130.70(5)
S2Rb1S2 ⁵	111.32(2)	O4Rb2I7 ⁴	130.70(5)
O2Rb1I4 ¹	79.91(5)	O1 ⁶ Rb2 I7 ⁴	68.24(5)
O2 ⁵ Rb1I4 ¹	79.91(5)	O1 ⁷ Rb2I7 ⁴	68.24(5)
O3Rb1I4 ¹	85.20(4)	O2 ⁷ Rb2 I7 ⁴	71.75(4)
O3 ⁵ Rb1I4 ¹	85.20(4)	O2 ⁶ Rb2I7 ⁴	71.75(4)
O4Rb1I4 ¹	114.21(5)	S1 ⁷ Rb2 I7 ⁴	69.205(12)
O4 ⁵ Rb1I4 ¹	114.21(5)	S1 ⁶ Rb2I7 ⁴	69.205(12)
S2Rb1I4 ¹	99.509(13)	I8 ⁴ Rb2I7 ⁴	42.743(8)

S2 ⁵ Rb1I4 ¹	99.509(13)	I5 ² Rb2I7 ⁴	141.795(12)
O2Rb1I6 ³	85.35(5)	O4 ⁵ Rb2 Rb1	38.70(5)
O2 ⁵ Rb1I6 ³	85.35(5)	O4 Rb2Rb1	38.70(5)
O3Rb1I6 ³	99.08(4)	O1 ⁶ Rb2 Rb1	109.06(4)
O3 ⁵ Rb1I6 ³	99.08(4)	O1 ⁷ Rb2Rb1	109.06(4)
O4Rb1I6 ³	80.60(5)	O2 ⁷ Rb2 Rb1	140.16(4)
O4 ⁵ Rb1I6 ³	80.60(5)	O2 ⁶ Rb2Rb1	140.16(4)
S2Rb1I6 ³	90.642(13)	S1 ⁷ Rb2 Rb1	125.787(11)
S2 ⁵ Rb1I6 ³	90.641(12)	S1 ⁶ Rb2Rb1	125.787(11)
I4 ¹ Rb1I6 ³	161.833(12)	I8 ⁴ Rb2Rb1	93.474(10)
O2Rb1I3 ¹	115.84(5)	I5 ² Rb2 Rb1	81.988(9)
O2 ⁵ Rb1I3 ¹	115.84(5)	I7 ⁴ Rb2Rb1	136.217(12)
O3Rb1I3 ¹	76.31(4)	O1S1O2	116.43(13)
O3 ⁵ Rb1I3 ¹	76.31(4)	O1S1C1	109.39(15)
O4 Rb1I3 ¹	77.22(5)	O2S1C1	109.06(14)
O4 ⁵ Rb1I3 ¹	77.22(5)	O1S1 I1	108.52(10)
S2Rb1I3 ¹	74.723(12)	O2S1 I1	109.37(10)
S2 ⁵ Rb1I3 ¹	74.724(12)	C1S1 I1	103.25(10)
I4 ¹ Rb1I3 ¹	44.875(8)	O1 S1 Rb2 ⁸	57.27(9)
I6 ³ Rb1I3 ¹	153.293(12)	O2S1Rb2 ⁸	59.34(9)
O2Rb1Rb2	137.44(4)	C1 S1Rb2 ⁸	132.84(10)

O2 ⁵ Rb1Rb2	137.44(4)	I1S1Rb2 ⁸	123.89(2)
O3Rb1Rb2	81.45(4)	O4S2O3	115.88(14)
O3 ⁵ Rb1Rb2	81.45(4)	O4S2C2	108.94(15)
O4Rb1 Rb2	34.40(4)	O3S2C2	108.89(15)
O4 ⁵ Rb1Rb2	34.40(4)	O4S2I2	109.81(10)
S2Rb1Rb2	58.087(11)	O3S2I2	108.12(9)
S2 ⁵ Rb1Rb2	58.088(11)	C2 S2 I2	104.60(10)
I4 ¹ Rb1Rb2	127.458(11)	O4S2Rb1	60.57(10)
I6 ³ Rb1Rb2	70.710(9)	O3S2Rb1	55.41(9)
I3 ¹ Rb1Rb2	82.583(9)	C2S2Rb1	124.62(10)
O4 ⁵ Rb2 O4	75.47(9)	I2S2Rb1	130.62(2)
O4 ⁵ Rb2 O16	147.76(7)	S1O1Rb2 ⁸	99.20(11)
O4Rb2O1 ⁶	73.37(7)	S1O2Rb1	144.05(13)
O4 ⁵ Rb2O1 ⁷	73.37(7)	S1O2Rb2 ⁸	96.96(10)
O4Rb2O1 ⁷	147.76(7)	Rb1O2Rb2 ⁸	111.87(7)
O1 ⁶ Rb2 O1 ⁷	135.29(9)	S2O3Rb1	101.22(11)
O4 ⁵ Rb2O2 ⁷	103.05(6)	S2O4Rb2	157.14(14)
O4Rb2O2 ⁷	152.07(7)	S2O4Rb1	95.71(11)
O1 ⁶ Rb2O2 ⁷	108.31(6)	Rb2O4Rb1	106.91(7)

¹2-X,1-Y,1-Z; ²1-X,1-Y,1-Z; ³1-X,1-Y,2-Z; ⁴-X,1-Y,2-Z; ⁵+X,1/2-Y,+Z; ⁶-1+X,+Y,+Z; ⁷-1+X,1/2-Y,+Z; ⁸1+X,+Y,+Z

C.1.5 Torsion angles (°) for (CH₃SO₂I)₂·RbI₃

O2 S1 O1 Rb2 ¹	4.93(16)	O4 S2 O3 Rb1	3.62(16)
C1 S1 O1 Rb2 ¹	129.10(12)	C2 S2 O3 Rb1	-119.56(12)
I1 S1 O1 Rb2 ¹	-118.93(6)	I2 S2 O3 Rb1	127.34(5)
O1 S1 O2 Rb1	139.0(2)	O3 S2 O4 Rb2	-175.1(3)
C1 S1 O2 Rb1	14.7(3)	C2 S2 O4 Rb2	-51.9(4)
I1 S1 O2 Rb1	-97.6(2)	I2 S2 O4 Rb2	62.1(4)
Rb2 ¹ S1 O2 Rb1	143.8(3)	Rb1 S2 O4 Rb2	-171.7(4)
O1 S1 O2 Rb2 ¹	-4.82(16)	O3 S2 O4 Rb1	-3.42(15)
C1 S1 O2 Rb2 ¹	-129.16(11)	C2 S2 O4 Rb1	119.74(12)
I1 S1 O2 Rb2 ¹	118.60(5)	I2 S2 O4 Rb1	-126.25(5)

¹1+X,+Y,+Z

C.1.6 Anisotropic atomic displacement parameters (Å²) for the crystals of (CH₃SO₂I)₂·RbI₃

The anisotropic atomic displacement factor exponent takes the form: $-2^2[h^2a^{*2}U_{11} + \dots + 2hka^*b^*U_{12}]$

Atom	U11	U22	U33	U12	U13	U23
I1	17.74(7)	17.18(7)	15.19(7)	-1.83(5)	0.10(5)	1.25(5)
I2	15.70(7)	15.55(6)	16.84(7)	-0.88(5)	2.39(5)	-1.75(5)
I3	14.18(9)	19.15(10)	20.17(10)	0	0.81(8)	0
I4	16.19(9)	13.84(8)	15.94(9)	0	3.16(7)	0
I5	13.63(9)	18.06(9)	16.46(9)	0	0.58(7)	0
I6	14.78(9)	16.29(9)	14.33(9)	0	1.76(7)	0
I7	16.51(9)	13.33(8)	15.87(9)	0	-0.28(7)	0
I8	15.71(10)	17.69(10)	32.44(13)	0	-5.24(9)	0
Rb1	14.03(13)	12.45(12)	14.47(13)	0	-0.01(10)	0
Rb2	16.56(14)	13.55(13)	21.90(15)	0	6.48(12)	0
S1	12.6(2)	12.5(2)	16.5(2)	-0.64(18)	-0.66(18)	-0.56(18)
S2	12.6(2)	12.0(2)	16.8(2)	-0.39(18)	1.12(18)	-0.03(18)
O1	16.1(8)	19.8(8)	25.0(10)	1.1(7)	-5.6(7)	0.5(7)
O2	19.9(8)	12.9(7)	25.7(10)	-2.4(7)	0.0(7)	-5.3(7)
O3	12.9(7)	20.8(8)	22.8(9)	0.6(7)	4.0(7)	-1.5(7)
O4	24.0(9)	14.0(8)	27.4(10)	-3.7(7)	7.2(8)	1.6(7)
C1	20.8(11)	18.9(10)	18.5(10)	2.7(9)	3.7(9)	0.0(9)
C2	22.4(12)	20.1(11)	20.0(11)	4.6(9)	-4.1(9)	-3.2(9)

C.1.7 Hydrogen atomic coordinates and isotropic atomic displacement parameters (\AA^2) for $(\text{CH}_3\text{SO}_2\text{I})_2\cdot\text{RbI}_3$

Atom	x	y	z	U(eq)
H1A	8014.84	4332.15	9541.17	29
H1B	7200.7	4927.79	8606.83	29
H1C	8469.97	5362.61	9366.65	29
H2A	3610.57	5420.66	5482.77	32
H2B	2252.49	4930	5895.93	32
H2C	3290.11	4382.68	5178.61	32

C.2 Crystallographic data for $(\text{CH}_3\text{SO}_2\text{I})_4\cdot\text{KI}_3\cdot 2\text{I}_2$

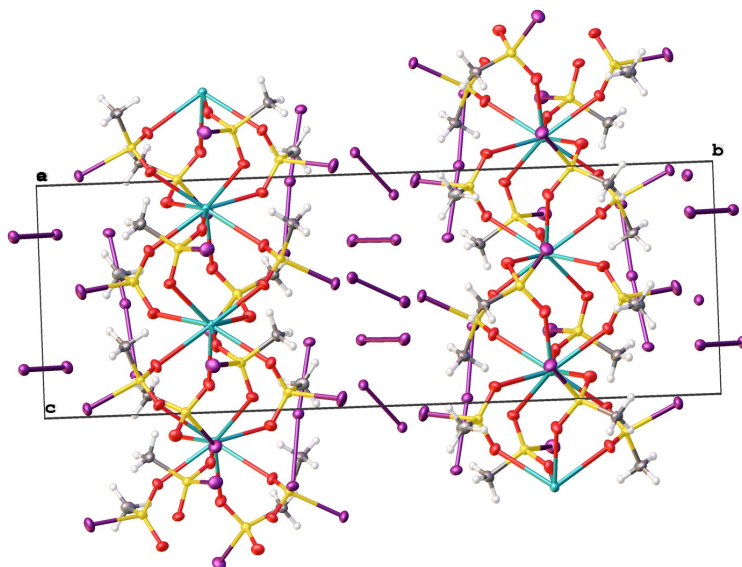


Figure C.4: Molecular packing of $(\text{CH}_3\text{SO}_2\text{I})_4\cdot\text{KI}_3\cdot 2\text{I}_2$ showing the infinite chain of $[(\text{CH}_3\text{SO}_2\text{I})_4\cdot\text{K}]$ extending along the c -axis

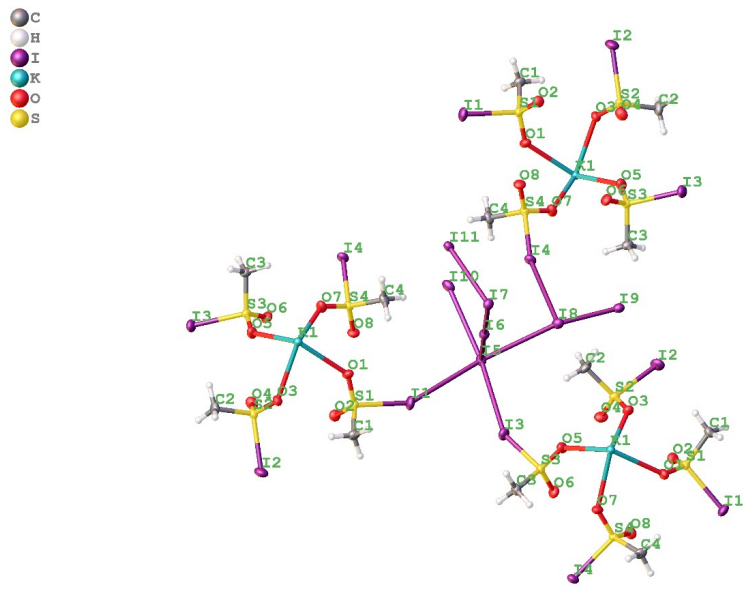


Figure C.5: Portion of the unit cell of $(\text{CH}_3\text{SO}_2\text{I})_4 \cdot \text{KI}_3 \cdot 2\text{I}_2$ showing some of the close I-I contacts between the $\text{CH}_3\text{SO}_2\text{I}$ and the polyiodide components

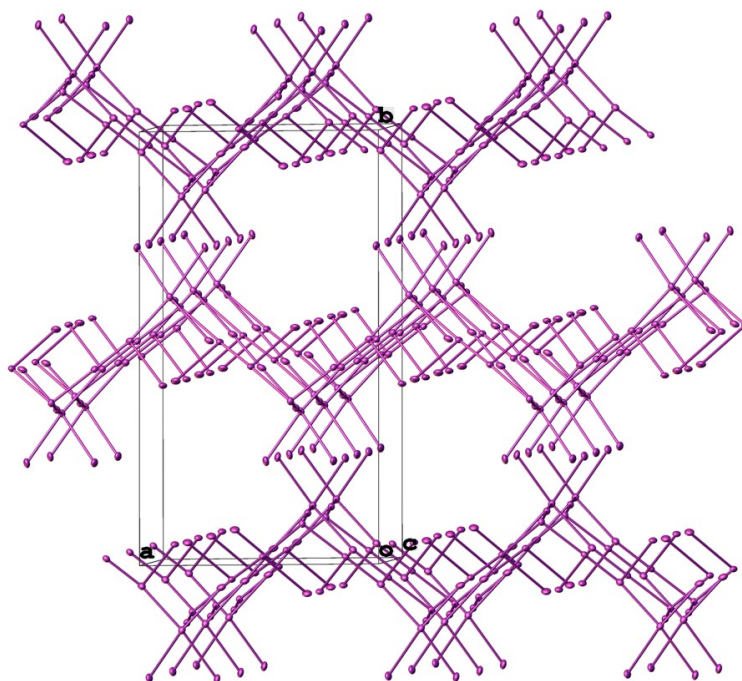


Figure C.6: Molecular packing diagram of $(\text{CH}_3\text{SO}_2\text{I})_4 \cdot \text{KI}_3 \cdot 2\text{I}_2$ viewed along the *ab* plane showing all iodine-iodine contacts less than 4.0 Å. (CH_3SO_2) and K removed for clarity

C.2.1 Sample and crystal data for CH₃SO₂I₄•KI₃•2I₂

Identification code	Stanbury072418
Chemical formula	C ₄ H ₁₂ I ₁₁ KO ₈ S ₄
Formula weight	1751.38 g/mol
Temperature	100(2) K
Crystal size	0.010 x 0.011 x 0.234 mm
Crystal habit	dark brown-green needle
Crystal system	monoclinic
Space group	P2 ₁ /c
Unit cell dimensions	$a = 14.6211(6) \text{ \AA}$, $\alpha = 90^\circ$ $b = 26.1593(9) \text{ \AA}$, $\beta = 108.9673(11)^\circ$ $c = 9.5131(3) \text{ \AA}$, $\gamma = 90^\circ$
Volume	3441.0(2) \AA^3
Z	4
Density (calculated)	3.381 g/cm ³
Absorption coefficient	10.290 mm ⁻¹
F(000)	3064
Diffractometer	Bruker D8 VENTURE κ -geometry diffractometer
Radiation source	Incoatec I μ S 3.0 microfocus sealed tube (Mo K α , $\lambda = 0.71073 \text{ \AA}$)

Theta range for data collection	2.26 to 34.35°
Index ranges	-22<=h<=23, -41<=k<=41, -13<=l<=15
Reflections collected	198851
Independent reflections	14349 [R(int) = 0.0673]
Absorption correction	Multi-Scan
Max. and min. transmission	0.9040 and 0.1970
Structure solution technique	direct methods
Structure solution program	SHELXT 2014/5 (Sheldrick, 2014)
Refinement method	Full-matrix least-squares on F ²
Refinement program	SHELXL-2017/1 (Sheldrick, 2017)
Function minimized	$\Sigma w(F_o^2 - F_c^2)^2$
Data / restraints / parameters	14349 / 0 / 258
Goodness-of-fit on F ²	1.088
Final R indices	12473 data; I>2σ(I), R1 = 0.0333, wR2 = 0.0669 all data, R1 = 0.0458, wR2 = 0.0728
Largest diff. peak and hole	2.428 and -1.947 eÅ ⁻³
R.M.S. deviation from mean	0.275 eÅ ⁻³

C.2.2 Atomic coordinates and equivalent isotropic atomic displacement parameters (\AA^2) for $(\text{CH}_3\text{SO}_2\text{I})_4 \cdot \text{KI}_3 \cdot 2\text{I}_2$

U(eq) is defined as one third of the trace of the orthogonalized U_{ij} tensor.

	x/a	y/b	z/c	U(eq)
I5	7409.6(3)	8625.0(2)	1695.4(4)	21.72(6)
I6	7506.7(3)	8749.2(2)	4787.4(4)	20.88(6)
I7	7583.2(3)	8949.2(2)	7858.1(4)	20.21(6)
I1	5973.2(3)	7488.2(2)	1980.6(5)	27.80(8)
I2	2538.5(3)	5602.6(2)	369.0(5)	30.87(8)
I3	-1040.8(3)	7495.6(2)	-1471.7(5)	27.27(8)
I4	2494.2(3)	9364.9(2)	323.8(4)	22.71(6)
K1	2473.1(8)	7493.8(4)	3730.7(10)	15.18(14)
S1	4499.1(9)	7073.0(5)	2072.0(13)	15.3(2)
S2	1744.0(9)	6393.3(5)	715.8(13)	16.6(2)
S3	449.4(9)	7912.2(5)	39.5(13)	15.9(2)
S4	3261.6(9)	8572.6(5)	1472.3(13)	15.8(2)
O1	4074(3)	7423.5(15)	2845(5)	21.4(7)
O2	3949(3)	6921.7(16)	583(4)	21.9(8)
O3	2378(3)	6632.8(14)	2022(4)	20.3(7)
O4	1471(3)	6667.9(16)	-666(4)	25.4(8)
O5	911(3)	7554.6(16)	1199(5)	24.5(9)
O6	956(3)	8076.3(16)	-941(4)	22.5(8)
O7	2589(3)	8327.1(14)	2071(4)	23.3(7)
O8	3572(3)	8303.0(16)	391(4)	22.2(8)

C1	4892(4)	6521(2)	3171(6)	21.5(10)
C2	688(4)	6185(3)	1056(7)	25.8(12)
C3	78(4)	8451(2)	816(6)	21.0(10)
C4	4287(4)	8773(2)	2956(6)	23.1(10)
I8	9136.5(3)	9640.7(2)	2164.3(4)	23.31(7)
I9	10611.4(3)	10279.6(2)	2120.3(4)	20.36(7)
I11	5744.0(3)	9724.7(2)	5934.3(4)	20.36(7)
I10	5654.6(3)	9619.2(2)	557.3(5)	26.95(8)

C.2.3 Bond lengths (Å) for (CH₃SO₂I)₄•KI₃•2I₂

I5I6	2.9166(5)	K1K1 ²	4.75665(15)
I6I7	2.9337(5)	S1O1	1.437(4)
I1S1	2.4402(13)	S1O2	1.439(4)
I2S2	2.4465(14)	S1C1	1.766(5)
I3S3	2.4425(13)	S2O3	1.431(4)
I4S4	2.4396(13)	S2O4	1.436(4)
K1O7	2.729(4)	S2C2	1.763(6)
K1O5	2.733(4)	S3O6	1.433(4)
K1O1	2.739(4)	S3O5	1.436(4)
K1O3	2.755(4)	S3C3	1.757(5)
K1O2 ¹	2.761(4)	S4O8	1.437(4)
K1O6 ¹	2.773(4)	S4O7	1.438(4)
K1O8 ¹	2.787(4)	S4C4	1.772(5)
K1O4 ¹	2.799(4)	I8I9	2.7393(5)
K1S3 ¹	3.7187(16)	I1I1I1 ³	2.7301(7)
K1S4 ¹	3.7361(16)	I10I10 ⁴	2.7273(9)
K1S1 ¹	3.7472(16)		

¹+X,3/2-Y,1/2+Z; ²+X,3/2-Y,-1/2+Z; ³1-X,2-Y,1-Z; ⁴1-X,2-Y,-Z

C.2.4 Bond angles (°) for (CH₃SO₂I)₄•KI₃•2I₂

I5I6I7	176.089(16)	O7K1K1 ²	52.83(9)
O7K1O5	68.58(12)	O5K1K1 ²	52.39(10)
O7K1O1	69.86(13)	O1K1K1 ²	54.21(9)
O5K1O1	106.60(12)	O3K1K1 ²	55.38(8)
O7K1O3	108.20(11)	O21K1K1 ²	112.35(9)
O5K1O3	70.12(12)	O61K1K1 ²	112.09(9)
O1K1O3	69.39(12)	O81K1K1 ²	112.61(9)
O7K1O2 ¹	75.18(12)	O41K1K1 ²	111.71(9)
O5K1O2 ¹	141.81(13)	S31K1K1 ²	126.54(3)
O1K1O2 ¹	70.43(13)	S41K1K1 ²	127.07(4)
O3K1O2 ¹	135.11(12)	S1 ¹ K1K1 ²	126.10(3)
O7K1O6 ¹	134.19(13)	O1S1O2	118.9(2)
O5K1O6 ¹	70.16(13)	O1S1C1	109.3(3)
O1K1O6 ¹	142.47(13)	O2S1C1	109.2(3)
O3K1O6 ¹	74.80(12)	O1S1I ¹	105.56(17)
O2 ¹ K1O6 ¹	135.53(11)	O2S1I1	107.77(18)
O7K1O8 ¹	142.40(13)	C1S1I1	105.30(19)
O5K1O8 ¹	134.87(13)	O1S1K1 ²	83.51(18)
O1K1O8 ¹	74.42(12)	O2S1K1 ²	38.09(17)
O3K1O8 ¹	68.42(12)	C1S1K1 ²	139.90(19)

O2 ¹ K1O8 ¹	82.29(12)	I1S1K1 ²	107.40(4)
O6 ¹ K1O8 ¹	82.46(12)	O3S2O4	119.0(2)
O7K1O4 ¹	68.16(13)	O3S2C2	109.6(3)
O5K1O4 ¹	77.99(13)	O4S2C2	108.9(3)
O1K1O4 ¹	132.25(13)	O3S2I2	106.58(17)
O3K1O4 ¹	146.34(13)	O4S2I2	107.60(19)
O2 ¹ K1O4 ¹	77.74(13)	C2S2I2	104.2(2)
O6 ¹ K1O4 ¹	84.67(13)	O6S3O5	118.8(3)
O8 ¹ K1O4 ¹	135.52(11)	O6S3C3	109.2(3)
O7K1S3 ¹	128.88(10)	O5S3C3	109.4(3)
O5K1S3 ¹	77.51(10)	O6S3I3	107.55(18)
O1K1S3 ¹	159.42(9)	O5S3I3	105.54(17)
O3K1S3 ¹	94.07(9)	C3S3I3	105.46(19)
O2 ¹ K1S3 ¹	119.09(9)	O6S3K1 ²	39.77(17)
O6 ¹ K1S3 ¹	19.30(9)	O5S3K1 ²	81.04(19)
O8 ¹ K1S3 ¹	88.36(9)	C3S3K1 ²	139.3(2)
O4 ¹ K1S3 ¹	68.19(10)	I3S3K1 ²	109.28(4)
O7K1S4 ¹	159.58(10)	O8S4O7	118.7(2)
O5K1S4 ¹	129.69(10)	O8S4C4	109.5(3)
O1K1S4 ¹	93.66(9)	O7S4C4	109.1(3)
O3K1S4 ¹	75.30(8)	O8S4I4	107.62(18)
O2 ¹ K1S4 ¹	88.19(9)	O7S4I4	106.42(17)

O6 ¹ K1S4 ¹	66.21(9)	C4S4I4	104.6(2)
O8 ¹ K1S4 ¹	19.25(9)	O8S4K1 ²	39.76(17)
O4 ¹ K1S4 ¹	120.35(9)	O7S4K1 ²	81.22(17)
S3 ¹ K1S4 ¹	69.61(3)	C4S4K1 ²	140.0(2)
O7K1S1 ¹	93.93(9)	I4S4K1 ²	109.21(4)
O5K1S1 ¹	159.05(10)	S1O1K1	139.1(2)
O1K1S1 ¹	76.25(10)	S1O2K1 ²	123.2(2)
O3K1S1 ¹	128.48(9)	S2O3K1	139.9(2)
O2 ¹ K1S1 ¹	18.76(9)	S2O4K1 ²	124.8(2)
O6 ¹ K1S1 ¹	120.52(9)	S3O5K1	139.8(2)
O8 ¹ K1S1 ¹	66.07(9)	S3O6K1 ²	120.9(2)
O4 ¹ K1S1 ¹	84.91(9)	S4O7K1	139.9(2)
S3 ¹ K1S1 ¹	107.34(3)	S4O8K1 ²	121.0(2)
S4 ¹ K1S1 ¹	69.77(3)		

¹ +X,3/2-Y,1/2+Z; ² +X,3/2-Y,-1/2+Z

C.2.5 Torsion angles (°) for (CH₃SO₂I)₄•KI₃•2I₂

O2S1O1K1	58.0(4)	C3S3O5K1	-61.1(5)
C1S1O1K1	-68.1(4)	I3S3O5K1	-174.2(3)
I1S1O1K1	179.1(3)	K1 ¹ S3O5K1	78.2(4)
K1 ¹ S1O1K1	72.8(3)	O5S3O6K1 ¹	20.3(4)
O1S1O2K1 ¹	24.2(4)	C3S3O6K1 ¹	146.7(2)
C1S1O2K1 ¹	150.4(3)	I3S3O6K1 ¹	-99.3(2)
I1S1O2K1 ¹	-95.7(2)	O8S4O7K1	63.6(4)
O4S2O3K1	58.6(4)	C4S4O7K1	-62.7(4)
C2S2O3K1	-67.5(4)	I4S4O7K1	-175.0(3)
I2S2O3K1	-179.7(3)	K1 ¹ S4O7K1	77.4(3)
O3S2O4K1 ¹	19.5(4)	O7S4O8K1 ¹	21.7(3)
C2S2O4K1 ¹	145.9(3)	C4S4O8K1 ¹	147.7(3)
I2S2O4K1 ¹	-101.7(2)	I4S4O8K1 ¹	-99.1(2)
O6S3O5K1	65.2(5)		

¹ +X, 3/2-Y, -1/2+Z

C.2.6 Anisotropic atomic displacement parameters (\AA^2) for crystals of $(\text{CH}_3\text{SO}_2\text{I})_4 \cdot \text{KI}_3 \cdot 2\text{I}_2$

The anisotropic atomic displacement factor exponent takes the form: $-2^2[h^2a^{*2}U_{11} + \dots + 2hka^*b^*U_{12}]$

Atom	U11	U22	U33	U12	U13	U23
I5	22.04(15)	26.03(15)	17.25(14)	-3.40(13)	6.61(13)	1.46(11)
I6	19.31(13)	21.96(13)	20.74(14)	0.00(12)	5.64(13)	1.24(11)
I7	18.80(14)	25.02(14)	15.95(13)	1.29(12)	4.45(12)	1.63(11)
I1	17.39(15)	36.3(2)	30.62(19)	-4.78(13)	9.08(16)	2.58(15)
I2	39.9(2)	19.07(15)	36.2(2)	-1.39(16)	15.9(2)	-8.35(14)
I3	17.86(14)	30.9(2)	27.88(18)	-2.82(13)	0.40(15)	-4.33(14)
I4	27.09(15)	14.64(12)	23.84(16)	0.62(13)	4.75(16)	3.44(11)
K1	15.7(4)	14.5(3)	15.5(4)	0.2(3)	5.3(4)	0.0(3)
S1	14.3(5)	16.9(5)	14.6(5)	1.3(4)	4.6(4)	1.4(4)
S2	19.8(5)	16.9(5)	14.0(5)	-4.5(4)	6.8(4)	-1.2(4)
S3	14.4(5)	16.7(5)	15.9(5)	1.6(4)	4.0(4)	-0.5(4)
S4	19.0(5)	14.2(5)	14.1(5)	-2.1(4)	5.1(4)	0.4(4)
O1	23.1(17)	18.1(17)	26(2)	4.2(14)	11.6(16)	1.0(15)
O2	23.0(18)	25(2)	14.5(16)	1.0(15)	2.5(14)	2.6(14)
O3	19.7(17)	19.3(16)	21.0(17)	-3.9(14)	5.5(14)	-4.1(13)
O4	33(2)	26(2)	17.0(17)	-4.8(17)	8.0(16)	2.7(15)
O5	20.0(18)	22.0(19)	25(2)	-0.3(15)	-1.9(16)	4.0(15)
O6	20.8(18)	30(2)	20.9(18)	1.8(15)	11.8(15)	-0.6(15)
O7	22.6(18)	19.1(16)	25.6(19)	-2.8(15)	4.5(16)	7.2(14)
O8	27(2)	22.4(19)	17.2(17)	2.1(15)	7.9(15)	-5.8(14)
C1	23(2)	21(2)	20(2)	4.8(19)	5.4(19)	3.2(18)

C2	21(2)	36(3)	24(3)	-9(2)	11(2)	-2(2)
C3	22(2)	24(3)	17(2)	5.0(19)	6.1(18)	-1.6(19)
C4	24(2)	26(3)	17(2)	-8(2)	3.7(19)	-3.9(19)
I8	26.31(16)	21.58(16)	24.27(17)	2.65(13)	11.30(14)	3.91(12)
I9	22.49(15)	19.98(15)	18.87(15)	3.99(12)	7.09(12)	0.57(12)
I11	21.98(15)	16.47(14)	19.97(15)	-1.17(11)	3.17(12)	0.13(11)
I10	37.2(2)	20.47(16)	25.26(17)	-8.01(14)	13.08(15)	-0.73(13)

C.2.7 Hydrogen bond distances (Å) and angles (°) for (CH₃SO₂I)₄•KI₃•2I₂

DHA	d(D-H)/Å	d(H-A)/Å	(D-A)/Å	D-H-A/°
C1H1BI5 ¹	0.98	3.28	112(5)	144.1
C2H2AI8 ²	0.98	3.27	4.249(6)	173.1
C2H2CI9 ³	0.98	3.16	3.791(6)	123.5
C3H3CI7 ⁴	0.98	3.16	4.031(5)	148.4
C4H4AI10	0.98	3.18	4.132(6)	165.2
C4H4CI11	0.98	3.3	3.852(5)	117.2

¹_{+X,3/2-Y,1/2+Z}; ²_{-1+X,3/2-Y,-1/2+Z}; ³_{1-X,-1/2+Y,1/2-Z}; ⁴_{-1+X,+Y,-1+Z}

C.2.8 Hydrogen atomic coordinates and isotropic atomic displacement parameters (\AA^2) for $(\text{CH}_3\text{SO}_2\text{I})_4 \cdot \text{KI}_3 \cdot 2\text{I}_2$

Atom	x	y	z	U(eq)
H1A	4331.25	6339.69	3275.73	32
H1B	5325.49	6620.21	4155.22	32
H1C	5238.31	6295.86	2690.96	32
H2A	295.51	5980.45	211.79	39
H2B	315.42	6481.95	1184.72	39
H2C	867.49	5975.87	1959.92	39
H3A	647.23	8643.53	1408.28	32
H3B	-293.53	8340.43	1453.58	32
H3C	-328.01	8668.8	17.89	32
H4A	4725.88	8963.38	2558.43	35
H4B	4623.06	8472.85	3501.12	35
H4C	4080.17	8993.23	3629.55	35

C.3 $\text{Ca}_2(\text{CH}_3\text{SO}_2)_2(\text{CH}_3\text{SO}_3)\text{I}_3 \cdot (\text{H}_2\text{O})_3$

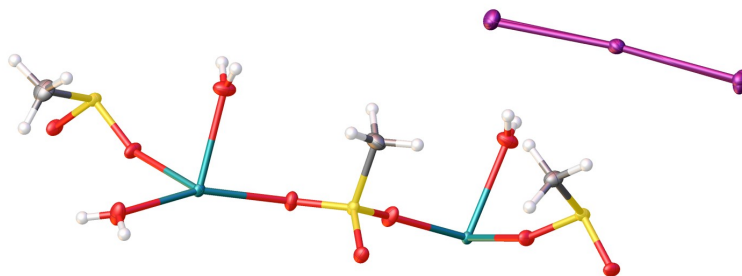


Figure C.7: Asymmetric unit $\text{Ca}_2(\text{CH}_3\text{SO}_2)_2(\text{CH}_3\text{SO}_3)\text{I}_3 \cdot (\text{H}_2\text{O})_3$

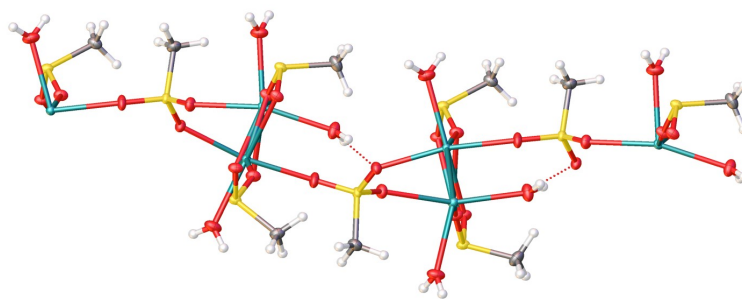


Figure C.8: Portion of $\text{Ca}_2(\text{CH}_3\text{SO}_2)_2(\text{CH}_3\text{SO}_3)\text{I}_3 \cdot (\text{H}_2\text{O})_3$ showing hydrogen bonding

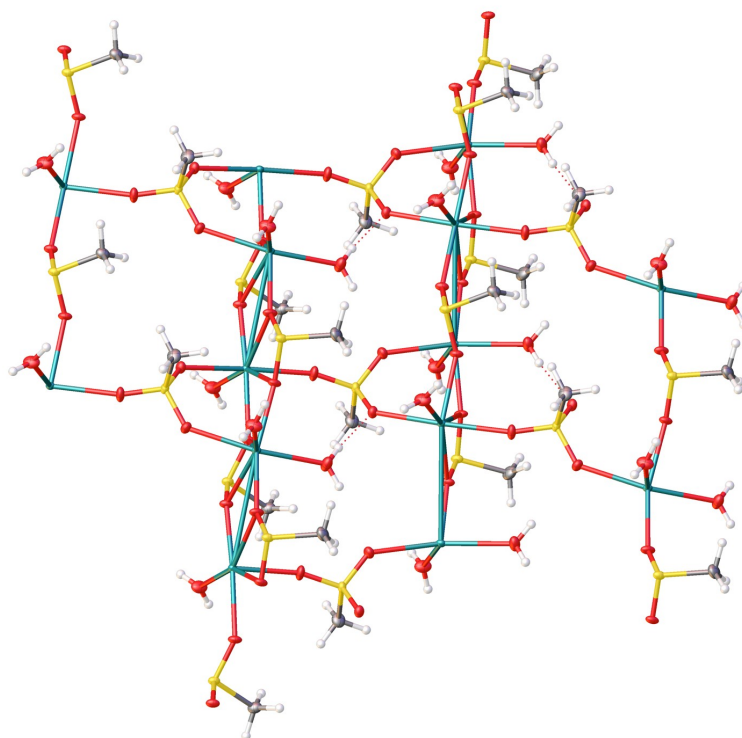


Figure C.9: Asymmetric unit of $\text{Ca}_2(\text{CH}_3\text{SO}_2)_2(\text{CH}_3\text{SO}_3)\text{I}_3 \cdot (\text{H}_2\text{O})_3$ showing network connectivity and hydrogen bonding. The I_3^- is eliminated for clarity

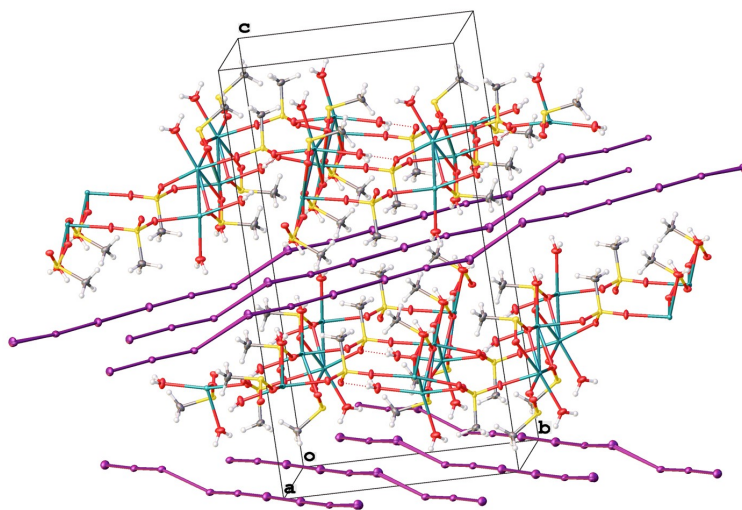


Figure C.10: Molecular packing of $\text{Ca}_2(\text{CH}_3\text{SO}_2)_2(\text{CH}_3\text{SO}_3)\text{I}_3 \cdot (\text{H}_2\text{O})_3$ showing the two-dimensional polyiodide sheeting

C.3.1 Crystal data and structure refinement for the crystals of



Identification code	Stanbury010418
Chemical formula	$\text{C}_3\text{H}_{15}\text{Ca}_2\text{I}_3\text{O}_{10}\text{S}_3$
Formula weight	768.19 g/mol
Temperature	100(2) K
Crystal size	0.040 x 0.063 x 0.536 mm
Crystal habit	clear pale blue-brown rod
Crystal system	monoclinic
Space group	$P2_1/n$
Unit cell dimensions	$a = 6.8708(3) \text{ \AA}$, $\alpha = 90^\circ$ $b = 12.7278(6) \text{ \AA}$, $\beta = 92.486(2)^\circ$ $c = 23.3016(11) \text{ \AA}$, $\gamma = 90^\circ$
Volume	$2035.81(16) \text{ \AA}^3$
Z	4
Density (calculated)	2.506 g/cm^3
Absorption coefficient	5.449 mm^{-1}
F(000)	1440
Diffractometer	Bruker D8 VENTURE κ -geometry diffractometer
Radiation source	Incoatec I μ S 3.0 microfocus sealed tube (Mo K α , $\lambda = 0.71073 \text{ \AA}$)
Theta range for data collection	2.37 to 36.37 $^\circ$

Index ranges	-11<=h<=11, -21<=k<=21, -38<=l<=38
Reflections collected	133232
Independent reflections	9887 [R(int) = 0.0367]
Absorption correction	Multi-Scan
Max. and min. transmission	0.8120 and 0.1580
Structure solution technique	direct methods
Structure solution program	SHELXT 2014/5 (Sheldrick, 2014)
Refinement method	Full-matrix least-squares on F ²
Refinement program	SHELXL-2017/1 (Sheldrick, 2017)
Function minimized	$\Sigma w(F_o^2 - F_c^2)^2$
Data / restraints / parameters	9887 / 9 / 239
Goodness-of-fit on F ²	1.244
Final R indices	9735 data; I>2 σ (I), R1 = 0.0178, wR2 = 0.0424 all data, R1 = 0.0181, wR2 = 0.0425
Largest diff. peak and hole	0.882 and -0.850 eÅ ⁻³

C.3.2 Atomic coordinates and equivalent isotropic atomic displacement parameters (Å²) for Ca₂(CH₃SO₂)₂(CH₃SO₃)I₃•(H₂O)₃

U(eq) is defined as one third of the trace of the orthogonalized U_{ij} tensor.

	x/a	y/b	z/c	U(eq)
Ca1	0.36393(3)	0.86685(2)	0.69699(2)	0.00947(4)
Ca04	0.63212(3)	0.33726(2)	0.72942(2)	0.00860(3)
S1	0.12342(4)	0.31870(2)	0.67232(2)	0.01153(5)
S2	0.63026(4)	0.62346(2)	0.69781(2)	0.01137(5)
S3	0.85675(4)	0.90217(2)	0.64040(2)	0.01204(5)
O1	0.29630(12)	0.31257(8)	0.71596(4)	0.01340(15)
O2	0.95590(13)	0.35921(8)	0.70727(4)	0.01442(15)
O1W	0.34757(16)	0.84078(10)	0.59604(5)	0.0217(2)
O3	0.59567(16)	0.51328(7)	0.70957(5)	0.01861(18)
O2W	0.36216(17)	0.05087(9)	0.71999(6)	0.0226(2)
O4	0.79315(14)	0.66580(7)	0.73387(4)	0.01441(15)
O3W	0.60823(17)	0.27070(10)	0.63298(5)	0.0215(2)
O5	0.45239(14)	0.68509(8)	0.70296(5)	0.01628(16)
O6	0.03215(13)	0.87518(9)	0.67997(4)	0.01558(16)
O7	0.68654(13)	0.89829(8)	0.68033(4)	0.01423(15)
C1	0.1813(2)	0.43268(12)	0.63171(6)	0.0180(2)
C2	0.6974(2)	0.63099(12)	0.62619(6)	0.0221(3)
C3	0.8853(2)	0.03940(12)	0.62859(7)	0.0237(3)
I1B	0.3395(3)	0.1051(2)	0.52467(11)	0.0255(4)
I2B	0.0276(5)	0.2612(3)	0.50943(11)	0.0119(3)
I3B	0.7114(3)	0.4149(2)	0.50544(7)	0.0140(3)
I1	0.34539(16)	0.10975(10)	0.52235(4)	0.01730(15)
I2	0.0218(3)	0.25794(16)	0.50981(7)	0.0170(3)
I3	0.7069(2)	0.40947(15)	0.50379(5)	0.0248(3)

C.3.3 Bond lengths (Å) for $\text{Ca}_2(\text{CH}_3\text{SO}_2)_2(\text{CH}_3\text{SO}_3)_3 \cdot (\text{H}_2\text{O})_3$

Ca1-O6	2.2993(9)	Ca1-O7	2.3018(9)
Ca1-O1W	2.3736(11)	Ca1-O5	2.3945(10)
Ca1-O2W	2.4028(11)	Ca1-O1	2.4490(9)
Ca1-O2	2.5058(10)	Ca1-S1	3.1037(4)
Ca1-Ca04	3.8152(3)	Ca1-Ca04	3.8994(3)
Ca04-O3	2.2991(10)	Ca04-O2	2.3224(9)
Ca04-O1	2.3363(9)	Ca04-O4	2.3916(9)
Ca04-O3W	2.4006(11)	Ca04-O6	2.4841(10)
Ca04-O7	2.5200(10)	Ca04-S3	3.1415(4)
S1-O2	1.5280(10)	S1-O1	1.5317(9)
S1-C1	1.7864(14)	S2-O3	1.4504(10)
S2-O5	1.4615(10)	S2-O4	1.4722(10)
S2-C2	1.7532(15)	S3-O6	1.5244(10)
S3-O7	1.5265(10)	S3-C3	1.7804(15)
I1B-I2B	2.932(3)	I2B-I3B	2.923(3)
I1-I2	2.9208(19)	I2-I3	2.897(2)

C.3.4 Bond angles (°) for $\text{Ca}_2(\text{CH}_3\text{SO}_2)_2(\text{CH}_3\text{SO}_3)\text{I}_3 \cdot (\text{H}_2\text{O})_3$

O6-Ca1-O7	156.58(4)	O6-Ca1-O1W	80.30(4)
O7-Ca1-O1W	82.05(4)	O6-Ca1-O5	107.57(4)
O7-Ca1-O5	86.21(4)	O1W-Ca1-O5	85.61(4)
O6-Ca1-O2W	88.79(4)	O7-Ca1-O2W	83.25(4)
O1W-Ca1-O2W	110.90(5)	O5-Ca1-O2W	158.84(4)
O6-Ca1-O1	71.21(3)	O7-Ca1-O1	131.26(3)
O1W-Ca1-O1	141.06(4)	O5-Ca1-O1	78.55(4)
O2W-Ca1-O1	94.79(4)	O6-Ca1-O2	127.10(3)
O7-Ca1-O2	73.43(3)	O1W-Ca1-O2	151.32(4)
O5-Ca1-O2	78.26(4)	O2W-Ca1-O2	81.16(4)
O1-Ca1-O2	58.27(3)	O6-Ca1-S1	99.42(3)
O7-Ca1-S1	102.33(3)	O1W-Ca1-S1	160.54(3)
O5-Ca1-S1	75.88(3)	O2W-Ca1-S1	88.51(3)
O1-Ca1-S1	29.09(2)	O2-Ca1-S1	29.21(2)
O6-Ca1-Ca04	162.89(3)	O7-Ca1-Ca04	39.75(2)
O1W-Ca1-Ca04	115.76(3)	O5-Ca1-Ca04	69.84(2)
O2W-Ca1-Ca04	90.53(3)	O1-Ca1-Ca04	91.82(2)
O2-Ca1-Ca04	36.14(2)	S1-Ca1-Ca04	63.469(8)
O6-Ca1-Ca04	37.00(2)	O7-Ca1-Ca04	163.21(3)
O1W-Ca1-Ca04	114.68(3)	O5-Ca1-Ca04	96.06(3)

O2W-Ca1-Ca04	89.03(3)	O1-Ca1-Ca04	34.48(2)
O2-Ca1-Ca04	90.70(2)	S1-Ca1-Ca04	62.440(8)
Ca04-Ca1-Ca04	125.900(9)	O3-Ca04-O2	86.28(4)
O3-Ca04-O1	90.33(4)	O2-Ca04-O1	159.44(3)
O3-Ca04-O4	168.80(4)	O2-Ca04-O4	89.80(4)
O1-Ca04-O4	96.94(4)	O3-Ca04-O3W	98.81(4)
O2-Ca04-O3W	82.05(4)	O1-Ca04-O3W	78.45(4)
O4-Ca04-O3W	91.02(4)	O3-Ca04-O6	86.11(4)
O2-Ca04-O6	129.83(3)	O1-Ca04-O6	69.99(3)
O4-Ca04-O6	88.38(4)	O3W-Ca04-O6	148.11(4)
O3-Ca04-O7	85.01(4)	O2-Ca04-O7	72.82(3)
O1-Ca04-O7	127.10(3)	O4-Ca04-O7	83.81(3)
O3W-Ca04-O7	154.31(4)	O6-Ca04-O7	57.13(3)
O3-Ca04-S3	86.32(3)	O2-Ca04-S3	101.51(3)
O1-Ca04-S3	98.49(2)	O4-Ca04-S3	84.19(3)
O3W-Ca04-S3	173.99(3)	O6-Ca04-S3	28.50(2)
O7-Ca04-S3	28.69(2)	O3-Ca04-Ca1	94.76(3)
O2-Ca04-Ca1	39.52(2)	O1-Ca04-Ca1	160.98(2)
O4-Ca04-Ca1	75.68(2)	O3W-Ca04-Ca1	118.65(3)
O6-Ca04-Ca1	92.05(2)	O7-Ca04-Ca1	35.74(2)
S3-Ca04-Ca1	63.672(7)	O3-Ca04-Ca1	84.53(3)

O2-Ca04-Ca1	161.83(3)	O1-Ca04-Ca1	36.40(2)
O4-Ca04-Ca1	96.26(3)	O3W-Ca04-Ca1	114.84(3)
O6-Ca04-Ca1	33.85(2)	O7-Ca04-Ca1	90.76(2)
S3-Ca04-Ca1	62.300(8)	Ca1-Ca04-Ca1	125.900(9)
O2-S1-O1	104.11(5)	O2-S1-C1	101.44(6)
O1-S1-C1	102.07(6)	O2-S1-Ca1	53.15(4)
O1-S1-Ca1	51.01(4)	C1-S1-Ca1	111.23(5)
O3-S2-O5	111.03(6)	O3-S2-O4	111.89(6)
O5-S2-O4	111.98(6)	O3-S2-C2	106.55(7)
O5-S2-C2	107.72(7)	O4-S2-C2	107.36(7)
O6-S3-O7	103.33(5)	O6-S3-C3	103.00(7)
O7-S3-C3	102.63(7)	O6-S3-Ca04	51.04(4)
O7-S3-Ca04	52.42(4)	C3-S3-Ca04	114.15(6)
S1-O1-Ca04	144.61(6)	S1-O1-Ca1	99.90(4)
Ca04-O1-Ca1	109.13(4)	S1-O2-Ca04	145.97(6)
S1-O2-Ca1	97.65(4)	Ca04-O2-Ca1	104.34(4)
S2-O3-Ca04	164.33(7)	S2-O4-Ca04	133.18(6)
S2-O5-Ca1	136.46(6)	S3-O6-Ca1	150.06(6)
S3-O6-Ca04	100.45(4)	Ca1-O6-Ca04	109.15(4)
S3-O7-Ca1	151.30(6)	S3-O7-Ca04	98.88(4)
Ca1-O7-Ca04	104.51(4)	I3B-I2B-I1B	174.78(13)
I3-I2-I1	176.75(7)		

C.3.5 Torsion angles (°) for $\text{Ca}_2(\text{CH}_3\text{SO}_2)_2(\text{CH}_3\text{SO}_3)\text{I}_3\cdot(\text{H}_2\text{O})_3$

O2-S1-O1-Ca04	-142.67(10)	C1-S1-O1-Ca04	-37.43(12)
Ca1-S1-O1-Ca04	-145.09(13)	O2-S1-O1-Ca1	2.41(6)
C1-S1-O1-Ca1	107.66(6)	O1-S1-O2-Ca04	-132.55(10)
C1-S1-O2-Ca04	121.73(11)	Ca1-S1-O2-Ca04	-130.21(12)
O1-S1-O2-Ca1	-2.35(6)	C1-S1-O2-Ca1	-108.06(5)
O5-S2-O3-Ca04	-166.5(3)	O4-S2-O3-Ca04	-40.5(3)
C2-S2-O3-Ca04	76.5(3)	O3-S2-O4-Ca04	-151.37(8)
O5-S2-O4-Ca04	-25.97(10)	C2-S2-O4-Ca04	92.07(9)
O3-S2-O5-Ca1	176.28(8)	O4-S2-O5-Ca1	50.41(11)
C2-S2-O5-Ca1	-67.41(11)	O7-S3-O6-Ca1	-167.23(13)
C3-S3-O6-Ca1	-60.66(15)	Ca04-S3-O6-Ca1	-171.35(16)
O7-S3-O6-Ca04	4.11(6)	C3-S3-O6-Ca04	110.69(7)
O6-S3-O7-Ca1	-148.50(12)	C3-S3-O7-Ca1	104.64(13)
Ca04-S3-O7-Ca1	-144.47(15)	O6-S3-O7-Ca04	-4.04(6)
C3-S3-O7-Ca04	-110.89(6)		

C.3.6 Anisotropic atomic displacement parameters (\AA^2) for the crystals of $\text{Ca}_2(\text{CH}_3\text{SO}_2)_2(\text{CH}_3\text{SO}_3)\text{I}_3 \cdot (\text{H}_2\text{O})_3$

The anisotropic atomic displacement factor exponent takes the form: $-2^2[h^2a^{*2}U_{11} + \dots + 2hka^*b^*U_{12}]$

	U11	U22	U33	U23	U13	U12
Ca1	0.00602(7)	0.01137(8)	0.01102(8)	0.00075(6)	0.00025(6)	0.00052(6)
Ca04	0.00612(7)	0.00936(8)	0.01030(8)	0.00012(6)	0.00019(6)	0.00021(6)
S1	0.00773(9)	0.01656(12)	0.01027(10)	-0.00103(9)	-0.00010(8)	-0.00075(8)
S2	0.01183(10)	0.00845(10)	0.01364(11)	-0.00042(8)	-0.00162(9)	0.00075(8)
S3	0.00842(10)	0.01708(12)	0.01060(10)	0.00217(9)	0.00023(8)	0.00055(9)
O1	0.0070(3)	0.0216(4)	0.0115(3)	-0.0001(3)	-0.0005(3)	-0.0004(3)
O2	0.0071(3)	0.0223(4)	0.0141(4)	-0.0002(3)	0.0019(3)	-0.0002(3)
O1W	0.0191(4)	0.0332(6)	0.0127(4)	-0.0018(4)	0.0004(3)	-0.0034(4)
O3	0.0199(4)	0.0086(3)	0.0267(5)	0.0017(3)	-0.0062(4)	-0.0009(3)
O2W	0.0187(4)	0.0145(4)	0.0341(6)	-0.0048(4)	-0.0057(4)	0.0022(3)
O4	0.0144(4)	0.0113(3)	0.0172(4)	-0.0015(3)	-0.0029(3)	-0.0005(3)
O3W	0.0198(4)	0.0304(5)	0.0145(4)	-0.0063(4)	0.0020(3)	-0.0021(4)
O5	0.0132(4)	0.0128(4)	0.0227(4)	-0.0005(3)	-0.0010(3)	0.0030(3)
O6	0.0069(3)	0.0248(4)	0.0149(4)	0.0045(3)	-0.0001(3)	0.0021(3)
O7	0.0069(3)	0.0209(4)	0.0151(4)	0.0040(3)	0.0016(3)	-0.0005(3)
C1	0.0162(5)	0.0223(6)	0.0153(5)	0.0037(4)	0.0009(4)	-0.0014(4)
C2	0.0291(7)	0.0220(6)	0.0154(5)	-0.0037(4)	0.0034(5)	0.0005(5)
C3	0.0241(6)	0.0200(6)	0.0271(7)	0.0097(5)	0.0026(5)	-0.0022(5)
I1B	0.0211(4)	0.0237(4)	0.0323(7)	0.0044(3)	0.0053(3)	0.0095(3)
I2B	0.0140(4)	0.0128(4)	0.0091(4)	-0.0020(3)	0.0025(3)	0.0002(3)
I3B	0.0173(4)	0.0147(3)	0.0098(4)	-0.00073(19)	-0.0010(2)	0.0049(2)
I1	0.01582(18)	0.02157(19)	0.0145(3)	0.00012(13)	0.00096(12)	0.00363(15)
I2	0.0194(4)	0.0181(4)	0.0134(3)	-0.00055(19)	-0.0008(2)	0.0009(2)
I3	0.0274(3)	0.0220(3)	0.0248(4)	0.00155(18)	-0.0009(2)	0.00840(19)

C.3.7 Hydrogen atomic coordinates and isotropic atomic displacement parameters (\AA^2) for $\text{Ca}_2(\text{CH}_3\text{SO}_2)_2(\text{CH}_3\text{SO}_3)\text{I}_3 \cdot (\text{H}_2\text{O})_3$

	x/a	y/b	z/c	U(eq)
H1A	1.2965	0.4186	0.6096	0.027
H1B	1.2081	0.4917	0.6579	0.027
H1C	1.0710	0.4503	0.6054	0.027
H2A	0.5932	0.6016	0.6010	0.033
H2B	0.8176	0.5910	0.6216	0.033
H2C	0.7190	0.7046	0.6159	0.033
H3A	0.0043	1.0517	0.6078	0.036
H3B	-0.1051	1.0760	0.6656	0.036
H3C	-0.2273	1.0660	0.6058	0.036
H1WA	0.258(3)	0.8128(19)	0.5759(10)	0.028
H1WB	0.423(3)	0.861(2)	0.5705(9)	0.028
H2WA	0.467(3)	1.0797(19)	0.7333(11)	0.028
H2WB	0.271(3)	1.0880(18)	0.7302(11)	0.028
H3WA	0.536(3)	0.2234(16)	0.6202(11)	0.028
H3WB	0.651(4)	0.3016(18)	0.6051(9)	0.028

**C.3.8 Hydrogen bond distances (Å) and angles (°) for the crystals of
 $\text{Ca}_2(\text{CH}_3\text{SO}_2)_2(\text{CH}_3\text{SO}_3)\text{I}_3 \cdot (\text{H}_2\text{O})_3$**

	Donor-H	Acceptor-H	Donor-Acceptor	Angle
O2W-H2WA...O4	0.852(16)	2.098(16)	2.9468(15)	174.(2)
O1W-H1WB...I1B'	0.842(16)	2.846(17)	3.679(4)	170.(2)
O3W-H3WA...I1B'	0.829(16)	2.962(19)	3.717(2)	152.(2)
O1W-H1WA...I2B'	0.838(16)	2.889(17)	3.717(4)	170.(2)
O2W-H2WB...O5	0.826(16)	2.555(18)	3.3391(16)	159.(2)
O3W-H3WB...I3B'	0.824(16)	2.780(17)	3.5899(19)	168.(2)
C2-H2A...I3B'	0.98	3.18	4.110(3)	158.5
C2-H2C...S3	0.98	2.74	3.6318(16)	151.9
C3-H3A...I1B'	0.98	3.15	4.118(4)	170.5